IMPERIAL

Imperial College London

Faculty of Engineering

Department of Chemical Engineering

Protic Ionic Liquid-Based Biorefinery—Pathways for Cellulose and Hemicellulose Valorization

Chaoyue Zhang

Supervised by:

Professor Jason P. Hallett

Professor Paul S. Fennell

A thesis submitted for the degree of Doctor of Philosophy

October 2025

Declaration of Originality

I declare that the work in this thesis was carried out at Imperial College London between October 2021 and October 2025. The work was conducted by me, except where stated otherwise, and has not been submitted for a postgraduate doctoral degree at this or any other university. Work undertaken with others and support from Bioataraxis Ltd is acknowledged in the text. Information derived from the published work of others is cited. I used ChatGPT-5, a generative AI tool developed by OpenAI (https://chat.openai.com), solely for language refinement. The tool was used only to improve grammar and clarity.

Copyright Declaration

The copyright of this thesis rests with the author. Unless otherwise indicated, its contents are licensed under a Creative Commons Attribution Non-Commercial 4.0 International License (CC BY-NC). Under this license, you may copy and redistribute the material in any medium or format. You may also create and distribute modified versions of the work. This is on the condition that you credit the author and do not use it, or any derivative works, for a commercial purpose. When reusing or sharing this work, ensure you make the license terms clear to others by naming the license and linking to the license text. Where a work has been adapted, you should indicate that the work has been changed and describe those changes. Please seek permission from the copyright holder for uses of this work that are not included in this license or permitted under UK Copyright Law.

Publications

(1) Max P. Papajewski, Suhaib Nisar, Chaoyue Zhang, Jason P. Hallett, Jakob Albert*. Boosting furfural production by combining polyoxometalates and ionic liquids for effective fractionation of lignocellulosic biomass. *RSC Advances*. 2025;15(18):14259–63.

(2) Chaoyue Zhang, Suhaib Nisar, Yichen Liu, Pedro Verdía Barbará, Pedro Nakasu, Paul S. Fennell*, Jason P. Hallett*. Process Intensification via Probe Sonication in Protic Ionic Liquid Pretreatment of Biomass (ready for submission).

(3) Chaoyue Zhang, Antonio Ovejero-Pérez, Paul S. Fennell*, Jason P. Hallett*, Amir Al Ghatta*. Design and Optimization of a New Efficient Furfural Production Technology via a Protic Ionic Liquid at “Quasi-Economic” Viability (ready for submission).

*Corresponding authors.

Abstract

Lignocellulosic biomass is a carbon-neutral feedstock for biofuels and biochemicals, but its potential depends on cost-effective fractionation and the full valorization of each component. Our group has developed low-cost protic ionic liquids (PILs), such as *N*,*N*-dimethylbutylammonium hydrogen sulfate ([DMBA][HSO_4]), that extract hemicellulose and lignin in a one-pot ionoSolv process, leaving a cellulose-rich pulp.

First, we evaluated probe sonication to accelerate the ionoSolv process at mild temperatures. The sonication effect was strongly feedstock-dependent: for *Miscanthus*, acceleration was confined to the early stage (0–1 h), whereas for recalcitrant spruce, it remained pronounced after 4 h at 130 °C. Quantitative analysis indicated that sonication-induced heating, rather than mass transfer enhancement, was the main driver.

Second, using the same PIL platform, we targeted hemicellulose valorization via furfural production. Prior work has confirmed furfural formation but faced side reactions due to inadequate in situ furfural separation, which forced low biomass loadings. We therefore coupled hemicellulose hydrolysis–dehydration with steam stripping to remove furfural as it formed and implemented strict process control with stepwise biomass feeding. At 30 wt% biomass loading, the system delivered a >75% isolated yield by minimizing the furfural residence time in the acidic, recyclable [DMBA][HSO_4], suppressing condensation with substrates and intermediates. A techno-economic analysis suggested that co-recovering cellulose would be essential for the process's commercial viability.

Finally, to extend the value chain, we developed a continuous process for oxidizing furfural to furoic acid, a higher-value intermediate for biopolymers and bio-based surfactants. Using a robust Ru/C catalyst in a high-pressure continuous-flow system, the process achieved a >90% furfural conversion and a >90% furoic acid yield with

stable operation, successfully scaling the technique to the liter level and offering guidance for further industrial deployment.

Collectively, these results support the development of an integrated PIL-based biorefinery for efficient cellulose and hemicellulose valorization.

Acknowledgments

As I write these acknowledgments, my Ph.D. thesis is nearing completion. Looking back, this has truly been a journey—full of hard-won joys and inevitable setbacks. I want to take this moment to thank all those who supported and guided me along the way. Without you, I could not have finished.

First and foremost, my deepest thanks go to my supervisors, Professor Jason Hallett and Professor Paul Fennell. Thank you for being patient with my mistakes, for standing by me, for giving me the freedom to explore, and for helping me grow. Your support when things were difficult meant more than I can say. It has been an honor to be under your supervision.

I am also grateful to my project mentor, Dr. Amir Al Ghatta. Your insight and advice were always meaningful and timely. I learned a great deal from you—not only scientifically but also in how to approach work and life. You were like an older brother to me: patient, kind, and caring.

My heartfelt thanks go to my “meal buddies”—Bryan, “JieJie” Priyanka, Ruihua, Xuantong, Mengjiao, and Boyuan. You lifted me up when experiments failed and reminded me to keep going. Your warmth gave me the strength to carry on.

I am grateful to all the colleagues and friends I had the pleasure of working with: Dr. Pedro Verdía, Dr. Pedro Nakasu, Dr. Yichen Liu, Dr. Yiyan Chen, Dr. Amir Mohammad Dezashibi, Dr. Antonio Ovejero-Pérez, Dr. Max Papajewski, Dr. Cariny Polesca, Dr. Perrakis Bistis, Dr. Aida Abouelela, Dr. Suhaib Nisar, Sasha, Sarah, Susi, Yongze, Chang Liu, Tongxin, Suri, Yiming, Wenyan, Wenli, Phuthiphong, Jules, Amarthya, James Strain, James Perry, Kirthiya, Shadrach, Heather, Isabel, Rupali, Peter, and Masahiro. Thank you for your help, your time, and the many things you taught me. It was a privilege to work with you.

Many thanks to Dr. Televantos for so kindly establishing the scholarship program that supported my Ph.D.

Above all, I thank my parents, as well as my uncle and aunt, for being my strongest support. I hope I have not let you down.

Glossary

$[Bmim]^+$	1-butyl-3-methylimidazolium
$[DMBA]^+$	*N,N*-dimethylbutylammonium
$[EtNH_3]^+$	Ethylammonium
$[Emim]^+$	1-ethyl-3-methylimidazolium
$[HC1im]^+$ or $[Hmim]^+$	1-methylimidazolium
$[HTMG]^+$	Tetramethylguanidinium
$[TEA]^+$	Triethylammonium
$[BF_4]^-$	Tetrafluoroborate
$[HC_2O_4]^-$	Hydrogen oxalate
$[HSO_4]^-$	Hydrogen sulfate
$[MeCO_3]^-$	Monomethyl carbonate
$[OAc]^-$	Acetate
$[OTf]^-$	Trifluoromethanesulfonate
$[PF_6]^-$	Hexafluorophosphate
$[RSO_3]^-$	Alkylsulfonate
AFEX	Ammonia fiber expansion
AIL	Acid insoluble lignin
ANOVA	Analysis of variance
APIL	Aprotic ionic liquid
ASL	Acid soluble lignin
at%	Atomic percentage
BET	Brunauer-Emmett-Teller
BJH	Barrett-Joyner-Halenda
BOD	Biochemical oxygen demand
BPR	Back-pressure regulator
BTX	Benzene, toluene, xylene
CAPEX	Capital expenditure
CHP	Combined heat and power

COD	Chemical oxygen demand
CPME	Cyclopentyl methyl ether
DCM	Dichloromethane
DFT	Density functional theory
DMSO	Dimethyl sulfoxide
EFB	Extractive-free biomass
FA	Ferulic acid
FDCA	2,5-furandicarboxylic acid
G	Guaiacyl
GHG	Greenhouse gas
GBL	γ-butyrolactone
GHL	γ-hexalactone
GVL	γ-valerolactone
H	p-hydroxyphenyl
HHV	Higher heating value
HMF	5-hydroxymethylfurfural
HPLC	High performance liquid chromatography
HSQC	Heteronuclear single quantum coherence
ICP-MS	Inductively coupled plasma mass spectrometry
IL	Ionic liquid
LA	Levulinic acid
LAS	Linear alkylbenzene sulfonate
LCA	Life cycle assessment
LCC	Lignin–carbohydrate complex
MD	Molecular dynamics
MIBK	Methyl isobutyl ketone
MSP	Minimum selling price
MWHT	Microwave-assisted hydrothermal
NMR	Nuclear magnetic resonance

NREL	National Renewable Energy Laboratory
ODW	Oven-dried weight
OPEX	Operating expenditure
PBR	Photobioreactor
PCA	p-coumaric acid
PEF	Polyethylene furanoate
PET	Polyethylene terephthalate
PIL	Protic ionic liquid
PMC	Particle migration and coalescence
PTFE	Polytetrafluoroethylene
S	Syringyl
SAF	Sulfonated alkyl furoate
SEM-EDX	Scanning electron microscopy with energy-dispersive X-ray spectroscopy
TEM	Transmission electron microscopy
THF	Tetrahydrofuran
THFA	Tetrahydrofurfuryl alcohol
UV-Vis	Ultraviolet-visible spectroscopy
XPS	X-ray photoelectron spectroscopy
XRD	X-ray diffraction
wt%	Weight percentage
1G	First generation
2G	Second generation
2-MeTHF	2-methyltetrahydrofuran
2-MF	2-methylfuran
3G	Third generation
$	United States dollar
€	Euro

Table of contents

Declaration of Originality 2

Copyright Declaration 2

Publications 2

Abstract 4

Acknowledgments 6

Glossary 8

List of Figures 16

List of Tables 27

Chapter 1: Introduction 28

1.1 Background and Research Gap 28

1.2 Thesis Structure 33

Chapter 2: Literature Review 36

2.1 Ionic Liquids 36

2.1.1 General Overview 36

2.1.2 Physicochemical Properties of Ionic Liquids 37

2.1.3 Commercialization of Ionic Liquids 40

2.1.4 Protic Ionic Liquids 42

2.1.5 Summary 48

2.2 Biorefinery 49

2.2.1 General Overview 49

2.2.2 Lignocellulose 52

2.2.3 Deconstruction of Lignocellulose 61

2.2.4 Summary 75

2.3 Furan Derivatives from Hemicellulose 76
2.3.1 Furfural Production 76
2.3.2 Catalytic Oxidation of Furfural to Furoic Acid 85
2.3.3 Summary 93
Chapter 3: Process Intensification via Probe Sonication in Protic Ionic Liquid Pretreatment of Biomass 95
3.1 Introduction 95
3.2 Materials and Methods 98
3.2.1 Feedstock 98
3.2.2 Biomass Moisture Content 98
3.2.3 Biomass Extractives 98
3.2.4 Synthesis of [DMBA][HSO_4] 99
3.2.5 Conventional IonoSolv Process 100
3.2.6 Sonication-Assisted IonoSolv Process 101
3.2.7 Separation of Fine and Coarse Pulp Layers after the Sonication-Assisted IonoSolv Process 102
3.2.8 Compositional Analysis 103
3.2.9 Enzymatic Hydrolysis 105
3.2.10 Quantitative Evaluation of Sonication-Induced Effects on the IonoSolv Process 106
3.2.11 Lignin Characterization 107
3.2.12 Errors and Uncertainties 107
3.3 Results and Discussion 108
3.3.1 Temperature Profiles for Different IonoSolv Methods 108

3.3.2 Effects of Different IonoSolv Processes on Grass Biomass Fractionation 110
3.3.3 Effects of Different IonoSolv Processes on Softwood Fractionation 118
3.3.4 Properties of the Upper (Finer) and Lower (Coarser) Pulp Layers Formed after the Sonication-Assisted IonoSolv Process 125
3.3.5 Quantitative Mechanistic Analysis of the Sonication-Induced Acceleration 128
3.3.6 Preliminary Techno-Economic Analysis 135
3.4 Conclusion 140
3.5 External Contributions 141
Chapter 4: Design and Optimization of a New Efficient Furfural Production Technology via a Protic Ionic Liquid at “Quasi-Economic” Viability 142
4.1 Introduction 142
4.2 Materials and Methods 145
4.2.1 Feedstock 145
4.2.2 Synthesis of [DMBA][HSO_4] 145
4.2.3 Semi-Continuous Furfural Production System 145
4.2.4 Stepwise Biomass Addition 147
4.2.5 Recovery and Recycling of [DMBA][HSO_4] 147
4.2.6 Characterization of Solid Residues from the IL Recycling Process 148
4.2.7 Sealed-Batch Furfural Production System 149
4.3 Results and Discussion 149
4.3.1 Reaction Setup 149
4.3.2 Effects of Key Process Parameters 153
4.3.3 Response Surface Methodology (RSM) of Process Parameters 155

4.3.4 Optimization of Furfural Yield at High Biomass Loading (30 wt%) 170
4.3.5 Recyclability Evaluation of [DMBA][HSO_4] 173
4.3.6 Characterization of Solid Residues from the IL Recycling Process 178
4.3.7 Preliminary Techno-Economic Analysis 181
4.3.8 Future Outlook 188
4.4. Conclusion 188
4.5 External Contributions 189
Chapter 5: High-Pressure Continuous-Flow Aerobic Oxidation of Furfural to Furoic Acid over Robust Ru/C 190
5.1 Introduction 190
5.2 Materials and Methods 193
5.2.1 Feedstock 193
5.2.2 High-Pressure Continuous-Flow System 194
5.2.3 Catalyst Characterization 196
5.3 Results and Discussion 198
5.3.1 Preliminary Batch Oxidation of Furfural to Furoic Acid 198
5.3.2 Continuous Oxidation of Furfural to Furoic Acid 198
5.3.3 Characterization of Fresh and Spent 10 wt% Ru/C Catalysts 210
5.3.4 Proposed Mechanisms for the Oxidation of Furfural to Furoic Acid over 10 wt% Ru/C 215
5.4 Conclusion 217
5.5 External Contributions 218
Chapter 6: Conclusions and Future Work 219
6.1 Thesis Conclusions 219
6.2 Suggestions for Future Work 222

Appendices 227

References..... 250

List of Figures

Figure 2.1. Representative cations and anions used in ionic liquids. 37

Figure 2.2. Number of publications and patents related to ionic liquids, 1990–2019. Reproduced from Greer et al. [79]. 41

Figure 2.3. (a) Total solvent cost, including direct production costs and indirect externalities; and (b) Total solvent production cost per unit mass of pretreated biomass. Reproduced from Baaqel et al. [145]..... 46

Figure 2.4. Reactor setup and associated electronic devices for protic ionic liquid production (schematic). Reproduced from Dezashibi et al. [146]. 48

Figure 2.5. Classification of three biorefinery types and their respective advantages and challenges. 52

Figure 2.6. Three-dimensional arrangement of cellulose, hemicellulose, and lignin within the cell walls of lignocellulosic biomass. Reproduced from Brethauer et al. [169], with the structures of cellulose, hemicellulose, and lignin adapted from Rozmysłowicz et al. [173]. 53

Figure 2.7. Interconversion between the linear (open-chain) and cyclic forms of glucose in the water. 54

Figure 2.8. Hierarchical scale of cellulose—from individual molecular chains to macroscopic sources. Reproduced from Lavoine et al. [182]. 55

Figure 2.9. Conversion pathway from cellulose to HMF and onward to LA. Reproduced from Ma et al. [205]..... 57

Figure 2.10. Major linkages and structural subunits in native lignin. Reproduced from Brandt-Talbot et al. [19]..... 60

Figure 2.11. Representative physicochemical phenomena induced by probe sonication in a liquid medium. Reproduced from Flores et al. [46]..... 75

Figure 2.12. Representative H_2SO_4-catalyzed (Brønsted acid–catalyzed) hydrolysis pathway from hemicellulose (homoxylan) to xylose and then to furfural. Reproduced from Enslow et al. [349]. 77

Figure 2.13. Schematic of the furfural production apparatus using GVL as the

reaction solvent, with furfural removed from the reaction mixture by steam stripping. Reproduced from Alonso et al. [357]. 80
Figure 2.14. Biphasic solvent system for furfural production from wheat straw. Reproduced from Xu et al. [366]. 82
Figure 2.15. Conversion pathway from xylose to furfural under Lewis- and Brønsted-acid catalysis. Adapted from Choudhary et al. [367], Ye et al. [368], and Wang et al. [363]. 82
Figure 2.16. Two pathways from HMF or furoic acid to FDCA. Reproduced from Zhang et al. [378]. 87
Figure 2.17. Synthesis of the bio-based surfactant SAF via esterification of furoic acid with fatty alcohols. Reproduced from Al Ghatta et al. [68]. 87
Figure 2.18. Possible catalytic mechanism for the base-assisted aerobic oxidation of furfural to furoic acid over a noble metal (non-oxide) catalyst. 92
Figure 2.19. Possible catalytic mechanism for the aerobic oxidation of furfural to furoic acid over a metal-oxide-based ($Mn_2Cu_1O_x$) heterogeneous catalyst. Reproduced from Yu et al. [383]. 93
Figure 3.1. Experimental setup for the sonication-assisted ionoSolv process. 102
Figure 3.2. Separation of two pulp layers after the sonication-assisted ionoSolv process. 103
Figure 3.3. Temperature profiles of the reaction mixtures during the oil-bath heating and sonication-assisted ionoSolv pretreatment. “Sonication (60%)” and “Sonication (80%)” denote sonication amplitudes of 60% and 80%, respectively. (a) *Miscanthus*, 110 °C; (b) *Miscanthus*, 130 °C; and (c) Spruce, 130 °C. 110
Figure 3.4. Pulp yields after *Miscanthus* pretreatment with 80 wt% [DMBA][HSO_4] and 20 wt% water at a biomass-to-solvent ratio of 1:10 (g/g). 112
Figure 3.5. Compositional analysis of *Miscanthus* pulps recovered after pretreatment with 80 wt% [DMBA][HSO_4] and 20 wt% water at a biomass-to-solvent ratio of 1:10 (g/g) and different times. 113
Figure 3.6. Key indicators of fractionation effectiveness for ionoSolv pretreatment

of *Miscanthus* with 80 wt% [DMBA][HSO_4] and 20 wt% water at a biomass-to-solvent ratio of 1:10 (g/g). 114
Figure 3.7. Precipitated lignin yields after *Miscanthus* pretreatment with 80 wt% [DMBA][HSO_4] and 20 wt% water at a biomass-to-solvent ratio of 1:10 (g/g) at 110 °C (left) and 130 °C (right). 115
Figure 3.8. Glucose release after 7 days of enzymatic saccharification of *Miscanthus* pulps obtained following pretreatment with 80 wt% [DMBA][HSO_4] and 20 wt% water at a biomass-to-solvent ratio of 1:10 (g/g). 116
Figure 3.9. Pulp yields after spruce pretreatment with 80 wt% [DMBA][HSO_4] and 20 wt% water at a biomass-to-solvent ratio of 1:10 (g/g) at 130 °C (left) and 150 °C (right). 120
Figure 3.10. Compositional analysis of spruce pulps recovered after pretreatment with 80 wt% [DMBA][HSO_4] and 20 wt% water at a biomass-to-solvent ratio of 1:10 (g/g) for varying lengths of time at 130 °C (left) and 150 °C (right). .. 121
Figure 3.11. Key indicators of fractionation effectiveness for ionoSolv pretreatment of spruce with 80 wt% [DMBA][HSO_4] and 20 wt% water at a biomass-to-solvent ratio of 1:10 (g/g) for varying lengths of time at 130 °C (left) and 150 °C (right). 122
Figure 3.12. Precipitated lignin yields after spruce pretreatment with 80 wt% [DMBA][HSO_4] and 20 wt% water at a biomass-to-solvent ratio of 1:10 (g/g) at 130 °C (left) and 150 °C (right)..... 123
Figure 3.13. Glucose release after 7 days of enzymatic saccharification of spruce pulps obtained following pretreatment with 80 wt% [DMBA][HSO_4] and 20 wt% water at a biomass-to-solvent ratio of 1:10 (g/g). 125
Figure 3.14. Photographs (a) and microscopy images (b) of the raw biomass and two pulp layers with different particle sizes. (For the *Miscanthus* pulp with finer particles, the material appeared powdery initially but clumped during air drying.) 126
Figure 3.15. Characterization of different pulp layers. (a) Pulp yield; (b) Compositional analysis, calculated relative to the recovered pulp; and (c)

Glucose release after 7 days of enzymatic saccharification. 128
Figure 3.16. Temperature profiles of the reaction medium during oil-bath heating and sonication-assisted ionoSolv processes. (a) *Miscanthus*: 110 °C oil bath versus 103 °C sonication for 0.25 h; (b) *Miscanthus*: 110 °C oil bath versus 103 °C sonication for 0.5 h; (c) Spruce: 130 °C oil bath versus 121 °C sonication for 0.5 h; and (d) Spruce: 130 °C oil bath versus 121 °C sonication for 1 h. 130
Figure 3.17. Characterization of *Miscanthus* pulps from different pretreatment conditions used for sonication mechanism exploration. (a) Compositional analysis; (b) Key indicators of fractionation effectiveness; and (c) Glucose release after 7 days of enzymatic saccharification. 131
Figure 3.18. Characterization of spruce pulps from different pretreatment conditions used for sonication mechanism exploration. (a) Compositional analysis; (b) Key indicators of fractionation effectiveness; and (c) Glucose release after 7 days of enzymatic saccharification. 132
Figure 3.19. HSQC NMR spectra of *Miscanthus* and spruce lignin isolated after the sonication-assisted ionoSolv process. “Ara” and “Xyl” refer to arabinose and xylose, respectively. “PL” refers to a plasticizer and could be attributed to leaching from the O-ring seals in the pressure tubes during the ionoSolv process [19]. 134
Figure 3.20. Abundance of major linkages and subunits in *Miscanthus* and spruce lignin isolated after different ionoSolv processes. 135
Figure 3.21. Industrial flow scheme for the combined ionoSolv-fermentation process. 138
Figure 3.22. MSPs for bioethanol from the conventional and sonication-assisted ionoSolv processes, together with their annualized CAPEX and OPEX (biomass processing scale: 125 kg h^{-1}). “*Miscanthus*” denotes conventional (oil-bath) ionoSolv at 130 °C for 2 h; “*Miscanthus* with sonication” denotes sonication-assisted ionoSolv (80% amplitude) at 130 °C for 1 h; “Spruce” denotes conventional (oil-bath) ionoSolv at 130 °C for 4 h; “Spruce with

sonication" denotes sonication-assisted ionoSolv (80% amplitude) at 130 °C for 2 h; and "Spruce with sonication (mass transfer only)" denotes sonication-assisted ionoSolv (80% amplitude) at 130 °C for 2 h, excluding any additional benefit from sonication-induced temperature increase. 139
Figure 3.23. MSPs for bioethanol from the conventional and sonication-assisted ionoSolv processes, together with their annualized CAPEX and OPEX (biomass processing scale: 83.33 ton h^{-1} (2,000 tons per day)). 140
Figure 4.1. Diagram of the apparatus used for furfural production. 150
Figure 4.2. Furfural release from the sealed-batch and semi-continuous systems. Sugarcane bagasse (180–850 μm) was treated at 170 °C using [DMBA][HSO_4]. 152
Figure 4.3. Effect of water feed rate on furfural release from the semi-continuous system using [DMBA][HSO_4] at 170 °C with 20 wt% solids loading of sugarcane bagasse (180–850 μm). (The pump used in this study had a minimum setpoint of 0.30 mL min^{-1}. Lower feed rates (0.25, 0.20, and 0.10 mL min^{-1}) were simulated by maintaining the water feed rate at 0.30 mL min^{-1} and proportionally increasing the initial masses of the PIL and sugarcane bagasse to match the target water feed-to-feedstock ratios.) 153
Figure 4.4. Effects of reaction temperature, reaction time, and biomass loading on furfural release from the semi-continuous production system using sugarcane bagasse (180–850 μm) and [DMBA][HSO_4]. 155
Figure 4.5. Five replicate runs at 170 °C and 20 wt% solids loading of sugarcane bagasse (180–850 μm), representing the center point in the RSM design. 156
Figure 4.6. Diagnostic plots of the reduced quadratic model fitted to the semi-continuous furfural production data from 10 to 30 min. 159
Figure 4.7. (a) 3D response surface plot of furfural yield at the initial reaction stage; and (b) The corresponding contour plot of furfural yield at the initial reaction stage. (Solids loading was fixed at 20 wt%.) 160
Figure 4.8. Diagnostic plots of the reduced quadratic model fitted to the semi-

continuous furfural production data from 30 to 70 min..... 162
Figure 4.9. (a) 3D response surface plots of furfural yield at the intermediate reaction stage; and (b) The corresponding contour plots of furfural yield at the intermediate reaction stage. (Solids loading was fixed at 20 wt% when temperature and time were taken as the variables, while time was fixed at 50 min when temperature and solids loading were taken as the variables.).. 163
Figure 4.10. Diagnostic plots of the reduced quadratic model fitted to the semi-continuous furfural production data from 70 to 110 min..... 165
Figure 4.11. (a) 3D response surface plots of furfural yield at the final reaction stage; and (b) The corresponding contour plots of furfural yield at the final reaction stage. (Solids loading was fixed at 20 wt% when temperature and time were taken as the variables, while time was fixed at 90 min when temperature and solids loading were taken as the variables.)..... 166
Figure 4.12. Diagnostic plots of the reduced quadratic model fitted to the semi-continuous furfural production data from 10 to 110 min..... 168
Figure 4.13. (a) 3D response surface plots of furfural yield for the whole production process; and (b) The corresponding contour plots of furfural yield for the whole production process. (Solids loading was fixed at 20 wt% when temperature and time were taken as the variables, while time was fixed at 60 min when temperature and solids loading were taken as the variables.)..... 169
Figure 4.14. Effect of stepwise biomass addition on furfural release from the semi-continuous production system at 170 °C for 120 min with 30 wt% solids loading of sugarcane bagasse (180–850 μm). (a) Two-step biomass addition with an addition interval of 20 or 40 min; and (b) Multi-step biomass additions with an addition interval of 20 min..... 171
Figure 4.15. Effect of particle size on furfural release from the semi-continuous production system at 170 °C for 120 min with 30 wt% biomass loading.. 173
Figure 4.16. Recyclability evaluation of [DMBA][HSO_4] at 170 °C for 60 min with 20 wt% solids loading of sugarcane bagasse (180–850 μm), using a two-step biomass addition protocol with a 20-min addition interval..... 174

Figure 4.17. ^{1}H NMR of fresh [DMBA][HSO_4]: δ_H (400 MHz, DMSO-d_6)/ppm: 9.22 (s, 1H, N–*H*), 3.07–2.97 (m, 2H, N–C*H*$_2$), 2.76 (d, *J* = 4.9 Hz, 6H, N–(C*H*$_3$)$_2$), 1.64–1.52 (m, 2H, N–CH$_2$–C*H*$_2$), 1.30 (h, *J* = 7.3 Hz, 2H, N–CH$_2$–CH$_2$–C*H*$_2$), 0.90 (t, *J* = 7.4 Hz, 3H, N–CH$_2$–CH$_2$–CH$_2$–C*H*$_3$). 175

Figure 4.18. ^{13}C NMR of fresh [DMBA][HSO_4]: δ_C (101 MHz, DMSO-d_6)/ppm: 56.48 (N–*C*H$_2$), 42.25 (N–(*C*H$_3$)$_2$), 25.72 (N–CH$_2$–*C*H$_2$), 19.19 (N–CH$_2$–CH$_2$–*C*H$_2$), 13.48 (N–CH$_2$–CH$_2$–CH$_2$–*C*H$_3$). 176

Figure 4.19. ^{1}H NMR of [DMBA][HSO_4] recovered from cycle 5: δ_H (400 MHz, DMSO-d_6)/ppm: 9.21 (s, 1H, N–*H*), 3.05–2.96 (m, 2H, N–C*H*$_2$), 2.75 (s, 6H, N–(C*H*$_3$)$_2$), 1.63–1.51 (m, 2H, N–CH$_2$–C*H*$_2$), 1.29 (h, *J* = 7.3 Hz, 2H, N–CH$_2$–CH$_2$–C*H*$_2$), 0.89 (t, *J* = 7.4 Hz, 3H, N–CH$_2$–CH$_2$–CH$_2$–C*H*$_3$). 177

Figure 4.20. ^{13}C NMR of [DMBA][HSO_4] recovered from cycle 5: δ_C (101 MHz, DMSO-d_6)/ppm: 56.64 (N–*C*H$_2$), 42.38 (N–(*C*H$_3$)$_2$), 25.84 (N–CH$_2$–*C*H$_2$), 19.27 (N–CH$_2$–CH$_2$–*C*H$_2$), 13.57 (N–CH$_2$–CH$_2$–CH$_2$–*C*H$_3$). 178

Figure 4.21. Van Krevelen diagram of sugarcane bagasse and its derived biochars (cycles 1–5). 181

Figure 4.22. Aspen Plus flowsheet for the simulation of the proposed furfural production process, including the CHP cycle used for energy generation (shown at the bottom). 183

Figure 4.23. Mass balance of the optimized furfural production process at 190 °C and 20 wt% biomass loading (Case 3). Approximately 120 kg h^{-1} of water is unaccounted for after the furfural recovery block because this portion leaves with the ethyl acetate during furfural extraction, a step not shown here. .. 184

Figure 4.24. Contributions to MSPs of furfural under different operating conditions. (a) Case 3: biomass processing scale of 1,000 kg h^{-1} and IL recovery rate of 98.1%; (b) Case 5: biomass processing scale of 1,000 kg h^{-1} and IL recovery rate of 98.1%; (c) Case 3: biomass processing scale of 30,000 kg h^{-1} and IL recovery rate of 99.9%; and (d) Case 5: biomass processing scale of 30,000 kg h^{-1} and IL recovery rate of 99.9%. 187

Figure 4.25. Sensitivity analysis of biomass processing scale and IL recovery rate

on MSPs of furfural. (a) Case 3; and (b) Case 5. 188
Figure 5.1. High-pressure continuous-flow system for 10 wt% Ru/C-catalyzed aerobic oxidation of furfural to furoic acid. 196
Figure 5.2. Effect of temperature on the continuous oxidation of furfural to furoic acid over 10 wt% Ru/C. Conditions: 1 wt% furfural aqueous solution; air pressure of 10 bar; 1:1 $NaHCO_3$-to-furfural molar ratio; liquid flow rate of 8 mL min^{-1}; and air flow rate of 125 mL min^{-1}. Temperatures: (a) 130 °C; (b) 150 °C; and (c) 160 °C. 200
Figure 5.3. Effect of air pressure on the continuous oxidation of furfural to furoic acid over 10 wt% Ru/C. Conditions: 1 wt% furfural aqueous solution; 160 °C; 1:1 $NaHCO_3$-to-furfural molar ratio; liquid flow rate of 8 mL min^{-1}; and air flow rate of 125 mL min^{-1}. Air pressures: (a) 10 bar; (b) 20 bar; and (c) 40 bar.202
Figure 5.4. Effect of $NaHCO_3$-to-furfural molar ratio on the continuous oxidation of furfural to furoic acid over 10 wt% Ru/C. Conditions: 1 wt% furfural aqueous solution; 160 °C; air pressure of 10 bar; liquid flow rate of 8 mL min^{-1}; and air flow rate of 125 mL min^{-1}. $NaHCO_3$-to-furfural molar ratios: (a) 0.9:1; (b) 1:1; and (c) 1.1:1. 204
Figure 5.5. Effect of liquid flow rate on the continuous oxidation of furfural to furoic acid over 10 wt% Ru/C. Conditions: 1 wt% furfural aqueous solution; 160 °C; air pressure of 10 bar; 1.1:1 $NaHCO_3$-to-furfural molar ratio; and air flow rate of 125 mL min^{-1}. Liquid flow rates: (a) 8 mL min^{-1}; and (b) 10 mL min^{-1}... 205
Figure 5.6. Effect of air flow rate on the continuous oxidation of furfural to furoic acid over 10 wt% Ru/C. Conditions: 1 wt% furfural aqueous solution; 160 °C; air pressure of 10 bar; 1.1:1 $NaHCO_3$-to-furfural molar ratio; and liquid flow rate of 10 mL min^{-1}. Air flow rates: (a) 25 mL min^{-1}; (b) 75 mL min^{-1}; and (c) 125 mL min^{-1}. 206
Figure 5.7. Continuous oxidation of furfural to furoic acid over 10 wt% Ru/C using a 2 wt% furfural aqueous solution. Conditions: 160 °C; air pressure of 10 bar; 1.1:1 $NaHCO_3$-to-furfural molar ratio; and liquid flow rate of 10 mL min^{-1}. Air flow rates: (a) 125 mL min^{-1}; (b) 250 mL min^{-1}; and (c) 500 mL min^{-1}. 208

Figure 5.8. Continuous oxidation of furfural to furoic acid over 10 wt% Ru/C using a 3 wt% furfural aqueous solution. Conditions: 160 °C; air pressure of 10 bar; 1.1:1 $NaHCO_3$-to-furfural molar ratio; liquid flow rate of 10 mL min^{-1}; and air flow rate of 500 mL min^{-1}. (a) First-pass oxidation; and (b) Second-pass oxidation. 209

Figure 5.9. Continuous oxidation of furfural to furoic acid over 10 wt% Ru/C using a 3 wt% furfural aqueous solution. Conditions: 160 °C; air pressure of 10 bar; 1.1:1 $NaHCO_3$-to-furfural molar ratio; air flow rate of 500 mL min^{-1}; and single-pass oxidation. Liquid flow rates: (a) 2.5 mL min^{-1}; (b) 5 mL min^{-1}; and (c) 10 mL min^{-1}. 210

Figure 5.10. XRD patterns of fresh and spent 10 wt% Ru/C catalysts.....211

Figure 5.11. XPS spectra in the Ru 3p region for fresh and spent 10 wt% Ru/C catalysts..... 212

Figure 5.12. SEM images and the corresponding EDX elemental maps (C, O, and Ru) of fresh and spent 10 wt% Ru/C catalysts. 214

Figure 5.13. TEM images of fresh and spent 10 wt% Ru/C catalysts. 215

Figure 5.14. Two proposed mechanisms for the oxidation of furfural to furoic acid over 10 wt% Ru/C. 217

Figure 6.1. Pressurized steam-assisted ionoSolv setup. 225

Figure S1. ^{1}H NMR of fresh [DMBA][HSO_4] for the ionoSolv process: δ_H (400 MHz, DMSO-d_6)/ppm: 9.24 (s, 1H, N–*H*), 3.06–2.97 (m, 2H, N–CH_2), 2.75 (s, 6H, N–(CH_3)$_2$), 1.63–1.51 (m, 2H, N–CH_2–CH_2), 1.29 (h, J = 7.4 Hz, 2H, N–CH_2–CH_2–CH_2), 0.88 (t, J = 7.4 Hz, 3H, N–CH_2–CH_2–CH_2–CH_3). 232

Figure S2. ^{13}C NMR of fresh [DMBA][HSO_4] for the ionoSolv process: δ_C (101 MHz, DMSO-d_6)/ppm: 56.59 (N–*C*H_2), 42.37 (N–(*C*H_3)$_2$), 25.83 (N–CH_2–*C*H_2), 19.28 (N–CH_2–CH_2–*C*H_2), 13.58 (N–CH_2–CH_2–CH_2–*C*H_3). 233

Figure S3. HSQC NMR spectrum of *Miscanthus* lignin isolated after the sonication-assisted ionoSolv process at 103 °C and 0.25 h. 234

Figure S4. HSQC NMR spectrum of *Miscanthus* lignin isolated after the sonication-assisted ionoSolv process at 103 °C and 0.5 h. 234

Figure S5. HSQC NMR spectrum of *Miscanthus* lignin isolated after the oil-bath heating ionoSolv process at 110 °C and 0.25 h. 235
Figure S6. HSQC NMR spectrum of *Miscanthus* lignin isolated after the oil-bath heating ionoSolv process at 110 °C and 0.5 h. 235
Figure S7. HSQC NMR spectrum of *Miscanthus* lignin isolated after the sonication-assisted ionoSolv process at 110 °C and 0.25 h. 236
Figure S8. HSQC NMR spectrum of *Miscanthus* lignin isolated after the sonication-assisted ionoSolv process at 110 °C and 0.5 h. 236
Figure S9. HSQC NMR spectrum of spruce lignin isolated after the sonication-assisted ionoSolv process at 121 °C and 0.5 h. 237
Figure S10. HSQC NMR spectrum of spruce lignin isolated after the sonication-assisted ionoSolv process at 121 °C and 1 h. 237
Figure S11. HSQC NMR spectrum of spruce lignin isolated after the oil-bath heating ionoSolv process at 130 °C and 0.5 h. 238
Figure S12. HSQC NMR spectrum of spruce lignin isolated after the oil-bath heating ionoSolv process at 130 °C and 1 h. 238
Figure S13. HSQC NMR spectrum of spruce lignin isolated after the sonication-assisted ionoSolv process at 130 °C and 0.5 h. 239
Figure S14. HSQC NMR spectrum of spruce lignin isolated after the sonication-assisted ionoSolv process at 130 °C and 1 h. 239
Figure S15. ^{1}H NMR of [DMBA][HSO_4] recovered after cycle 1. 240
Figure S16. ^{13}C NMR of [DMBA][HSO_4] recovered after cycle 1. 240
Figure S17. ^{1}H NMR of [DMBA][HSO_4] recovered after cycle 2. 241
Figure S18. ^{13}C NMR of [DMBA][HSO_4] recovered after cycle 2. 241
Figure S19. ^{1}H NMR of [DMBA][HSO_4] recovered after cycle 3. 242
Figure S20. ^{13}C NMR of [DMBA][HSO_4] recovered after cycle 3. 242
Figure S21. ^{1}H NMR of [DMBA][HSO_4] recovered after cycle 4. 243
Figure S22. ^{13}C NMR of [DMBA][HSO_4] recovered after cycle 4. 243
Figure S23. Furfural solutions collected at 10-min intervals from the semi-continuous furfural production system. 244

Figure S24. HPLC chromatogram (UV, λ = 254 nm) showing the furfural peak at *t* = 42.47 min. (Column: Aminex HPX-87H, 60 °C; mobile phase: 0.005 M H_2SO_4, 0.6 mL min^{-1} flow rate.)..... 245
Figure S25. HPLC chromatogram (UV, λ = 254 nm) showing the furoic acid peak at *t* = 28.21 min. (Column: Aminex HPX-87H, 60 °C; mobile phase: 0.005 M H_2SO_4, 0.6 mL min^{-1} flow rate.)..... 246
Figure S26. Full-range (survey) XPS spectra of fresh and spent 10 wt% Ru/C catalysts..... 246
Figure S27. SEM micrographs of fresh and spent 10 wt% Ru/C at 5,000× to 20,000× magnification..... 247

List of Tables

Table 2.1. Comparative review of IL pretreatments for lignocellulosic biomass: effects on delignification and enzymatic hydrolysis. 70

Table 3.1. Summary of prices used for the techno-economic analysis. 138

Table 3.2. Costing methodology for each type of unit considered in the process. 139

Table 4.1. ANOVA results for the reduced quadratic model fitted to the semi-continuous furfural production data from 10 to 30 min..... 158

Table 4.2. ANOVA results for the reduced quadratic model fitted to the semi-continuous furfural production data from 30 to 70 min..... 161

Table 4.3. ANOVA results for the reduced quadratic model fitted to the semi-continuous furfural production data from 70 to 110 min. 164

Table 4.4. ANOVA results for the reduced quadratic model fitted to the semi-continuous furfural production data from 10 to 110 min. 167

Table 4.5. Characterization of sugarcane bagasse (SB) and biochars on an oven-dried basis. 180

Table 4.6. Furfural productivities, purities, and MSPs under various process conditions. 186

Table 5.1. XPS surface elemental composition and Ru chemical-state distribution of fresh and spent Ru/C catalysts. 213

Table S1. Effects of different pretreatment methods on the composition and structure of lignocellulosic biomass. 231

Table S2. List of the different utility prices employed for the economic estimation. 244

Table S3. List of parameters employed for the total capital cost estimation..... 244

Table S4. List of parameters employed for the fixed cost estimation. 245

Table S5. Summary of the copyright permissions. 247

Chapter 1: Introduction

1.1 Background and Research Gap

In recent years, as concerns about energy security and environmental pollution have risen, researchers have shifted their focus from the intensive exploitation of fossil resources to the development and use of renewable resources [1, 2]. At present, the rapid growth of solar, wind, geothermal, and nuclear energy has reduced human dependence on fossil resources. However, these technologies are still primarily aimed at meeting the global power demand [1, 3]. Fossil resources are not limited to the energy sector. They also serve as feedstocks for a wide range of chemicals—plastics, fertilizers, surfactants, solvents, and pharmaceuticals—that are indispensable across numerous industries [4-6]. To further reduce reliance on fossil resources in these sectors, it is necessary to seek alternative carbon sources that are both renewable and environmentally friendly. As one of the most abundant carbon resources on Earth, biomass has been widely studied as a substitute for fossil resources, and its renewability and carbon-neutral properties make it an ideal candidate [2, 7, 8].

Biomass refers to organisms and their wastes derived from photosynthesis, including plants, microorganisms, animals, and their residues [9]. Converting biomass into value-added biofuels or biochemicals is defined as a biorefinery [10]. The first generation (1G) biorefinery uses food-based (edible) biomass, mainly sucrose- and starch-rich crops such as sugarcane, sugar beet, wheat, and corn [11, 12], or oil-bearing plants such as rapeseed, sunflower, soybean, and oil palm [12-14]. Because edible biomass has a relatively simple composition, it can be converted into 1G bioethanol by fermentation or biodiesel by transesterification [12, 15]. Edible biomass is the main feedstock in the current biofuel industry [15]. However, its large-scale utilization raises concerns about food security and the excessive consumption of land and water resources [16-18]. In contrast, the second-generation (2G) biorefinery utilizes lignocellulosic biomass, which can offer a more cost-effective route because its cultivation typically requires less fertilizer and water and can give higher yields per unit

of land [19, 20]. The inedible nature of lignocellulosic biomass also reduces concerns that energy production competes with the food supply [21]. Lignocellulosic biomass has diverse sources, including agricultural residues (e.g., wheat straw, corn stover, and sugarcane bagasse), forestry wastes (e.g., wood chips and sawdust), energy crops (e.g., switchgrass and *Miscanthus*), and invasive plants (e.g., Rhododendron and Japanese knotweed) [11, 12, 16, 22-24]. However, the main challenge is the robust structure of lignocellulose. Specifically, typical dry lignocellulosic biomass contains 35–50 wt% cellulose, 20–35 wt% hemicellulose, and 15–30 wt% lignin [25-27]. These components form a compact three-dimensional matrix through complex interactions [11]. While this structure provides excellent mechanical strength, it also impedes the conversion of lignocellulose to high-value products [28, 29]. Efficient pretreatment is therefore needed to deconstruct or fractionate the matrix and improve processability [28, 29].

The main aim of pretreatment is to disrupt or remove lignin in lignocellulosic biomass, because it is the principal barrier limiting enzyme accessibility to cellulose and hemicellulose—the polysaccharides used to produce 2G bioethanol and other bioproducts [30-32]. However, owing to significant energy and solvent requirements, pretreatment is usually a costly step in the biorefinery process, accounting for approximately 20% of the total capital and operating expenditures [33]. To date, a range of methods have been developed—physical, chemical, biological, and hybrid—each with specific advantages and limitations [34, 35]. These will be reviewed in detail in the next chapter. Recently, Prof. Jason Hallett's group at Imperial College London has investigated low-cost, recyclable protic ILs (PILs) for pretreating recalcitrant lignocellulose (the "ionoSolv" process) [19, 24, 36, 37]. Experimental results have shown that ionoSolv enables efficient fractionation: PILs selectively dissolve lignin and hemicellulose while yielding a cellulose-rich pulp in a one-pot process. The recovered pulp can serve as a feedstock for 2G bioethanol or as a precursor to high-value products such as nanocellulose [38]. Dissolved hemicellulose can be valorized into furan compounds such as furfural [19, 39]. In addition, lignin can be precipitated by

adding an anti-solvent (e.g., water) and then used for power generation or carbon fiber production [19, 40].

Although numerous ionoSolv-related advantages have been reported, PILs still suffer from inherent drawbacks such as high viscosity [41], which negatively affects mass transfer efficiency between biomass and PILs. This issue leads to extended pretreatment times (up to 8 hours), especially at mild temperatures (e.g., 120 °C) [19]. Mechanical stirring is commonly used to improve mass transfer, but in such viscous systems, its effect is limited and it significantly increases energy consumption [42]. In contrast, the application of ultrasound offers a more promising route to accelerate lignocellulose fractionation. Its core mechanism is acoustic cavitation, which generates localized high temperatures and pressures, intense shear forces and shock waves, and reactive radicals during the instantaneous collapse of thousands of microbubbles [43-46]. These effects penetrate viscous liquid–solid systems and can directly disrupt lignin–carbohydrate complexes (LCCs), rather than merely enhancing system mixing. For analytical convenience, the macroscopic effects of ultrasound on the system can be treated as two measurable parts: mass transfer enhancement and temperature increase. The latter usually shows a non-uniform spatial distribution, especially near the ultrasound probe [46, 47]. In our study, we developed a sonication-assisted ionoSolv process to accelerate biomass fractionation under relatively mild conditions. Meanwhile, to obtain a more complete mechanistic picture, we isolated and independently evaluated the contributions of mass transfer enhancement and temperature increase to the overall fractionation performance. Finally, while ultrasonic equipment may be cost-prohibitive for industrial applications at present, elucidating the underlying mechanisms and benefits will aid the decision-making process regarding any potential incorporation [48].

In studying derivative products from the ionoSolv process, our group conducted in-depth investigations into the utilization of cellulose-rich pulp and lignin, achieving a series of advances [19, 36-38, 40, 49]. However, pathways to valorize hemicellulose

and its dehydration products remain insufficiently explored. This is mainly because hemicellulose is usually the first to degrade into small molecules, such as monosaccharides and furan-based chemicals, during processing. Without effective separation, these species tend to remain dissolved in PILs and can react further to form humins and other degradation products [19], complicating recovery and downstream applications. Nevertheless, comprehensive valorization of all lignocellulosic components is crucial for the economic viability and sustainability of biorefineries [50]. Our preliminary techno-economic analysis also confirmed this, highlighting the critical role of hemicellulose valorization in improving the overall profitability of the *Miscanthus* ionoSolv process [19]. Among hemicellulose derivatives, furfural stands out as a promising platform compound due to its broad industrial applications and growing market demand [51]. Currently, global furfural output has exceeded 400,000 tons per year, with China as the major producer [52-54]. Although numerous studies have successfully converted hemicellulose to furfural, most processes still face constraints. Chief among them are the poor recyclability of conventional solvents (e.g., aqueous sulfuric acid) [55, 56] and the low solids-to-liquid ratios [57, 58]. First, limited solvent recyclability raises operating costs and generates highly acidic wastewater, which poses serious ecotoxicity risks if discharged without proper treatment [57, 59]. Second, at high biomass loadings, elevated concentrations of substrates (e.g., lignin and sugars) increase the likelihood of side reactions with furfural, substantially reducing the overall yield [19, 53, 60]. For example, the world's first industrial furfural production process developed by Quaker Oats Technology achieved only ~50% yield because of severe side reactions [51, 55, 61]. These problems not only increase production costs but also run counter to the principles of the circular economy and green chemistry. Therefore, to achieve cost-effective, high-yield, and scalable furfural production, we developed a semi-continuous process in which a low-cost, recyclable PIL served as the reaction medium, and furfural was rapidly removed from the reaction substrates by vapor stripping. This timely separation effectively suppressed undesired side reactions and improved overall process efficiency even at high biomass loadings (10–30 wt%).

As noted above, furfural, a representative bio-based platform chemical, owes its versatility to a wide range of high-value derivatives, including furoic acid, furfuryl alcohol, 2-methylfuran (2-MF), tetrahydrofurfuryl alcohol (THFA), and 2-methyltetrahydrofuran (2-MeTHF) [52, 60, 62]. Among these, the oxidation of furfural to furoic acid has attracted considerable attention because furoic acid can serve as an alternative to 5-hydroxymethylfurfural (HMF) for producing 2,5-furandicarboxylic acid (FDCA) [63, 64]. FDCA is the monomer for the bio-based polyester polyethylene furanoate (PEF), a greener substitute for the petroleum-derived plastic polyethylene terephthalate (PET) [65-67]. In addition, our team recently developed and commercialized a bio-based surfactant, sulfonated alkyl furoate (SAF), via simple esterification of furoic acid with fatty alcohols [68]. Experiments showed that SAF delivers emulsifying and cleaning performance comparable to, or even better than, the conventional petroleum-based surfactant linear alkylbenzene sulfonate (LAS). A detailed techno-economic analysis demonstrated that the key to the successful large-scale application of SAF lies in the cost-effective oxidation of furfural to furoic acid. Motivated by these factors, we aim to develop an efficient, scalable furoic acid production process. Although aerobic oxidation of furfural over noble-metal heterogeneous catalysts has been widely studied with promising furoic acid yields, most reports remain limited to bench-scale batch operations [69-72]. In addition, the poor durability of many catalysts leads to increased process costs, thereby hindering industrial feasibility. To address these challenges and meet commercial-scale demands, we developed, for the first time, a high-pressure continuous-flow system employing a robust and durable 10 wt% ruthenium on carbon (Ru/C) catalyst. This system successfully scaled furoic acid production from a milliliter-scale batch reaction to a liter-scale continuous operation. We believe this work provides useful guidance for further developing cost-effective, industrially viable processes for furoic acid production.

In summary, this thesis aims to develop an integrated PIL-based fractionation and

valorization platform that expands the lignocellulosic value chain by linking cellulose recovery, hemicellulose-derived furfural production, and the downstream upgrading of furfural to furoic acid. The work starts from the ionoSolv concept, in which the low-cost, recyclable PIL [DMBA][HSO_4] enables one-pot fractionation of recalcitrant biomass. To address mass and heat transfer limitations in this viscous medium, sonication is introduced so that lignin and hemicellulose can be solubilized rapidly and selectively, while a cellulose-rich pulp is retained even at relatively mild temperatures. With this PIL platform in place, the thesis then turns to hemicellulose valorization by producing furfural directly from raw biomass at high solids loadings. Importantly, in situ vapor stripping is used to remove furfural from the acidic solvent system as it forms, thereby suppressing side reactions and enabling PIL recycling. Finally, to extend the furan-based product portfolio and strengthen overall biorefinery economics, furfural is upgraded to furoic acid via aerobic oxidation over the 10 wt% Ru/C heterogeneous catalyst, with an emphasis on robust and scalable operation under continuous-flow conditions suitable for industrial translation. In combination, these steps connect pretreatment, product separation, and catalytic upgrading into a single process narrative, and they establish a route from lignocellulosic feedstocks to higher-value chemicals while maintaining a focus on solvent recyclability, process intensification, and full biomass-component valorization.

1.2 Thesis Structure

Part 1 (Chapter 2). A detailed literature review introduces the background of the research topics, identifies key research gaps in the 2G biorefinery process, and highlights opportunities to use low-cost PILs to valorize two important components—cellulose and hemicellulose—in lignocellulosic biomass, with the downstream conversion of the hemicellulose dehydration product (furfural) to the higher-value derivative furoic acid.

Part 2 (Chapters 3–6). This part presents three experimental studies and a concluding chapter:

(1) **Sonication-assisted ionoSolv pretreatment.** This chapter aims to develop a less time-consuming and less energy-intensive ionoSolv process with the aid of sonication. Two biomass types with different recalcitrance—grass biomass (*Miscanthus*) and softwood (spruce)—were treated with the low-cost PIL *N,N*-dimethylbutylammonium hydrogen sulfate ([DMBA][HSO_4]). More importantly, the study also tried to clarify the acceleration mechanism of sonication in the ionoSolv process by quantifying the separate contributions of the two most evident macroscopic effects induced by ultrasound: mass transfer enhancement and temperature increase.

(2) **Semi-continuous furfural production.** This chapter aims to realize the effective separation and recovery of furfural produced from hemicellulose during the ionoSolv process—a key step toward an integrated PIL-based biorefinery. An efficient semi-continuous system was designed, with rapid furfural removal from reaction substrates via vapor stripping and [DMBA][HSO_4] as the reaction solvent. This system tackled two major issues in current furfural production: the recyclability of the reaction solvent ([DMBA][HSO_4]) and high furfural yields at high biomass-to-solvent loadings (10–30 wt%), both of which are critical for improving overall process economics.

(3) **Continuous high-pressure oxidation of furfural to furoic acid.** This chapter targets the downstream upgrading of furfural. Given that furfural is a platform chemical with a bulk market price of approximately \$1.1–1.3 kg^{-1} [73], further upgrading it to the more valuable derivative furoic acid (market price: \$11–15 kg^{-1} [74]) has strong market potential owing to furoic acid's roles in FDCA and bio-based surfactant synthesis. To meet industrial requirements, a high-pressure continuous-flow system for the aerobic oxidation of furfural to furoic acid was designed and operated in place of bench-scale batch reactors. High furfural conversion and furoic acid selectivity were achieved by optimizing multiple process parameters. The production scale was successfully upgraded from the milliliter-scale to the liter-scale, providing valuable insights for full industrial

implementation.

(4) **Conclusions and outlook.** This chapter summarizes the conclusions of the thesis, the remaining research gaps, and future work.

Overall statement. We believe the outcomes of this thesis support the development of an economically competitive and environmentally friendly PIL-based biorefinery with strong potential to produce advanced biofuels and other furan-based commodities.

Chapter 2: Literature Review

2.1 Ionic Liquids

2.1.1 General Overview

Conventional ionic substances (e.g., NaCl, Na_2CO_3, and K_2CO_3) generally exist in the solid state under ambient conditions because of the presence of strong electrostatic interactions between small, highly charged ions. Meanwhile, these ions are highly symmetrical, which favors the formation of stable crystal lattices. These factors give such salts large lattice energies. Significant heat is therefore needed to melt them, resulting in high melting points. Conversely, ionic liquids (ILs) are salts consisting of cations and anions that remain liquid at much lower temperatures, usually below 100 °C [75]. The liquid state of ILs stems from the asymmetric structures of their constituent ions, which hinder the formation of an ordered crystal lattice. In addition, the bulkiness of these ions lowers their charge density, weakening electrostatic interactions and reducing lattice energies [76]. As a result, ILs melt at much lower temperatures than conventional inorganic salts.

The first IL reported was ethylammonium nitrate ($[EtNH_3][NO_3]$), discovered by Paul Walden in 1914, with a melting point of 12 °C [77]. For decades, ILs attracted little interest because early-stage haloaluminate-based ILs were extremely moisture-sensitive [78, 79]. For example, in 1982, Wilkes and co-workers synthesized dialkylimidazolium chloroaluminates for potential applications in electrochemistry, spectroscopy, and synthesis [80]. However, the synthesis process had to be conducted under a dry argon atmosphere. Based on their earlier work, in 1992, Wilkes et al. reported a new class of air- and moisture-stable 1-ethyl-3-methylimidazolium-based ILs, such as $[Emim][BF_4]$ and $[Emim][MeCO_2]$ [81]. This breakthrough prompted serious consideration of ILs as alternatives to conventional organic solvents. Welton later noted that IL research was “reborn” in the late 1980s and throughout the 1990s [82]. Since then, the field has expanded rapidly. According to a bibliometric analysis, the number of IL-related publications grew from only a few in the 1990s to more than

7,000 per year by 2016, although growth has recently plateaued [77, 79]. Figure 2.1 lists representative IL building blocks. Common nitrogen-based cations include imidazolium, pyrrolidinium, pyridinium, and ammonium, which are paired with a range of anions, including organic anions such as carboxylate and alkylsulfonate ($[RSO_3]^-$), and inorganic anions such as halides (e.g., Cl^-), hydrogen sulfate ($[HSO_4]^-$), tetrafluoroborate ($[BF_4]^-$), and hexafluorophosphate ($[PF_6]^-$).

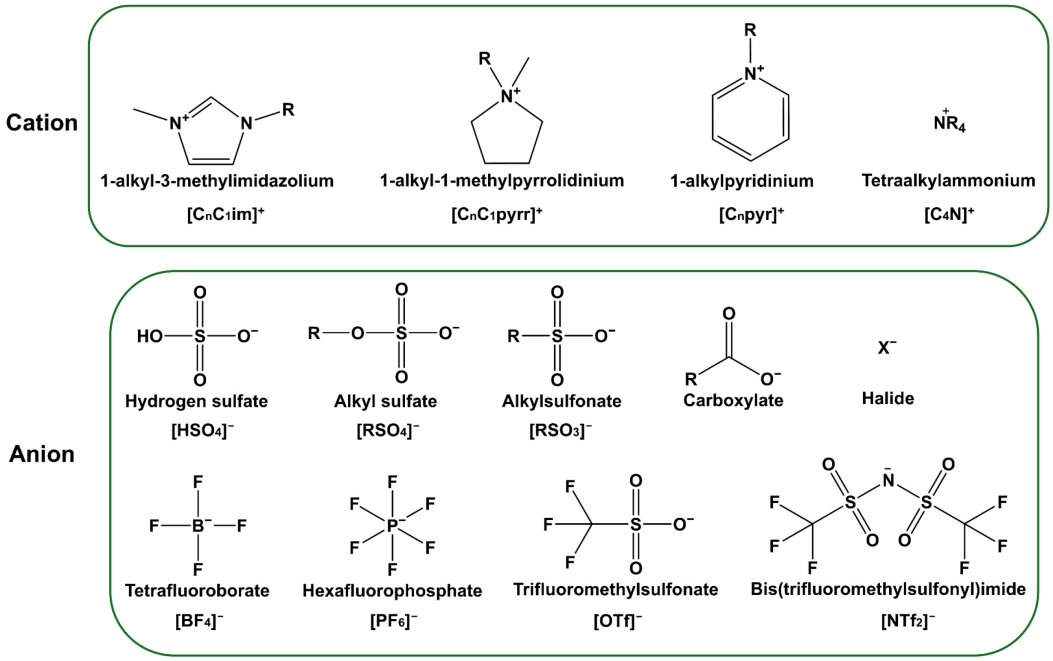


Figure 2.1. Representative cations and anions used in ionic liquids.

2.1.2 Physicochemical Properties of Ionic Liquids

ILs were branded as the “solvent of the future” in 2003 [83], because they can be applied in a wide range of fields such as green catalysis [84-86], electrochemistry [87], carbon dioxide capture [88, 89], biomass pretreatment [11, 19, 36], and metal extraction [90, 91]. More importantly, ILs are viewed as promising alternatives to conventional organic solvents, which are typically flammable and highly volatile. Their versatility stems from several key physicochemical properties. (1) Low vapor pressure and high thermal stability [92, 93]. Most ILs have negligible vapor pressure at room temperature, so they can be used in high-vacuum systems without atmospheric

emissions and are easy to recycle [94]. Low volatility also gives ILs non-flammability and high thermal stability, allowing their use at elevated temperatures without significant concerns regarding safety or degradation. For example, the decomposition temperature of 1,2-dimethyl-3-ethylimidazolium hexafluorophosphate can reach approximately 500 °C [95]. Moreover, due to their negligible vapor pressure, ILs usually have wide liquid ranges. Unlike water and organic solvents, whose liquid ranges are limited by their boiling points, many ILs decompose before reaching their boiling points [75]. (2) Strong and tunable solvation. ILs can dissolve a wide range of organic and inorganic compounds because their polarity supports diverse solvent–solute interactions, including dipolar, Coulombic, hydrogen-bonding, and Lewis acid-base (electron pair donor and acceptor) interactions [96]. The polarity of ILs is often quantified with the Kamlet–Taft parameters: α (hydrogen-bond donating ability), β (hydrogen-bond accepting ability), and π* (dipolarity/polarizability) [97, 98]. These values are determined from solvatochromic shifts in the UV-Vis absorption spectra of specific molecular dyes dissolved in the ILs [99]. Higher α, β, and π* numbers indicate stronger hydrogen bonding and greater polarizability. ILs typically show π* ≈ 1, similar to polar molecular solvents such as water (1.09), DMSO (1.00), and nitrobenzene (1.01) [96, 100]. In contrast, α and β depend strongly on the cation-anion pair, ranging from 0.2–1.2 for α and 0–1.61 for β [96], allowing researchers to tune hydrogen-bond donating and accepting strengths by modifying the ions. For comparison, water has α = 1.17 and β = 0.18 [100]. Despite their polarity, some ILs are immiscible with water and form biphasic systems. The hydrophobicity of ILs generally increases with the number of substituents on the organic cations and follows the trend $[Cl]^-$<$[HSO_4]^-$<$[BF_4]^-$<$[PF_6]^-$<$[NTf_2]^-$ for anions [75]. (3) Wide electrochemical windows and useful conductivity. The electrochemical window is defined as the voltage range within which the liquid remains electrochemically inert (neither reduced nor oxidized) [101]. The window width depends strongly on hydrophobicity, and many ILs exceed 4 V, making them attractive as battery electrolytes [95, 101]. Meanwhile, certain ILs (e.g., alkylammonium-based PILs) exhibit high ionic conductivity, supporting efficient ion transport in fuel cell applications [102]. In addition, ILs have recently gained attention

as promising media for the electrodeposition of both reactive metals (e.g., Ti, Al, and Mg) [103, 104] and heavy metals (e.g., Cr, Cu, Cd, and Pb) [90].

In addition to the physicochemical advantages described above, ILs display several other noteworthy features. Most ILs behave as Newtonian fluids and, at 20 °C, show viscosities from roughly 10 to 500 mPa s—far higher than that of water (1 mPa s) or common solvents such as ethanol (1.2 mPa s), acetone (0.32 mPa s), and ethyl acetate (0.45 mPa s) [75]. The viscosity of ILs depends on several factors. (1) Ion structure. Cations bearing longer or multiple alkyl chains increase viscosity through stronger van der Waals and hydrogen-bond interactions [95]. (2) Temperature. Like that of water, IL viscosity is strongly temperature-dependent and can drop to near-aqueous values at sufficiently high temperatures [105]. (3) Additives/impurities. Polar co-solvents (e.g., dimethylformamide and 3-picoline) sharply lower the viscosity of ILs such as 1-butyl-3-methylimidazolium tetrafluoroborate, *N*-methyl-*N*-butylpyrrolidinium bis(trifluoromethylsulfonyl)imide, and *N*-methyl-*N*-hexylpyrrolidinium bis(trifluoromethylsulfonyl)imide [106], whereas adding 1.5–6.0 wt% chloride can raise the viscosity of a non-haloaluminate alkylimidazolium IL by 30–600% [75]. Water has a similar impact: just 2 wt% reduces the viscosity of [Bmim][BF_4] by about half [75]. Although high viscosity can be useful (for lubrication, for instance), it may pose limitations in applications such as electrodeposition and biomass pretreatment, where it can hinder ion transport, reduce conductivity, and impair mass transfer efficiency. Another key property is acidity, which varies with the IL structure and affects its suitability for different chemical reactions. The Hammett acidity function (H_0) is commonly employed to quantify the acidity of non-aqueous systems, serving as an analogue to pH and enabling the characterization of strongly acidic media beyond the conventional pH range [107, 108]. The H_0 values of neat ILs are typically determined by UV-Vis spectroscopy using a series of Hammett dyes [107-109]. The toxicity of ILs is a critical measure of their “greenness.” Although toxicological data are still incomplete, evidence indicates that some ILs display higher ecotoxicity than conventional molecular solvents [110]. Toxicity depends on both the cation and the

anion. For alkyl-imidazolium ILs, cations with longer alkyl chains correlate with higher toxicity, likely because extended chains facilitate the insertion of the cation into cell membranes, causing destabilization and eventual rupture [110-113]. For a given cation, ILs with chloride anions generally exhibit lower toxicity, whereas those with fluorinated anions (e.g., [NTf_2]) are markedly more toxic [114]. Notably, because most ILs are chemically stable and poorly biodegradable, their potential to accumulate in the environment—especially on an industrial scale—has raised concern and spurred interest in biodegradable or biocompatible alternatives [115]. One strategy is to prepare bio-based ILs from renewable feedstocks such as amino acids, carbohydrates, and lignin [116]. For example, Trivedi et al. reported highly biodegradable, non-toxic surfactant ILs by combining amino acids with renewable sodium lauryl sulfate [117]. Additionally, PILs have been found to exhibit lower toxicity than imidazolium-based aprotic ILs (APILs) [113], and much lower toxicity than phosphonium-based APILs [114]. For example, Peric et al. showed that PILs derived from aliphatic amines and organic acids are potentially biodegradable in water and markedly less harmful to aquatic organisms than several common APILs [113]. The lower toxicity of PILs can be attributed to their simple molecular structure with smaller and more hydrophilic ions. In contrast, APILs often contain bulky heterocyclic cations with hydrophobic alkyl side chains [111, 112]. In practice, selecting ILs with shorter alkyl chains and higher hydrophilicity is advisable to minimize environmental impact [118, 119].

2.1.3 Commercialization of Ionic Liquids

Commercial interest in ILs has risen noticeably over the past decade, as shown by patent statistics (Figure 2.2). About 1,000 IL-related patents were published worldwide in 2010; by 2019, the figure had doubled to roughly 2,100 [79]. From 2002 to 2015, patents claiming ILs as products declined, while those covering their use in specific processes increased, suggesting that IL synthesis is well understood but its applications still need exploration [79, 120]. One early industrial example came from the Texas Eastman Division of the Eastman Chemical Company, which in 1996 used a tetraalkylphosphonium iodide-based IL (serving as both a solvent and a phase-

transfer catalyst) to isomerize 3,4-epoxy-1-butene to 2,5-dihydrofuran, an intermediate for tetrahydrofuran production [79, 121]. The continuous reactor was recorded to produce approximately 1,400 tons of 2,5-dihydrofuran per year, but the plant closed in 2004 after the demand for furan derivatives fell [122, 123]. Moreover, the BASIL™ (biphasic acid scavenging utilizing ionic liquids) process, developed by BASF, is often cited as the most successful large-scale IL application [86, 124]. The commercial operation of the BASIL™ process began in 2002 at Ludwigshafen, efficiently producing alkoxyphenylphosphine, a generic photoinitiator precursor [125, 126]. In the BASIL™ process, 1-methylimidazole was used to replace triethylamine, which was the base used in the original route as the acid scavenger. This replacement led to the formation of the IL 1-methylimidazolium chloride, which not only enabled the efficient removal of acidic by-products but could also be easily separated from the reaction mixture via biphasic liquid–liquid separation, avoiding the formation of a dense, insoluble triethylammonium chloride paste that previously hindered reaction efficiency and handling [79]. In 2004, a continuous jet-stream reactor was built to replace the original batch vessel, raising the space–time yield 86,000-fold—from 8 kg m^{-3} h^{-1} to 690,000 kg m^{-3} h^{-1} [79]. This process now runs at a scale of 1,000 tons of product per year, demonstrating the feasibility of industrial IL applications.

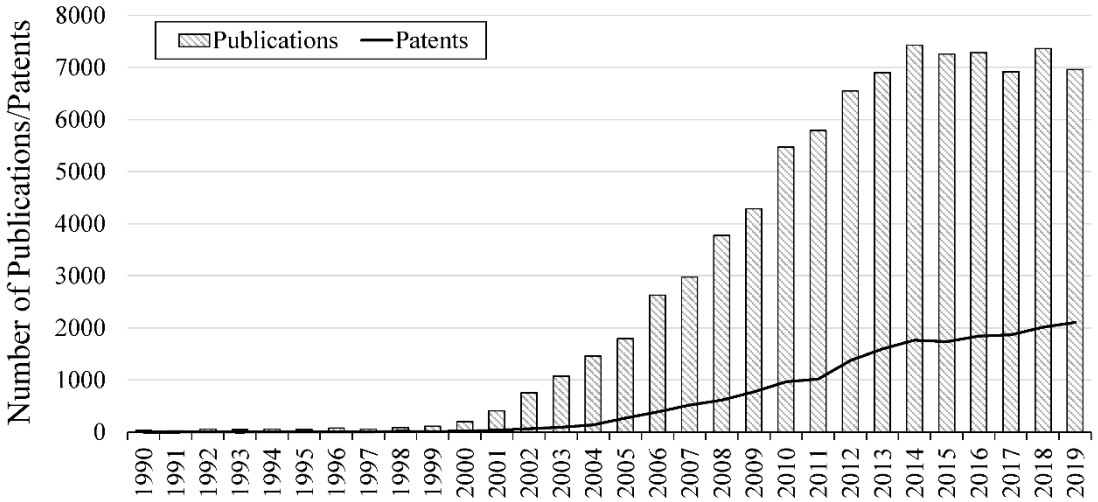


Figure 2.2. Number of publications and patents related to ionic liquids, 1990–2019. Reproduced from Greer et al. [79].

More recently, there have also been some IL-commercialization cases contributed by our group (Prof. Jason Hallett's group) at Imperial College London. Lixea Ltd, a clean-technology company founded in 2017 by Dr. Florence Gschwend, Dr. Agi Brandt-Talbot, and Prof. Jason Hallett, owns the patented Dendronic® process, which converts waste wood, agricultural residues, and energy crops into greener, value-added alternatives to petrochemical products using low-cost, safe, and recyclable PILs [127]. A pilot plant in Bäckhammar, Sweden, is now fully operational. DyeRecycle Ltd, founded in 2022 by Dr. Aida Rafat and Prof. Hallett, focuses on extracting dyes from waste textiles with recyclable ILs [128]. The recovered dye-rich IL can recolor new fabrics, while the decolorized fibers become valuable by-products. This route avoids harsh chemicals and promotes circularity in the fashion and textile industries. In 2024, DyeRecycle Ltd secured about $2.2 million in pre-seed and equity-free match funding (provided by Innovate UK) to support further technical and commercial scale-up. Notably, despite these promising large-scale examples, the industrial deployment of ILs remains challenging. High material costs are a primary barrier, and although some PILs are promoted as low-cost options, their usefulness is often confined to specific niches. Moreover, commercial success is never determined by technical feasibility alone but also heavily relies on factors such as market demand, policy changes, investor expectations, and the characteristics of the target industry [129].

2.1.4 Protic Ionic Liquids

When considering industrial applications, the high cost of APILs remains a critical hurdle [86]. Several factors drive these prices [130]: (1) expensive starting materials and complicated synthesis routes; (2) low atom-utilization efficiency in the alkylation and salt-metathesis reactions typically used to synthesize many ILs; (3) energy-intensive isolation and purification steps, owing to the non-volatile nature of ILs; and (4) the need to treat highly saline wastewater generated during processing. At the time of writing, the supplier Proionic lists the prices of commonly used [Emim]-based APILs, 1-ethyl-3-methylimidazolium acetate ([Emim][OAc]) and 1-ethyl-3-methylimidazolium

trifluoromethanesulfonate ([Emim][OTf]), at €280 kg^{-1} and €330 kg^{-1}, respectively, for ≥10 kg orders [131]. Although these quotations apply only to small-scale purchases and cannot serve as benchmarks for full commercial production, it is generally accepted that APILs cost 5–20 times more than conventional organic solvents [86]. The belief that ILs are inherently expensive persisted for years until attention shifted to PILs and detailed techno-economic analyses of their manufacture.

PILs are a class of ILs that can be synthesized through a straightforward Brønsted acid-base neutralization without the need for further purification [132]. Common Brønsted acids include mineral [133, 134] and carboxylic acids [135, 136], while the Brønsted bases include alkanolamines [135], alkylamines [133, 134], and imidazoles [137]. During PIL formation, a proton transfers from the Brønsted acid to the Brønsted base, generating the conjugate pair $[BH^+][A^-]$ (Equation 2.1) [132]. The proton on the cation is labile, which, on the one hand, enables a hydrogen-bond network between the cation and anion [138] and, on the other hand, establishes a reversible equilibrium with the parent acid and base (the proton can be transferred back from the cation to the anion) [105]. This acid-base equilibrium gives PILs distinctive physicochemical properties, most notably a non-negligible vapor pressure. Some PILs can reach a vapor pressure of 1 atm when heated at ambient pressure, allowing them to boil directly rather than decompose via reverse proton transfer to the more volatile parent acid and base species [138]. Specifically, the reversibility of proton transfer is governed by the pK_a difference (ΔpK_a) between the acid and base. A larger ΔpK_a generally means a more complete proton transfer, lower volatility, and a higher boiling point [105, 138]. $\Delta pK_a \approx 10$ is often cited as the threshold above which the boiling points of PILs become inaccessible because such PILs tend to decompose before they can reach their boiling points [139, 140]. This is common for combinations of strong inorganic acids (e.g., H_2SO_4 and HCl) with strong organic bases (e.g., alkylamine and imidazole) [105]. For instance, the $[HSO_4]^-$-based PIL triethylammonium hydrogen sulfate ($[TEA][HSO_4]$) is thermally stable up to 263–277 °C, where it decomposes before reaching its boiling point [134, 138]. In contrast, PILs with a smaller ΔpK_a show less

proton transfer and higher volatility. They can be purified by evaporation under reduced pressure, thereby giving rise to the term “distillable” ILs [92]. For example, several acetate-based PILs with relatively low ΔpK_a are highly volatile and begin to lose mass once the temperature exceeds 35–74 °C [141]. Notably, if the ΔpK_a is too low, the proton shuttles back and forth between the acid and the base, preventing the formation of a stable ion pair. As a result, a significant fraction of unprotonated neutral species (B and H−A) remains in the mixture. Such systems are better described as acid-base molecular complexes rather than true PILs. According to accepted definitions, a product is classified as a pure PIL only when the degree of proton transfer exceeds 99% [142].

$$H{-}A + B \leftrightarrow BH^+ + A^- \quad (2.1)$$

Compared with APILs, there is no doubt that the clearest advantage of PILs is their much lower production cost, removing a long-standing barrier to commercialization [143]. This cost benefit arises from their simplified synthesis. For example, Chen et al. showed that the PIL [TEA][HSO_4] can be made in 7 steps from basic feedstocks (petroleum, N_2, H_2, S_8, and O_2), whereas producing the widely studied APIL [Emim][OAc] requires 29 steps [144]. Chen et al. also performed the first industrial-scale techno-economic analysis of two common PILs, estimating production costs of \$1.24 kg^{-1} for [TEA][HSO_4] and \$2.96–5.88 kg^{-1} for 1-methylimidazolium hydrogen sulfate [HC1im][HSO_4] [144]. Using the same methodology, Chiappe et al. estimated the production costs of three tetramethylguanidinium-based PILs: \$1.94 kg^{-1} for tetramethylguanidinium hydrogen sulfate ([HTMG][HSO_4]), \$1.84 kg^{-1} for tetramethylguanidinium hydrogen oxalate ([HTMG][HC_2O_4]), and \$2.94 kg^{-1} for tetramethylguanidinium monomethyl carbonate ([HTMG][$MeCO_3$]) [143]. These prices are comparable to those of commonly used organic solvents such as acetone and ethyl acetate, which range from \$1.30 kg^{-1} to \$1.40 kg^{-1} [144]. The production costs of PILs depend largely on the costs of the starting materials [144], and since mineral acids are generally inexpensive, they are predominantly dictated by the costs of the organic base precursors [134]. In addition to these economic advantages, the straightforward

synthesis of PILs produces less waste, requires lower energy input, achieves higher atom economy, and therefore leaves a smaller environmental footprint than the routes used for APILs [134].

It should be noted that the preceding cost figures for PILs were derived from standard economic assessments and therefore reflect only direct production costs. Such analyses exclude environmental externalities—unpriced side effects of economic activity on human health, ecosystem quality, and resource availability. To capture these indirect costs, Baaqel et al. combined life cycle assessment (LCA) with monetization, converting environmental impacts into currency and adding them to the direct cost [145]. The total cost can then be expressed as a single index that combines the solvent's direct production cost (economic) with its externalities (environmental). In this study, total costs were calculated for two PILs: [TEA][HSO_4] and [HC_1im][HSO_4] ([HMIM][HSO_4]), and for two conventional solvents: fossil-derived acetone and bio-derived glycerol. These results (Figure 2.3 a) showed that indirect costs exceeded direct costs for all four solvents. [TEA][HSO_4] had both the lowest direct cost (\$0.78 kg^{-1}) and the lowest indirect cost (\$1.09 kg^{-1}), giving the lowest total cost (\$1.87 kg^{-1}), followed by acetone, [HC_1im][HSO_4], and glycerol. Although the precursor triethylamine for [TEA][HSO_4] was about \$1.40 kg^{-1} more expensive than the precursors of acetone or glycerol, the direct production cost was offset by the very low price of the reactant sulfuric acid (\$0.05 kg^{-1}). Moreover, [TEA][HSO_4] showed a lower indirect cost because it caused less damage to human health and ecosystem quality. On the other hand, [HC_1im][HSO_4] had the highest direct cost at about \$1.46 kg^{-1}, largely because its precursor, 1-methylimidazole, cost \$2.80 kg^{-1}. Even the inexpensive sulfuric acid could not fully compensate. Even so, the total cost of [HC_1im][HSO_4] was lower than that of glycerol because glycerol carried high externalities, mainly through human health and ecosystem damage. This result challenges the usual belief that bio-based solvents such as glycerol always have smaller environmental footprints than fossil-derived solvents such as PILs and acetone. In this analysis, glycerol showed the greatest external cost of the four solvents

considered.

In addition to the comparison of total costs, Baaqel et al. also emphasized that solvents should be evaluated by combining their production costs with their performance in a specific use phase, thereby providing a more comprehensive assessment for a given application [145]. For instance, they re-evaluated the total costs of the four solvents in biomass pretreatment by calculating the total monetized cost per kilogram of pretreated biomass (Figure 2.3 b). The results showed that the total costs of both PILs, [TEA][HSO_4] and [HC_1im][HSO_4], on a per-weight basis of pretreated biomass were significantly lower than those of acetone and glycerol. This was mainly attributed to the near-quantitative recycling ability of PILs, which led to a very small makeup amount (32 kg t^{-1}) compared with conventional solvents. For instance, because glycerol had a poor recycling rate (about 75% recovery), approximately 2,500 kg of glycerol makeup per ton of pretreated biomass was required, about 80 times more than for PILs. Overall, the study demonstrates that PILs are not necessarily more expensive or environmentally detrimental than conventional solvents. In fact, when economic factors, environmental externalities, and specific application scenarios are considered, PILs can achieve comparable or even lower total costs.

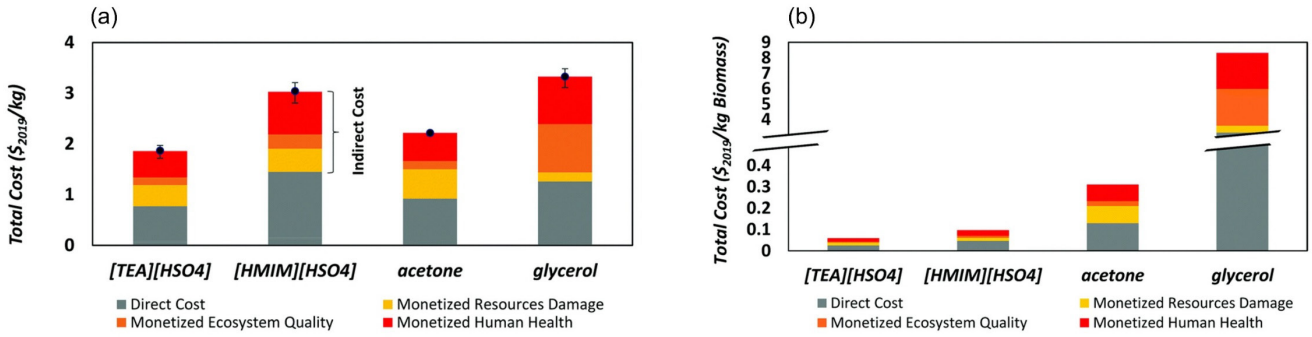


Figure 2.3. (a) Total solvent cost, including direct production costs and indirect externalities; and (b) Total solvent production cost per unit mass of pretreated biomass. Reproduced from Baaqel et al. [145].

Large-scale production of PILs is essential for lowering their cost because it enables

economies of scale. Recently, Dezashibi et al. from our group have designed and evaluated a new semi-batch reactor for bulk (pilot-scale) PIL production (Figure 2.4) [146]. During scale-up trials, it was found that the strongly exothermic acid-base neutralization generated localized hot spots, and limited mass transfer plus density differences between the acid and base led to incomplete conversion to PILs. The high corrosiveness and reactivity of the feedstock also required specialized reactor materials. To meet these engineering challenges, Dezashibi et al. customized a continuously stirred-tank reactor (CSTR) fitted with a cooling jacket. The jacket thickness was chosen to maintain turbulent flow (a high Reynolds number), improving heat dissipation between the cooling water and the reaction mixture. Mechanical impeller mixing was used to enhance mass transfer and ensure complete acid-base neutralization. The reactor was lined with polytetrafluoroethylene (PTFE), which provides excellent chemical resistance even under extreme pH and harsh conditions. At the same time, real-time monitoring of the reactor temperature and outlet PIL conductivity was developed, allowing precise control of reaction conditions through the adjustment of the amine feed pump rate and ensuring consistent, targeted PIL properties. Currently, the reactor has been commissioned at a pilot-scale throughput of 0.8 kg h^{-1} of [TEA][HSO_4] (20 wt% water content) and has produced a cumulative 800 kg of PILs. Scale-up analysis suggested that, with a similar geometry, the design could be extended to an industrial throughput of 105 kg h^{-1}. Nevertheless, issues related to heat management, liner material properties, mixing performance, and real-time control precision must be carefully re-evaluated and addressed to ensure a successful transition to full industrial PIL manufacture.

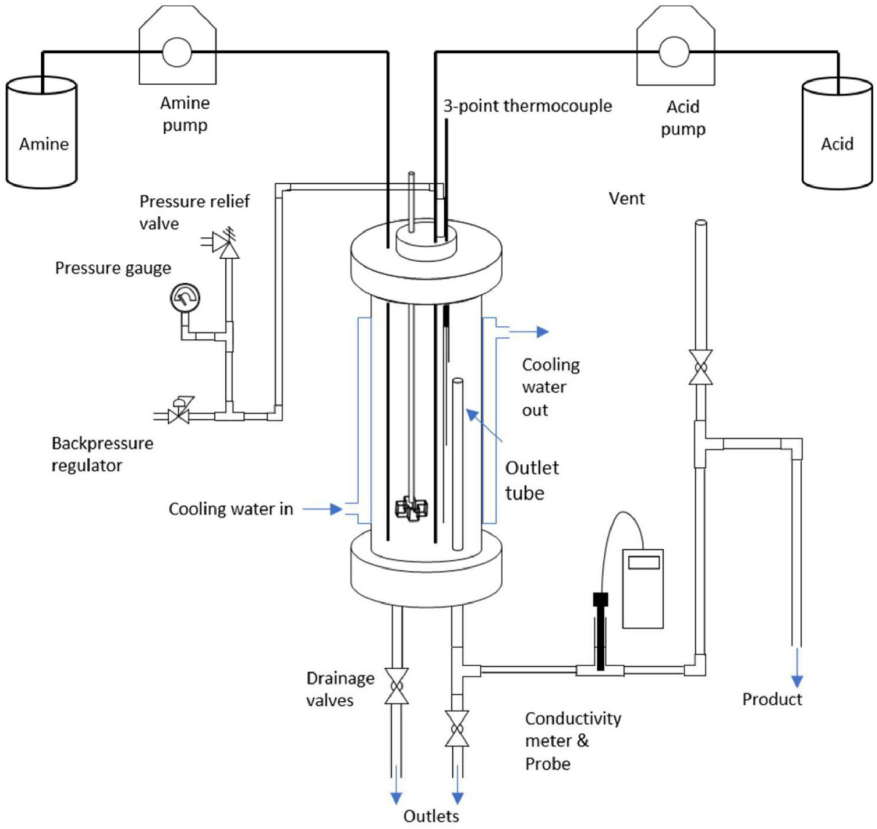


Figure 2.4. Reactor setup and associated electronic devices for protic ionic liquid production (schematic). Reproduced from Dezashibi et al. [146].

2.1.5 Summary

ILs have been proven effective across a range of fields, and their versatility stems from their promising physicochemical properties, including high thermal stability, low volatility, and strong solvation ability. Accordingly, ILs are often branded as the “solvent of the future”. To realize the true “greenness” of ILs, however, it is crucial to develop IL species with low toxicity and high biodegradability. From an industrial perspective, the high cost of APILs remains the major economic barrier to broader applications, whereas PILs have emerged as a low-cost alternative due to their simplified synthesis processes. Consistent with this, techno-economic analysis and life-cycle assessment indicate that alkylammonium hydrogen sulfate PILs (e.g., [TEA][HSO_4]) can be produced at a cost much lower than that of traditional organic solvents, offering clear advantages for industrial-scale biomass processing, particularly owing to their high

recyclability.

2.2 Biorefinery

2.2.1 General Overview

Biomass can be broadly defined as organic material derived from living or recently living organisms (e.g., plants, animals, and microorganisms) and their wastes [9, 147]. Unlike fossil resources, biomass is regarded as a renewable and clean carbon source owing to its unique carbon cycle [7]. Specifically, the carbon contained in biomass originates from the fixation of atmospheric CO_2 through photosynthesis. During biomass utilization, the fixed carbon is released back as CO_2 and then recaptured by the next cycle of biomass growth, completing a closed carbon loop [148]. This balance renders biomass utilization effectively carbon-neutral. By contrast, CO_2 from fossil fuels comes from carbon fixed millions of years ago, outside the modern carbon cycle. The overexploitation of fossil resources has disrupted today's carbon balance, leading to significant greenhouse gas (GHG) effects. To address these issues, biomass valorization to biofuels, electricity, and bio-based chemicals through chemical or biological routes has attracted widespread interest. To differentiate this approach from conventional fossil fuel refining, the National Renewable Energy Laboratory (NREL) has termed this integrated biomass conversion methodology the "biorefinery" process [149].

According to the types of biomass feedstocks, biorefineries can be divided into three categories (Figure 2.5), which include first-generation (food crops) [150], second-generation (lignocellulosic biomass) [134], and third-generation (algal biomass) biorefineries [151]. The first-generation (1G) biorefinery utilizes food crops rich in sugars and starch, such as sugarcane, sugar beet, wheat, and corn, to produce 1G bioethanol [11, 12], and oil-containing plants, such as rapeseed, sunflower, soybean, and oil palm, to produce biodiesel [12-14]. After decades of development, the 1G biorefinery has reached a mature stage, establishing a complete supply chain, reliable production infrastructure, and a well-recognized market system. However, its

development also faces severe challenges. The use of food crops as feedstocks has raised people's concerns about food security [16], while the intensive consumption of land and water resources for crop cultivation has posed significant pressure on the ecological environment [17, 18]. In recent years, the trade-off between the benefits of 1G biofuel production and its adverse impacts on environmental sustainability and food security has aroused extensive debate. These controversies have prompted researchers to explore the technical routes for producing advanced biofuels and bio-based materials from non-food feedstocks.

The second-generation (2G) biorefinery adopts lignocellulosic biomass as a raw material, including agricultural residues, forestry by-products, energy crops, and even invasive plants [11, 16, 22-24]. These feedstocks are mainly derived from the non-edible parts of plants, effectively preventing competition with food crops for land and resources. Meanwhile, lignocellulosic biomass often comes with low or even negative feedstock costs for two main reasons: (1) the cultivation of energy crops requires less water and fertilizer, while maintaining high yields per unit of land [19, 20], and (2) agricultural residues, waste wood, and invasive plants are abundant, and often carry negative value because their removal and disposal require substantial labor and financial resources [12, 24, 152, 153]. Leveraging these wastes as biorefinery feedstocks can therefore offset those management costs. The typical value-added products from the 2G biorefinery include 2G bioethanol [11] and various bio-based chemicals (e.g., furfural and HMF) [53]. However, the complex three-dimensional structure of lignocellulosic biomass requires a step called “pretreatment” to fractionate cellulose, hemicellulose, and lignin before conversion [28, 149]. Pretreatment is regarded as the most energy-consuming and expensive process in the 2G biorefinery, which directly affects the energy return on investment (EROI) and the economic feasibility of the entire system [154, 155]. Therefore, the optimization of pretreatment technology is a key bottleneck for the commercialization of the 2G biorefinery.

The third-generation (3G) biorefinery primarily utilizes algal biomass, both macroalgae

and microalgae [156], as its feedstocks. Macroalgae, such as kelp and laver, are multicellular aquatic organisms that typically grow attached to the seafloor or other substrates within the photic zone [157, 158]. Although macroalgae are rich in polysaccharides and have certain industrial potential [151], their large-scale cultivation remains challenging. This is because the growth of macroalgae is highly dependent on marine ecological conditions, including seasonal changes, climate variations, and sea states, which are very difficult to control [157]. Therefore, macroalgae are not the core feedstocks of the 3G biorefinery. On the contrary, microalgae are unicellular or simple multicellular organisms with high photosynthetic efficiency (CO_2 fixation capacity), fast growth rates, and strong adaptability to environmental conditions [159]. Microalgae can be cultivated efficiently in open raceway ponds or closed photobioreactors (PBRs) [151, 160], which require minimal land use [161]. In addition, essential nutrients, such as nitrogen and phosphorus, can be sourced directly from agricultural or municipal wastewater in large-scale microalgae cultivation, reducing reliance on conventional fertilizers and fresh water [162]. These characteristics make microalgae ideal feedstocks for the 3G biorefinery. Common microalgae species include cyanobacteria (*Cyanophyceae*), green algae (*Chlorophyceae*), golden algae (*Chrysophyceae*), and diatoms (*Bacillariophyceae*) [151, 159, 163, 164]. They are important reservoirs of proteins, carbohydrates, and lipids (with the proportions varying among species), thereby providing various high-value application potentials [151, 159, 165]. The bioenergy products of the 3G biorefinery involve various forms, including biodiesel produced by lipid transesterification, 3G bioethanol produced by polysaccharide hydrolysis and fermentation, and biohydrogen produced by anaerobic digestion [151, 159, 162]. In addition to bioenergy production, the application of the 3G biorefinery also covers the field of biochemical conversion, including nutrition and food supplements, pharmaceuticals, pigments, cosmetics, and antioxidants [159, 163, 166, 167]. Despite these advantages of the 3G biorefinery, it still faces critical technological bottlenecks similar to those encountered in 2G systems. Specifically, the cell wall structure of microalgae is complex, and the efficient extraction and conversion of valuable components can only be achieved through energy-intensive cell wall

disruption and pretreatment [151]. These additional processes substantially increase energy consumption and operational costs. Therefore, reducing the energy costs of pretreatment and improving the overall system EROI are still the core challenges for future technological optimization of the 3G biorefinery. Due to space limitations, the following sections will focus on a detailed introduction to the lignocellulosic biomass (2G) biorefinery and its state-of-the-art pretreatment methods.

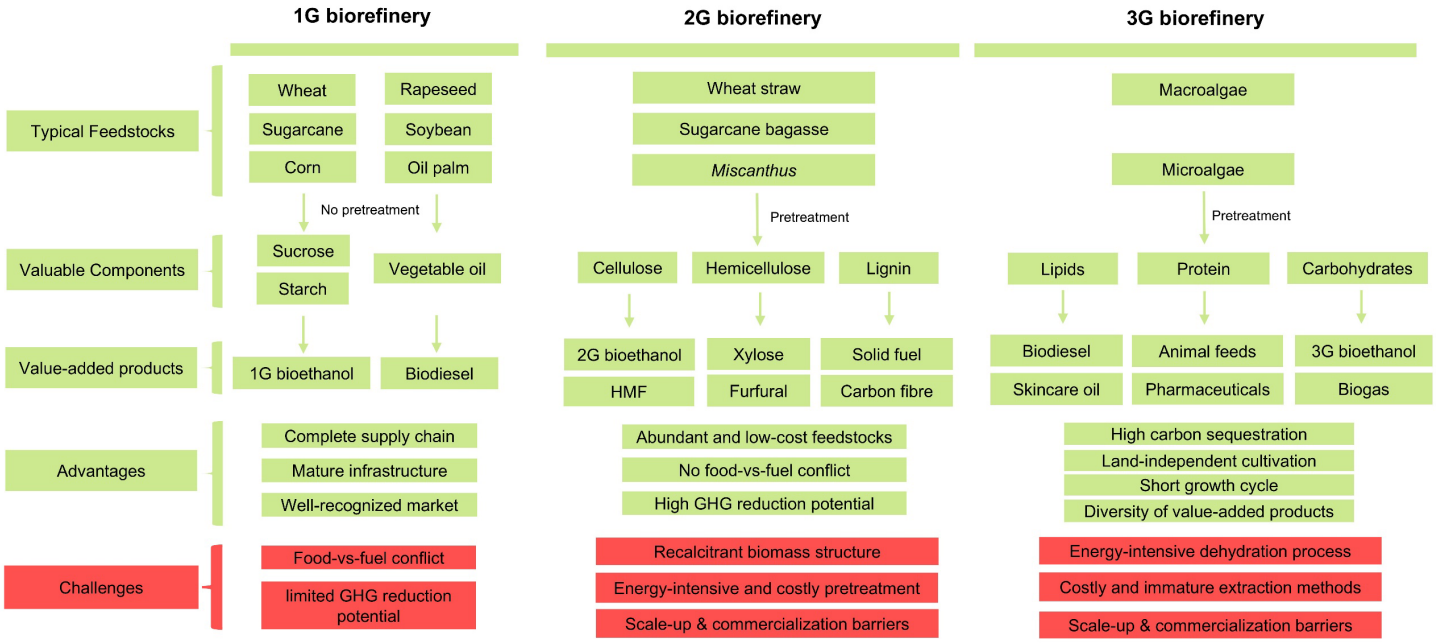


Figure 2.5. Classification of three biorefinery types and their respective advantages and challenges.

2.2.2 Lignocellulose

Lignocellulosic biomass is a composite of three biopolymers—cellulose, hemicellulose, and lignin—which together account for approximately 90% of the dry weight of biomass [168]. Both cellulose and hemicellulose are polysaccharides, whereas lignin is an aromatic polymer. The remaining minor components include proteins, lipids, pectins, and inorganic ash [11]. The three main biopolymers join to form a highly functional, three-dimensional network (Figure 2.6) [169]. Linear cellulose fibers are sheathed by hemicellulose through hydrogen bonding and van der Waals forces, while

hemicellulose is covalently linked to lignin [11, 170]. Hemicellulose therefore bridges cellulose and lignin and fills the spaces between them. These interactions give plant cell walls structural integrity and recalcitrance, making them highly resistant to mild chemical or biological attacks [28, 29]. Therefore, to produce 2G bioethanol or other biochemicals, a pretreatment step is needed to deconstruct or fractionate the lignocellulose matrix, facilitating subsequent enzymatic hydrolysis or other transformations [28, 29].

Lignocellulosic biomass can be grouped into three broad categories: grass biomass, hardwood (flowering plants), and softwood (seed-bearing plants) [171]. Each category contains promising candidates for the 2G biorefinery, yet their recalcitrance varies [11]. Softwood is generally the most recalcitrant, followed by hardwood and then grass biomass, mainly because of variations in their lignin subunit composition [11, 16, 172].

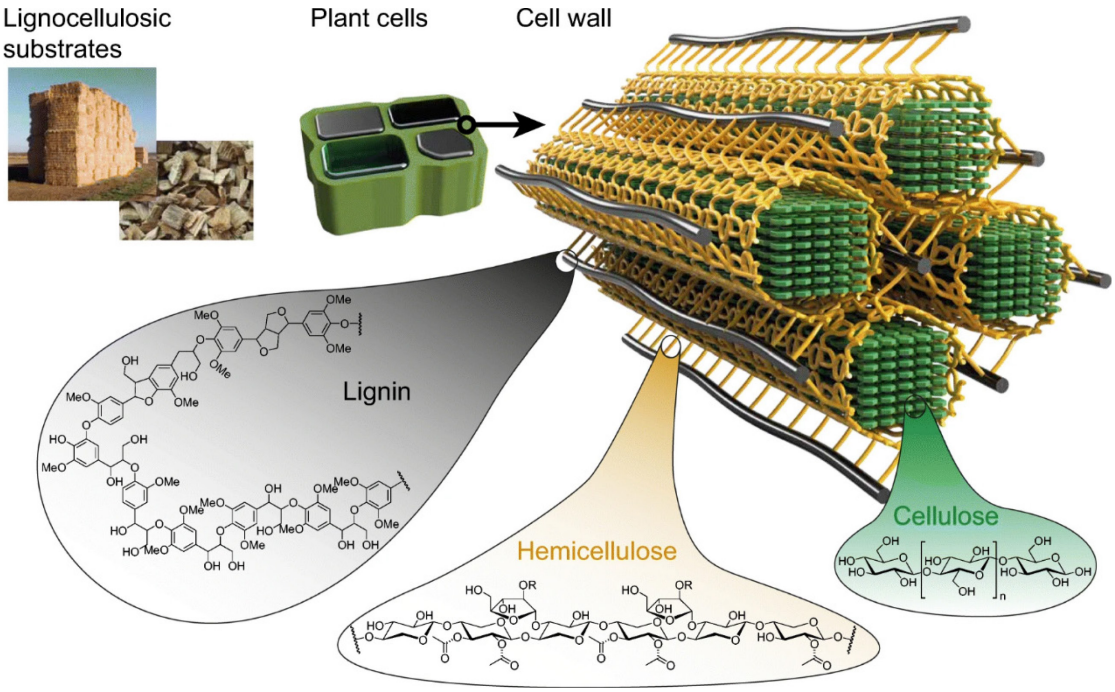


Figure 2.6. Three-dimensional arrangement of cellulose, hemicellulose, and lignin within the cell walls of lignocellulosic biomass. Reproduced from Brethauer et al. [169], with the structures of cellulose, hemicellulose, and lignin adapted from Rozmysłowicz et al. [173].

2.2.2.1 Cellulose

Cellulose is the most abundant natural polymer on Earth, accounting for 35–50 wt% of dry lignocellulosic biomass [11, 174]. Cellulose is solely composed of glucose units, with the general formula $(C_6H_{10}O_5)_n$, where n, the degree of polymerization, typically ranges from 10,000 to 15,000 [175]. Glucose, the basic structural unit of cellulose, is an aldohexose. In water, glucose exists in three interconvertible forms (Figure 2.7). Only a very small fraction is in the linear aldehyde form, while most is present as the cyclic isomers α-D-glucopyranose and β-D-glucopyranose. Both cyclic isomers are created by an intramolecular reaction between the C1 aldehyde group and the C5 hydroxyl group [176]. As a result, the initial aldehyde group in the linear form is transformed into a hemiacetal. The two cyclic isomers differ in the orientation of the C1 hydroxyl relative to the C5–CH_2OH substituent. In α-D-glucopyranose, these groups lie on opposite faces of the ring, whereas in β-D-glucopyranose, they are on the same face. Moreover, α-D-glucopyranose is the monomeric unit of starch, while β-D-glucopyranose forms the cellulose polymer [177].

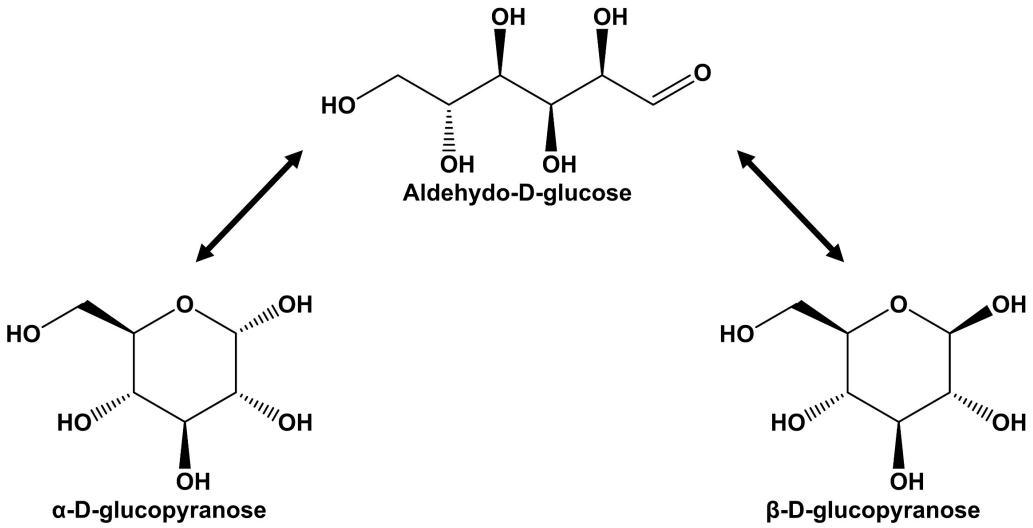


Figure 2.7. Interconversion between the linear (open-chain) and cyclic forms of glucose in the water.

In cellulose, glucose units are linked by β-1,4-glycosidic bonds, which are covalent

bonds formed via dehydration (condensation) between the C1 hydroxyl of one glucose and the C4 hydroxyl of the next [177, 178]. This linkage imparts rigidity and a linear arrangement to the glucan chain [179]. In addition to β-1,4-glycosidic bonds, the glucan chain is further reinforced through intramolecular and intermolecular hydrogen bonds [155, 180, 181]. Intramolecular hydrogen bonds help maintain the single-chain structure, while intermolecular hydrogen bonds connect adjacent chains, allowing them to be closely packed. Together with van der Waals forces, these interactions aggregate multiple glucan chains into “microfibrils” [155, 179], which in turn assemble into larger fiber structures (Figure 2.8) [179, 182]. Due to the high degree of polymerization of microfibrils, cellulose fibers are generally insoluble in water and most inorganic solvents [180]. However, cellulose fibers show a strong water-swelling capacity [183]. This is because each glucose unit contains a primary hydroxyl at the C6 position and two secondary hydroxyls at the C2 and C3 positions, which endow cellulose with hydrophilicity.

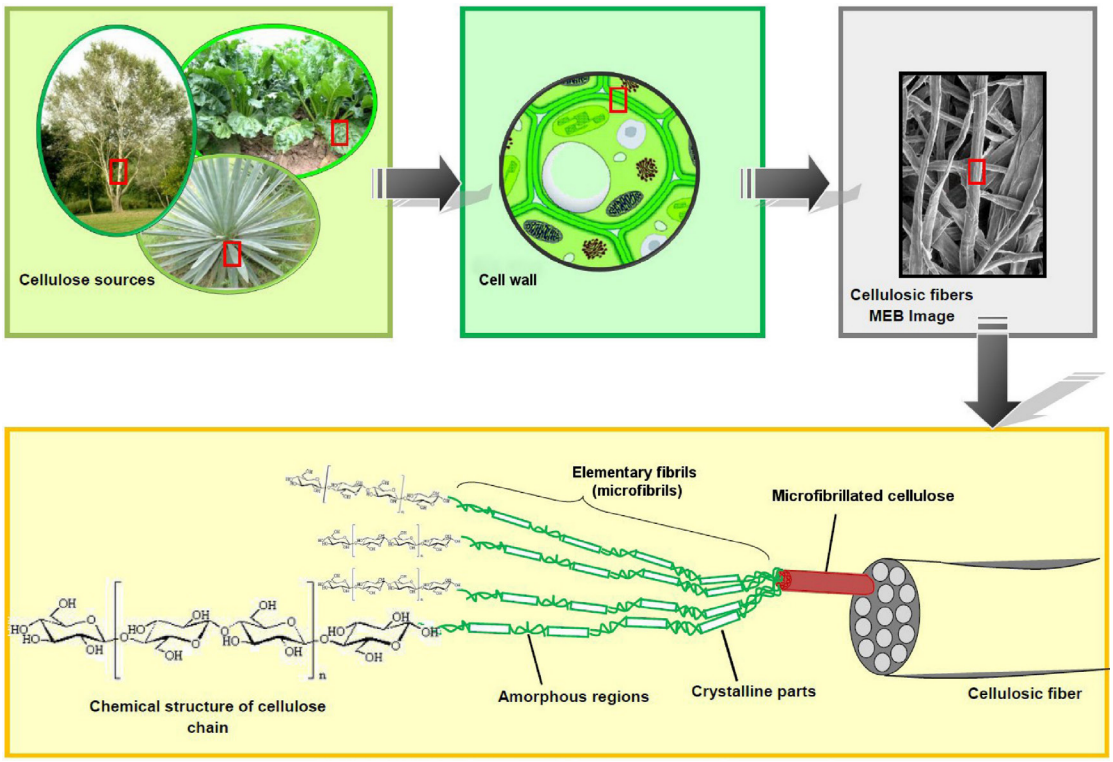


Figure 2.8. Hierarchical scale of cellulose—from individual molecular chains to macroscopic sources. Reproduced from Lavoine et al. [182].

In microfibrils, most glucan chains are aligned in a highly ordered, compact manner, forming crystalline regions [184]. These crystalline regions exhibit excellent mechanical strength and are resistant to chemical reagents and enzymes [185, 186]. Microfibrils also contain domains where glucan chains are loosely and randomly arranged. These regions are defined as amorphous regions [187]. The formation of amorphous regions can be attributed to multiple factors. A common cause is the physical entrapment of “impurities” such as hemicellulose and lignin within microfibrils during plant cell wall biosynthesis, which disrupts orderly chain packing and hinders crystalline structure formation [188]. Compared with crystalline regions, amorphous areas are more vulnerable to chemical or biological attacks [186, 189]. The proportion of crystalline regions in cellulose is defined as crystallinity, which varies according to different plant species, with a typical range of 40–70% [190]. Notably, the required degree of crystallinity is field-dependent and directly influences process design. For example, in traditional papermaking, the processes are designed to remove lignin and hemicellulose from biomass while maintaining high cellulose crystallinity to preserve mechanical strength for paper fibers [191]. By contrast, in biorefinery processes, a key pretreatment goal is to disrupt cellulose crystallinity and convert it to a more reactive amorphous form, thereby improving accessibility for chemical or enzymatic hydrolysis and promoting subsequent conversion to value-added chemicals [192].

Cellulose valorization has been extensively explored. Beyond papermaking, current research focuses on hydrolyzing cellulose to glucose for glucose-based biorefinery processes. The primary products include bioethanol [193] and HMF [194, 195]. Notably, HMF is a key bio-based platform chemical, consisting of a furan ring bearing an aldehyde at C2 and a hydroxymethyl group at C5 [53]. Among its derivatives, FDCA is particularly promising [196]. It serves as the monomer for polyethylene furanoate (PEF) [65-67, 197], a bio-based polyester whose gas barrier properties surpass those of petroleum-derived polyethylene terephthalate (PET) from terephthalic acid [198], significantly extending the shelf life of food when used as food packaging material [197,

199-201]. Under acidic conditions, HMF can also hydrolyze and rearrange to levulinic acid (LA) [202, 203], a versatile five-carbon platform compound used to produce liquid fuels, pesticides, spices, and pharmaceuticals [204]. The relevant conversion pathway is displayed in Figure 2.9 [205]. In 2004, both FDCA and LA were named among the twelve “Top Value-Added Chemicals from Biomass” by the U.S. Department of Energy [206].

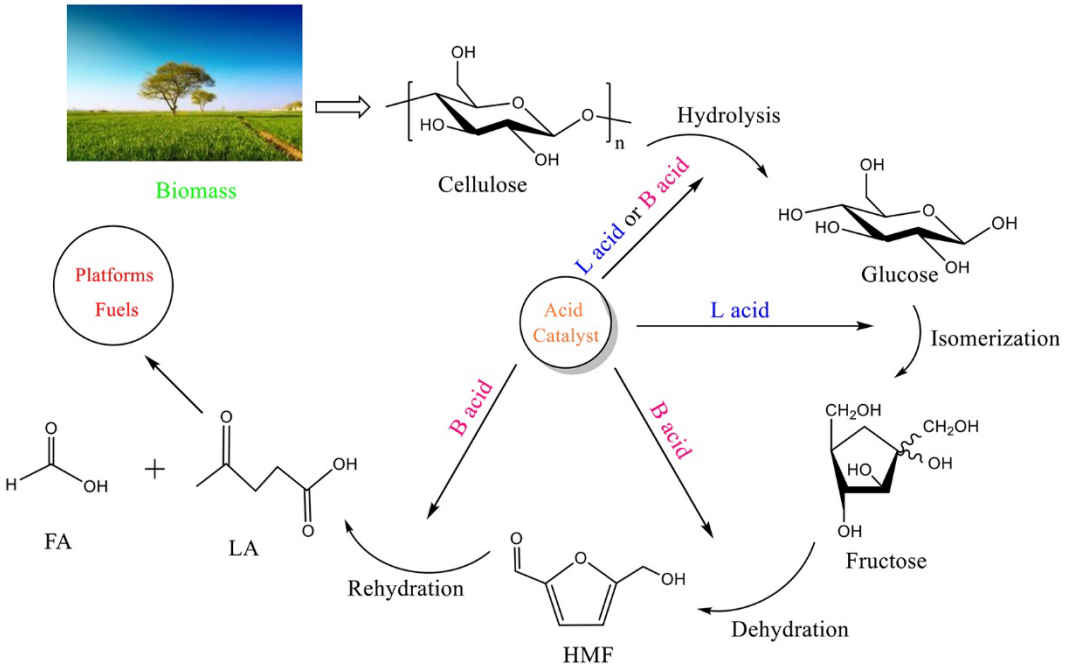


Figure 2.9. Conversion pathway from cellulose to HMF and onward to LA. Reproduced from Ma et al. [205].

2.2.2.2 Hemicellulose

Hemicellulose is a heterogeneous polysaccharide, making up 20–35 wt% of dry lignocellulosic biomass [26, 155]. Hemicellulose is composed of hexose sugars (e.g., glucose, mannose, and galactose) and pentose sugars (e.g., xylose and arabinose) [207]. The proportions of these monosaccharides in hemicellulose vary with plant species. In hardwood and grass biomass, the xylose unit is the main component, forming glucuronoxylan polysaccharides, while in softwood, the mannose unit is more abundant, making up galactoglucomannan polysaccharides [11, 155, 191]. Meanwhile, hemicellulose also contains uronic acids (e.g., D-glucuronic acid, D-galacturonic acid,

and 4-O-methyl-D-glucuronic acid) and acetyl groups [208]. In contrast to cellulose, the hemicellulose chains are shorter (typically 100–200 units), highly branched, and largely amorphous [11, 208]. They can connect with lignin via covalent bonds (e.g., glycosidic linkages, ester linkages, and benzyl ether linkages), generating lignin–carbohydrate complexes (LCCs) [209, 210].

Compared with cellulose, the degree of polymerization of hemicellulose is much lower, making it more readily hydrolyzed, especially under acidic conditions [180]. Hexose units in hemicellulose can be converted to HMF as in cellulose, whereas pentose units are dehydrated to furfural [53]. Like HMF, furfural is a versatile platform chemical with downstream applications in resins, pharmaceuticals, plastics, agrochemicals, fuel additives, and surfactants [53, 211, 212]. Different from HMF, furfural is one of the few bio-based platform chemicals already produced at a large commercial scale, with an annual output of over 400,000 tons and a market size of about $700 million [53, 54, 213]. Currently, most commercial plants use improved versions of the Quaker Oats process developed in the 1920s [53].

2.2.2.3 Lignin

Lignin is a highly branched, heterogeneous aromatic polymer that accounts for roughly 15–30 wt% of dry lignocellulosic biomass [27]. Unlike hemicellulose, lignin is a highly polymerized compound with a high molecular weight, which endows the cell wall with water insolubility and hydrophobicity [11]. Functionally, lignin acts as a structural “glue” that links and embeds other polysaccharides, producing a rigid three-dimensional network that shields cellulose and hemicellulose from enzymatic, microbial, and physicochemical degradation [11, 27, 214]. Lignin is biosynthesized by the radical polymerization of three monomers, including coniferyl alcohol, sinapyl alcohol, and p-coumaryl alcohol [215]. Once polymerized, these monomers, also known as monolignols, are categorized based on their aromatic structures, corresponding to guaiacyl (G), syringyl (S), and p-hydroxyphenyl (H) subunits, respectively [16, 19]. The molecular structures of these three subunits are displayed in Figure 2.10. The S unit

is characterized by two methoxy groups located symmetrically at the C3 and C5 positions of the aromatic ring. The G unit has a single methoxy group at the C3 position, while the H unit has none. Chemically, the G unit is more reactive than the S unit because its free C5 position promotes C–C linkages during lignification or delignification [216]. In contrast, such C–C linkages cannot form in the S unit because its C5 site is already occupied by a methoxy group. These C–C bonds hinder lignin removal, making biomass more recalcitrant to pretreatment. The proportion of these subunits varies across plant species, leading to different degrees of lignocellulose recalcitrance [217]. Softwood is composed almost entirely of G units, which readily undergo condensation, making delignification particularly difficult. Hardwood contains roughly equal proportions of G and S units, whereas grass biomass includes all three units [218]. Notably, studies on the impact of the H unit on biomass recalcitrance are limited. However, several investigations have indicated that higher H unit content in grass biomass reduces recalcitrance, possibly due to the lower molecular weight of H-rich lignin [219]. Softwood also has the highest lignin content (25–30 wt%), compared with hardwood (20–25 wt%) and grass biomass (10–30 wt%) [155, 220, 221]. These factors combine to make softwood lignin highly recalcitrant, so its deconstruction is more energy-intensive and costly than that of hardwood or grass biomass [16, 36]. Beyond these three basic units, grass biomass also contains substantial amounts of ferulic acid (FA) and p-coumaric acid (PCA) units, which cross-link lignin monomers (monolignols) and hemicellulose chains to form LCCs (e.g., lignin–ferulate–polysaccharide ester linkages) [222-224]. In contrast, softwood has only trace amounts of FA and PCA [224, 225]. LCCs in softwood form through more direct benzyl ether and benzyl ester linkages between lignin and hemicellulose [11, 224].

Connections between lignin units involve a range of C–O–C and C–C linkages (Figure 2.10). Among the C–O–C bonds, the β-O-4′ ether linkage is dominant, accounting for roughly 50% of the bonds in native lignin, whereas other ether linkages such as 4-O-5′ occur to a lesser extent [226, 227]. The main C–C linkages are β-5′, β-1′, β-β′, and 5-5′ [228, 229]. The β-O-4′ ether bond is the most labile and therefore the primary

cleavage target during delignification [230]. To date, a complete structural picture of native lignin is still lacking. The presence of more than 20 distinct bond types makes lignin one of the most complex biopolymers known [216]. Numerous studies have proposed genetically engineering plants to produce more homogeneous, less recalcitrant lignin with greater valorization potential, but this research remains in its early stages [217, 231-233].

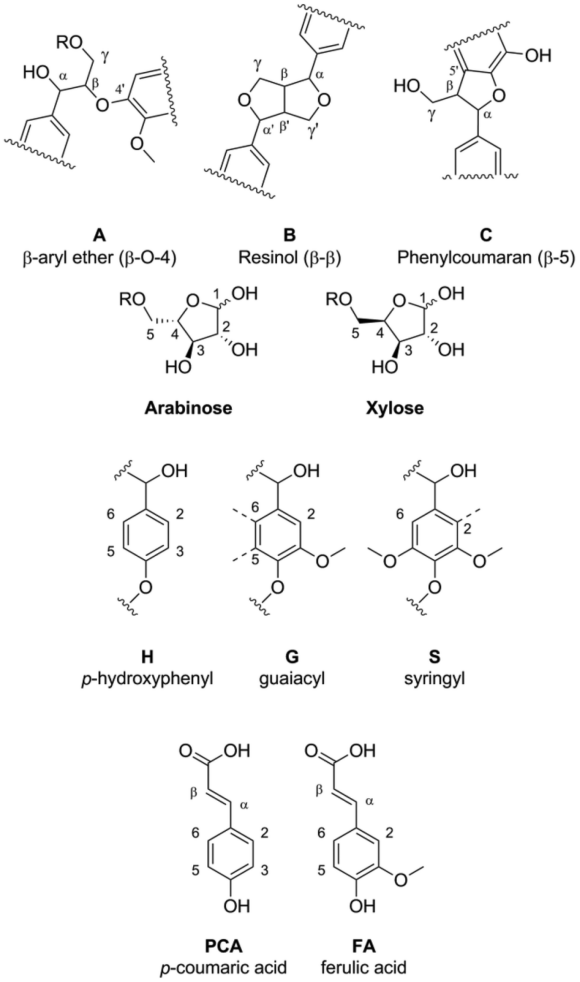


Figure 2.10. Major linkages and structural subunits in native lignin. Reproduced from Brandt-Talbot et al. [19].

As mentioned earlier, lignin in lignocellulosic biomass is the principal barrier to efficient polysaccharide utilization because it physically blocks enzymes from accessing cellulose and hemicellulose. Pretreatment to remove lignin is therefore essential in the 2G biorefinery [228, 234]. However, given the high cost of pretreatment, valorizing only

the polysaccharide fraction is seldom sufficient for economic viability. Thus, the valorization of extracted lignin becomes critical [235]. At present, the most common valorization strategy is to burn lignin directly to supply heat and power for the biorefinery [53]. Alternatively, lignin can be converted by pyrolysis into bio-oils with relatively high calorific values [236]. Such oils are complex mixtures of phenolic compounds [237], and are unsuitable for direct use as liquid fuels because their high oxygen content results in acidity, reactivity, viscosity, and corrosiveness [238]. Catalytic hydrodeoxygenation is therefore required to upgrade the bio-oils [239], and hydrogen consumption during this step must be carefully managed to maintain overall energy efficiency [240]. Producing benzene, toluene, and xylene (BTX)—important petrochemical precursors—via lignin hydrocracking has also attracted interest, as it offers a renewable, carbon-neutral alternative to petroleum-derived sources. Nevertheless, large-scale BTX production via lignin hydrocracking remains economically challenging because of the low theoretical yield [53, 241]. Additionally, lignin can be used directly, or after minor structural modification, as a polymeric material. Its potential applications include serving as a starting material for resin synthesis [242], biocompatible nanofibers [243], soil conditioners [244], heavy metal sorbents [245], and UV filters [246]. Because each use calls for lignin with specific properties, suitable isolation or purification methods are required to obtain lignin with targeted and consistent functionalities for downstream processing.

2.2.3 Deconstruction of Lignocellulose

2.2.3.1 Kraft Pulping

Currently, as attention has shifted to the effective utilization of lignocellulosic biomass, a series of methods have been investigated for its deconstruction and fractionation [34, 35, 247]. In fact, the concept of biomass deconstruction can be traced back to the 19th century with the advent of the papermaking industry [248]. The Kraft pulping process, also known as the sulfate process, is the most widely adopted chemical pulping method. In this process, wood chips and other lignocellulosic feedstocks are treated with a mixed aqueous solution of sodium hydroxide and sodium sulfide (“white liquor”)

in batch or continuous digesters at 150–180 °C and 7–9 bar for several hours [249-251]. During the reaction, ether bonds in lignin are cleaved via nucleophilic attack by hydrosulfide ions (HS^-), facilitating lignin removal and suppressing its recondensation [11, 252]. At the same time, hemicellulose is degraded under alkaline conditions through the peeling reaction, in which monosaccharide residues are stepwise eliminated from the reducing ends of the polysaccharide chains [191]. However, cellulose, protected by its high crystallinity and extensive interchain hydrogen bonding, remains largely intact [191, 253]. As a result, most lignin and hemicellulose are dissolved in the liquor, yielding a cellulose-rich fibrous pulp. After the pulp is separated and washed, the spent liquor, known as “black liquor”, is concentrated and incinerated in a recovery boiler to generate energy [251, 254]. The remaining inorganic sodium salts, primarily sodium carbonate and sodium sulfide, melt at high temperatures at the furnace bottom and are subsequently recovered as “green liquor”. By adding CaO, “green liquor” is converted back into “white liquor”, enabling aqueous stream recycling [254]. Following decades of development and optimization, Kraft pulping is a mature process focused on producing high-purity cellulose with long fiber length and high strength for subsequent bleaching and papermaking [254, 255]. These goals do not necessarily match those of the 2G biorefinery, which aims to produce high sugar yields for fermentation, along with other value-added streams [256, 257], in an economically feasible and environmentally friendly manner. Meanwhile, Kraft pulping raises environmental concerns such as waste gas emissions, water pollution, and odor [258, 259]. To distinguish modern biorefinery practice from traditional pulping, lignocellulose deconstruction in this context is referred to as “pretreatment”.

2.2.3.2 Biomass Pretreatment

Up to now, several pretreatment methods have been explored with the aim of disrupting the lignin–hemicellulose matrix that surrounds cellulose microfibrils. These methods can be broadly categorized into physical, chemical, biological, and combined approaches [34, 35]. From the perspective of commercial viability, an effective pretreatment should generally meet several key criteria [34, 260]: low energy and

chemical consumption, high efficiency in biomass fractionation, scalability to industrial levels, and minimal environmental impact. For these reasons, physical and chemical pretreatments are normally more viable than biological ones [34]. Biological pretreatment depends on costly fungi or enzymes to break down lignin and generally requires long reaction times, leading to slower product turnover [35, 261]. Moreover, these biological agents are highly sensitive to pH, temperature, and moisture content [262, 263]. If conditions deviate from the optimal range, the process can become uncontrollable, leading to the formation of unwanted by-products. These factors increase the difficulty of scaling up [264-266]. Notably, the choice of a pretreatment method must also consider the nature of the lignocellulosic feedstock, as different biomass sources contain lignin with distinct types and structures. For example, softwood normally possesses the most recalcitrant lignin among hardwood and grass biomass and, hence, needs to be pretreated under more severe physicochemical conditions. A brief overview of the main pretreatment methods is presented below.

2.2.3.2.1 Physical Pretreatment

Physical pretreatment of lignocellulosic biomass is usually carried out before other steps [267]. Its main goals are to modify the biomass mechanically, including reducing particle size, increasing surface area, lowering the degree of polymerization and crystallinity, and improving enzyme access [266]. Because no toxic chemicals are added or generated, physical pretreatment is considered environmentally benign. However, the main issue with physical pretreatment is its high energy cost [268]. For grass biomass such as corn stover and switchgrass, the energy consumption for size reduction is relatively low, reaching 11.0 and 27.6 kWh t^{-1}, respectively, while for woody biomass such as poplar and pine chips, the demand rises to 85.4 and 118.5 kWh t^{-1}, respectively [266]. Common physical pretreatment methods involve milling, extrusion, and irradiation [267]. Among them, milling and irradiation are described in depth below, while details of extrusion are provided in the Appendices.

Milling is widely used to reduce both particle size and crystallinity of lignocellulosic

biomass. Depending on the equipment, it can be classified as ball milling [269], vibratory milling [270], hammer milling [271], knife milling [272], or disk milling [273]. Ball and vibratory mills are effective for producing fine material with micron-scale particles, whereas hammer, knife, and disk mills are suited to coarser products such as chips and fibers. Obtaining an appropriate particle size before converting biomass to value-added products is essential because smaller particles increase surface area and lower structural recalcitrance. For example, Gu et al. studied the optimization of sugar release from Douglas-fir forest residues pretreated by planetary ball milling [274]. The results showed that ball milling for 7–30 min at 250 rpm reduced the crystallinity index from 40.73% to 34.63–11.70% and increased glucose yield from 13.39% to 24.45–59.67% after enzymatic hydrolysis. However, this improvement came at high energy costs of 500–2150 kWh t^{-1} for 7–30 min of milling. Overall, milling is a useful first-stage pretreatment for many types of lignocellulosic biomass. However, its high energy demand remains a major challenge.

In addition to conventional mechanical pretreatment, several innovative physical methods have been explored, including microwave irradiation, ultrasonic irradiation, and electron beam irradiation [266, 275]. Microwave irradiation uses rapid dielectric heating to disrupt biomass integrity by inducing thermal expansion [276]. Ultrasonic irradiation relies on acoustic cavitation, which generates localized high temperatures, pressures, and shear forces that break chemical and mechanical barriers in the cell wall, thereby facilitating the release of cellulose, hemicellulose, and their derivatives [46]. Moreover, electron beam irradiation employs high-energy ionizing radiation to induce chemical bond breakage in plant cells, thereby modifying the lignocellulosic matrix, lowering cellulose crystallinity and the degree of polymerization, and boosting the overall reactivity of biomass [277]. These non-conventional techniques share the same advantage of rapid processing, thanks to high thermal efficiency. However, due to the requirement for expensive, specialized equipment (e.g., microwave generators, sonication probes, and accelerator/radiation sources), these novel pretreatment methods have little commercial appeal at the current stage and are used primarily at

the laboratory scale.

In practice, to overcome the inherent drawbacks of physical pretreatments (high energy costs and low delignification efficiency), these methods are often combined with chemical pretreatment to improve the overall valorization efficiency of biomass. The integration of ultrasonic irradiation with various chemical pretreatment strategies is discussed in detail in Section 2.2.3.2.4.

2.2.3.2.2 Biological Pretreatment

Biological pretreatment employs specific microorganisms (e.g., fungi, bacteria, and their extracellular enzymes) to break down polysaccharides and/or lignin [278]. The main fungal groups are white-rot, brown-rot, and soft-rot [266]. White-rot fungi are preferred for cellulose valorization because they secrete lignin-degrading enzymes (e.g., laccase, lignin peroxidase, and manganese peroxidase) that selectively remove lignin and improve cellulose accessibility [279-281]. Brown-rot fungi focus on cellulose and hemicellulose hydrolysis [282, 283], while soft-rot fungi act on all components of the plant cell wall [284, 285]. Biological pretreatment is considered non-toxic (without using harsh chemicals) and environmentally friendly (without producing inhibitory by-products). In addition, it can operate at mild temperatures with a low energy demand [278, 279, 286]. However, the main obstacles to its commercialization are long treatment durations and difficult process control [266].

To improve industrial viability, researchers have combined biological pretreatment with other methods. For example, Zhang et al. integrated steam explosion with microbial consortium degradation to treat eucalyptus root, bagasse, and corn straw [287]. Lignin degradation reached 35.3%, 37.6%, and 44.2%, respectively, after just seven days, which is far shorter than typical biological runs. Meanwhile, the enzymatic sugar conversion efficiency of biomass subjected to this combined treatment was more than twice that achieved with steam explosion alone.

2.2.3.2.3 Chemical Pretreatment

Chemical pretreatment is already well established in laboratories and industry for fractionating lignocellulosic biomass. It relies on chemical solvents to separate biomass components and is effective even for recalcitrant feedstocks [288]. Based on the solvent, chemical pretreatment can be classified as dilute acid, alkaline, oxidative, organosolv, and IL pretreatment. Although all these routes aim to lower biomass recalcitrance, each solvent system has different effects on cellulose, hemicellulose, and lignin [32]. Most chemical pretreatments can disrupt the compact LCC matrix, remove barriers to enzyme access, and increase sugar yields. However, they also present challenges, including the formation of fermentation inhibitors, the generation of large volumes of wastewater, high chemical consumption, and related environmental and safety concerns [32]. The dilute acid, alkaline, and IL pretreatments are discussed in detail below, whereas overviews of oxidative and organosolv pretreatments are provided in the Appendices.

Dilute Acid Pretreatment

Dilute acid pretreatment reacts lignocellulosic biomass with mineral acids (e.g., H_2SO_4, HCl, H_3PO_4, and HNO_3) at dilute concentrations of <4.0 wt% and temperatures of 100–220 °C for minutes to hours [32, 289, 290]. H_2SO_4 is the most common because of its low cost [291]. Although acid catalysis can alter lignin structure and partially dissolve cellulose, hemicellulose hydrolysis is the primary target [266]. After appropriate dilute acid pretreatment, high hemicellulose removal, along with the disruption of LCCs, can be achieved, greatly improving enzyme access to cellulose [292]. During hydrolysis, hemicellulose sugars are released as C6 and C5 monomers (e.g., glucose and xylose) and can dehydrate to HMF and furfural [292]. Acetyl groups on xylan are cleaved, yielding acetic acid [293]. HMF, furfural, and acetic acid are valuable platform chemicals but inhibit subsequent cellulase and yeast activity [32, 278, 293], so separating them before cellulose saccharification is necessary. Currently, dilute acid pretreatment is a mature method, well studied by scholars. For example, Kuglarz et al. showed that steam treating industrial hemp with 1.5% (w/v) H_2SO_4 at 180 °C for 10

min hydrolyzed 74% of hemicellulose while retaining 95% of cellulose and 99% of lignin in the solid fraction [294]. Enzymatic hydrolysis then gave a 72% glucose yield, and fermentation achieved an 81% ethanol yield. Martins et al. reported that pretreating sugarcane leaf with 2% H_2SO_4 (mass of acid per mass of dry biomass) at 180 °C for 1 h produced a solid fraction that yielded 94.56% glucose [295]. Although dilute acid pretreatment offers simple operation, broad feedstock applicability, and high efficiency, it requires effluent neutralization, accelerates equipment corrosion, and offers limited opportunities for acid recovery [32, 266]. Additionally, the process readily forms fermentation inhibitors such as furfural, HMF, and humins (pseudo-lignin) [28], so precise control of reaction conditions is essential.

Alkaline Pretreatment

Alkaline pretreatment uses bases, such as NaOH, KOH, $Ca(OH)_2$ (lime), and NH_4OH, to process lignocellulosic biomass [266]. Among these, NaOH is generally the most effective and therefore the most widely applied [296]. Different from dilute acid, the main target of alkaline pretreatment is lignin, allowing high-efficiency delignification [297]. Specifically, lignin fragments dissolve in the alkaline liquor and are converted into phenolic compounds [298, 299]. This removal is driven mainly by the saponification (cleavage) of the ester bonds linking lignin to hemicellulose [278, 279, 297, 300]. The process also causes partial dissolution of hemicellulose fragments, disrupting the LCC matrix [32]. Acetyl and uronic acid groups on hemicellulose are eliminated [266], further exposing the remaining polysaccharides (mainly cellulose) to enzymes. At the same time, hydroxide ions penetrate deep into the fibers, causing the cellulose to swell and partially dissolve [292, 301]. These combined effects boost subsequent enzymatic hydrolysis. Extensive studies have confirmed the effectiveness of alkaline pretreatment. For example, Haque et al. achieved 84.8% delignification and 79.5% hemicellulose removal by treating barley straw with 2% NaOH at 105 °C for 10 min [302]. The pretreated biomass then gave a promising 86.5% reducing sugar yield after enzymatic hydrolysis. Kim et al. treated corn stover with $Ca(OH)_2$ at 25–55 °C for 16 weeks under non-oxidative and oxidative conditions [303]. Non-oxidative treatment

preserved glucan and xylan (93.7% and 79.3% retention) but removed only 47.7% of lignin, whereas oxidative treatment raised delignification to 87.5% but reduced glucan and xylan retention to 71.0% and 50.3%. However, when the glucan and xylan dissolved in the pretreatment liquor were considered, enzymatic hydrolysis of the pretreated corn stover, conducted for 4 weeks at 55 °C with aeration, yielded promising 93.2% glucose and 79.5% xylose yields. Oladi et al. investigated liquid ammonium hydroxide pretreatment of energy cane bagasse, focusing on parameter optimization [304]. Under optimized conditions of 208 °C for 36 min with an ammonium hydroxide-to-solid ratio of 0.4:1 (v/w), 60.26% of the lignin was removed while 90.99% of the glucan was retained. Subsequent saccharification yielded 30.32 g of glucose per 100 g of untreated biomass (30.32 g/100 g), a marked increase over the raw energy cane bagasse (4.13 g/100 g). Although alkaline pretreatment is effective, it still faces major challenges in recovering the alkali, managing the wastewater produced, and protecting equipment from alkaline corrosion [32]. Furthermore, its performance is feedstock-dependent, giving better results with low-lignin grass biomass than with hardwood [278].

Ionic Liquid Pretreatment

Compared with the chemical pretreatments mentioned above, using ILs to fractionate lignocellulosic biomass has a relatively short history but has already shown strong commercial promise. ILs are salts that remain liquid below 100 °C and have negligible vapor pressure, so biomass can be treated at atmospheric pressure. For lignocellulosic biomass pretreatment, ILs can be divided into two broad categories: cellulose-dissolving ILs and lignin-dissolving ILs. Among the former, 1-ethyl-3-methylimidazolium acetate ([Emim][OAc]) is the most widely studied. Labbé et al. investigated the effects of [Emim][OAc] on yellow poplar, and found that the regenerated cellulose pulp had low crystallinity and achieved an excellent saccharification yield (up to 98.6% after activation in [Emim][OAc] for 72 hours) [305]. Cellulose-dissolving APILs also work on recalcitrant feedstocks like softwood [306]. However, their drawbacks include low water tolerance (necessitating energy-intensive

drying), high prices, and limited thermal stability, all of which hinder their application in an industrial-scale biorefinery [19, 130, 307, 308]. More recently, PILs have emerged as practical alternatives. PILs can selectively dissolve lignin and hemicellulose, leaving a cellulose-rich pulp that hydrolyzes readily to glucose and then to ethanol. The lignin can be further precipitated through the addition of an anti-solvent (water) [16, 19, 37, 91]. This process is known as “ionoSolv”, which was developed by Professor Jason Hallett’s group at Imperial College London. Compared with APILs, PILs have lower bulk production costs (e.g., an estimated \$1.24 kg^{-1} for [TEA][HSO_4]) since they can be synthesized through a simple acid-base neutralization [144]. PILs also have excellent thermal stabilities. For example, [TEA][HSO_4] remains stable until temperatures reach 277 °C, while [Emim][OAc] tends to decompose at 215 °C [134]. Meanwhile, PILs work well at 10–40 wt% water content for biomass fractionation. Therefore, neither the biomass nor the solvent needs energy-intensive drying [76, 137]. More importantly, PILs exhibit great suitability for diverse feedstocks such as grass biomass, softwood, and even hazardous waste wood. For example, Brandt-Talbot et al. reported that *Miscanthus* (grass biomass) pretreated with ([TEA][HSO_4]) yielded a cellulose-rich pulp giving 77–82% glucose release after saccharification, and the [TEA][HSO_4] could be reused for several cycles with no performance loss [19]. Gschwend et al. demonstrated that quantitative (100%) glucose release from pine (a recalcitrant softwood) can be achieved after pretreatment with [HBim][HSO_4] [36]. In a separate study, Gschwend et al. further proved that [HC_1im]Cl can be a promising solvent to simultaneously fractionate chromated copper arsenate (CCA)-treated wood and extract 80–100% of the metal species. These extracted metals can be recovered by electrodeposition [91]. Abouelela et al. found that [DMBA][HSO_4] can effectively extract polycyclic aromatic hydrocarbons (PAHs) from hazardous creosote wood, producing a highly digestible, PAH-free, cellulose-rich pulp [309]. These successes have drawn global interest to the ionoSolv process.

Table 2.1. Comparative review of IL pretreatments for lignocellulosic biomass: effects on delignification and enzymatic hydrolysis.

Lignocellulosic biomass	Ionic liquid	Process parameters	Delignification	Saccharification yield	Ref
Yellow poplar	[Emim][OAc]	60 °C, 72 h, biomass-to-IL ratio of 4 wt%	–	>98.6%	[305]
Switchgrass	[Emim][OAc]	160 °C, 3 h, biomass-to-IL ratio of 0.3:9.7 (g/g)	70.6%	32.6 g gluclose/100 g raw biomass	[306]
Eucalyptus	[Emim][OAc]	160 °C, 3 h, biomass-to-IL ratio of 0.3:9.7 (g/g)	54.9%	31.6 g gluclose/100 g raw biomass	[306]
Pine	[Emim][OAc]	160 °C, 3 h, biomass-to-IL ratio of 0.3:9.7 (g/g)	49.1%	30.7 g gluclose/100 g raw biomass	[306]
Miscanthus	[TEA][HSO_4]	120 °C, 8 h, biomass-to-solvent ratio of 1:10 (g/g) [a]	~90%	77%	[19]
Miscanthus	[TEA][HSO_4]	150 °C, 45 min, biomass-to-solvent ratio of 1:5 (g/g) [a]	63%	75%	[37]
Miscanthus	[TEA][HSO_4]	180 °C, 15 min, biomass-to-solvent ratio of 1:5 (g/g) [a]	68%	76%	[37]
Pine	[HBim][HSO_4]	170 °C, 30 min, biomass-to-solvent ratio of 1:10 (g/g) [a]	~80%	71%	[36]
Pine	[HBim][HSO_4]	170 °C, 30 min, biomass-to-solvent ratio of 1:10 (g/g) [a]	–	102.2% (Wet pine pulp)	[36]
Pine	[DMBA][HSO_4]	170 °C, 30 min, biomass-to-solvent ratio of 1:10 (g/g) [a]	–	74%	[36]
Rhododendron	[DMBA][HSO_4]	170 °C, 30 min, biomass-to-solvent ratio of 1:5 (g/g) [a]	~85%	75.6%	[24]

Japanese Knotweed	[DMBA][HSO_4]	150 °C, 1 h, biomass-to-solvent ratio of 1:5 (g/g) [a]	~90%	85%	[24]
CCA treated wood	[H_1Cim]Cl	170 °C, 30 min, biomass-to-solvent ratio of 1:5 (g/g) [a]	–	55%–75% (cycle 1–cycle 6)	[91]
Hazardous creosote wood	[DMBA][HSO_4]	170 °C, 45 min, biomass-to-solvent ratio of 1:5 (g/g) [a]	~60%	Over 70%	[309]

[a] The solvent consisted of 80 wt% IL and 20 wt% water.

2.2.3.2.4 Physicochemical Pretreatment

Steam Explosion

Steam explosion is one of the most widely used physicochemical pretreatment methods. In this process, biomass is exposed to saturated steam at 160–260 °C and 7–48 bar for a few seconds to several minutes [278, 310]. The steam penetrates the cell structure, softening and swelling the LCC matrix. A rapid, explosive decompression to atmospheric pressure then “pops” the bulk material into loose fibers [311]. Beyond this mechanical disruption, hemicellulose undergoes partial hydrolysis: the glycosidic bonds break, releasing monomers that can further dehydrate to furfural and HMF, while the cleavage of acetyl groups yields acetic acid, lowers the pH, and drives further autohydrolysis of hemicellulose [278, 312]. The β-O-4′ ether linkages in lignin are cleaved, generating lignin fragments, but overall delignification remains limited because these fragments can further repolymerize (condense), forming more stable polymers [32, 181, 313]. Adding a scavenger (e.g., 2-naphthol) for carbonium ions has been reported to effectively suppress repolymerization, yielding a more uniform, low-molecular-weight, readily extractable lignin with high chemical value [313]. Cellulose is largely preserved, with only slight depolymerization under suitable conditions [181]. Vivekanand et al. studied steam explosion severity on birch and achieved 97% of the theoretical maximum glucose release at 220 °C for 10 min [314]. A positive correlation between severity and Klason lignin was observed, likely due to pseudo-lignin formed from polysaccharide degradation products (furfural). The excessive accumulation of

pseudo-lignin under harsh steam explosion conditions negatively affects subsequent enzymatic hydrolysis. It has been shown that acid catalysts such as H_2SO_4, H_3PO_4, and SO_2 can effectively lower the severity of the optimal explosion conditions and suppress inhibitor generation [32, 278, 279, 315, 316]. For example, Guerrero et al. studied the optimal conditions for H_2SO_4-catalyzed steam explosion of banana pseudostem [317]. A 91.0% overall glucose yield was obtained under optimal conditions of 170 °C for 5 min with 2% (v/v) H_2SO_4. Wang et al. compared H_2SO_4 and SO_2 impregnation for continuous steam pretreatment of spruce at 195–215 °C for 7 min [318]. Although liquor from SO_2-treated spruce inhibited enzymes and yeast more strongly, the solid residue achieved 99% cellulose digestibility at 215 °C, which was about three times higher than with H_2SO_4. This can be attributed to the fact that SO_2 impregnation enhanced delignification and cellulose degradation, which further produced finer solid residues with increased surface area for enzymes. Notably, commercial adoption of steam explosion is underway. For example, Beta Renewables built the world's first cellulosic ethanol plant in Crescentino, Italy, using Proesa™ steam-explosion technology to process energy grass and wheat straw at a capacity of 76 million liters of ethanol per year [319, 320]. Moreover, Raízen in Brazil began producing 2G ethanol from sugarcane bagasse in 2014 at a capacity of 42.2 million liters of ethanol per year, employing dilute-acid impregnation followed by steam explosion [320, 321]. Steam explosion is considered energy-efficient, saving up to 70% of energy compared with conventional mechanical methods to achieve the same size reduction [279, 322]. It is also one of the most cost-effective pretreatment methods for agricultural residues (grass biomass) and hardwood, despite being less effective for softwood [279, 323]. However, the formation of fermentation inhibitors (e.g., furfural, HMF, and acetic acid) and the high cost of equipment remain challenges that need to be addressed [32].

Ammonia Fiber Expansion (AFEX)

Ammonia fiber expansion (AFEX) is a thermochemical pretreatment in which lignocellulosic biomass is exposed to anhydrous liquid ammonia (biomass:ammonia =

1:1–1:2 (w/w)) at 15–25 bar and 60–150 °C for 5–60 min in a closed vessel [324-326], causing cellulose to swell. A rapid depressurization then vaporizes the ammonia and “explosively” disrupts the biomass structure. AFEX does not effectively remove lignin or hemicellulose [327], but it does cleave LCC linkages and disrupt the crystalline lattice of cellulose, thereby enhancing enzymatic hydrolysis [32, 279, 292, 325, 326]. AFEX generates negligible fermentation inhibitors [32, 278]. Moreover, despite the high cost of ammonia [32], most of the ammonia (>99%) can be recovered and reused, reducing processing costs [328, 329]. The remaining 0.5–1% retained in the biomass supplies a nitrogen source for yeast cell growth during the subsequent fermentation [325], thereby eliminating the need for extensive washing after pretreatment [329]. Uppugundla et al. investigated the AFEX pretreatment of corn stover at 140 °C for 15 min (anhydrous ammonia:biomass = 1:1 (w/w)) and found that, aside from the complete removal of acetyl groups, the overall composition remained unchanged; yet, the pretreated substrate was highly digestible and yielded 20.5 kg of ethanol per 100 kg of corn stover [330]. However, AFEX’s limited lignin-removal capacity reduces its effectiveness on high-lignin feedstocks (e.g., softwood) [278], and the corrosive, volatile nature of ammonia increases equipment costs and safety risks [32, 331].

Ultrasound-Assisted Biomass Pretreatment

Sonication of lignocellulosic biomass is a physical treatment that uses ultrasound waves to deliver energy into a biomass/solvent slurry. Ultrasound comprises acoustic waves with frequencies above 16–20 kHz. Depending on the frequency, ultrasound is classified as high-energy (power) ultrasound (16–100 kHz), high-frequency ultrasound (100 kHz–1 MHz), and low-energy (diagnostic) ultrasound (1–10 MHz) [332]. Among these options, only power ultrasound provides sufficient energy for biomass pretreatment, while low-intensity ultrasound is more effective for the conversion of sugar to bioethanol during the fermentation process [333]. In practice, ultrasound is delivered either indirectly, via a water or oil bath (where much energy is lost as waves travel through the coupling medium), or directly, via an immersed probe that oscillates at ultrasonic frequency and transfers energy more efficiently into the slurry [334]. Direct

probe sonication has been shown to outperform bath systems for disrupting solid biomass suspensions, whereas baths are more useful when live cells are present [335, 336].

The key mechanism of ultrasonic pretreatment is acoustic cavitation (Figure 2.11). Specifically, sonication can produce a rapid cycle of low-pressure (rarefaction) and high-pressure (compression) phases, which cause microscopic bubbles to form and then collapse violently [44, 46]. Their implosion generates shock waves and microjets that create intense local mixing (acoustic streaming) that dramatically enhances mass transfer between the biomass and solvent (physical effect) [337]. Simultaneously, the collapse of cavitation microbubbles results in instantaneous increases in local temperatures (~5,000 K) and pressures (~50 MPa), producing reactive radicals that accelerate chemical reactions between the biomass and solvents (chemical effect) [334, 338]. Together, these physical and chemical effects shorten reaction times and lower energy requirements compared with conventional heating [339-342]. The efficacy of cavitation intensity can be affected by several factors, including sonication duration, temperature, power, amplitude, frequency, medium properties, and the solid-to-solvent ratio [333].

Up to now, a large number of studies have investigated the combination of ultrasound and conventional dilute acid, alkaline, organic solvent, and IL biomass pretreatments, with the aim of boosting sugar yields, reducing reaction times, and cutting chemical loads. For example, Feng et al. applied power ultrasound to corncob in dilute sulfuric acid and achieved 39% xylan extraction in 43 min at 121 °C, an approximately 97% reduction in pretreatment time compared with the 34% xylan extraction obtained in 24 h without ultrasound [343]. Sri Bala et al. demonstrated that ultrasound waves accelerated cellulose-chain disruption during alkaline pretreatment [341]. Sun et al. investigated the use of ultrasound in organic solvent pretreatment of wheat straw with 0.5 M NaOH in 60% methanol and found that sonication increased the hemicellulose yield by 2.9–9.2% compared with a non-sonicated control [344]. For the combination

with ILs, Ab Rahim et al. reported that probe sonication with [Emim][OAc] achieved complete bamboo dissolution in 40 min at 40% acoustic power without external heating, whereas conventional heating took 12–17 h at 110–120 °C to match this result [339]. Moreover, Ninomiya et al. reported that sonication in ILs ([Bmim]Cl, [Amim]Cl, [Emim]Cl, and [Emim][Dep]) hydrolyzed 60–95% of kenaf cellulose to glucose at room temperature after 120 min, whereas conventional heating at 110 °C for the same duration yielded only 20% cellulose hydrolysis [342]. Hence, combining ultrasound with other conventional pretreatments offers a promising strategy to accelerate biomass deconstruction and boost overall efficiency.

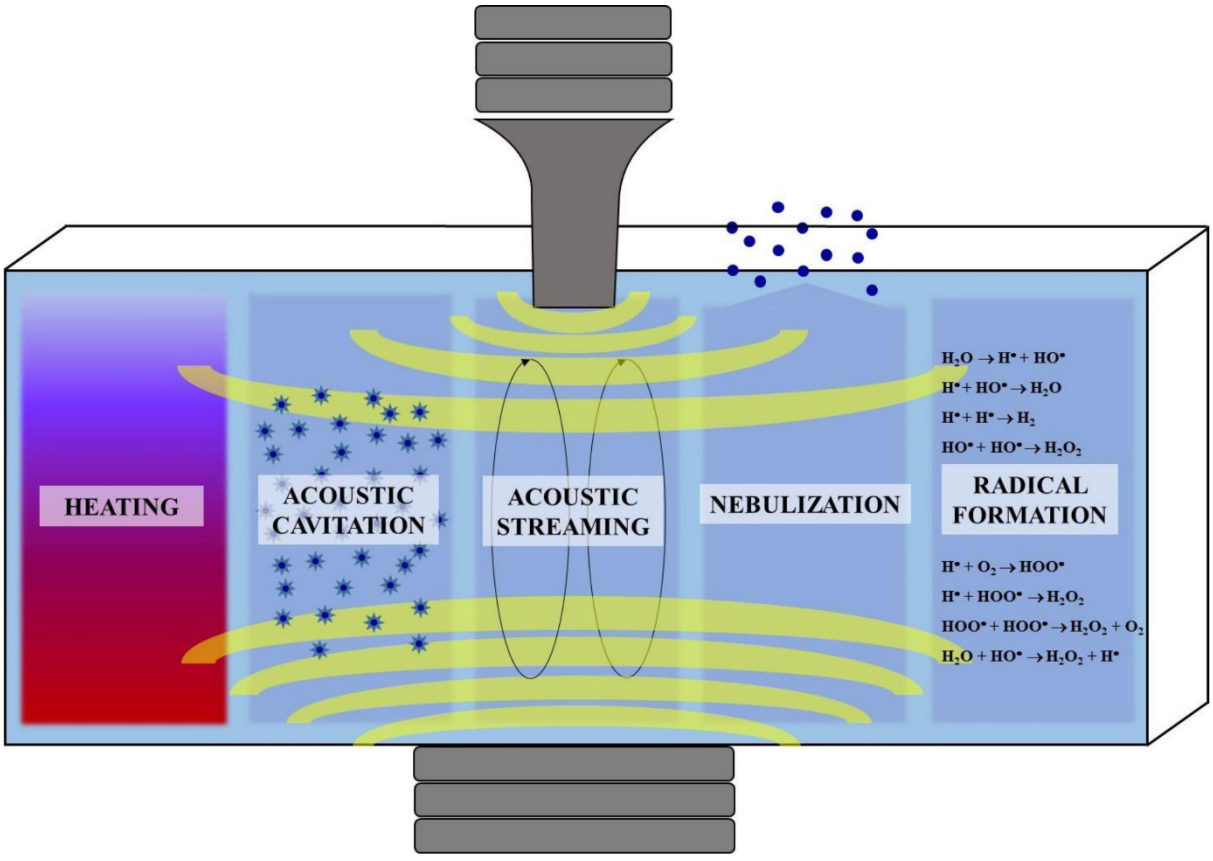


Figure 2.11. Representative physicochemical phenomena induced by probe sonication in a liquid medium. Reproduced from Flores et al. [46].

2.2.4 Summary

The 2G biorefinery adopts lignocellulosic biomass—such as agricultural residues, forestry waste, energy crops, and even invasive plants—as feedstocks, holding great

promise for producing renewable 2G bioethanol and other bio-based chemicals, thereby improving carbon neutrality. The recalcitrance of lignocellulosic biomass stems primarily from the high crystallinity of cellulose and its sheathing by the LCC matrix. Accordingly, a variety of pretreatment methods have been developed to lower recalcitrance by removing or redistributing lignin and hemicellulose, reducing cellulose crystallinity, and increasing surface area and enzyme accessibility, although each approach has its own advantages and limitations. An effective pretreatment strategy should enable the fractionation and valorization of all biomass components. Specifically, in addition to maximizing cellulose utilization, the recovery of hemicellulose-derived intermediates (e.g., xylose and furfural) and the upgrading of lignin to high-value products (rather than its current use as boiler fuel) are important for improving the overall economics of the 2G biorefinery. Ultimately, the commercial viability of the 2G biorefinery requires appropriate trade-offs among capital and operating costs, environmental performance, and product metrics (type, yield, and value). Meanwhile, reliable solvent and catalyst recovery, inhibitor control, and a stable feedstock supply remain crucial.

2.3 Furan Derivatives from Hemicellulose

2.3.1 Furfural Production

Furfural ($C_5H_4O_2$), also called 2-furaldehyde, is a furan-based aldehyde in which the hydrogen at the 2-position of the furan ring is replaced by a formyl group (–CHO) [345]. Listed among the top 30 bio-based platform chemicals by the U.S. Department of Energy, furfural serves as a precursor to a wide range of furan-derived compounds and finds various applications in fine chemicals, polymers, resins, antiseptics, surfactants, pharmaceuticals, and flavorings [51, 346]. Furfural is a bio-based chemical produced by the acid hydrolysis of hemicellulose into pentoses (xylose and arabinose), which are then dehydrated to yield furfural by losing three water molecules [347]. The sulfuric acid-catalyzed pathway is shown in Figure 2.12. Although furfural can also be synthesized from petroleum feedstocks (for example, via the catalytic oxidation of 1,3-butadiene), that route is not economically competitive [60, 348]. Today, furfural is a

commodity chemical with an annual production exceeding 400,000 tons, and China is the world's largest producer [52-54]. Over the past twenty years, bulk prices have fluctuated between \$0.40 kg^{-1} and over \$2.00 kg^{-1}, driven by changes in market demand and feedstock availability [53]. Its large-scale manufacture remains one of the most successful cases of hemicellulose valorization in the 2G biorefinery.

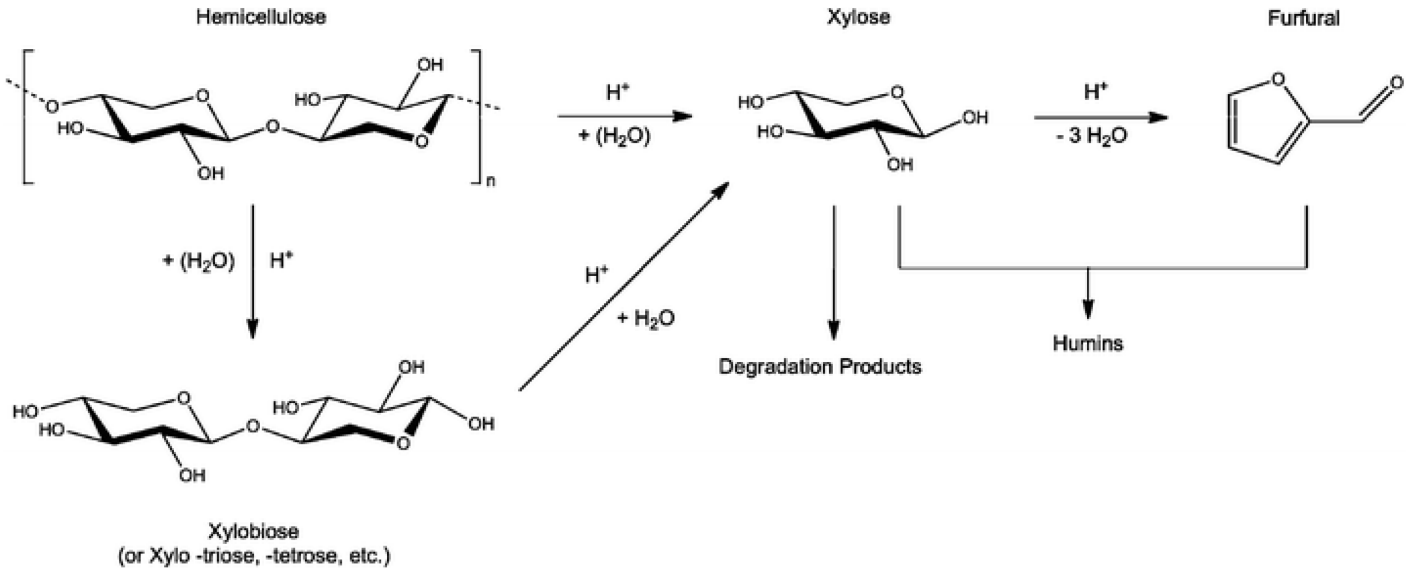


Figure 2.12. Representative H_2SO_4-catalyzed (Brønsted acid–catalyzed) hydrolysis pathway from hemicellulose (homoxylan) to xylose and then to furfural. Reproduced from Enslow et al. [349].

In 1921, the Quaker Oats Company implemented the world's first commercial furfural production using batch reactors [51, 61]. The process comprises two steps: first, at 153 °C, waste lignocellulosic feedstocks (e.g., oat hulls, corn cobs, and sugarcane bagasse) are mixed with dilute sulfuric acid to hydrolyze hemicellulose into xylose and arabinose, which are further dehydrated to furfural. Second, steam vapor is introduced into the reactor to strip the furfural, which is then condensed and purified. Modern industrial plants still employ a variant of this acid-catalyzed route [53], but yields remain limited, typically around 50% [55], due to side reactions such as the resinification of furfural and furfural condensation with sugars and intermediates [60]. For instance, it has been reported that glucose, released by cellulose or hemicellulose hydrolysis, is highly detrimental to furfural formation [53]. One effective strategy to mitigate these

side reactions is to continuously remove furfural from the reaction medium as it forms, thereby limiting its exposure to degrading conditions. This principle underlies the SupraYield process, developed by Dr. Karl Zeitsch in the late 1990s [350]. In this process, sugarcane bagasse is mixed with sulfuric or phosphoric acid and heated to the boiling point of the aqueous mixture (180–240 °C). As furfural forms, it is immediately flashed off via adiabatic distillation, transferring it from the liquid to the vapor phase [55, 351]. By minimizing its residence time in the solvent, side reactions are suppressed, and furfural yields of 50–70% can be achieved [351]. In 2009, this process was commercialized by the Proserpine Cooperative Sugar Mill in Australia [55, 351]. Despite improved furfural yields, the process still faces high energy demands for steam generation, severe equipment corrosion under acidic conditions, large volumes of acidic wastewater, and complex downstream purification [352, 353]. To overcome these drawbacks, recent research has explored the utilization of monophasic systems, biphasic systems, and recyclable ILs. In the following section, we compare the effects of these solvent systems on furfural production from pentose sugars.

2.3.1.1 Monophasic Solvent Systems

Pure water can serve as a low-cost, green monophasic system for furfural production. At elevated temperatures, the endothermic ionization of water generates hydronium ions that catalyze the dehydration of xylose to furfural [353, 354]. Moreover, during the direct hydrothermal treatment of biomass, acetic and other organic acids released by hemicellulose hydrolysis further promote pentosan-to-furfural conversion [26]. Liu et al. achieved a 73% furfural yield from hardwood chips via a two-step production process, involving autohydrolysis at 180 °C followed by vapor release at 200 °C, without the use of an external catalyst [355]. Nevertheless, in pure water, xylose degradation tends to follow multiple pathways, leading to side-product generation and reduced furfural selectivity [353]. Additionally, in H_2SO_4–water systems, the challenge is even greater. The activation energy for furfural formation exceeds that for its degradation, making it difficult to achieve high yields [356].

Adding a water-miscible co-solvent to the H_2SO_4–water system has been found useful in improving furfural production. Biomass-derived γ-valerolactone (GVL) has emerged as a highly effective co-solvent for furfural production. When blended with water, GVL accelerates the dissolution of biomass or xylan into xylose, alleviating solids-clogging issues [357]. Moreover, in H_2SO_4–water systems, GVL significantly lowers the activation energy for furfural formation relative to its degradation, thereby suppressing side reactions and boosting selectivity [356, 358]. In 2012, Alonso et al. designed an innovative furfural production system in which GVL served as a reactive solvent to dissolve corn stover, while water was continuously introduced and vaporized to strip furfural from the reaction mixture, thereby minimizing its degradation (Figure 2.13) [357]. Using 0.05 M H_2SO_4 at 160 °C for 7 h, this setup achieved a 79% furfural yield from the direct conversion of corn stover. Sener et al. then explored acid-catalyzed xylose dehydration in a monophasic 80 wt% GVL/20 wt% H_2O system at 200–250 °C [359]. Kinetic analysis indicated that higher temperatures reduced the bimolecular condensation of xylose and furfural but increased carbon loss via accelerated xylose degradation, demonstrating the trade-off between temperature choices. Temperatures of 205–225 °C have been identified as optimal for xylose dehydration, delivering over 90% furfural yields. The use of heterogeneous catalysts in GVL media has also proven effective. In 2020, Yang et al. developed a carbon-based solid acid (SC-GCa-800) and tested it with GVL, γ-butyrolactone (GBL), and 1,4-dioxane for xylose dehydration [360]. At 140 °C for 40 min, nearly complete xylose conversion was obtained, with furfural yields of 85.9%, 82.1%, and 76.9%, respectively. Despite GVL's superior yield, the study claimed that the lower boiling point of 1,4-dioxane makes it more attractive for solvent–furfural separation by distillation. Inspired by this, Song et al. combined 1,4-dioxane with artificial Hβ zeolite, which can generate positive synergistic effects [361]. On the one hand, multiple immobilized acid sites on the zeolite catalyzed the isomerization of xylose to xylulose, which can further dehydrate to furfural; on the other hand, the 1,4-dioxane solvent protected the zeolite's crystal framework and acid centers and suppressed furfural polymerization. Under mild conditions (140 °C and 40 min), this approach achieved a 93.6% furfural yield from xylose and 85.9% from xylan.

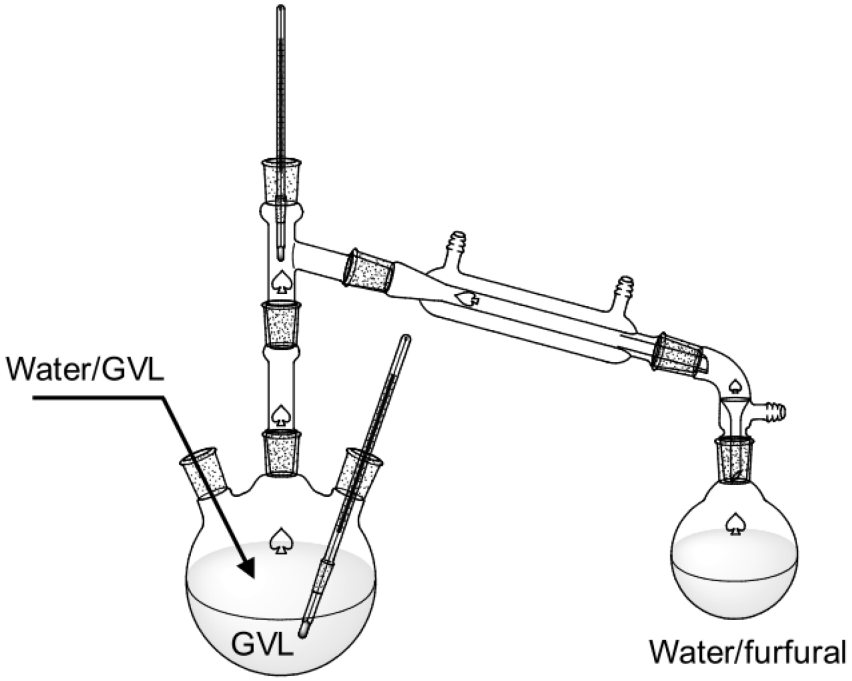


Figure 2.13. Schematic of the furfural production apparatus using GVL as the reaction solvent, with furfural removed from the reaction mixture by steam stripping. Reproduced from Alonso et al. [357].

In 2019, Romo et al. investigated a range of monophasic organic–water solvent mixtures (sulfolane, GBL, GVL, γ-hexalactone (GHL), and tetrahydrofuran (THF)) and found that both reaction severity (R_0) and solvent polarity (δ_P) were positively correlated with furfural yield during the autocatalytic dehydration of xylose [362]. A semi-empirical model was developed to estimate xylose conversion and furfural yield from R_0 and δ_P. The accuracy of the model was validated by showing that, for any given R_0 and δ_P, comparable xylose conversions and furfural yields were obtained across different combinations of reaction time, temperature, and solvent composition. In the future, it would be valuable to extend this framework to systems containing acid catalysts, to see how they shift the optimal R_0–δ_P balance and further boost furfural production.

2.3.1.2 Biphasic Solvent Systems

Organic solvents in monophasic systems serve as the reaction medium, directly

contacting substrates and catalysts and thus influencing reaction rates, equilibria, and pathways. By contrast, in a biphasic system, the water-immiscible organic phase plays a simpler role, continuously extracting furfural from substrates (in the aqueous phase) as it forms to avoid side reactions, while the acidic aqueous phase remains the true reaction medium [363]. Common extraction solvents include toluene, 2-butanol, methyl isobutyl ketone (MIBK), and 2-methyltetrahydrofuran (2-MeTHF) [364]. In 2013, Pholjaroen et al. evaluated xylose dehydration over niobium phosphate in various biphasic media [365]. Toluene/water and MIBK/water systems boosted furfural yields versus the pure water system, whereas 2-butanol/water and n-butanol/water systems increased xylose conversion but eroded selectivity due to the acetalization reaction between furfural and alcohols. Hexane proved ineffective due to its poor affinity for furfural. Xu et al. examined xylose and wheat straw conversion to furfural over chromium phosphate ($CrPO_4$) in various biphasic media (Figure 2.14) [366]. Except for 2-butanol and n-butanol, when using a water-to-organic solvent ratio of 1:3 (v/v) (water saturated with NaCl) at 160 °C for 60 min, THF, MIBK, 2-MeTHF, and toluene each delivered >95% xylose conversion and >70% furfural yield, far outperforming a simple water system. Among them, THF/water proved optimal, giving an 88% furfural yield. Remarkably, the same THF/water/$CrPO_4$ system converted raw wheat straw to a 67% furfural yield and a 32% HMF yield at 180 °C for 90 min. Notably, both Pholjaroen et al. and Xu et al. employed catalysts featuring Lewis and Brønsted acid sites, a combination that proves essential for efficient xylose-to-furfural conversion [365, 366]. In this bifunctional mechanism, the Lewis acid site first isomerizes xylose to xylulose, as the pathway via xylulose features a lower activation energy than direct Brønsted acid-catalyzed xylose dehydration [367]. The Brønsted acid site then provides H^+ to dehydrate xylulose into furfural (Figure 2.15) [57, 363, 368]. Additionally, Gupta and co-workers used D_2O-labeling experiments to reveal another stepwise dehydration mechanism catalyzed by the Lewis acid sites of amorphous Nb_2O_5 [369]. In a biphasic water/toluene system, the addition of Nb_2O_5 drove complete xylose conversion with a 72% furfural selectivity.

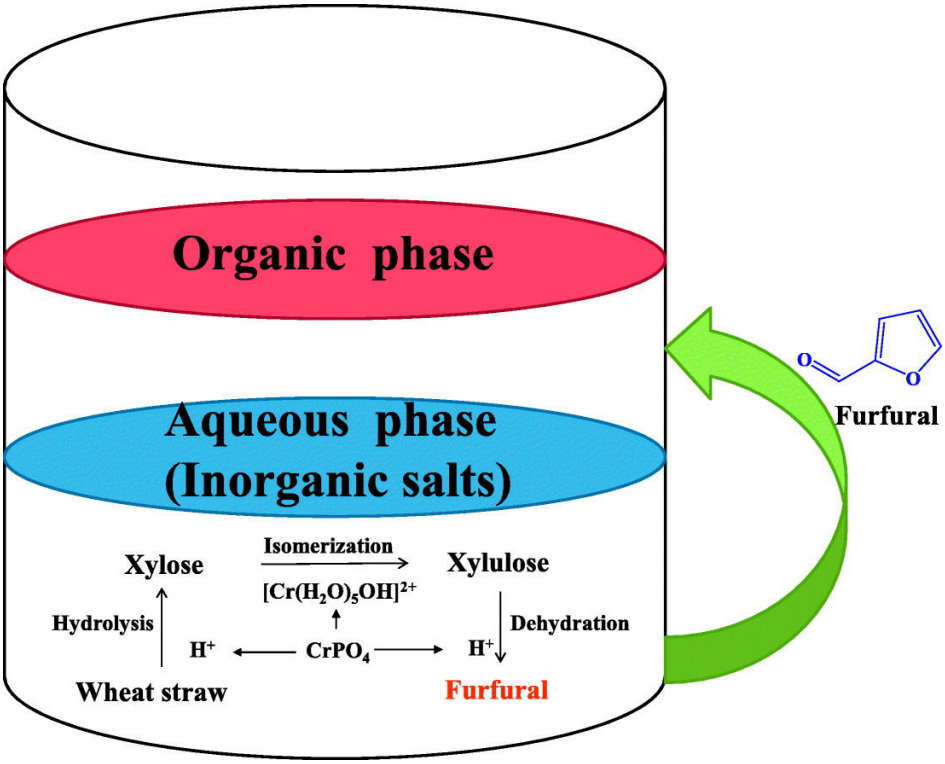


Figure 2.14. Biphasic solvent system for furfural production from wheat straw. Reproduced from Xu et al. [366].

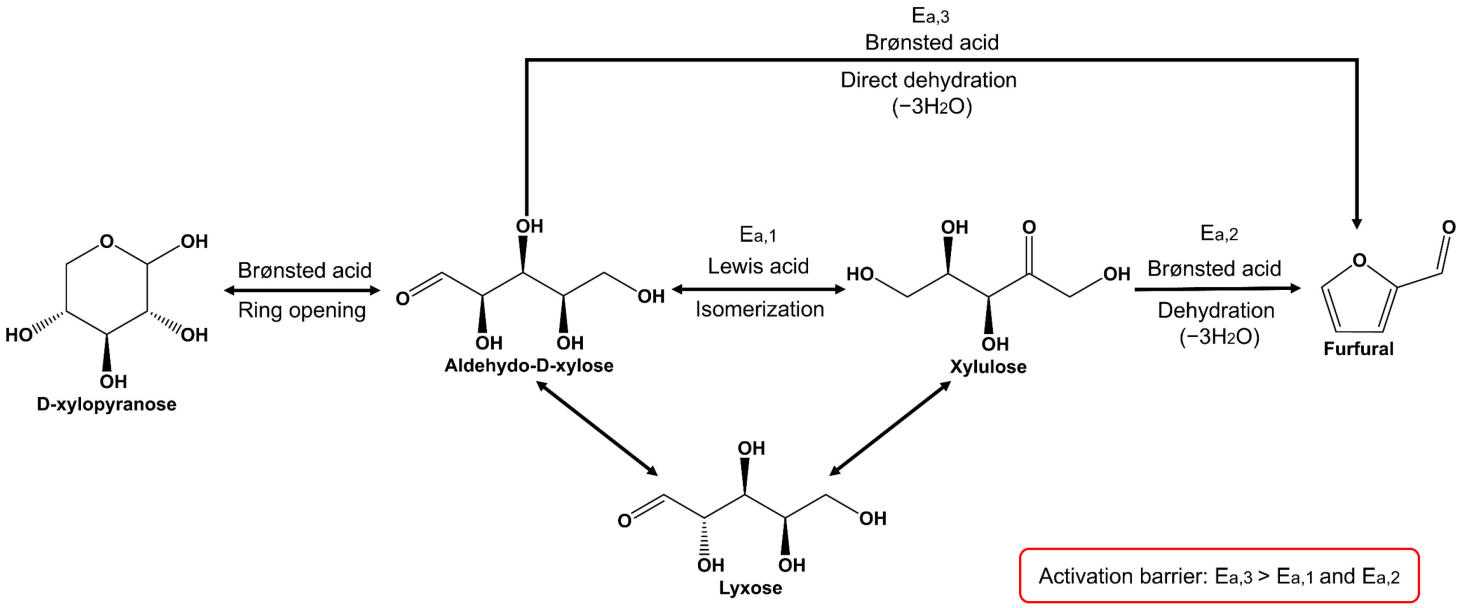


Figure 2.15. Conversion pathway from xylose to furfural under Lewis- and Brønsted-acid catalysis. Adapted from Choudhary et al. [367], Ye et al. [368], and Wang et al. [363].

Lin et al. further investigated how organic solvents promote xylose-to-furfural conversion in biphasic systems by combining experimental work with molecular dynamics (MD) simulations and density functional theory (DFT) calculations [364]. Six common biphasic systems—dichloromethane (DCM)/H_2O, 2-butanol/H_2O, 2-MeTHF/H_2O, cyclopentyl methyl ether (CPME)/H_2O, MIBK/H_2O, and toluene/H_2O—were tested without added catalysts. They found that conversion correlated primarily with the solvation free energy (ΔG_{sol}) of furfural in the organic phase: the more negative the ΔG_{sol}, the stronger the affinity of furfural for the organic solvent and the more effectively furfural partitions out of the aqueous phase. The measured ΔG_{sol} values ranked DCM (−37.39 kJ mol^{-1}) < 2-butanol (−34.09 kJ mol^{-1}) < 2-MeTHF (−30.62 kJ mol^{-1}) ≈ CPME (−30.54 kJ mol^{-1}) < MIBK (−26.34 kJ mol^{-1}) < toluene (−23.53 kJ mol^{-1}), which closely matched the experimental xylose-to-furfural conversion efficiency: DCM/H_2O > 2-MeTHF/H_2O > 2-butanol/H_2O ≈ MIBK/H_2O > CPME/H_2O > toluene/H_2O. Small discrepancies were attributed to three other factors: the maximum solubility of furfural in organic solvents, the organic solvents' own ΔG_{sol} in water, and the rate of furfural side reactions in organic solvents. Under optimal conditions (180 °C and 60 min), the DCM/H_2O system achieved complete xylose conversion and an 81.6% furfural yield, significantly outperforming the other solvent systems. Notably, toluene/H_2O proved least effective in this catalyst-free context, whereas in studies using solid acid catalysts, it often performs better [365, 366].

2.3.1.3 Ionic Liquid Systems

Over the past two decades, several groups have demonstrated furfural production from xylan and xylose using acidic imidazolium-based ILs, which served as both solvent and catalyst. In 2009, Lima et al. showed that acidic 1-ethyl-3-methylimidazolium hydrogen sulfate ([Emim][HSO_4]) converted 0.67 M xylose to furfural with a 62% yield in a monophasic IL system at 100 °C for 0.5 h, while the yield fell to 40% and 28% after 4 h and 6 h, respectively [370]. Introducing toluene as an IL-immiscible extraction phase cut the initial furfural yield to 33% at 0.5 h but then significantly boosted it to 82%

at 4 h and 84% at 6 h. Further raising the temperature to 120 °C or the xylose concentration to 1.11 M in this biphasic system accelerated side reactions and lowered selectivity. The recyclability of the [Emim][HSO_4]/toluene system was shown to be feasible. The furfural yield from 0.67 M xylose remained stable over four consecutive runs at 100 °C for 4 h. Conversely, another vacuum-driven furfural removal method has been proven ineffective, yielding only 12% furfural after 4 h, due to intense condensation of substrates (xylose) leading to the generation of black residues. Notably, substituting xylan for xylose in the biphasic system dropped the furfural yield remarkably. The authors also demonstrated that using the non-acidic 1-butyl-3-methylimidazolium chloride ([Bmim][Cl])/toluene system without H_2SO_4 produced no reaction, but adding 0.04 M H_2SO_4 delivered a 44% furfural yield from xylose, confirming that Brønsted acidity at the $[HSO_4]^-$ anion drove xylose dehydration. Peleteiro et al. also demonstrated efficient xylose-to-furfural conversion using an acidic IL, 1-butyl-3-methylimidazolium hydrogen sulfate ([Bmim][HSO_4]), paired with an extraction co-solvent (toluene, dioxane, or MIBK) in a biphasic system [371]. The [Bmim][HSO_4]/dioxane system delivered the highest furfural yield with 82.2% at 140 °C for 4 h, yet the same system proved less effective when applied to solid saccharides (a mixture of poly-, oligo-, and mono-pentoses) from hydrothermally hydrolyzed Eucalyptus hemicellulose, achieving only a 59.1% furfural yield under optimal conditions of 160 °C and 4 h [372]. Building on this work, Xia et al. further discovered that adding water markedly boosted furfural production from bamboo hemicellulose in a microwave-heated [Bmim][HSO_4]/dioxane biphasic system [373]. Using a 10:1 [Bmim][HSO_4] dosage (IL/substrate, mass ratio) with a 0.6 mL water addition at 130 °C for 30 min, a promising 85.69% furfural yield was obtained. The [Bmim][HSO_4] remained active over multiple reuse cycles. Except for these widely used alkylimidazolium-based ILs, another acidic imidazolium IL ([GlyIm][HSO_4]) has also been synthesized using glycine as the starting material. Gomes et al. showed that [GlyIm][HSO_4] greatly enhanced furfural production from sugarcane bagasse acid hydrolysates [374]. Under optimal conditions (180 °C and 10 min) in a [GlyIm][HSO_4]–water/2-MeTHF biphasic system, furfural yields exceeded 90%. However, the IL's

activity declined on reuse, with the furfural yield dropping to 54% by the fifth cycle.

In addition, the use of low-cost, alkylammonium-based PILs for direct furfural production from lignocellulosic biomass has been explored by our group. For example, Brandt-Talbot et al. used [TEA][HSO_4] to pretreat *Miscanthus* [19]. Furfural was a valuable by-product in this process. However, its yield was relatively low (around 40–50 mg g^{-1} *Miscanthus*) after a 12 h reaction at 120 °C. This was because the generated furfural was constantly consumed via polymerization with lignin, leading to the formation of pseudo-lignin. More recently, we have developed a feasible furfural production system by combining the cost-effective [DMBA][HSO_4] with polyoxometalates ($H_4SiW_{12}O_{40}$) and used Design of Experiments (DoE) for optimization [39]. In a one-pot process (150 °C, 5 wt% biomass loading, 90 min), we achieved a promising 73.4% furfural yield from sugarcane bagasse. Future work should target high-biomass-loading systems (>10 wt%) that maintain high furfural yields, alongside cost-effective furfural isolation and purification.

2.3.1.4 Challenges and Prospects

In most furfural production studies, xylose is the primary feedstock for revealing catalytic mechanisms. However, from a practical perspective, producing furfural from pure xylose or xylose-rich hydrolysates is economically unfeasible. This is because the market price of isolated xylose is over \$4 kg^{-1}, while furfural sells for \$1.1–1.3 kg^{-1} [53, 73]. One-pot conversion from lignocellulosic biomass therefore holds greater commercial promise, despite being more challenging than using purified substrates [53]. To make this route more cost-effective, two issues must be addressed urgently [353, 375]: (1) developing a robust system capable of operating at high biomass loadings with sustained high furfural yields; and (2) establishing an integrated biorefinery that simultaneously recovers and valorizes the residual cellulose and lignin fractions.

2.3.2 Catalytic Oxidation of Furfural to Furoic Acid

Furfural is a versatile precursor for a wide range of furan-based chemicals. It can undergo typical aldehyde reactions, such as reduction to alcohols, oxidation to carboxylic acids, aldol condensation, and acylation. The furan ring of furfural is also amenable to reactions such as hydrogenation, oxidation, halogenation, nitration, and polymerization [60]. Through catalytic processes, furfural can be converted into derivatives such as furfuryl alcohol, 2-methylfuran (2-MF), 2-furancarboxylic acid (furoic acid), and others [52, 60, 62], each with distinct applications: furfuryl alcohol for the acid-catalyzed production of furan resins [376]; 2-MF as a next-generation biofuel [377]; and furoic acid, which is attracting attention in two emerging areas. First, furoic acid can serve as an alternative to HMF, since it can be converted to FDCA via catalytic techniques (Figure 2.16) [378]. For example, furoic acid can undergo carboxylation in a CO_2-rich environment catalyzed by carbonates (e.g., Cs_2CO_3 and K_2CO_3), yielding FDCA salts that are then protonated to FDCA with a strong acid [63]. FDCA is a highly promising bio-based feedstock for synthesizing the degradable plastic PEF, which holds the potential to replace petroleum-derived plastic PET on a large scale [64-66]. Second, furoic acid also serves as the basic starting material for a novel bio-based furan surfactant, sulfonated alkyl furoate (SAF), which was invented by our group [68]. Specifically, SAF can be synthesized through the esterification of furoic acid and fatty alcohols, followed by a sulfonation step, giving a surfactant with emulsification properties and detergency that match or exceed those of petroleum-derived linear alkylbenzene sulfonate (LAS) but with fewer environmental concerns (Figure 2.17).

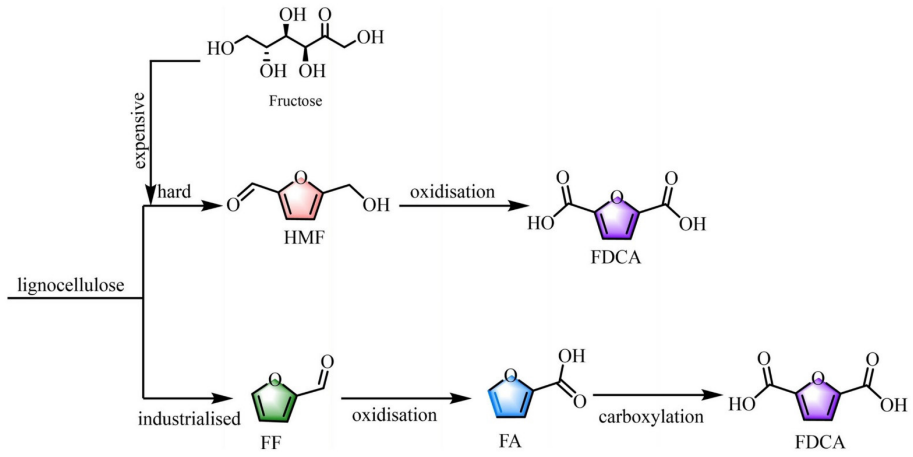


Figure 2.16. Two pathways from HMF or furoic acid to FDCA. Reproduced from Zhang et al. [378].

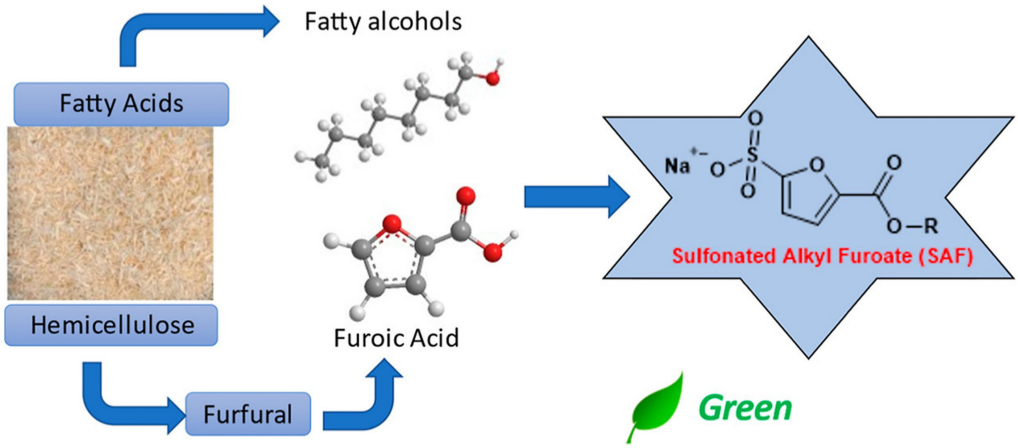


Figure 2.17. Synthesis of the bio-based surfactant SAF via esterification of furoic acid with fatty alcohols. Reproduced from Al Ghatta et al. [68].

Industrially, furoic acid is still mainly produced by the gas-phase Cannizzaro reaction of furfural with stoichiometric NaOH [64]. This route is inherently capped at a 50% furoic acid yield because it co-produces an equimolar amount of furfuryl alcohol [64, 65, 379]. To improve selectivity, the direct oxidation of furfural with O_2 or H_2O_2 has been explored, whereas pure O_2 or air is generally preferred for safety and cost reasons

[379]. These aerobic oxidation methods rely on the use of heterogeneous catalysts—typically noble metals, such as Au, Pd, Pt, Ru, and Ag, supported on oxides or carbon. Choosing catalysts that are inexpensive, robust, active, and recyclable is crucial for achieving both high selectivity and economic benefits. In the following section, we briefly review the performance of various metal-based heterogeneous catalysts for converting furfural into furoic acid.

2.3.2.1 Gold-Based Catalysts

Au-based catalysts are among the most efficient noble metals for oxidizing furfural to furoic acid, exhibiting excellent stability in the presence of O_2 and water [65, 71]. Douthwaite et al. demonstrated that 1 wt% AuPd/$Mg(OH)_2$ (with $Mg(OH)_2$ as the support) exhibited excellent activity for oxidizing furfural to furoic acid [380]. The synergy between Au and Pd markedly outperformed the monometallic 1 wt% Au/$Mg(OH)_2$ and 1 wt% Pd/$Mg(OH)_2$ catalysts. AuPd/$Mg(OH)_2$ proved highly reusable, with furoic acid yields remaining stable over four reuse cycles, despite some particle agglomeration upon recycling. Three competing pathways—oxidation, the Cannizzaro reaction, and polymerization—were found to operate in parallel. While NaOH promoted the Cannizzaro reaction, AuPd/$Mg(OH)_2$ not only drove the direct oxidation of furfural to furoic acid but also catalyzed the oxidative dehydrogenation of the furfuryl alcohol formed via the Cannizzaro reaction back to furfural and onward to furoic acid, thereby enhancing overall selectivity. Furfural self-polymerization to humins can be minimized by optimizing reaction parameters. Under optimal conditions (30 °C, 4 h, 3 bar O_2, and a 1:1 furfural-to-NaOH molar ratio), a 93.2% furoic acid yield was achieved from 0.3 M furfural. Au catalysts have also proven active under base-free conditions. Ferraz et al. screened Au on various oxide supports (e.g., MgO, TiO_2, CeO_2, NiO_2, and ZrO_2) and found that Au/MgO delivered a 100% furoic acid yield (and a 90% FDCA yield from HMF) at 110 °C for 2 h without the introduction of an external base [69]. During the catalytic oxidation, MgO, as a basic oxide, reacted with water to form $Mg(OH)_2$, which raised the pH and promoted both furoic acid and FDCA formation. By contrast, CeO_2 (less basic), ZrO_2 (neutral), and TiO_2/NiO_2 (acidic) supports exhibited much lower

activity. Although Au/MgO delivered excellent selectivity, the partial leaching of Mg into the solution was detrimental to the reuse of the catalyst. To address this, a mixed MgF_2–MgO support was developed. At a 0.4 MgF_2–0.6 MgO molar ratio, the mixed support matched the activity of pure MgO, achieving a 99% furoic acid yield after 2 h, while effectively suppressing Mg leaching. Even at a 0.6 MgF_2–0.4 MgO molar ratio, over a 70% furoic acid yield could be achieved at a final solution pH of 3.8, allowing the direct isolation of furoic acid without protonation by strong acids. Ferraz et al. also evaluated three MnO_2 morphologies as supports for Au catalysts [381]. The study showed that, when MnO_2 was engineered into a nanoflower (NF) morphology with a high surface area and pore volume, it could host ultra-small, highly active $Au^{\delta+}$ species (with a ratio up to 26%), creating abundant active sites for oxidation. The resulting Au/MnO_2-NF catalyst achieved very high furoic acid selectivity. Under optimal conditions (110 °C, 4 h, 12 bar air, and a 100:1 furfural-to-Au molar ratio), it delivered an 82% furoic acid yield under base-free conditions. Papanikolaou et al. then explored another novel support, zeolite-templated carbon derived from BETA zeolite (β-ZTC) [72]. The Au/ZTC catalyst, with highly dispersed Au nanoparticles, oxidized a 0.02 M furfural solution in methanol to furoic acid at 120 °C under 12 bar O_2 without adding a base. Compared with a commercial Vulcan support, β-ZTC outperformed it, achieving 89% furfural conversion and 100% furoic acid selectivity after 3 h.

2.3.2.2 Ruthenium-Based Catalysts

The effectiveness of the noble metal Ru for oxidizing furfural to furoic acid has also been demonstrated. Lokhande et al. prepared noble metal catalysts (Pt, Pd, and Ru) supported on carbon or Al_2O_3 by wet impregnation followed by H_2 reduction [379]. Among these, 5 wt% Ru/C demonstrated the highest catalytic activity. By using Na_2CO_3 to maintain the pH at 11–11.5 (which suppressed side reactions that occur under stronger bases), an 83% furoic acid yield was obtained under mild alkaline conditions (0.5 wt% furfural, 110 °C, 15 bar O_2, 8 h, and a 0.5:1 Na_2CO_3-to-furfural molar ratio). No catalyst agglomeration or Ru leaching was observed, and the Ru/C could be recycled after mild H_2 reduction at 150 °C. Acidification of the resulting sodium

furoate with 0.1 M HCl gave furoic acid of approximately 96% purity. Wu et al. found that depositing Ru on δ-MnO_2 dramatically boosted activity [67]. Specifically, δ-MnO_2 alone converted 50.07% of furfural at 100 °C for 1 h, whereas $Ru_{0.25}$/δ-MnO_2 increased conversion by 27.90% and, at 120 °C, delivered a 99.55% furoic acid yield. Interestingly, in 2022, Kar et al. even reported homogeneous Ru complexes with acridine-based PNP pincer ligands that oxidized furfural and HMF to furoic acid and FDCA in alkaline water with a >95% yield, producing H_2 as a valuable by-product [382], although homogeneous systems fall beyond this review's scope.

2.3.2.3 Silver-Based Catalysts

In addition to Au- and Ru-based catalysts, Ag-based catalysts have also shown promise. Tian et al. prepared nanosized Ag_2O/CuO by impregnating CuO nanopowder with $AgNO_3$ and calcining it [70]. Under basic conditions, they tested temperature (50–80 °C), pH (10–14), catalyst loading (15–35 wt%), and catalyst particle size (30 nm versus 150 nm). Under optimal conditions, Ag_2O/CuO obtained a 92% furoic acid yield, which was higher than the 86.6% achieved with CuO alone. Notably, although smaller particles usually offer a greater surface area and more active sites, 30 nm Ag_2O/CuO instead promoted the Diels–Alder reaction over the furfural-to-furoic acid oxidation. During reuse, Ag_2O gradually detached from the CuO support, causing the yield to fall to approximately 65% after 18 cycles. Sadier et al. evaluated Ag/TiO_2 for furfural oxidation [71]. At room temperature under 15 bar air for 3 h, with a 1:1 NaOH-to-furfural molar ratio, Ag/TiO_2 obtained a 96% furoic acid yield. However, the catalytic activity of Ag/TiO_2 dropped sharply during reuse, falling from an 82% furoic acid yield in the first cycle to around 52% by the third. No Ag leaching was detected. Instead, the authors attributed catalyst deactivation to nanoparticle aggregation (particle size growth).

2.3.2.4 Non-Noble Manganese-Based Bimetallic Oxides

Non-noble Mn-based bimetallic oxides have also shown excellent activity for aldehyde-to-acid oxidation. Nocito et al. compared high-energy milling (HEM) and microwave-assisted hydrothermal (MWHT) routes to prepare MnO_2–CeO_2 catalysts [65]. The

MWHT-derived MnO_2@CeO_2 featured a perfect core–shell structure, with MnO_2 on the surface and CeO_2 in the core. Under optimized conditions, MnO_2@CeO_2 obtained 96% furfural conversion with 100% furoic acid selectivity. Even after ten 5-h cycles (50 h in total), its performance remained basically unchanged. Furthermore, Yu et al. synthesized Mn–Cu bimetallic oxides via a modified hydrothermal–redox method [383]. They reported 99% furfural conversion and quantitative furoic acid selectivity using $Mn_2Cu_1O_x$ at 120 °C, 1 MPa O_2, 3 h, and a furfural-to-NaOH molar ratio of 1:2. Excellent recyclability of $Mn_2Cu_1O_x$ was also demonstrated, with the furoic acid yield remaining above 90% after five runs. This performance was mainly attributed to the incorporation of the CuO component, which can weaken the Mn–O bond and enhance lattice oxygen reactivity, thereby boosting catalytic activity.

2.3.2.5 Proposed Oxidation Mechanisms

Although a variety of metal-based heterogeneous catalysts have been studied for oxidizing furfural to furoic acid, their mechanisms fall into two broad categories based on the role of O_2.

First, for supported noble metal catalysts—where the active phase is in a non-oxide (metallic) state (e.g., Au/MgO, Pt/C, and Pd/C)—O_2 acts as the terminal oxidant. Specifically, molecular O_2 is activated on the catalyst surface (its O═O bond is cleaved in the presence of water) to form active oxygen species (e.g., OOH*, O*, and OH*; * denotes surface adsorption) [384-386], while furfural is also chemisorbed at nearby sites. In the absence of any added base (e.g., NaOH and Na_2CO_3) or basic supports, these active oxygen species can directly abstract the hydrogen atom from the aldehyde group and convert it to the carboxyl group [384], though this pathway is relatively inefficient. Adding a base greatly accelerates the reaction. OH^- first promotes the reversible hydration of furfural to the geminal diol (and, at high pH, to the deprotonated geminal diol monoanion), which then undergoes oxidative dehydrogenation by active oxygen species to yield furoate (furoic acid upon acidification) (Figure 2.18) [71, 387, 388]. Because the barrier for geminal diol oxidation is much lower than that for direct

furfural oxidation, the base-promoted route tends to deliver far higher efficiencies [389].

Second, metal oxide catalysts, whether noble-metal-based or non-noble-metal-based (e.g., Ag_2O/CuO, nano CuO, and Mn–Cu bimetallic oxides), typically follow a two-step redox cycle (Mars–Van Krevelen mechanism) in which O_2 serves to reoxidize the reduced catalyst (Figure 2.19) [383]. Under alkaline conditions, furfural reversibly hydrates to the geminal diol. Lattice oxygen then oxidizes the geminal diol to the furoate (which gives furoic acid upon acidification), thereby reducing the metal centers. Molecular O_2 subsequently reoxidizes the catalyst and replenishes lattice oxygen, closing the catalytic cycle. Because this route depends on continuous metal redox cycling, these materials are more prone to deactivation via metal leaching or nanoparticle aggregation [70].

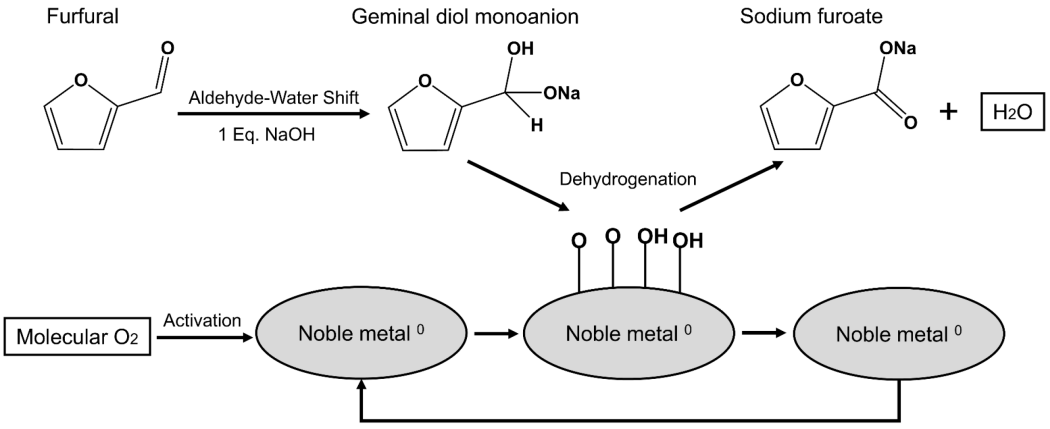


Figure 2.18. Possible catalytic mechanism for the base-assisted aerobic oxidation of furfural to furoic acid over a noble metal (non-oxide) catalyst.

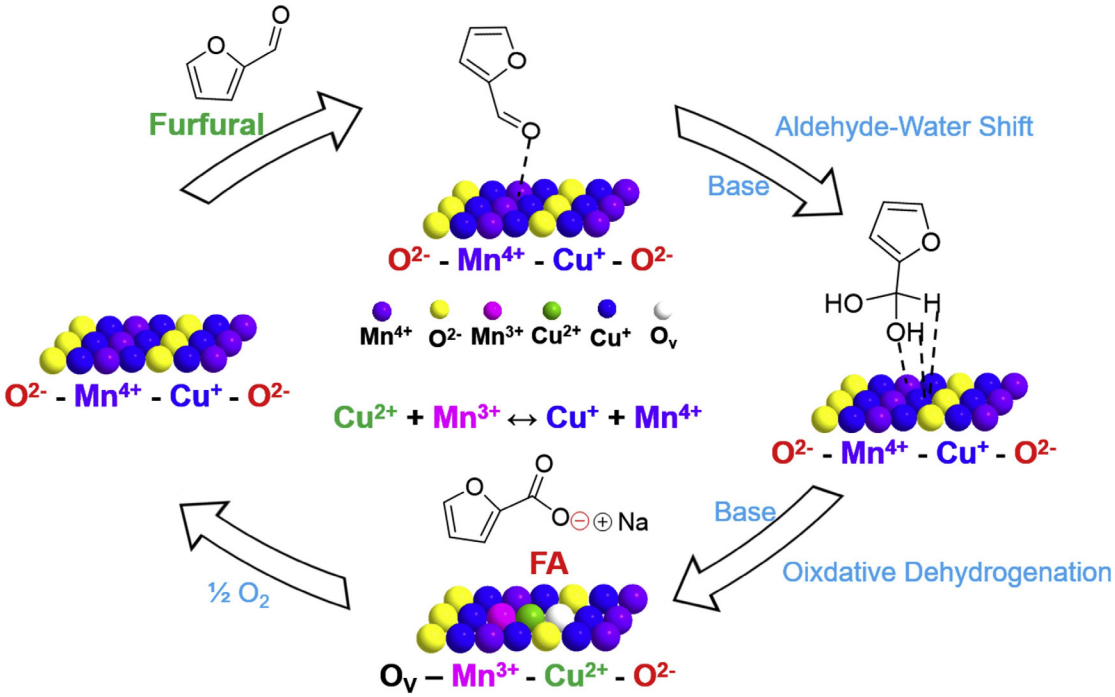


Figure 2.19. Possible catalytic mechanism for the aerobic oxidation of furfural to furoic acid over a metal-oxide-based ($Mn_2Cu_1O_x$) heterogeneous catalyst. Reproduced from Yu et al. [383].

2.3.3 Summary

During the acid-catalyzed hydrolysis of hemicellulose and the dehydration of xylose, furfural yields are limited by side reactions, including self-resinification and the furfural condensation with carbohydrates and other reaction intermediates. In situ removal of furfural from the acidic aqueous phase both suppresses its degradation and drives the equilibrium toward product formation. Effective furfural removal methods include steam stripping and biphasic aqueous–organic solvent systems. From an economic standpoint, furfural production from xylose alone is generally uneconomic, and economically competitive biorefineries should instead produce furfural directly from raw biomass at high solids loadings, with the concurrent valorization of cellulose and lignin. To further expand the furan-based chemical value chain, numerous noble- and base-metal heterogeneous catalysts have been studied for the aerobic oxidation of furfural to furoic acid. For industrial applications, catalysts should be inexpensive, highly active, durable, and recyclable. Mechanistically, two pathways have been

proposed for aerobic oxidation over metal-based heterogeneous catalysts, distinguished by the role of molecular O_2: direct oxidation, in which molecular O_2 participates in the surface oxidation of furfural (or its geminal diol), and indirect oxidation, in which molecular O_2 serves as the oxidant that reoxidizes the catalyst active sites.

Chapter 3: Process Intensification via Probe Sonication in Protic Ionic Liquid Pretreatment of Biomass

3.1 Introduction

Over the past few decades, biomass-derived energy and chemicals have received considerable attention as potentially carbon-neutral alternatives to fossil fuels [390, 391]. International efforts to cut greenhouse gas (GHG) emissions and decarbonize the economy have further underscored the value of bioenergy and bio-based products [37]. As a result, most of the recent research has focused on inedible lignocellulosic feedstocks, including agricultural residues, forest waste, and dedicated energy crops, for producing second-generation biofuels such as cellulosic ethanol [11, 16, 22, 23]. These lignocellulosic feedstocks are abundant and require less labor and fertilizer compared with those required for food crops [20, 24, 392]. Life-cycle studies also suggest that replacing gasoline with cellulosic ethanol or butanol derived from inedible lignocellulosic feedstocks can cut GHG emissions by up to 90%, whereas corn-based biofuels achieve only about a 40% reduction [16, 393, 394].

Lignocellulosic feedstocks contain three biopolymers—cellulose, hemicellulose, and lignin—whose proportions vary by species and growth stage [11, 37]. Cellulose and hemicellulose can be enzymatically hydrolyzed to monosaccharides such as glucose and xylose, which are then fermented to (hemi)cellulosic ethanol. Lignin, built from three primary phenyl units, binds tightly to the carbohydrate matrix and blocks enzyme access, thereby lowering bioethanol yields [24, 395]. Consequently, a pretreatment step is required to remove or disrupt lignin before hydrolysis and fermentation [28, 396]. Pretreatment, however, remains the main economic hurdle to commercial biorefineries, driven by energy demand, solvent and catalyst consumption, and process complexity [16, 28, 397]. Accordingly, applying cost-effective or recyclable solvents and streamlining operational steps can help reduce these expenses.

Among the various pretreatment strategies, ionic liquid (IL) pretreatment has drawn particular interest over the past decade because of its ability to fractionate lignocellulosic biomass into its constituent polymers [19]. Two distinct IL-based strategies have been explored. In the first, some ILs can disrupt the hydrogen-bond network and dissolve most of the lignocellulose, including highly crystalline cellulose [11, 398]. The carbohydrate-rich solid can then be regenerated by adding an anti-solvent [305]. The regenerated material shows an excellent saccharification yield and achieves up to a 50-fold increase in enzymatic hydrolysis rates [305, 399]. However, this approach relies largely on aprotic ionic liquids (APILs) with strongly hydrogen-bond-accepting (basic) anions [19], such as 1-ethyl-3-methylimidazolium acetate ([Emim][OAc]), whose high cost (\$20–101 kg^{-1}), arising from costly raw materials and multi-step synthesis, together with low thermal stability and poor moisture tolerance, restricts its industrial application [307, 308]. To address these drawbacks, the “ionoSolv” process (the second strategy) has emerged, using low-cost protic ionic liquids (PILs) that can be less expensive than some common solvents such as acetone and glycerol [19, 145]. This process fractionates lignocellulose by dissolving lignin and hemicellulose while preserving a cellulose-rich pulp [19, 137]. PILs are synthesized by simple acid-base neutralization and offer high thermal stability, moisture tolerance, low volatility, and excellent recyclability [19, 36, 37]. Various PILs, such as 1-methylimidazolium chloride ([H_1Cim]Cl), triethylammonium hydrogen sulfate ([TEA][HSO_4]), and *N,N*-dimethylbutylammonium hydrogen sulfate ([DMBA][HSO_4]), have given promising saccharification yields from different types of biomass, including *Miscanthus*, pine wood, CCA-treated wood, postconsumer waste wood, creosote wood, rhododendron, and Japanese knotweed [24, 90, 91, 152, 309]. Additionally, PILs have proven useful for extracting heavy metals from waste wood and sewage sludge [90, 91]. The current limitation of the ionoSolv process is the long residence time required for effective pretreatment at low temperatures. Brandt-Talbot et al. found that *Miscanthus* in [TEA][HSO_4] at 120 °C required 8 h for optimal fractionation [19]. To shorten the reaction time, raising the temperature is common practice. Gschwend et al. demonstrated that increasing the temperature from 120 to 150 °C or higher reduced

pretreatment time by about 90% without compromising the saccharification yield [37]. Nevertheless, higher temperatures increase heat loss and demand additional energy for rapid heating, which can affect overall process economics. Moreover, our ongoing research indicates that the corrosivity of PILs increases significantly at elevated temperatures, potentially accelerating the corrosion of stainless steel equipment and raising concerns for industrial-scale deployment.

Ultrasound is a mechanical acoustic wave with frequencies ranging from 16 kHz to 500 MHz [400]. When integrated with the ionoSolv process, ultrasound can deliver substantial energy to PILs through acoustic cavitation and its secondary effects [395]. Acoustic cavitation is the growth and collapse of numerous microbubbles in a liquid medium caused by the compression and expansion phases of mechanical waves [340]. The transient, nearly adiabatic implosion of these bubbles generates extremely high local temperatures (~5,000 K) and pressures (~50 MPa) [334, 338]. These events enhance mass transfer through intense local convection and accelerate reactions by forming reactive radicals during bubble collapse [334, 338, 401, 402]. Thus, sonication offers a promising route to reduce both extraction temperature and processing time in biomass treatment. For instance, Sarwono et al. successfully shortened reaction times from hours (h) to minutes (min) by applying probe sonication for HMF production from cellulose and bamboo using 1-butyl-3-methylimidazolium chloride ($[C_4C_1im]Cl$) [334]. Sukor et al. likewise observed a synergistic effect between probe sonication and the IL 1-butyl-3-methylimidazolium bis(trifluoromethylsulfonyl)imide ($[Bmim][Tf_2N]$), greatly improving phenolic acid extraction from oak galls [340]. However, probe sonication has not yet been applied to the ionoSolv process. More crucially, this study provides the first quantitative assessment that separates the sonication-induced temperature increase from mass transfer enhancement, identifying their individual contributions to the acceleration of the ionoSolv process. A preliminary techno-economic analysis also compares conventional and sonication-assisted ionoSolv, evaluating the potential economic benefits from introducing ultrasound.

3.2 Materials and Methods

3.2.1 Feedstock

In this study, *Miscanthus* was obtained from the Silwood Park campus of Imperial College London (UK), and spruce was supplied by the MORE research facility (Luleå, Sweden). Both feedstocks were air-dried, milled in a knife mill, and passed through 20-mesh and 80-mesh screens to give a particle-size range of 180–850 μm. The milled feedstocks were stored in sealed plastic bags at room temperature and protected from light.

3.2.2 Biomass Moisture Content

The moisture contents of the raw biomass and the recovered cellulose-rich pulp were determined according to the National Renewable Energy Laboratory (NREL) protocol "Determination of Total Solids in Biomass and Total Dissolved Solids in Liquid Process Samples" [403]. Specifically, 400–500 mg of air-dried sample was weighed and wrapped in pre-weighed aluminum foil. The wrapped sample was then transferred to a convection oven and dried at 105 °C for 24 h. After drying, the sample was cooled in a desiccator for 20 min and weighed again. The moisture content of the sample was calculated as follows:

$$\text{Moisture content (\%)} = \frac{\text{Mass of air dried pulp+foil} - \text{Mass of oven dried pulp+foil}}{\text{Mass of air dried pulp+foil} - \text{Mass of foil}} \times 100 \quad (3.1)$$

For air-dried biomass and pulp, their oven-dried weight (ODW) can be calculated as follows:

$$\text{ODW} = \text{Mass of air dried sample} \times (1 - \text{Moisture content of sample (\%)}) \quad (3.2)$$

The raw *Miscanthus* and spruce contained 7.20 wt% and 7.02 wt% moisture, respectively.

3.2.3 Biomass Extractives

The extractive content of the raw biomass was determined following the NREL protocol "Determination of Extractives in Biomass" [404]. Approximately 5 g of raw biomass (on an oven-dried basis) was placed in a pre-weighed cellulose thimble and Soxhlet-

extracted with refluxing deionized water (150 mL) for 20 h. The solvent was then replaced with absolute ethanol (150 mL), and extraction continued for a further 20 h. The thimble was air-dried overnight in a fume hood and weighed. The moisture content of the extractive-free biomass (EFB) was measured, and the extractive content was calculated as follows:

$$\text{Extractives (\%)} = \left(1 - \frac{\text{Mass of air dried EFB} \times (1 - \text{Moisture content of EFB (\%)})}{\text{Mass of oven dried raw biomass}}\right) \times 100 \qquad (3.3)$$

3.2.4 Synthesis of [DMBA][HSO_4]

The PIL [DMBA][HSO_4] was prepared by one-step acid-base neutralization according to the standard synthesis procedure in our laboratory [36, 107]. *N,N*-dimethylbutylamine (>98 wt%) and 72 wt% sulfuric acid (both from Sigma-Aldrich, used as received) were employed in equimolar amounts. *N,N*-dimethylbutylamine (505.8 g, 5 mol) was placed in a 1 L round-bottom flask cooled in an ice bath. With continuous stirring, 72 wt% H_2SO_4 (694.7 g, 5 mol) was added dropwise. The mixture was then stirred overnight, yielding [DMBA][HSO_4] as a clear, viscous liquid.

The water content of [DMBA][HSO_4] was measured with a V20 volumetric Karl Fischer Titrator (Mettler-Toledo), and the acid-base ratio was determined using a G20S Compact Titrator (Mettler-Toledo) with 0.1 M NaOH. To reach the target water content of 20 wt%, water was added or removed with a rotary evaporator (Büchi). The desired acid-base ratio (1.000 ± 0.005 mol/mol) was obtained by adding small amounts of either *N,N*-dimethylbutylamine or sulfuric acid.

To verify the purity and structural integrity of the IL, ^{1}H and ^{13}C nuclear magnetic resonance (NMR) spectra of [DMBA][HSO_4] were recorded using a JEOL 400 MHz spectrometer with DMSO-d_6 as the solvent (Appendices: Figures S1–S2). Chemical shifts (δ) are reported in ppm.

3.2.5 Conventional IonoSolv Process

The conventional ionoSolv process followed the protocol established in our laboratory [405]. For each pretreatment, *Miscanthus* or spruce (2 g, on an oven-dried basis) was mixed with 20.00 ± 0.02 g of [DMBA][HSO_4] (20 wt% water content) in a pressure tube (Ace Glass), giving a biomass-to-solvent ratio of 1:10 (g/g). The pressure tube was capped, and the IL–biomass mixture was mixed with a vortex shaker. The sealed pressure tube was then heated in a convection oven or silicone oil bath at set temperatures (110, 130, or 150 °C) for required times (0.25, 0.5, 1, 2, 3, or 4 h). After heating, the pressure tube was cooled to room temperature in a fume hood.

The pretreated mixture was transferred into a 50 mL Falcon centrifuge tube with 40 mL of absolute ethanol, vortexed, and then centrifuged at 3,500 rpm for 30 min. The dark brown supernatant was poured into a pre-labelled 250 mL round-bottom flask. The cellulose-rich pulp was washed three more times with 40 mL of absolute ethanol, and all supernatants were combined for later processing. The remaining pulp was transferred into a pre-weighed cellulose thimble and further washed by Soxhlet extraction with refluxing absolute ethanol (150 mL) for 20 h. The thimble was air-dried overnight in a fume hood. Then, the pulp-containing thimble was weighed, the moisture content of the pulp was measured, and the pulp yield was calculated as follows:

$$\text{Pulp yield (\%)} = \frac{(\text{Mass of air dried pulp+thimble} - \text{Mass of empty thimble}) \times (1 - \text{Moisture content of pulp (\%)})}{\text{Mass of oven dried raw biomass}} \times 100 \quad (3.4)$$

The ethanol used for Soxhlet extraction was combined with the previous washings and removed by rotary evaporation at 40 °C under reduced pressure. The resulting brown, viscous liquid, containing [DMBA][HSO_4] and extracted lignin, was transferred into a 50 mL centrifuge tube with 40 mL of deionized water as an anti-solvent. After thorough vortexing, the mixture was left for 2 h to allow lignin to precipitate. The tube was then centrifuged at 3,500 rpm for 30 min. The supernatant was collected, and the recovered lignin was washed three more times with 40 mL of deionized water. Finally, the collected lignin was freeze-dried for 2 days to remove moisture and weighed to

calculate the lignin recovery yield.

$$\text{Lignin recovery yield (\%)} = \frac{\text{Mass of freeze dried precipitated lignin+tube} - \text{Mass of empty tube}}{\text{Mass of oven dried raw biomass} \times \text{Lignin content in the raw biomass (\%)}} \times 100 \quad (3.5)$$

3.2.6 Sonication-Assisted IonoSolv Process

For each run, *Miscanthus* or spruce (2 g, on an oven-dried basis) was mixed with 20.00 ± 0.02 g of [DMBA][HSO_4] (20 wt% water content) in a pressure tube (Ace Glass). Subsequently, the pressure tube was sealed with a customized lid featuring a hole in the middle, through which a titanium tip (1/8 inch in diameter) of the probe sonicator (Fisherbrand™ Model 120 Sonic Dismembrator) could be inserted to about one-third of the liquid depth. Sonication was carried out in an oil bath at 110, 130, or 150 °C for 0.25, 0.5, 1, 2, 3, or 4 h, using 60% or 80% amplitude, a 20 kHz frequency, a 120 W power, and a 10 s on/10 s off pulse cycle. After the sonication-assisted ionoSolv process, the pressure tube was cooled to room temperature, and the remaining steps were the same as those of the conventional pretreatment. The device for sonication pretreatment is shown in Figure 3.1.

To clarify the mechanism of the sonication pretreatment, we monitored the temperature profile of the reaction medium. Using our existing customized PTFE lid, we drilled two additional small holes adjacent to the central probe port. Thermocouples were inserted through these holes at two depths: one near the probe tip and the other at the bottom of the pressure tube, corresponding to the highest and lowest temperatures in the sonication system, respectively, as determined through trial and error. Both openings were then sealed with a high-temperature-resistant epoxy resin. Temperature was logged continuously during sonication, and parallel measurements were taken during the oil-bath ionoSolv process for comparison.

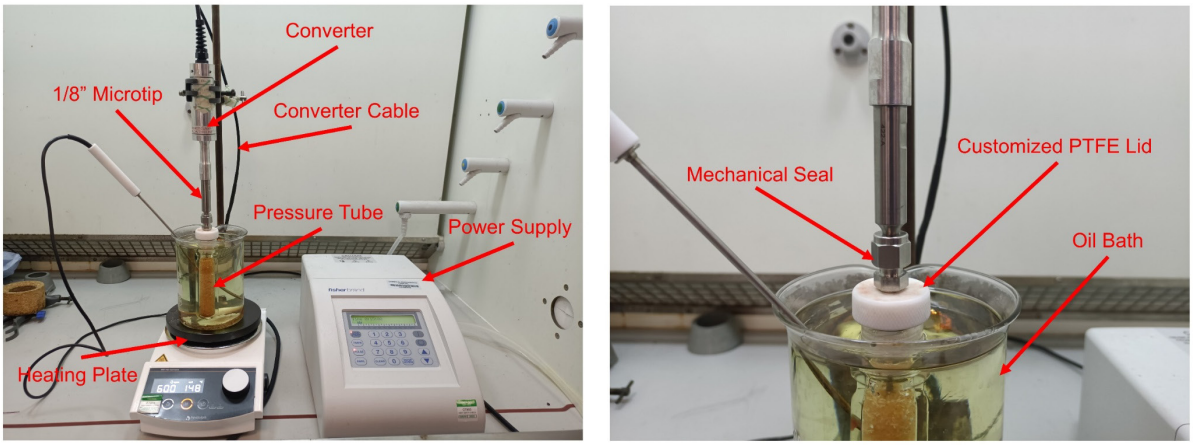


Figure 3.1. Experimental setup for the sonication-assisted ionoSolv process.

3.2.7 Separation of Fine and Coarse Pulp Layers after the Sonication-Assisted IonoSolv Process

After the sonication-assisted ionoSolv process, centrifugation separated the pulp into two distinct layers: an upper layer with finer particles and a lower layer with coarser particles (Figure 3.2). To assess the impact of this particle-size difference on pulp quality, we selected two representative sonicated pulps (*Miscanthus* and spruce, pretreated at 130 °C for 2 h at 80% amplitude). Each Soxhlet-washed pulp was centrifuged at 3,500 rpm for 30 min in a 50 mL Falcon tube to form the two layers. The upper layer was carefully transferred to a new Falcon tube. Subsequently, the separated upper and lower layers were air-dried for further characterization.

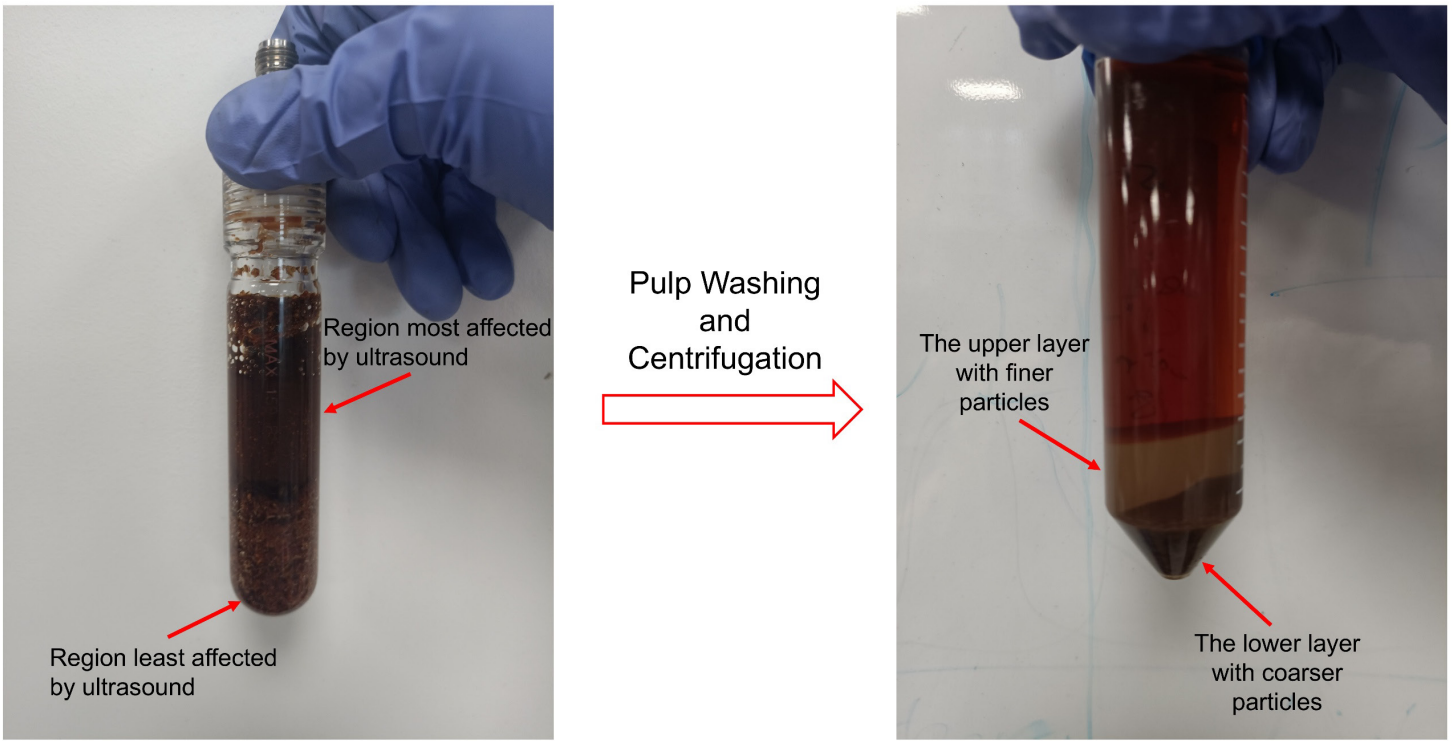


Figure 3.2. Separation of two pulp layers after the sonication-assisted ionoSolv process.

3.2.8 Compositional Analysis

Compositional analysis of the extractive-free raw biomass and recovered cellulose-rich pulps followed the NREL protocol “Determination of Structural Carbohydrates and Lignin in Biomass” [406]. The cellulose, hemicellulose, acid insoluble lignin (AIL), acid soluble lignin (ASL), and ash contents of each sample were measured. The equipment used during compositional analysis included an analytical balance (Sartorius CPA 1003 S), a water bath sonicator (Fisherbrand™ EASY 300H), an autoclave (Sanyo Labo ML5 3020U), a pH meter (VWR SB70P), a UV-Vis spectrometer (Perkin Elmer Lambda 650 with an STD detector module), a high performance liquid chromatography (HPLC) system with a refractive index detector (RID) (Shimadzu, Aminex HPX-87P from Bio-Rad, 300 × 7.8 mm, purified water as the mobile phase at 0.6 mL min^{-1}, column temperature of 85 °C, and a 25 min run), a 105 °C oven (VWR Venti-Line 115), and a

muffle oven (Nabertherm with a Controller P330).

Specifically, 300 mg of sample (on an oven-dried basis) was weighed and mixed with 3 mL of 72 wt% sulfuric acid in a 100 mL Ace pressure tube. The pressure tube was then heated in a 30 °C water bath for 1 h, and the slurry was stirred with a Teflon rod every 15 min to ensure adequate mixing. Afterward, the mixture was diluted with 84 mL of deionized water, sealed, and autoclaved at 121 °C for 1 h. The hydrolyzed slurry was filtered through a pre-weighed ceramic crucible to separate the solid residue (AIL and ash) from the filtrate containing ASL and hydrolyzed sugars. The filtrate was collected in two 50 mL Falcon tubes for UV-Vis measurement of ASL and HPLC determination of glucose, xylose, galactose, arabinose, and mannose. The ASL content was calculated as follows:

$$\text{ASL (\%)} = \frac{\text{UV absorbance} \times \text{Volume filtrate} \times \text{Dilution}}{\varepsilon \times \text{L} \times \text{Mass of oven dried sample}} \times 100 \quad (3.6)$$

Where UV absorbance is the UV-Vis absorbance of the sample at the wavelength of 240 nm, which should fall between 0.7 and 1.0. The volume of the filtrate is 86.73 mL. The dilution factor is the ratio of the total diluted volume to the original filtrate volume (the filtrate is diluted to keep absorbance within 0.7–1.0). ε is the absorptivity of *Miscanthus* (25 L $g^{-1}cm^{-1}$) or spruce (12 L $g^{-1}cm^{-1}$) at the wavelength of 240 nm [406]. L is the cuvette path length (1 cm in this case). Mass of oven dried sample is the mass of the raw biomass or pulp on an oven-dried basis, in mg.

For HPLC analysis, the filtrate needed to be neutralized by adding calcium carbonate to reach a pH value of 5, transferred into an HPLC vial through a 0.22 μm PTFE syringe filter, and finally submitted for analysis. Calibration standards of glucose, xylose, galactose, arabinose, and mannose were prepared at 0.1, 1, 2, and 4 mg g^{-1}, with an additional glucose standard at 8 mg g^{-1}. The relevant formulas for calculating sugar contents in the sample can be found in the literature [19]. Notably, because this protocol cannot distinguish glucose released from cellulose versus hemicellulose, the reported glucan content represents the total glucose originating from both fractions,

while the hemicellulose content refers to the combined amounts of xylose, galactose, arabinose, and mannose.

The crucible containing the solid residue was dried overnight at 105 °C, weighed, and then ashed at 575 °C in a muffle oven. After cooling, the crucible with ash was weighed again. Therefore, three masses, including the empty crucible, the crucible with acid insoluble residue (AIL and ash), and the crucible with ash, were recorded. The AIL and ash contents can be calculated using the following equations:

$$\text{AIL (\%)} = \frac{\text{Mass of crucible+acid insoluble residue} - \text{Mass of crucible+ash}}{\text{Mass of oven dried sample}} \times 100 \quad (3.7)$$

$$\text{Ash content (\%)} = \frac{\text{Mass of crucible+ash} - \text{Mass of crucible}}{\text{Mass of oven dried sample}} \times 100 \quad (3.8)$$

On an oven-dried basis, the raw *Miscanthus* contained glucan (49.46 ± 0.25 wt%), xylan (21.28 ± 0.08 wt%), arabinan (1.75 ± 0.07 wt%), ASL (3.33 ± 0.04 wt%), AIL (20.90 ± 0.18 wt%), ash (0.23 ± 0.03 wt%), and extractives (3.05 ± 0.29 wt%). The raw spruce contained glucan (43.37 ± 0.04 wt%), xylan (5.54 ± 0.01 wt%), galactan (2.38 ± 0.01 wt%), arabinan (1.03 ± 0.03 wt%), mannan (12.25 ± 0.004 wt%), ASL (1.49 ± 0.002 wt%), AIL (25.79 ± 0.05 wt%), ash (0.03 ± 0.03 wt%), and extractives (8.12 ± 0.34 wt%).

Based on the resulting data, several fractionation indicators, including glucan recovery, hemicellulose removal, and delignification, were calculated as follows:

$$\text{Glucan recovery (\%)} = \frac{\text{Glucan content in the pulp (\%)} \times \text{Pulp yield (\%)}}{\text{Glucan content in the raw biomass (\%)}} \times 100 \quad (3.9)$$

$$\text{Hemicellulose removal (\%)} = \left(1 - \frac{\text{Hemicellulose content in the pulp (\%)} \times \text{Pulp yield (\%)}}{\text{Hemicellulose content in the raw biomass (\%)}}\right) \times 100 \quad (3.10)$$

$$\text{Delignification (\%)} = \left(1 - \frac{\text{Lignin content in the pulp (\%)} \times \text{Pulp yield (\%)}}{\text{Lignin content in the raw biomass (\%)}}\right) \times 100 \quad (3.11)$$

3.2.9 Enzymatic Hydrolysis

The enzymatic hydrolysis (saccharification) of both raw biomass and recovered cellulose-rich pulps was performed according to the NREL protocol “Low Solids

Enzymatic Saccharification of Lignocellulosic Biomass" [407]. In brief, 100 mg of raw biomass or cellulose-rich pulp (on an oven-dried basis) was weighed into a 25 mL Sterilin tube. Subsequently, 9.9 mL of enzyme buffer—consisting of 5 mL of sodium citrate buffer (100 mM, pH 4.8), 40 µL of tetracycline solution (10 mg mL^{-1} in 70:30 (v/v) ethanol:deionized water), 30 µL of cycloheximide solution (10 mg mL^{-1} in 100% deionized water), deionized water (4.81 mL for *Miscanthus*, 4.78 mL for spruce), and the Novozymes experimental enzyme mixture Cellic® CTec2 (20 µL for *Miscanthus*, 50 µL for spruce)—was added. The pulp–enzyme mixture was sealed and incubated at 50 °C and 250 rpm for 7 days in a Stuart orbital incubator (S1500). In addition, three blank samples were prepared to correct for any sugar background concentrations. For each blank, 9.9 mL of enzyme buffer was mixed with 100 µL of deionized water in place of pulp. After 7 days, 1 mL of the saccharification mixture was collected and filtered into an HPLC vial using a 0.22 µm PTFE syringe filter. Sugar concentrations of the sample were measured by the Shimadzu HPLC system described in the compositional analysis section. The same calibration standards from the compositional analysis section were also used. The saccharification yield was calculated according to the NREL protocol, taking into account the anhydrous correction factors for polysaccharides, the pretreated pulp yield, and the glucan content of the raw materials (*Miscanthus* and spruce).

3.2.10 Quantitative Evaluation of Sonication-Induced Effects on the IonoSolv Process

The impacts of two sonication-induced factors, mass transfer enhancement and temperature increase, on the ionoSolv process of *Miscanthus* were quantified using the following equations:

$$\text{Contribution of mass transfer enhancement (\%)} = \frac{\text{Saccharification yield for MP from sonication at 103 °C} - \text{Saccharification yield for MP from oil bath at 110 °C}}{\text{Saccharification yield for MP from sonication at 110 °C} - \text{Saccharification yield for MP from oil bath at 110 °C}} \times 100 \quad (3.12)$$

$$\text{Contribution of temperature increase (\%)} =$$

$$\frac{\text{Saccharification yield for MP from sonication at 110 °C} - \text{Saccharification yield for MP from sonication at 103 °C}}{\text{Saccharification yield for MP from sonication at 110 °C} - \text{Saccharification yield for MP from oil bath at 110 °C}} \times 100 \quad (3.13)$$

Similarly, the influences of these sonication-induced factors on the ionoSolv process of spruce were calculated as follows:

$$\text{Contribution of mass transfer enhancement (\%)} = \frac{\text{Saccharification yield for SP from sonication at 121 °C} - \text{Saccharification yield for SP from oil bath at 130 °C}}{\text{Saccharification yield for SP from sonication at 130 °C} - \text{Saccharification yield for SP from oil bath at 130 °C}} \times 100 \quad (3.14)$$

$$\text{Contribution of temperature increase (\%)} = \frac{\text{Saccharification yield for SP from sonication at 130 °C} - \text{Saccharification yield for SP from sonication at 121 °C}}{\text{Saccharification yield for SP from sonication at 130 °C} - \text{Saccharification yield for SP from oil bath at 130 °C}} \times 100 \quad (3.15)$$

Where MP and SP refer to *Miscanthus* pulp and spruce pulp, respectively.

3.2.11 Lignin Characterization

The variations in lignin interunit linkages and subunits derived from different ionoSolv conditions were analyzed by two-dimensional (2D) ^{1}H–^{13}C heteronuclear single quantum coherence (HSQC) nuclear magnetic resonance (NMR) spectroscopy. Approximately 20 mg of precipitated lignin was dissolved in 0.25 mL of DMSO-d_6, loaded into a Shigemi tube, and spectra were acquired on a Bruker 800 MHz spectrometer (pulse sequence hsqcetgpsi2; spectral widths: 10 ppm in F2 (^{1}H, 2048 data points) and 160 ppm in F1 (^{13}C, 256 data points); 16 scans; 1 s interscan delay). Spectra were processed in MestReNova (v8.0.0, Mestrelab Research, 2012) following our previously reported protocol [19, 36]. Integration regions were selected manually according to the peak assignments in those studies.

3.2.12 Errors and Uncertainties

In this chapter, all ionoSolv experiments were conducted at least in duplicate. Values in the text are reported as the mean ± 1 standard deviation. Error bars in all figures represent ± 1 standard deviation.

3.3 Results and Discussion

3.3.1 Temperature Profiles for Different IonoSolv Methods

This study compared the temperature profiles of three ionoSolv pretreatment methods—oven heating, oil-bath heating, and sonication-assisted—at 110 and 130 °C. Our earlier work showed that oven heating is non-isothermal, taking roughly 30 min to reach the set temperature and another 30 min to cool to room temperature, thereby hindering pretreatment efficiency [37]. As we know, the heating medium (air or oil) has a strong influence on the heat-up rate and the time needed to reach the target temperature. Sonication can also raise the solvent temperature, especially near the probe tip [408]. Tracking the temperature profiles of reaction mixtures is therefore essential for understanding the mechanisms behind each pretreatment method.

Figure 3.3 a presents the temperature profiles for oil-bath heating and sonication (60% amplitude) during the ionoSolv pretreatment of *Miscanthus* at 110 °C. The oil-bath heating method reached the setpoint from room temperature in 15 min, cutting the heat-up time in half compared with the oven heating method, because silicone oil conducts heat much better than air. Cooling in ambient air still required about 30 min. Sonication produced an uneven temperature field. The profile at the tube bottom, far from the probe tip, showed almost no ultrasonic heating and followed the oil-bath curve, whereas the profile closer to the tip was 14–15 °C higher. The gradient stems from localized heating by acoustic cavitation near the probe tip and slower heat dissipation to more distant regions [333, 409]. Despite this difference, both areas reached 110 °C in 15 min, and cooling again took roughly 30 min.

Similar behavior was observed at 130 °C (Figure 3.3 b). Heating and cooling times were 15 and 30 min, respectively, for both the oil-bath and sonication runs. With 60% amplitude, the region near the probe tip was 13–15 °C higher than the bottom area. Increasing the amplitude to 80% supplied more acoustic energy but still left the bottom profile unchanged, confirming that ultrasound-induced heating remained localized.

Near the probe tip, the higher amplitude caused pronounced temperature fluctuations: an initial rise to 146–147 °C during 0.25–0.75 h (about 4–5 °C above the 60% case), a drop to 131–133 °C between 0.75 and 1.5 h, likely due to a short-term shutdown of the ultrasound generator triggered by excessive heat accumulation at the probe tip, and a subsequent rise afterward. A parallel experiment with spruce at 80% amplitude (Figure 3.3 c) showed a similar mid-run temperature dip during 1.25–1.6 h near the probe tip, indicating that transient generator shutdowns at higher amplitudes were common across feedstocks and may signal reduced ultrasonic effectiveness during the middle stage of pretreatment.

In summary, oil-bath heating cut the heat-up time from 30 to 15 min compared with oven heating, whereas sonication produced a non-uniform temperature field, with the highest temperature near the probe tip and the lowest temperature farther away.

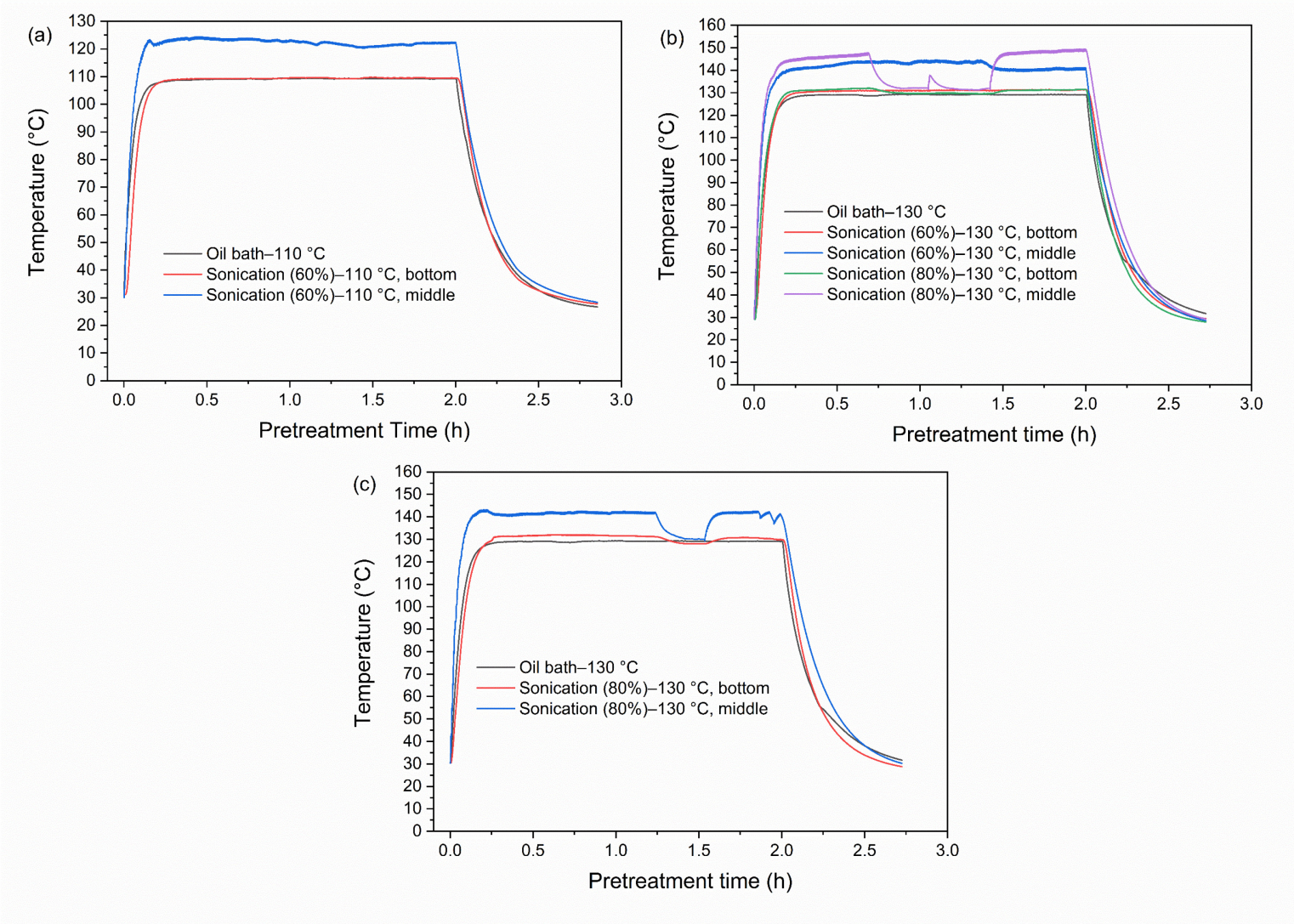


Figure 3.3. Temperature profiles of the reaction mixtures during the oil-bath heating and sonication-assisted ionoSolv pretreatment. “Sonication (60%)” and “Sonication (80%)” denote sonication amplitudes of 60% and 80%, respectively. (a) *Miscanthus*, 110 °C; (b) *Miscanthus*, 130 °C; and (c) Spruce, 130 °C.

3.3.2 Effects of Different IonoSolv Processes on Grass Biomass Fractionation

Directly comparing oven heating with sonication-assisted ionoSolv would simultaneously introduce two variables: the change in the heating medium (air versus silicone oil) and the presence of ultrasound. To maintain single-variable control, we added the oil-bath heating ionoSolv process. Thus, the oven-versus-oil-bath comparison isolates the effect of the heating medium, while the oil-bath-versus-

sonication comparison isolates the effect of ultrasound. Notably, every instance of "sonication" discussed in Sections 3.3.2.1–3.3.2.4 refers to sonication carried out at 60% amplitude. All three methods fractionated the biomass into two solid streams: a cellulose-rich pulp and precipitated lignin.

3.3.2.1 Recovery of *Miscanthus* Pulp

The cellulose-rich pulp is the undissolved fraction recovered after pretreatment. Figure 3.4 shows pulp yields for the three ionoSolv processes. Yields fell steadily as the pretreatment time increased from 0.25 to 2 h at both 110 and 130 °C, indicating that more *Miscanthus* dissolved into [DMBA][HSO_4] over time. At every time point, runs at 130 °C gave lower yields than those at 110 °C, confirming that the higher temperature accelerated hemicellulose and lignin removal, consistent with earlier findings [37].

At both 110 and 130 °C, oil-bath heating produced lower pulp yields than oven heating during the first 0.25–0.5 h, but the gap narrowed after 1–2 h. The temperature profile data can explain this phenomenon. The oven needed about 0.5 h to reach the setpoint, whereas the oil bath needed only 0.25 h. Therefore, the biomass in the oil bath experienced a higher average temperature early on and dissolved faster. Once both methods reached the target temperature, the difference diminished.

Sonication consistently gave lower pulp yields than oil-bath heating, confirming that cavitation promoted more extensive biomass dissolution by disrupting cell walls, raising local temperatures, and improving mass transfer [334, 340]. The yield gap was larger at 110 °C (9.6–4.0%) than at 130 °C (5.8–3.5%), indicating greater sonication effectiveness at the lower temperature. The milder temperature better preserved the biomass structure, allowing cavitation to play a greater role in breaking it down. The yield gap was also more obvious during the early stage of pretreatment (0.25–1 h) and narrowed when the reaction time was extended to 2 h, suggesting that the acceleration effect of sonication on *Miscanthus* dissolution weakened over time, likely due to the reduced availability of hemicellulose and lignin. This trend matches our earlier work on

Miscanthus pretreatment with [TEA][HSO_4] at 120 °C, where biomass dissolution progressively slowed down over time, with minimal changes in pulp yield and composition after 8 h [19].

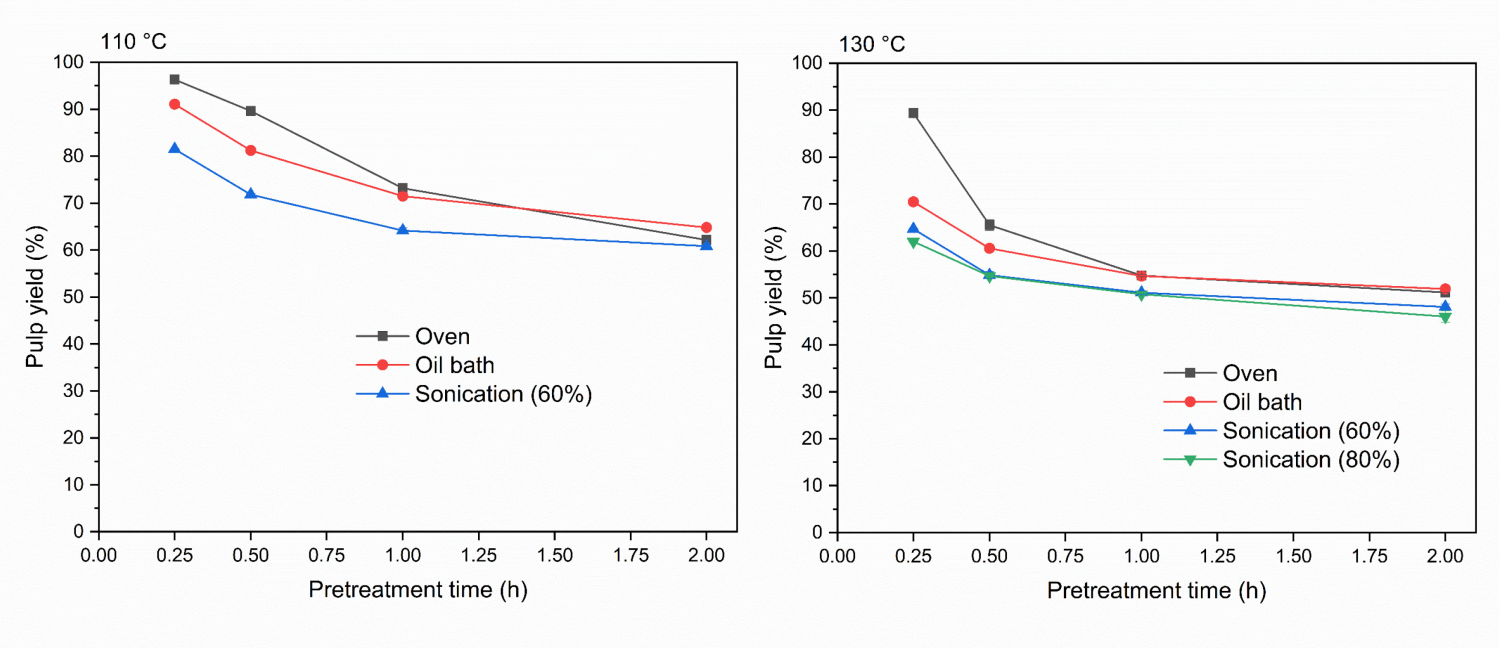


Figure 3.4. Pulp yields after *Miscanthus* pretreatment with 80 wt% [DMBA][HSO_4] and 20 wt% water at a biomass-to-solvent ratio of 1:10 (g/g).

3.3.2.2 Compositional Analysis of *Miscanthus* Pulp

Figure 3.5 shows the composition of raw *Miscanthus* and the corresponding pulps. Not surprisingly, the data indicated that pretreatment with [DMBA][HSO_4] dissolved much of the lignin and hemicellulose, which accounted for the observed mass loss, while the cellulose remained basically unchanged and showed little hydrolysis.

The effects of different pretreatment conditions are summarized in Figure 3.6 through three key fractionation metrics: glucan recovery, hemicellulose removal, and delignification. At 110 °C, glucan recovery remained above 90% for all ionoSolv processes up to 2 h, indicating minimal cellulose degradation. Raising the temperature to 130 °C reduced glucan recovery slightly to 84–96%, because the higher temperature disrupted crystalline cellulose and produced more hydrolyzable amorphous cellulose

[37, 410, 411]. Sonication at 130 °C slightly reduced glucan recovery compared with the oil-bath method, indicating that ultrasound induced additional cellulose degradation. Hemicellulose removal and delignification occurred rapidly in the first hour at both temperatures but slowed over time. The oil-bath method achieved higher hemicellulose removal and delignification in the first 0.25–0.5 h compared with the oven method, but the difference diminished after 1–2 h because both systems had reached the target temperature. Compared with the oil bath, sonication increased hemicellulose removal and delignification at 110 °C, most noticeably within the first hour, while the effects diminished by 2 h. At 130 °C, sonication continued to improve hemicellulose removal throughout, whereas its impact on delignification was confined to the first 0.25–0.5 h and became negligible thereafter. These results suggest that sonication accelerated *Miscanthus* fractionation mainly during the early stage (first hour) of pretreatment, when the cell wall polymers were still largely intact and thus offered greater scope for cavitation-driven enhancement. Further extending the reaction time resulted in only marginal improvement, allowing the oil-bath method to catch up with the performance of sonication rapidly.

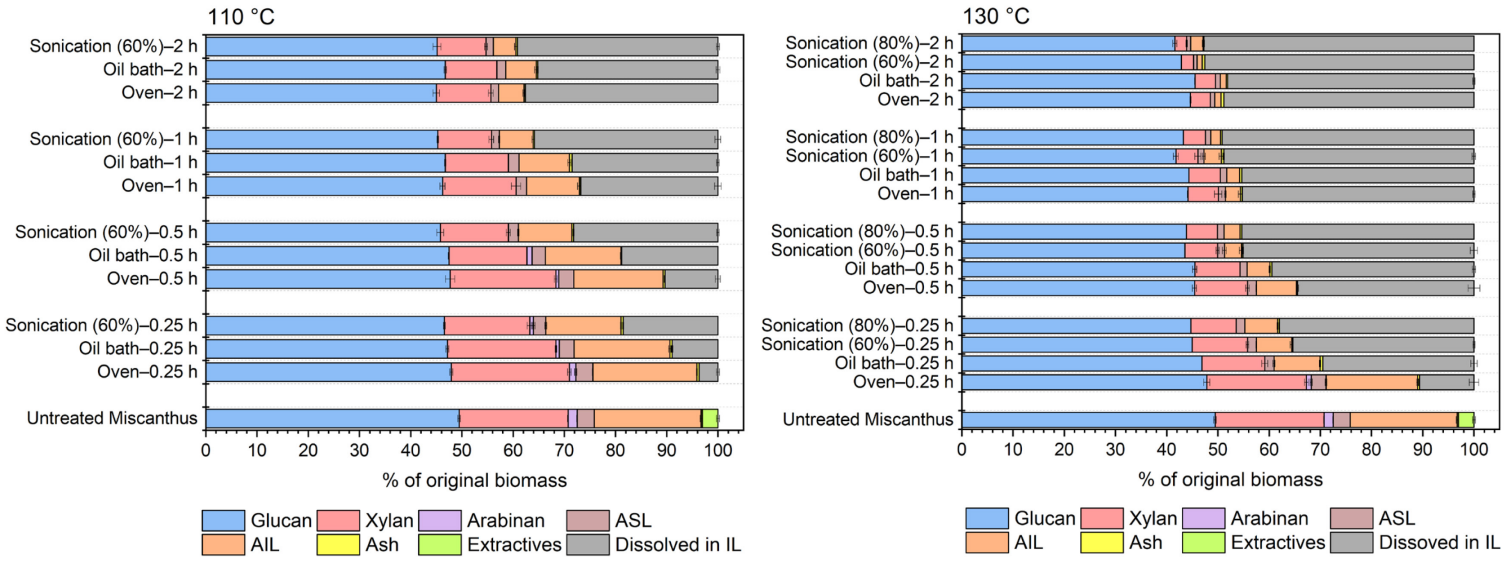


Figure 3.5. Compositional analysis of *Miscanthus* pulps recovered after pretreatment with 80 wt% [DMBA][HSO_4] and 20 wt% water at a biomass-to-solvent ratio of 1:10 (g/g) and different times.

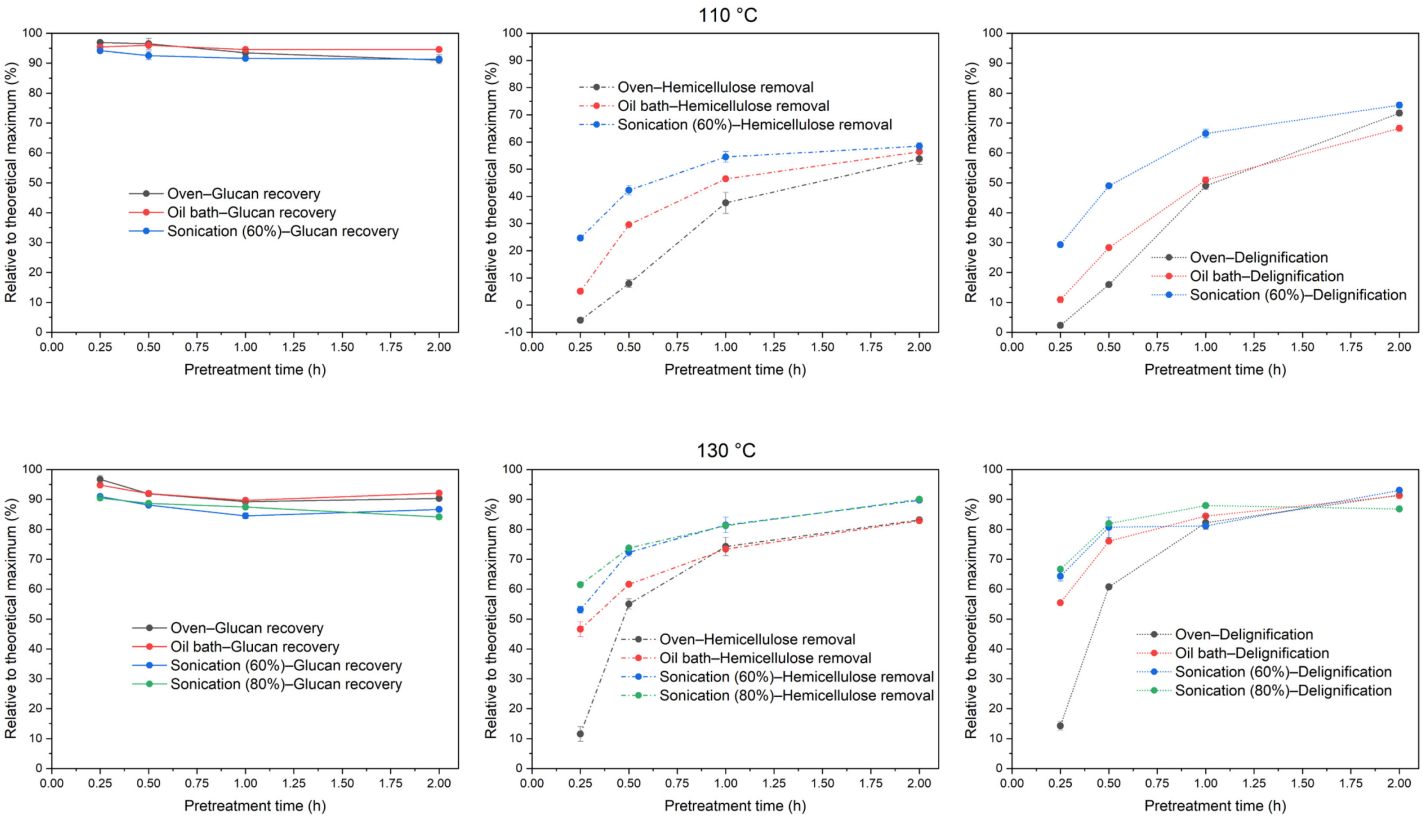


Figure 3.6. Key indicators of fractionation effectiveness for ionoSolv pretreatment of *Miscanthus* with 80 wt% [DMBA][HSO_4] and 20 wt% water at a biomass-to-solvent ratio of 1:10 (g/g).

3.3.2.3 Correlation Between Precipitated Lignin Yield and Pulp Delignification (*Miscanthus*)

At 110 °C, lignin yields from pretreatment using the oven, oil-bath, and sonication methods increased from 8.4%, 11.4%, and 27.1% at 0.25 h to 64.5%, 59.3%, and 65.6% at 2 h, respectively (Figure 3.7). Lignin yields were positively correlated with pulp delignification but were generally lower than the corresponding delignification values (except for the oven method at 0.25 and 0.5 h and the oil-bath method at 0.25 h). This discrepancy was likely caused by certain water-soluble lignin fractions forming colloidal suspensions during water washing, which were not precipitated or separated and remained in the IL even after multiple centrifugations [16]. At the higher temperature of 130 °C, increased delignification led to correspondingly higher lignin yields. However,

as with the 110 °C results, lignin yields were generally lower than their corresponding delignification values, except for the oven method at 0.25 h.

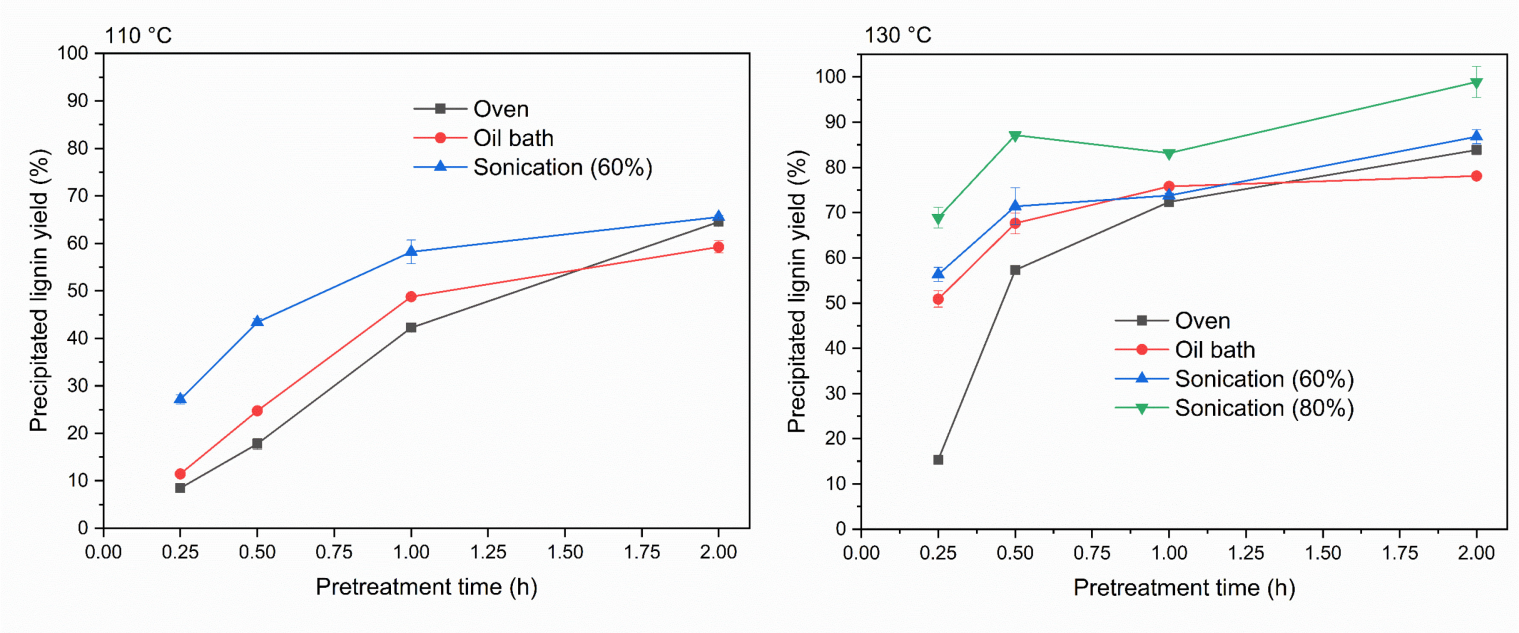


Figure 3.7. Precipitated lignin yields after *Miscanthus* pretreatment with 80 wt% [DMBA][HSO_4] and 20 wt% water at a biomass-to-solvent ratio of 1:10 (g/g) at 110 °C (left) and 130 °C (right).

3.3.2.4 Enzymatic Hydrolysis of *Miscanthus* Pulp

Saccharification yield, the ratio of glucose released from the pulp to the glucan in the raw biomass, is often selected as a primary indicator of pretreatment effectiveness [19]. Additionally, glucan digestibility, the ratio of glucose released to the glucan remaining in the pulp, reflects the quality of the pulp. Both metrics are shown in Figure 3.8.

Untreated *Miscanthus* had a saccharification yield of 4.5%, confirming that lignin blocked enzyme access to cellulose. At 110 °C, the saccharification yield increased with pretreatment time for all three methods, because longer exposure removed more lignin and eased enzymatic hydrolysis. Our previous research supports this observation, showing a positive correlation between delignification and saccharification yield [19]. From 0.25 to 1 h, the oil bath outperformed the oven owing

to better heat transfer, while sonication exceeded the oil bath, benefiting from cavitation. However, by 2 h, these differences had nearly disappeared, and all three methods converged on yields of 55.5–58.6%. Higher saccharification yield correlated with increased glucan digestibility. Across all reaction times, sonication gave the highest glucan digestibility, achieving 54.4% at 1 h (15.2% above the oil bath) and even matching the oil bath's 58.8% at 2 h.

Raising the temperature to 130 °C improved saccharification, with sonication providing the fastest early gains. From 0.25 to 1 h, its yield climbed ahead of the oil-bath and oven methods. Sonication, however, entered an "overtreatment" stage sooner: by 2 h, its saccharification yield was 83.1%, slightly below the oil-bath (87.0%) and oven (85.8%) methods, owing to glucan degradation under the more severe conditions. Glucan digestibility with sonication reached 91.7% at 1 h, approaching the oil-bath value at 2 h (94.4%). However, after 2 h, ultrasound offered only marginal additional benefit, and all three methods achieved comparable digestibility (94.4–95.8%), indicating similar pulp quality for enzymatic hydrolysis. Thus, sonication shortens the time required for high glucose release but must be carefully controlled to prevent "overtreatment".

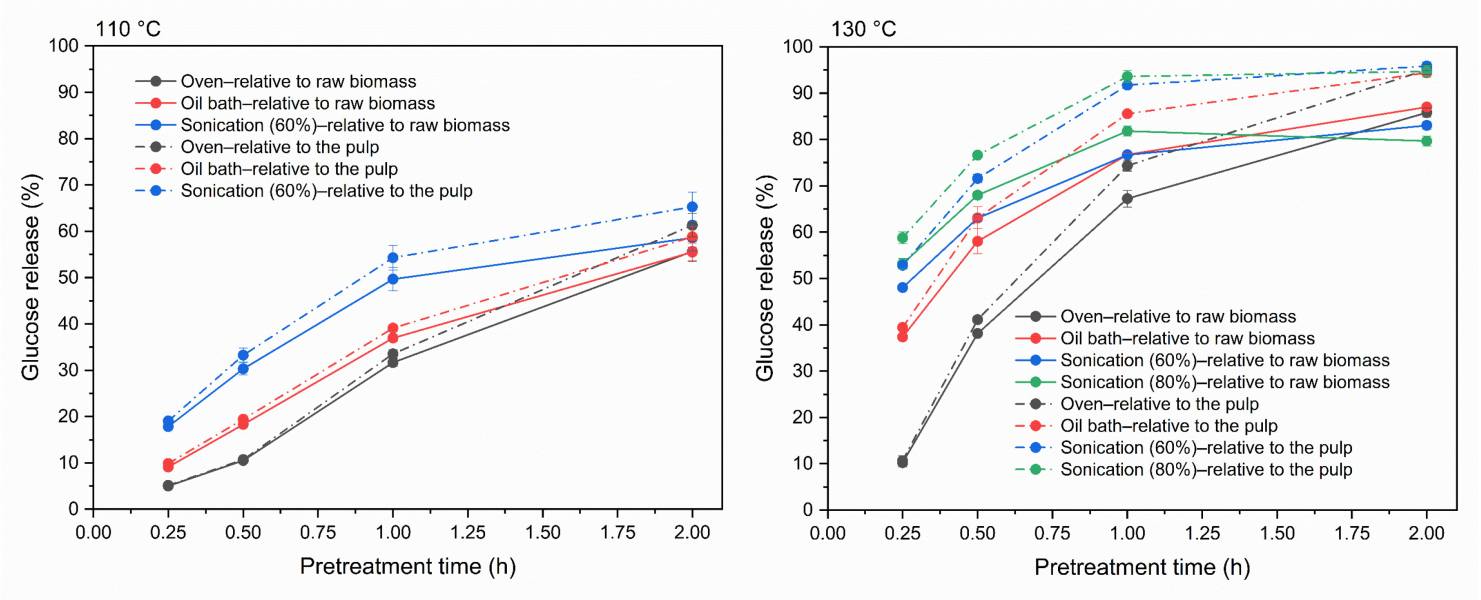


Figure 3.8. Glucose release after 7 days of enzymatic saccharification of *Miscanthus*

pulps obtained following pretreatment with 80 wt% [DMBA][HSO_4] and 20 wt% water at a biomass-to-solvent ratio of 1:10 (g/g).

3.3.2.5 Effect of Probe Amplitude on *Miscanthus* Fractionation

Probe amplitude is the maximum displacement of the probe tip during each oscillation. Higher amplitudes transmit more energy and intensify both the mechanical and thermal disruption of biomass. Temperature profile data showed that an 80% amplitude raised the medium temperature near the probe tip by roughly 4–5 °C compared with a 60% amplitude, making it necessary to examine how amplitude affects *Miscanthus* fractionation.

Sonication-assisted ionoSolv at 80% amplitude was conducted at 130 °C for 0.25–2 h (see Figures 3.4–3.8). At 0.25 h, the higher amplitude produced slightly greater biomass dissolution than the 60% amplitude, but this difference disappeared by 0.5 h. Glucan recovery at 80% amplitude remained steady (84.1–90.4%), indicating that the additional energy input did not accelerate cellulose degradation. Hemicellulose removal followed a similar trend to pulp yield. It was initially faster at 80% amplitude, but the rates at 60% and 80% amplitudes became similar after 0.5 h. Delignification at 80% amplitude reached 88.0% at 1 h and declined to 86.8% at 2 h, whereas delignification at 60% amplitude rose continuously to 93.0%. The decline at 80% amplitude is consistent with pseudo-lignin formation, in which lignin fragments and carbohydrate degradation products (e.g., 5-HMF and furfural) condense and deposit on the pulp surface [16, 19, 37]. The significantly higher precipitated lignin yield (98.9%) compared with its corresponding delignification value (86.8%) at 2 h further supports this interpretation. Additionally, although delignification at 80% amplitude exceeded that at 60% amplitude by only 1.2–6.9% (except for at 2 h), the precipitated lignin yield was 9.3–15.7% higher across all reaction times, likely due to increased lignin condensation under more vigorous conditions, which facilitated easier precipitation.

The higher (80%) amplitude raised saccharification yields by 4.9–5.2% between 0.25

and 1 h, likely due to a more efficient breakdown of the cellulose–lignin matrix, enhancing enzyme accessibility. Notably, the saccharification yield peaked at 81.8% after 1 h at 80% amplitude but slightly fell to 79.7% at 2 h, below the 83.1% achieved at 60% amplitude. The drop likely stemmed from pseudo-lignin deposition and partial glucan decomposition, again emphasizing the need to strictly monitor sonication conditions to avoid “overtreatment”.

3.3.2.6 Assessment of Sonication-Induced Acceleration in *Miscanthus* Fractionation

Using saccharification yield as the criterion, we can conclude that sonication accelerates *Miscanthus* fractionation only in the early stage of pretreatment, and its benefit largely disappears by 2 h. This early boost is likely tied to the lignin composition of *Miscanthus* (a grass), whose lignin contains roughly half syringyl (S) subunits [19]. Methoxy groups at the C3 and C5 positions of these S units hinder their interunit cross-linking, rendering the lignin more amenable to extraction. Initially, sonication provides significant mechanical and thermal disruption, aiding lignin breakdown and extraction, especially under milder conditions (e.g., lower temperature). However, as pretreatment progresses, the readily extractable lignin is largely removed, and the sonication-induced acceleration wanes. By 2 h, the oil-bath run attains a similar level of delignification for this easily removed fraction, narrowing sonication’s initial advantage.

3.3.3 Effects of Different IonoSolv Processes on Softwood Fractionation

The fractionation results for *Miscanthus* showed that sonication effects were not durable for the less recalcitrant grass biomass, limiting its potential. To explore sonication performance on more recalcitrant feedstocks, spruce—a softwood whose lignin is composed primarily of guaiacyl (G) units—was chosen [36, 412]. Unlike S units, G units carry a single methoxy group at the C3 position and leave the C5 position free. This free position makes the aromatic ring more reactive and prone to C–C cross-linking during pretreatment. Therefore, the delignification of spruce is more challenging than that of grass biomass [36, 216]. Similarly, spruce was pretreated using three

methods: oven heating, oil-bath heating, and sonication-assisted ionoSolv (at 80% amplitude).

3.3.3.1 Recovery of Spruce Pulp

The spruce pulp yields from the three ionoSolv processes are shown in Figure 3.9. At 130 °C for 0.5 h, the oil-bath method produced 4.4% less pulp than oven heating, and this difference diminished over time, indicating that higher thermal conductivity affected softwood dissolution mainly in the early stage. In contrast to *Miscanthus*, spruce pulp yields after sonication remained consistently lower than those from the oil-bath method throughout the test period. The yield gap grew from 10.2% at 0.5 h to 15.7% at 2 h, then narrowed to 9.3% by 4 h. Notably, after 1 h, the sonicated pulp yield (56.4%) nearly matched the oil-bath result at 4 h (58.1%), demonstrating that sonication can efficiently and durably accelerate the dissolution of recalcitrant biomass. Between 2 and 4 h, the sonicated pulp yield stabilized at approximately 49%, indicating that spruce dissolution had reached a dynamic equilibrium. This trend is consistent with previous results for pine (softwood) fractionation using [HBim][HSO_4] at 150 °C, where the pulp yield dropped sharply up to 4 h before leveling off [36].

When the temperature was raised from 130 to 150 °C, spruce pulp yields declined markedly, although the overall trend remained unchanged. At 150 °C for 0.5 h, the oil-bath method produced 9.5% less pulp than oven heating, but the influence of the heating medium on yield had largely disappeared by 1 h. Sonication continued to significantly accelerate spruce dissolution, giving pulp yields that were 12.3% and 9.9% lower than those from the oil-bath method at 0.5 and 1 h, respectively. Notably, further extending the pretreatment time for sonication-assisted ionoSolv at 150 °C was unfeasible at the current stage, because the sonication device would overload from heat accumulation if operated for more than 1 h. Consequently, a high-temperature-resistant sonication device will be essential for future research.

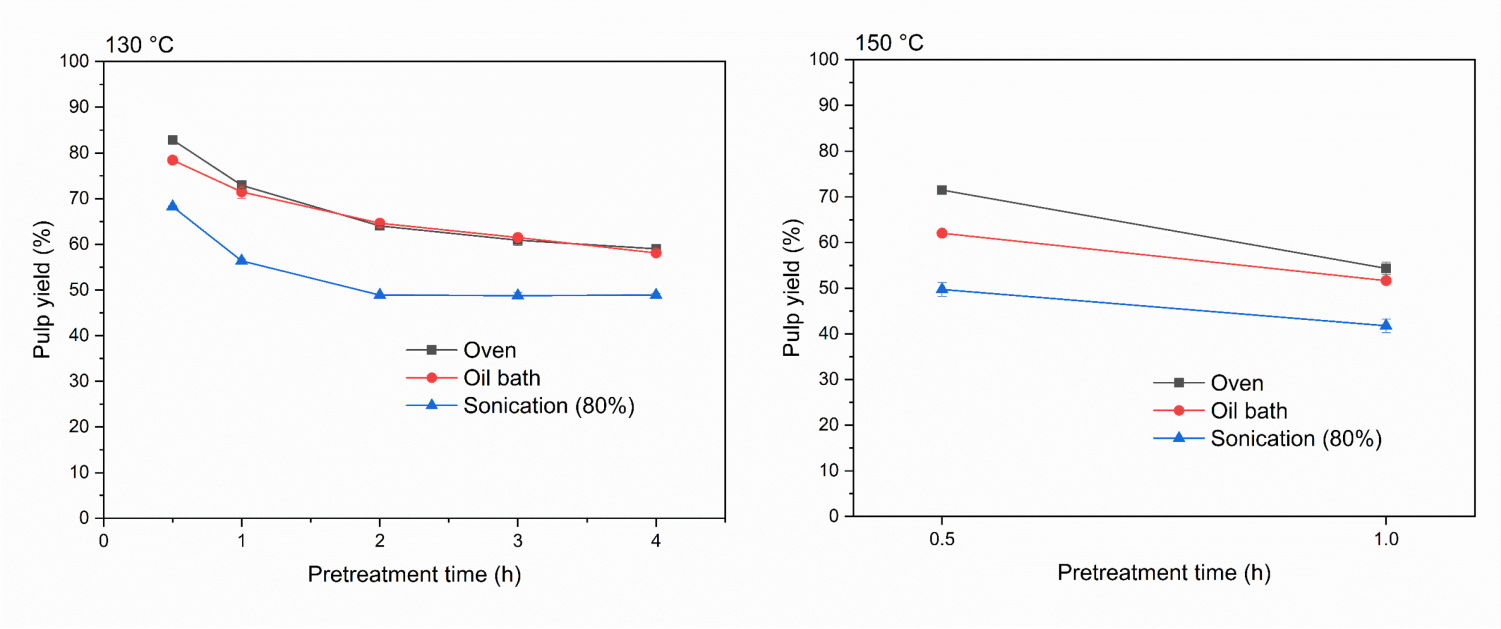


Figure 3.9. Pulp yields after spruce pretreatment with 80 wt% [DMBA][HSO_4] and 20 wt% water at a biomass-to-solvent ratio of 1:10 (g/g) at 130 °C (left) and 150 °C (right).

3.3.3.2 Compositional Analysis of Spruce Pulp

Figures 3.10–3.11 summarize the compositional analysis of raw spruce and its pulps, together with the key fractionation indicators. At 130 °C, both the oil-bath and sonication methods showed high glucan recovery initially. After 2 h, however, glucan recovery declined more sharply under sonication (79.8%) than under the oil bath (94.7%), and then stabilized for both treatments up to 4 h. This trend suggests that sonication, by generating higher average system temperatures and enhancing mass transfer, can disrupt cellulose stability and reduce glucan recovery. Sonication was also markedly more effective in hemicellulose removal and delignification across all time points. Compared with the oil bath, the improvement in hemicellulose removal due to sonication rose quickly, peaked at 30.4% at 1 h, and then sharply fell to 13.0% at 4 h. However, the greatest enhancement in delignification appeared at 2 h (19.6%), followed by a decrease to 10.2% at 4 h. This delayed peak in delignification improvement reflects the greater recalcitrance of lignin compared with hemicellulose in spruce, which requires a longer sonication time to achieve effective lignin removal.

At 150 °C, sonication caused greater glucan loss, with a recovery of 81.7–71.5% versus 96.9–93.5% for the oil-bath method. Hemicellulose removal was still more effective under sonication, reaching nearly complete removal (98.0%) at 1 h compared with 91.3% in the oil bath. Delignification also improved with sonication, although the advantage narrowed by 1 h, with sonication achieving 67.2% versus 64.7% for the oil-bath method.

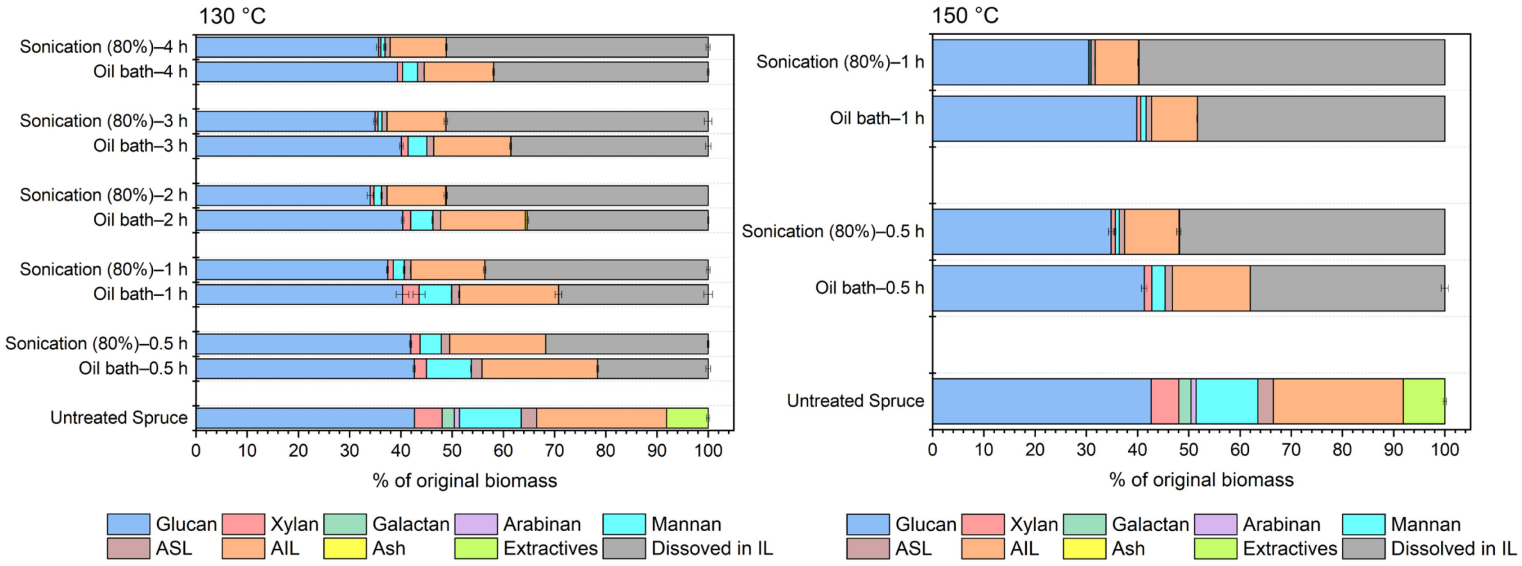


Figure 3.10. Compositional analysis of spruce pulps recovered after pretreatment with 80 wt% [DMBA][HSO_4] and 20 wt% water at a biomass-to-solvent ratio of 1:10 (g/g) for varying lengths of time at 130 °C (left) and 150 °C (right).

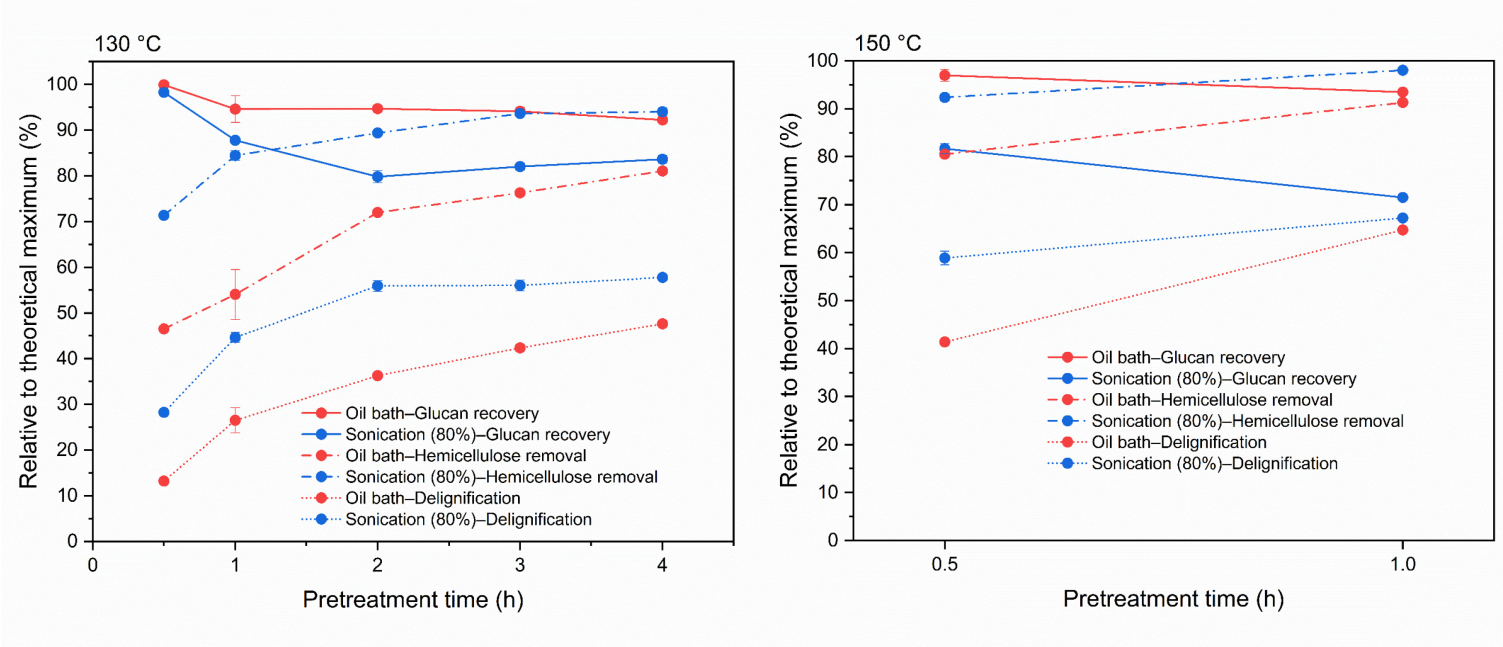


Figure 3.11. Key indicators of fractionation effectiveness for ionoSolv pretreatment of spruce with 80 wt% [DMBA][HSO_4] and 20 wt% water at a biomass-to-solvent ratio of 1:10 (g/g) for varying lengths of time at 130 °C (left) and 150 °C (right).

3.3.3.3 Correlation Between Precipitated Lignin Yield and Pulp Delignification (Spruce)

At 130 °C, precipitated lignin yields increased over time for both the oil-bath and sonication methods, from 16.1% and 30.5% to 45.4% and 83.2%, respectively (Figure 3.12). Between 1 and 4 h, oil-bath lignin yields were consistently lower than their corresponding delignification values. In contrast, sonication lignin yields exceeded their corresponding delignification values, with the discrepancy widening from 12.6% to 25.5% between 1 and 4 h. This discrepancy suggests that sonication can promote the condensation of spruce lignin with non-lignin components, such as 5-HMF and furfural derived from hemicellulose hydrolysis and dehydration, resulting in pseudo-lignin formation [19, 36, 37]. At 150 °C, pseudo-lignin formation was more pronounced under sonication. As a result, sonication lignin yields reached 68.2% and 96.6% at 0.5 and 1 h, respectively, significantly exceeding their corresponding delignification values by 9.3% and 29.4%. These gaps were notably larger than the corresponding values of

2.3% and 12.6% observed at 130 °C.

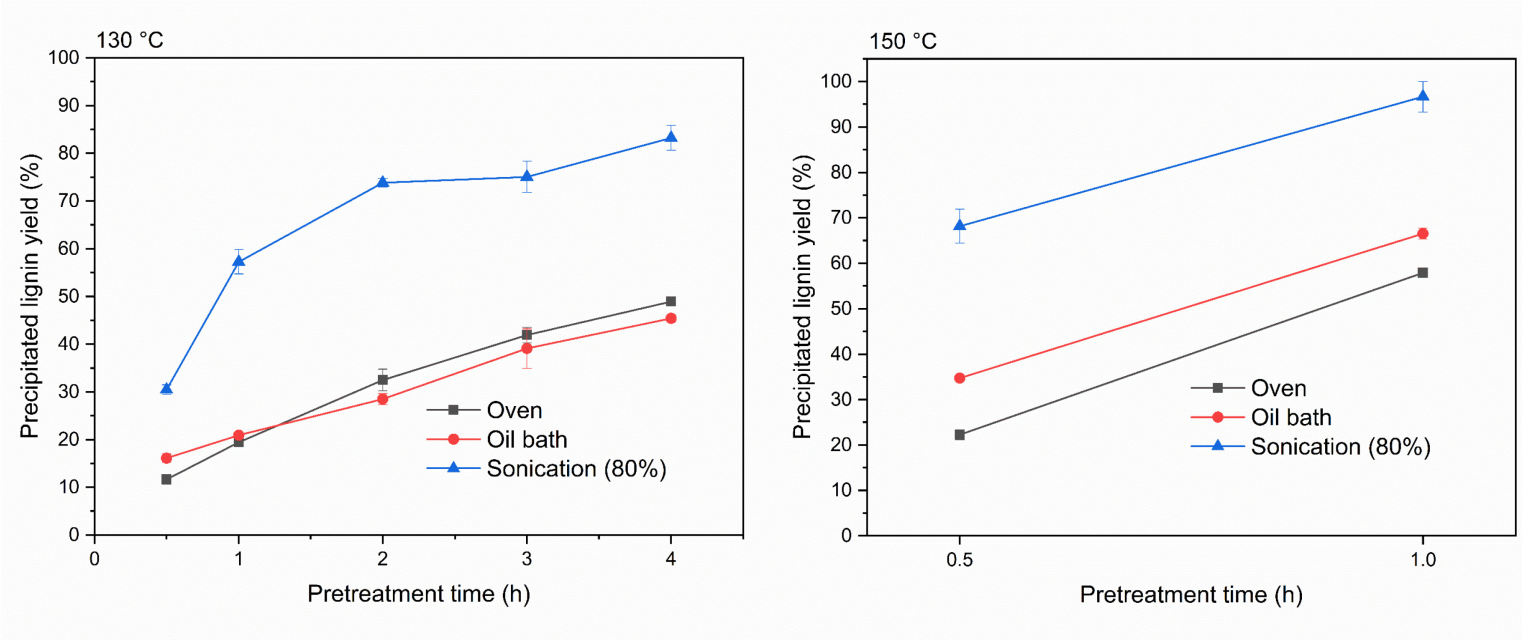


Figure 3.12. Precipitated lignin yields after spruce pretreatment with 80 wt% [DMBA][HSO_4] and 20 wt% water at a biomass-to-solvent ratio of 1:10 (g/g) at 130 °C (left) and 150 °C (right).

3.3.3.4 Enzymatic Hydrolysis of Spruce Pulp

Figure 3.13 shows the saccharification yields and glucan digestibility of spruce pulp. The saccharification yield of untreated spruce was low, at 5.8%. At 130 °C, the oven and oil-bath methods increased saccharification yields only modestly, from 5.8% and 6.1% at 0.5 h to 18.0% and 18.1% at 4 h, respectively, reflecting the challenge of enzymatically hydrolyzing softwood pulp in the presence of recalcitrant lignin. Previous work indicates that effective lignin extraction from softwood typically requires operation above the glass transition temperature of lignin (130–150 °C) [36]. In contrast, sonication delivered a 17.2% saccharification yield in just 0.5 h, equivalent to that achieved by the oil-bath method at 4 h. Yields then peaked at 47.6% after 3 h and stabilized thereafter. This demonstrates that sonication efficiently accelerates the fractionation of recalcitrant lignin even below its glass transition temperature. Glucan digestibility in the oil bath closely matched saccharification yields, suggesting that

enzymatic hydrolysis was limited by pulp accessibility. However, except for the case at 0.5 h, sonication produced significantly higher glucan digestibility than the saccharification yield, peaking at 58.1% after 3 h.

When the temperature increased from 130 to 150 °C, saccharification yields for the oven and oil-bath methods remained low, rising only to 28.8% and 36.6% after 1 h. By contrast, sonication boosted yields to 47.3% and 53.4% at 0.5 and 1 h, respectively. The acceleration effects of sonication remained evident at 150 °C. The saccharification yield of sonicated pulp at 0.5 h significantly exceeded that of the oil bath at 1 h. However, this advantage proved less durable at higher temperatures. Specifically, at 150 °C, sonication improved the saccharification yield by 33.2% over the oil bath at 0.5 h, but this gap rapidly narrowed to 16.8% by 1 h. At 130 °C, enhancements of 31.5–34.1% persisted from 1 to 3 h before slightly falling to 28.1% at 4 h, suggesting that milder pretreatment conditions maximize sonication's benefit. Similar to the results at 130 °C, sonication at 150 °C significantly enhanced glucan digestibility, reaching 74.7% at 1 h.

Using saccharification yield as the metric, it is clear that sonication's acceleration effect depends on feedstock recalcitrance: the more resistant the biomass, the greater and longer-lasting the benefit. Across all tested reaction times, conventional ionoSolv methods failed to match the saccharification yields achieved by sonication. However, glucan loss in spruce during sonication remains problematic and must be addressed in future optimizations.

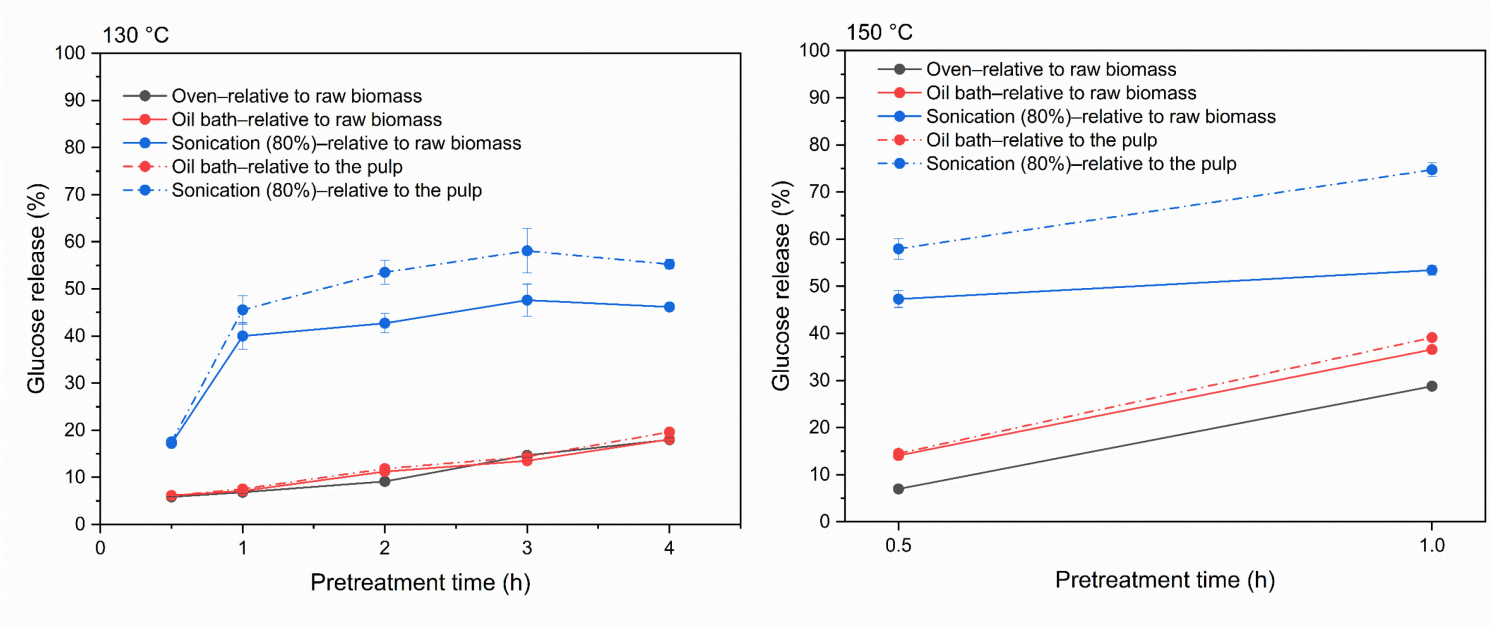


Figure 3.13. Glucose release after 7 days of enzymatic saccharification of spruce pulps obtained following pretreatment with 80 wt% [DMBA][HSO_4] and 20 wt% water at a biomass-to-solvent ratio of 1:10 (g/g).

3.3.4 Properties of the Upper (Finer) and Lower (Coarser) Pulp Layers Formed after the Sonication-Assisted IonoSolv Process

In the sonication-assisted ionoSolv process, spatially non-uniform ultrasonic energy input—evidenced by temperature gradients—produced pulp with heterogeneous particle sizes, with the greatest disruption occurring near the probe tip. This size difference was apparent after centrifugation during pulp washing, which yielded an upper, finer-particle layer and a lower, coarser-particle layer. In the earlier pulp characterization, these layers were mixed uniformly, thereby obscuring their unique properties. Therefore, in this section, each layer from *Miscanthus* and spruce pulps was analyzed separately after pretreatment at 130 °C for 2 h with 80% probe amplitude, where clear layer separation occurred. Their fiber length and surface morphology are presented in Figure 3.14. Notably, this analysis used different batches of [DMBA][HSO_4] compared with the time- and temperature-course studies. Slight differences in their acid-base ratios caused small variations in pulp and saccharification yields [19]. Even

so, the results still offer valuable insights into the unique properties of each pulp layer, enabling more targeted applications.

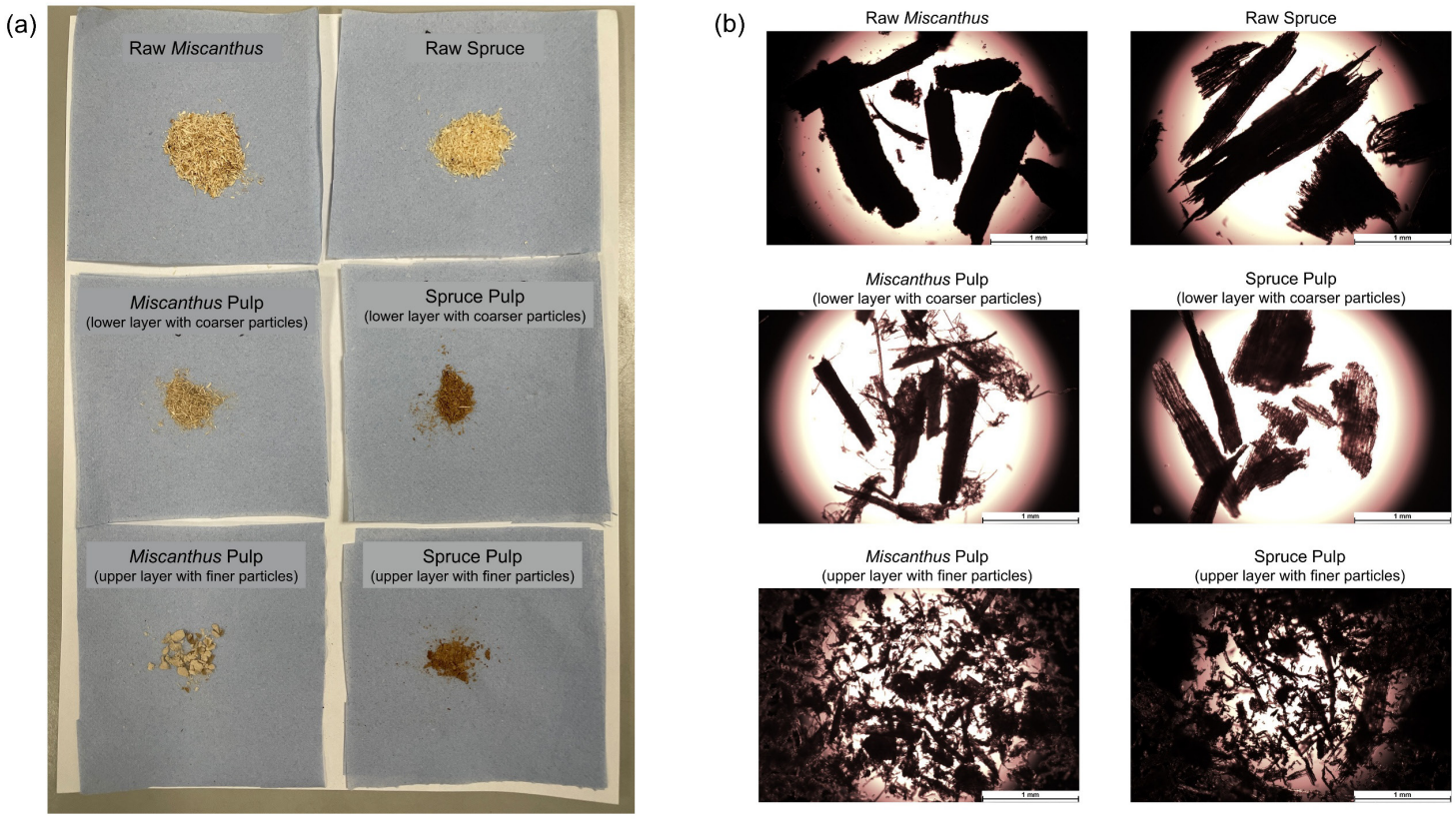


Figure 3.14. Photographs (a) and microscopy images (b) of the raw biomass and two pulp layers with different particle sizes. (For the *Miscanthus* pulp with finer particles, the material appeared powdery initially but clumped during air drying.)

The characterization of the pulp layers is summarized in Figure 3.15. For the *Miscanthus* pulp, the coarse lower layer had a higher yield of 29.9% (66.7% of the total pulp), whereas the fine upper layer had a yield of 14.9% (33.3% of the total pulp). Both layers showed comparable compositions (calculated relative to the pulp itself rather than raw *Miscanthus*). The upper layer contained slightly more cellulose and correspondingly less hemicellulose and lignin. Despite receiving more ultrasonic energy, the glucan digestibility of the upper layer (97.8%) essentially matched that of the lower layer (95.5%), indicating that both layers had reached their fractionation limit. Nevertheless, the saccharification yield (glucose release relative to raw *Miscanthus*)

of the lower layer (50.9%) was about twice that of the upper layer (26.3%), owing to its higher pulp yield.

For the spruce pulp, the coarse lower layer also had a higher yield (40.1%, 71.6% of the total pulp) than the upper layer (15.9%, 28.4% of the total pulp). Unlike *Miscanthus*, the upper spruce layer contained significantly more glucan (71.3% versus 66.0%) and less hemicellulose and lignin, indicating more effective fractionation. This efficiency was also reflected in the results of enzymatic hydrolysis. Both spruce pulp layers achieved identical saccharification yields of 18.4%, even though the upper layer had a much lower pulp yield. This was due to the higher glucan digestibility of the upper layer, with 69.5% of its cellulose hydrolyzed compared with 29.6% in the lower layer.

Overall, under the test conditions, differences between the layers in the *Miscanthus* pulp were minimal, and both layers reached their fractionation limits. In contrast, for the more recalcitrant spruce, the upper layer exhibited a glucan digestibility 2.3 times higher than that of the lower layer, suggesting that the acceleration effects of sonication mainly stemmed from the upper layer pulp. To mitigate pulp heterogeneity, reducing biomass loading or increasing sonication power could be effective strategies.

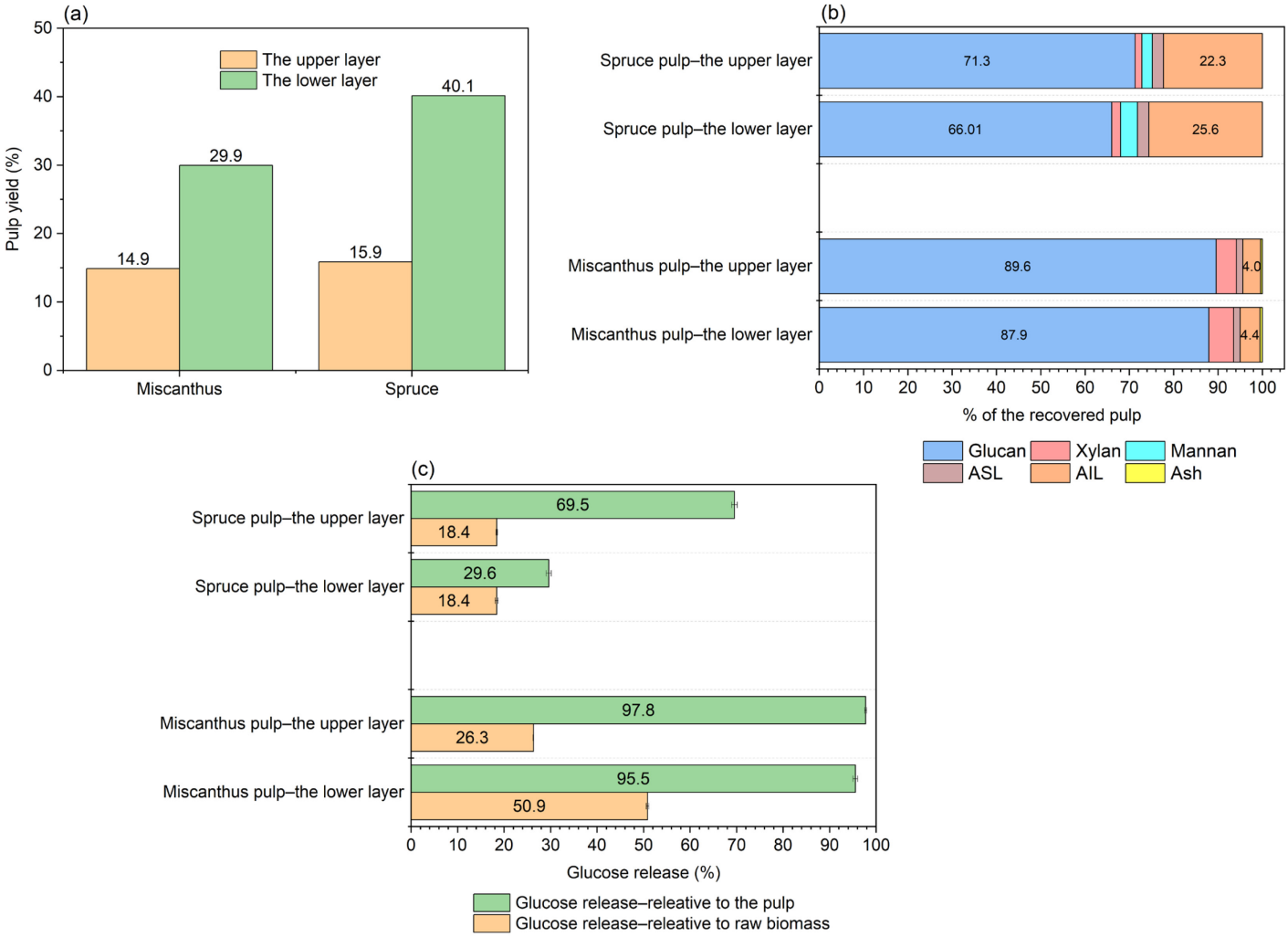


Figure 3.15. Characterization of different pulp layers. (a) Pulp yield; (b) Compositional analysis, calculated relative to the recovered pulp; and (c) Glucose release after 7 days of enzymatic saccharification.

3.3.5 Quantitative Mechanistic Analysis of the Sonication-Induced Acceleration

3.3.5.1 Quantitative Effects of Temperature Increase and Mass Transfer Enhancement on Cellulose-Rich Pulp

Localized temperature increase and enhanced mass transfer are the two main macroscopic outcomes induced by ultrasonic cavitation [334, 401, 409, 413]. To clarify the role of sonication in ionoSolv pretreatment, we separated and quantified the individual contributions of temperature and mass transfer. Because localized heating near the probe tip created an uneven temperature distribution, we estimated the

average system temperature as the mean of the highest and lowest readings. This approach is practical, particularly when temperature fluctuations are moderate.

To isolate the influence of enhanced mass transfer from that of the temperature increase, we applied sonication-assisted ionoSolv (60% amplitude) to *Miscanthus* at 103 °C (determined by trial and error), which gave an average system temperature of 110 °C (Figure 3.16 a–b). Comparing this case with the oil-bath ionoSolv at 110 °C removed the ultrasound-induced temperature effect and allowed us to assess mass transfer alone. A further comparison between sonication at 103 and 110 °C clarified the temperature effect while keeping mass transfer conditions similar. Pretreatment times were set at 0.25 and 0.5 h. Initial results (Figure 3.17) showed that pulp yields from sonication at 103 °C were only slightly lower than those from the oil bath at 110 °C, indicating a limited mass transfer impact on *Miscanthus* dissolution. Compositional analysis confirmed this, with a significant difference observed only in hemicellulose removal at 0.25 h. Regarding enzymatic hydrolysis, glucose release remained largely unchanged at 0.25 h but showed modest improvements at 0.5 h due to mass transfer enhancement, with increases of 3.2% (relative to pulp) and 3.6% (relative to biomass). In contrast, the temperature increase had a more pronounced effect. Sonication at 110 °C (average system temperature of 116–117 °C) significantly improved *Miscanthus* dissolution, hemicellulose removal, delignification, and glucose release compared with sonication at 103 °C. Saccharification yield was chosen as the metric for quantifying the effects of these two sonication-induced factors on *Miscanthus* fractionation. At 0.25 h, mass transfer enhancement accounted for only 10.2% of the total sonication effect, whereas the temperature increase contributed 89.8%. By 0.5 h, the contribution of mass transfer rose to 26.5%, and the temperature contribution decreased to 73.5%. These findings confirm that, in the sonication-assisted ionoSolv process, it is the temperature increase, rather than enhanced mass transfer, that primarily drives *Miscanthus* fractionation.

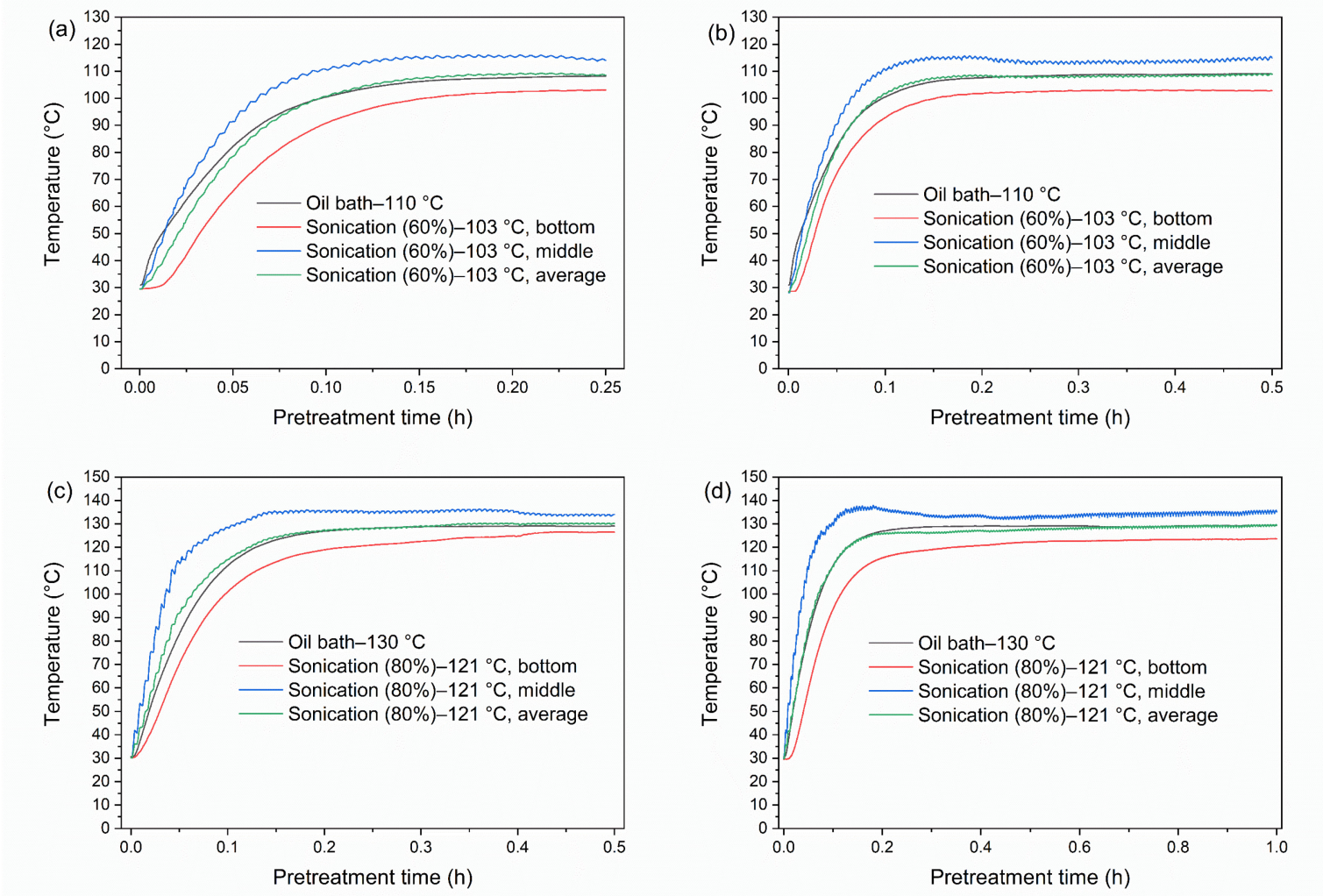


Figure 3.16. Temperature profiles of the reaction medium during oil-bath heating and sonication-assisted ionoSolv processes. (a) *Miscanthus*: 110 °C oil bath versus 103 °C sonication for 0.25 h; (b) *Miscanthus*: 110 °C oil bath versus 103 °C sonication for 0.5 h; (c) Spruce: 130 °C oil bath versus 121 °C sonication for 0.5 h; and (d) Spruce: 130 °C oil bath versus 121 °C sonication for 1 h.

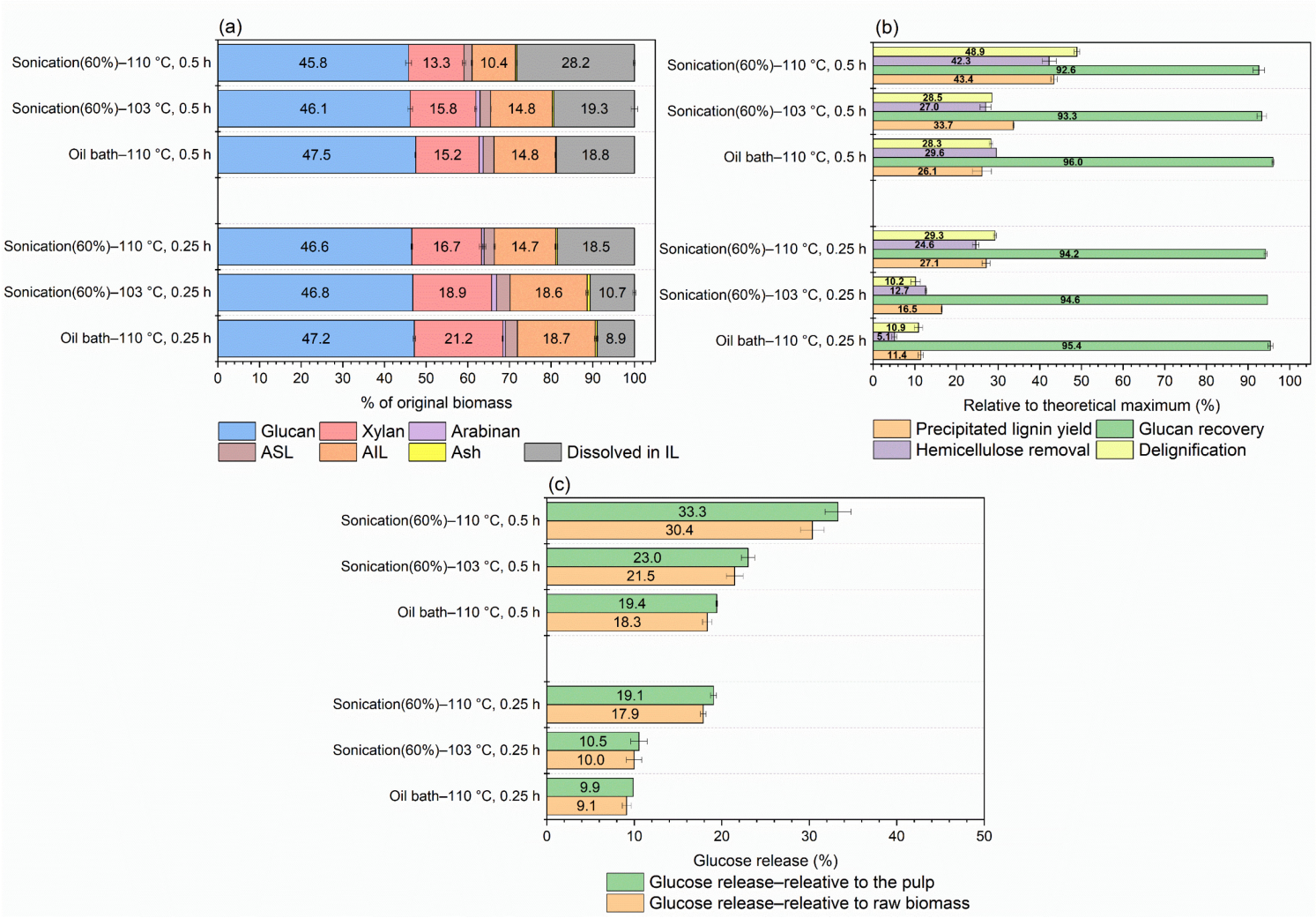


Figure 3.17. Characterization of *Miscanthus* pulps from different pretreatment conditions used for sonication mechanism exploration. (a) Compositional analysis; (b) Key indicators of fractionation effectiveness; and (c) Glucose release after 7 days of enzymatic saccharification.

For spruce, to isolate the impact of the temperature increase, sonication-assisted ionoSolv (80% amplitude) was conducted at 121 °C, giving an average system temperature of 130 °C (Figure 3.16 c–d). The effect of enhanced mass transfer was assessed by comparing sonication at 121 °C with the oil-bath ionoSolv at 130 °C, while the impact of the temperature increase was evaluated by comparing sonication at 121 and 130 °C. Pretreatment times were set at 0.5 and 1 h. Compositional results (Figure 3.18) showed that mass transfer enhancement had minimal influence on spruce dissolution, resulting in negligible changes in pulp yield. In contrast, the temperature

increase was the main driver, lowering yields by 7.8% and 15.4% at 0.5 and 1 h, respectively. Both factors promoted hemicellulose removal, but only the temperature increase significantly affected lignin removal. Using the saccharification yield as the metric, we found that at 0.5 h, enhanced mass transfer accounted for 27.8% of the change, while the temperature increase contributed 72.2%. At 1 h, the mass transfer share rose to 38.7%, while the temperature share fell to 61.3%. Thus, although the influence of enhanced mass transfer grew over time, the temperature increase remained the dominant factor driving the effectiveness of sonication in accelerating the spruce ionoSolv process.

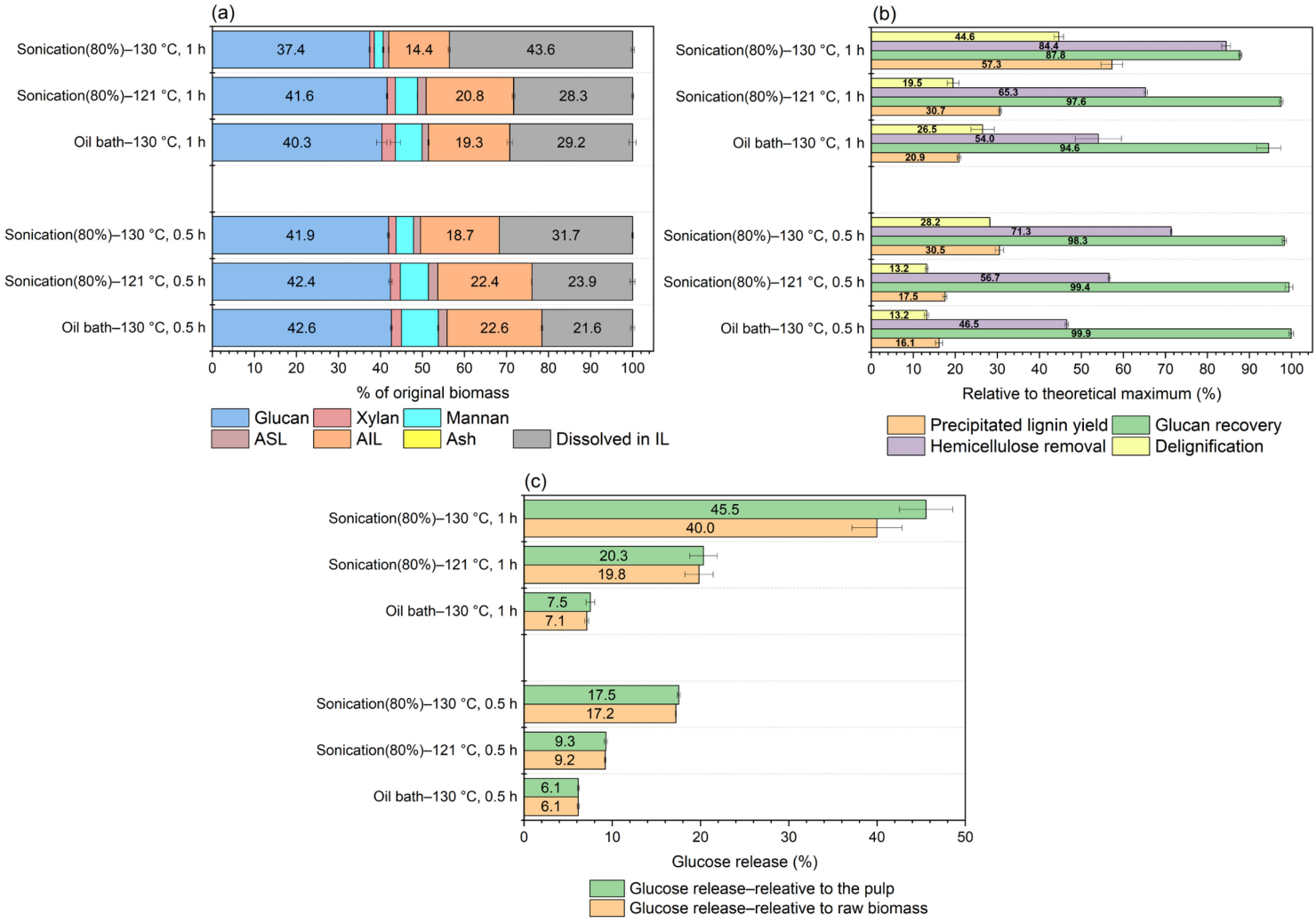


Figure 3.18. Characterization of spruce pulps from different pretreatment conditions used for sonication mechanism exploration. (a) Compositional analysis; (b) Key indicators of fractionation effectiveness; and (c) Glucose release after 7 days of

enzymatic saccharification.

3.3.5.2 Quantitative Effects of Temperature Increase and Mass Transfer Enhancement on Precipitated Lignin

Enhanced mass transfer had a more pronounced effect on *Miscanthus*-derived precipitated lignin than on the pulp itself, yet the temperature increase remained dominant, accounting for 67.5% and 56.1% of the total lignin yield increase at 0.25 and 0.5 h, respectively. These findings align with those of Chambon et al., who reported that increasing stirring speed (mass transfer) slightly reduced pulp yield but markedly increased precipitated lignin yield during [TEA][HSO_4] fractionation of *Miscanthus* in a 100-fold scale-up ionoSolv process [42]. For spruce, mass transfer had little impact on lignin yield at 0.5 h, while the temperature accounted for 90.3% of the total yield increase. By 1 h, the growing influence of mass transfer reduced the temperature contribution to 73.2%.

To further assess the structural changes in lignin caused by sonication, 2D ^{1}H–^{13}C HSQC NMR spectroscopy was employed to analyze major linkages and subunits in precipitated lignin. According to Figure 3.19, the primary linkages in *Miscanthus* lignin were β-O-4′ ether (A), β-β′ resinol (B), and β-5′ phenylcoumaran (C), while the main subunits were guaiacyl (G_2, G_5, and G_6), syringyl ($S_{2,6}$), ferulic acid (FA_β), and *p*-coumaric acid ($PCA_{2,6}$, $PCA_{3,5}$, and PCA_β). In contrast, spruce lignin contained similar linkages but was predominantly composed of G units (G_2, G_5, G_6, and G_2cond.). The chemical structures of these linkages and subunits are provided in our previous work [19]. To estimate the abundance of these linkages and subunits, a semi-quantitative analysis was carried out using peak volume integration. Figure 3.20 displays all signal intensities as percentages relative to the sum of the G_2 and G_2cond. integrals, which are believed to remain stable for lignin recovered from various pretreatment conditions [16, 19]. While this method provides a comparative framework, it is important to note that the inherent uncertainty in NMR peak integration, arising from signal overlap and baseline noise, may influence the calculated values. For *Miscanthus* lignin, the signal

intensities of linkages and subunits remained basically unchanged under all conditions (except for β-O-4′), indicating no significant structural modifications, likely because the pretreatment was mild. For spruce lignin, both sonication-induced mass transfer and temperature increase promoted ether bond cleavage and G unit condensation, decreasing the intensities of β-O-4′, G_2 and G_6 while increasing that of G_2cond. Notably, the sonication-induced temperature increase had a more pronounced impact on these structural changes.

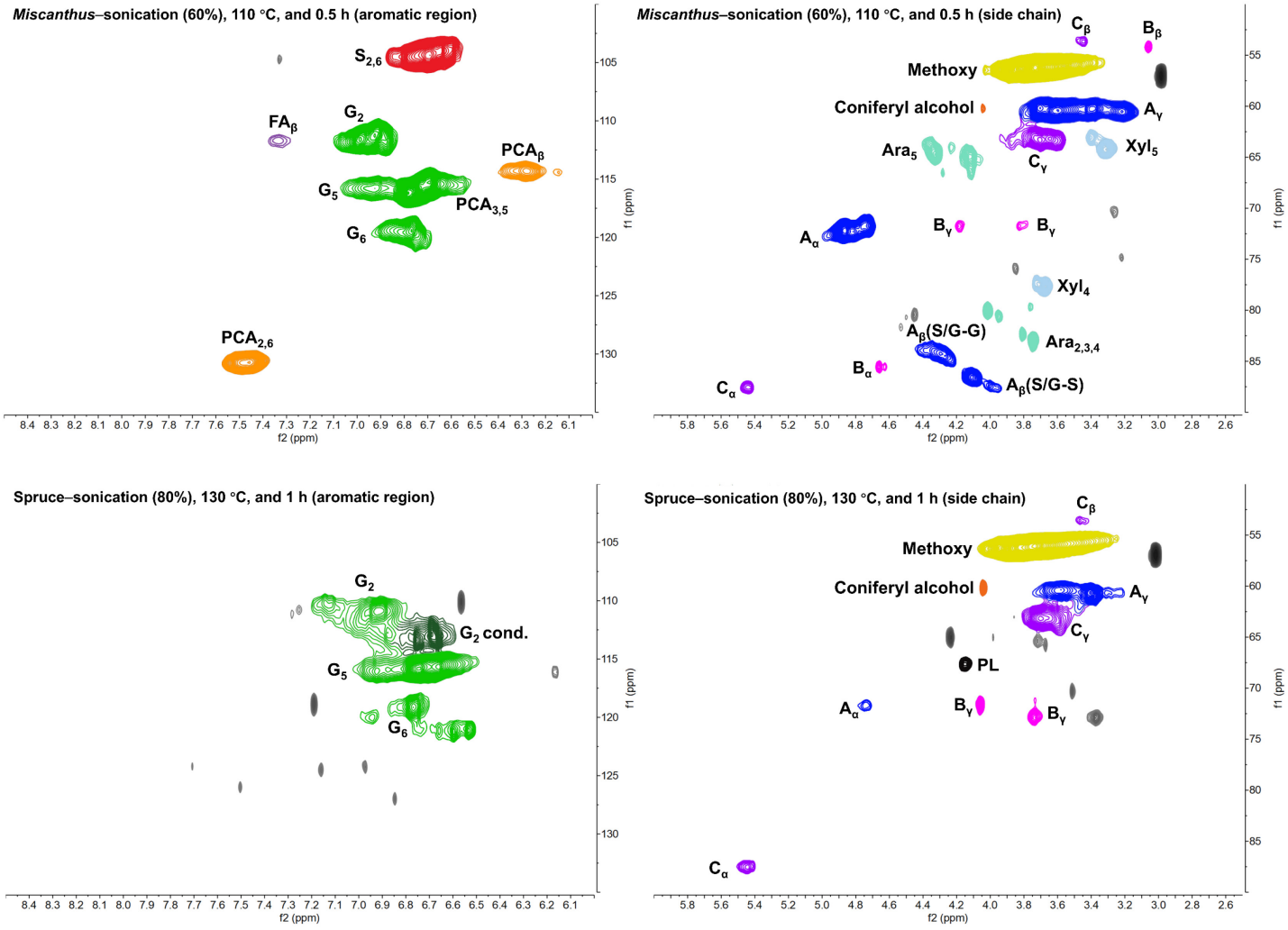


Figure 3.19. HSQC NMR spectra of *Miscanthus* and spruce lignin isolated after the sonication-assisted ionoSolv process. “Ara” and “Xyl” refer to arabinose and xylose, respectively. “PL” refers to a plasticizer and could be attributed to leaching from the O-ring seals in the pressure tubes during the ionoSolv process [19].

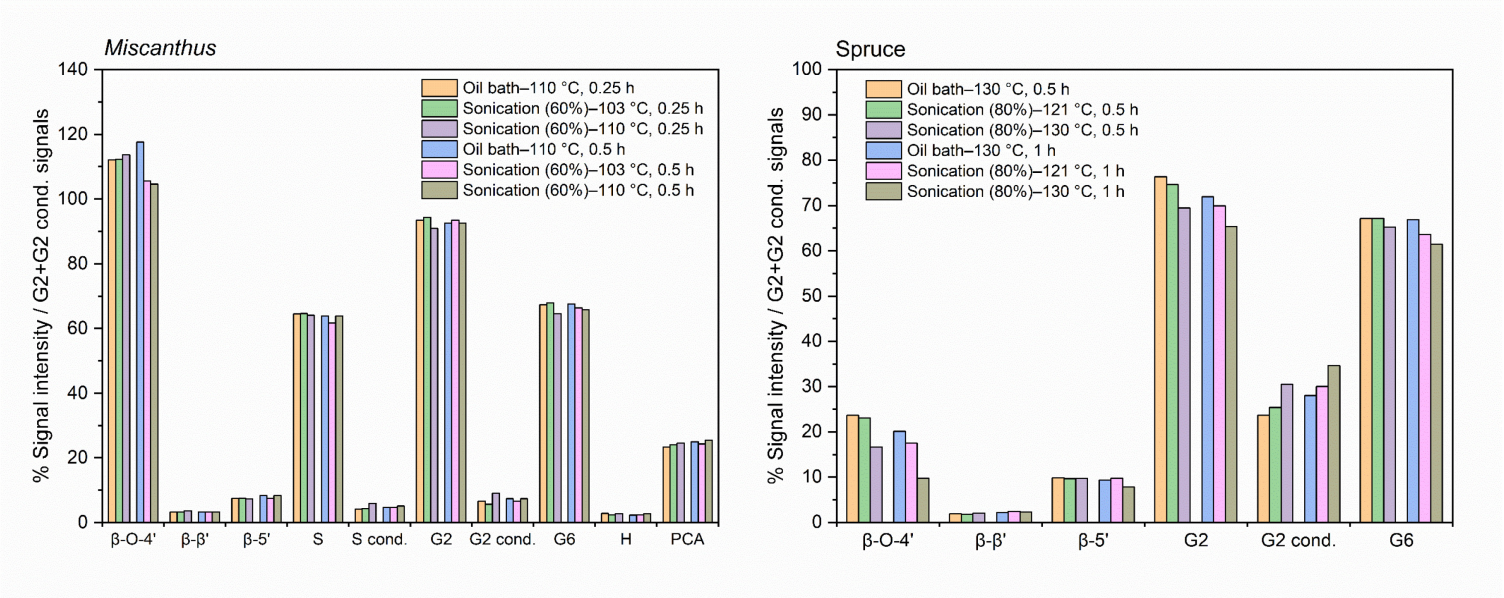


Figure 3.20. Abundance of major linkages and subunits in *Miscanthus* and spruce lignin isolated after different ionoSolv processes.

3.3.6 Preliminary Techno-Economic Analysis

A preliminary techno-economic analysis was conducted to assess the combined PIL pretreatment and sonication process, covering the process boundary from the biomass feedstock to ethanol production. Figure 3.21 presents a potential industrial flow scheme. Table 3.1 lists the prices used for the various feedstocks, utilities, and products. A recycling rate of 99% was assumed for [DMBA][HSO_4] based on our previous work [19]. Water was also recycled through the process with minimal losses. Heat integration was performed for the IL regeneration system, which utilized a multi-effect evaporator. Based on the experimentally measured saccharification yield, the ethanol yield from fermentation was calculated using a stoichiometric maximum of 0.51 g of ethanol per g of glucose equivalent [414]. Table 3.2 summarizes the costing methodology for each unit. For the ultrasonication unit, there are very few such units that exist for the scale considered. Khanpit et al. previously considered a similar ultrasonication unit for their process based on one of the few industrial-scale examples [415]. Due to the limited availability of such data, the cost from that study was also adopted here. The parameters employed for the capital and fixed operating cost

calculations follow the methodology outlined in our previous work (Appendices, Tables S3–S4) [416]. A plant operating lifetime of 20 years and a discount rate of 10% were assumed when annualizing the capital expenditure (CAPEX). Initially, all scenarios considered a biomass processing capacity of 1,000 tons per year (125 kg h^{-1}), assuming the plant operated for 8,000 hours annually.

Four scenarios were selected based on the experimental results, representing suitable pretreatment conditions at 130 °C for *Miscanthus* or spruce under either conventional or sonication-assisted ionoSolv processes. Figure 3.22 shows the results of the techno-economic analysis. Spruce-derived ethanol was estimated to be more expensive than *Miscanthus*-derived ethanol due to the much lower glucose release of spruce pulp after saccharification, along with a slightly higher feedstock cost. The effect of sonication on *Miscanthus* was minimal, with a slightly higher minimum selling price (MSP) arising from the capital-intensive sonication system and higher electricity consumption. The saccharification yield was also relatively unaffected in the case of *Miscanthus*, suggesting that sonication was not needed for boosting ethanol production in this case. For spruce, however, there was a significant reduction in the MSP of nearly 50%. Although both the CAPEX and operating expenditure (OPEX) were higher for the sonication case, the saccharification yield was nearly boosted threefold. This suggests that the sonication method is promising for more recalcitrant feedstocks, such as softwood.

Notably, in the spruce ionoSolv case above, we implicitly assumed that, at a large scale, probe sonication would affect the bulk PIL system in a manner similar to the bench-scale setup, including a comparably widespread sonication-induced temperature increase. In practice, improved heat removal via a recirculated oil jacket and continuous-flow operation will likely dampen this temperature increase. If so, mass transfer enhancement rather than bulk heating would become the dominant sonication benefit, and the temperature-driven acceleration observed in the laboratory would be partially or fully lost. To test the sensitivity of the economics to this assumption, we

conducted a conservative sensitivity analysis in which only part of the experimentally observed acceleration was retained at scale. Specifically, our bench-scale mechanistic analysis suggested that the share attributed to the sonication-induced mass transfer enhancement increased over time (27.8% at 0.5 h and 38.7% at 1 h). Based on this upward trend, a 50% contribution from enhanced mass transfer at 2 h was selected as an illustrative midpoint for scale-up, assuming that the remaining benefit arising from sonication-induced bulk heating would not persist under industrial temperature control. Based on this assumption and our experimental correlations, the saccharification yield of spruce pulp obtained from sonication-assisted ionoSolv (2 h pretreatment) would decrease to ~27%. The corresponding pulp yield, lignin yield, and composition were also adjusted in the same manner. Consequently, the corresponding MSP of spruce-derived ethanol would increase markedly, becoming close to (though still slightly lower than) that of the conventional ionoSolv process (Figure 3.22).

Additionally, several other mitigating factors must be considered. First, the pretreatment temperatures in this study were much lower than those typically used for ionoSolv fractionation (e.g., 150 °C for grass biomass [37] and 170 °C for softwood [36]) due to the experimental temperature limit of the sonication probe. These lower temperatures slowed lignin removal and reduced saccharification yields, thereby worsening the process economics. Second, there are few examples of sonication equipment being deployed on an industrial scale. This constraint led to the choice of a smaller biorefinery in our techno-economic analysis, with fewer savings from economies of scale. For example, if the plant is scaled up to process 2,000 tons of biomass per day (a typical NREL design basis for a commercial biorefinery [249]), the MSPs drop markedly to \$3.5–4.7 kg^{-1} for *Miscanthus*-derived ethanol and \$9.9–21.0 kg^{-1} for spruce-derived ethanol (Figure 3.23). Nevertheless, these estimated MSPs were still significantly higher than recently reported ethanol market prices [417]. Therefore, further valorization of additional biomass fractions and diversification of the product slate toward higher-value co-products (e.g., nanocellulose and hemicellulose-derived compounds) could be a practical route to improve the economic viability of the

(sonication-assisted) ionoSolv process. Third, guidelines for costing large-scale sonication equipment are scarce, complicating the cost estimation for such units. Nevertheless, this analysis provides additional context on the potential of sonication equipment for processing more recalcitrant biomass feedstocks.

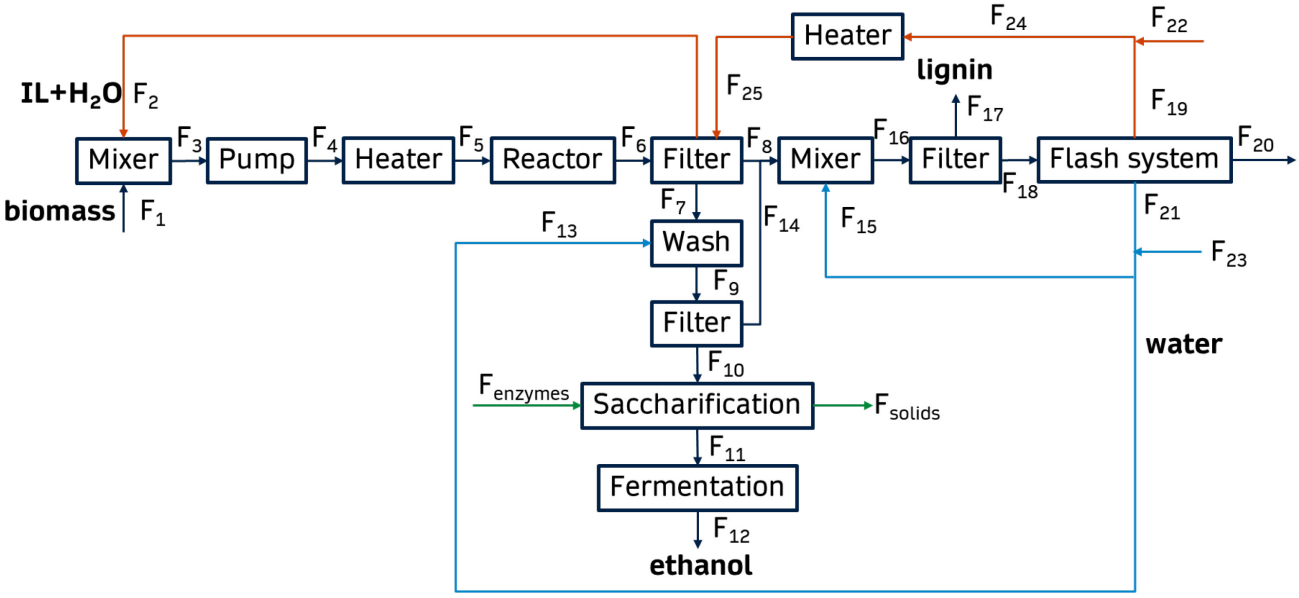


Figure 3.21. Industrial flow scheme for the combined ionoSolv-fermentation process.

Table 3.1. Summary of prices used for the techno-economic analysis.

Utility/Feedstock/Product	Price ($ per functional unit)	Source
Miscanthus ($ ton^{-1})	35.00	[19]
Spruce ($ ton^{-1})	43.23	[418]
Electricity ($ kWh^{-1})	0.300	[416]
LP Steam ($ kg^{-1})	0.116	[419]
MP Steam ($ kg^{-1})	0.120	[419]
Cooling Water ($ m^{-3})	0.0557	[419]
Make-up [DMBA][HSO_4] ($ kg^{-1})	1.240	[145]
Lignin ($ kg^{-1})	0.250	[19]

Table 3.2. Costing methodology for each type of unit considered in the process.

Unit	Costing Methodology
Conveyors	Towler and Sinnott [420]
Tanks	Towler and Sinnott [420]
Mixers	Towler and Sinnott [420]
Pumps	Towler and Sinnott [420]
Motors	Towler and Sinnott [420]
Multi-effect evaporator	Aspen
Ethanol Recovery	Aspen
Heaters/Coolers	Aspen

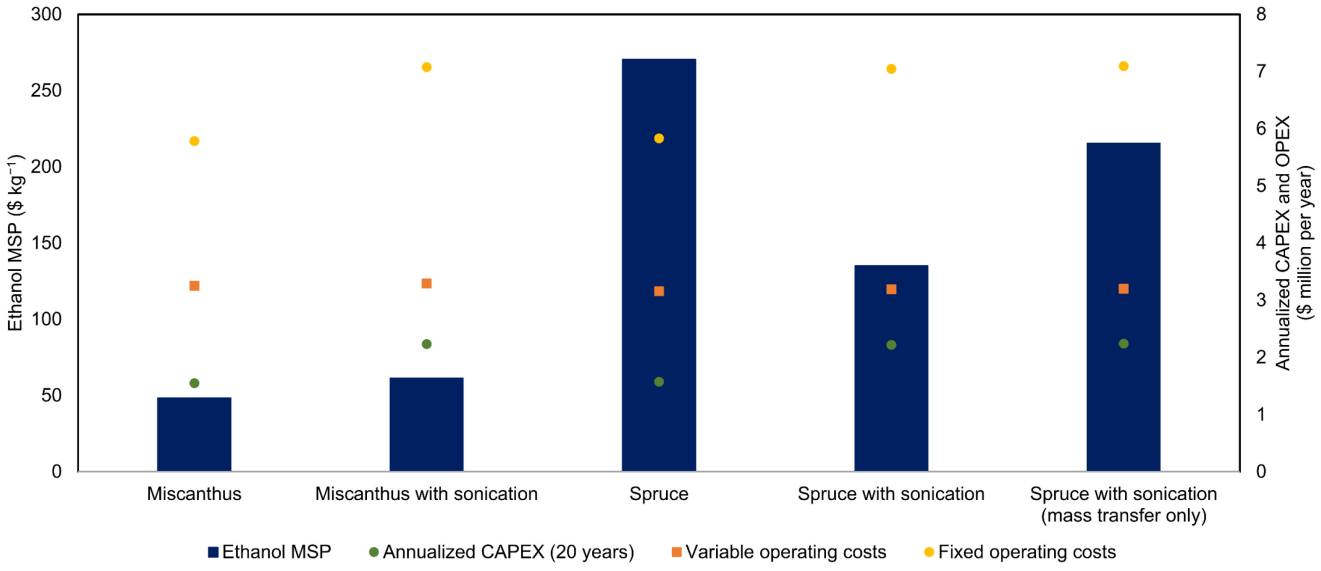


Figure 3.22. MSPs for bioethanol from the conventional and sonication-assisted ionoSolv processes, together with their annualized CAPEX and OPEX (biomass processing scale: 125 kg h^{-1}). "*Miscanthus*" denotes conventional (oil-bath) ionoSolv at 130 °C for 2 h; "*Miscanthus* with sonication" denotes sonication-assisted ionoSolv (80% amplitude) at 130 °C for 1 h; "Spruce" denotes conventional (oil-bath) ionoSolv at 130 °C for 4 h; "Spruce with sonication" denotes sonication-assisted ionoSolv (80% amplitude) at 130 °C for 2 h; and "Spruce with sonication (mass transfer only)" denotes

sonication-assisted ionoSolv (80% amplitude) at 130 °C for 2 h, excluding any additional benefit from sonication-induced temperature increase.

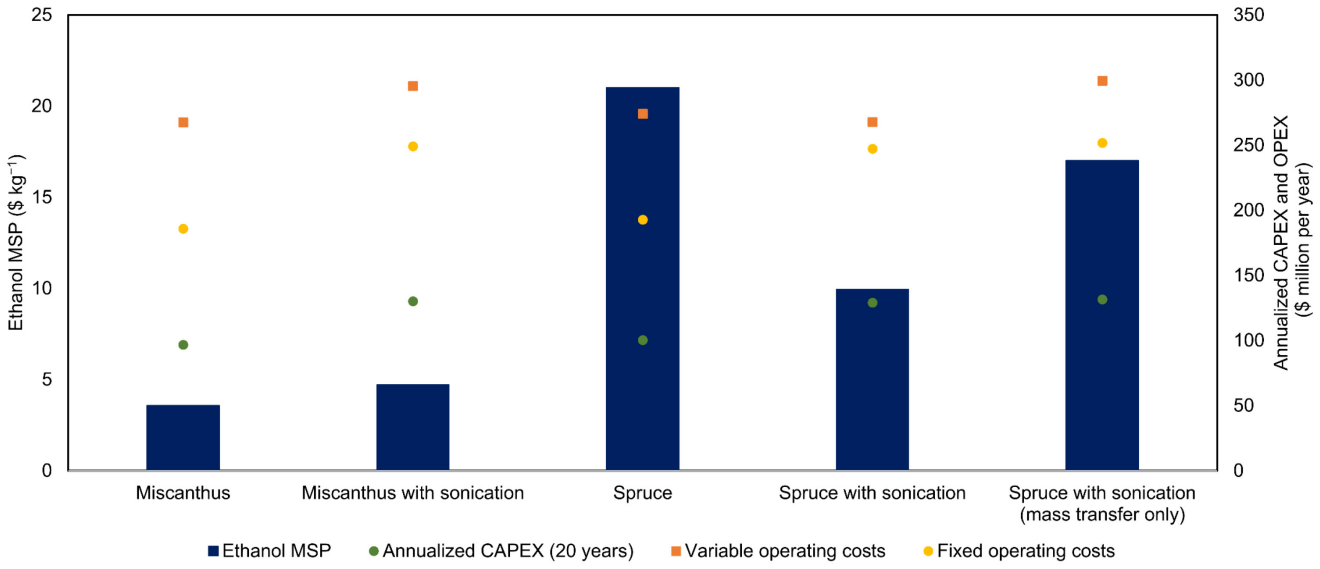


Figure 3.23. MSPs for bioethanol from the conventional and sonication-assisted ionoSolv processes, together with their annualized CAPEX and OPEX (biomass processing scale: 83.33 ton h^{-1} (2,000 tons per day)).

3.4 Conclusion

In this study, sonication was applied to enhance the ionoSolv process using the PIL [DMBA][HSO_4], and its effect was strongly feedstock-dependent. For *Miscanthus* (grass biomass), the acceleration effect was notable only during the first hour of pretreatment, and diminished rapidly by 2 h at both 110 and 130 °C. By contrast, for the more recalcitrant spruce (softwood), the acceleration effect was pronounced and durable. Spruce pulp treated with sonication-assisted ionoSolv at 130 °C for 0.5 h achieved a saccharification yield comparable to that obtained after 4 h of conventional ionoSolv. The efficacy of sonication was also temperature-dependent, with lower temperatures producing stronger acceleration.

Sonication produced two pulp layers with different particle sizes. For spruce, the fine

upper layer had a lower pulp yield but a much higher glucan digestibility than the coarse lower layer. Reducing biomass loading or increasing ultrasonic power may improve pulp homogeneity.

Temperature increase and mass transfer enhancement were the primary phenomena induced by sonication. Quantitative analysis showed that the temperature increase was the dominant factor boosting the pulp saccharification yield, although its relative contribution declined over time—from 89.8% to 73.5% between 0.25 and 0.5 h for *Miscanthus*, and from 72.2% to 61.3% between 0.5 and 1 h for spruce.

A preliminary techno-economic analysis indicated that applying sonication during softwood fractionation could reduce the MSP of spruce-derived ethanol by up to ~50% relative to the conventional ionoSolv route. However, this improvement depends strongly on the contribution from the sonication-induced temperature increase, which may be partially or fully attenuated at larger scales, thereby diminishing the economic benefit attributed to sonication. Even at a representative commercial scale (2,000 tons per day), the projected MSPs remain uncompetitive against recently reported ethanol market prices, underscoring the need to valorize additional biomass fractions to strengthen the overall economic feasibility of the (sonication-assisted) ionoSolv process.

3.5 External Contributions

Dr. Suhaib Nisar contributed to the Aspen Plus process modelling and the CAPEX/OPEX calculations for the techno-economic analysis comparing the conventional and sonication-assisted ionoSolv processes.

Chapter 4: Design and Optimization of a New Efficient Furfural Production Technology via a Protic Ionic Liquid at "Quasi-Economic" Viability

4.1 Introduction

To maximize the economic potential of a biorefinery, it is essential to deeply optimize key compounds derived from each biomass component. Currently, ethanol remains the primary product derived from the cellulosic fraction [16, 34], but the high capital and operating expenditures (CAPEX and OPEX) per unit of ethanol limit its competitiveness [421]. To maximize output and profitability, additional value needs to be extracted from hemicellulose and lignin as well. Decades of research have sought to convert lignin into aromatic chemicals, such as benzene, toluene, and xylene (BTX), via hydrocracking, but commercial viability remains uncertain [53]. The main constraint is low conversion efficiency, with reported BTX yields of only 14% [422]. With limited progress over the past three decades, lignin in biorefineries has been used primarily as a solid fuel for heat and power generation [423]. In contrast, hemicellulose is a valuable resource for the sustainable production of furan-based chemicals that could serve as substitutes for aromatics [53, 74]. Among these, furfural—produced via pentose dehydration—is a key platform chemical [424, 425]. In our previous work, we highlighted the promising application of furfural in the surfactant industry [68, 74, 426]. Its furan-based structure enables versatile surfactant design and delivers high performance and environmental benefits, serving as a sustainable alternative to petroleum-derived aromatic surfactants such as linear alkylbenzene sulfonates (LASs). Furthermore, multiple studies have shown that furfural can be converted into polymerizable monomers, expanding its commercial routes to renewable polyesters that could replace petroleum-derived aromatic polyesters such as polyethylene terephthalate (PET) [427, 428]. Today, global furfural production exceeds 400,000 tons per year, with extensive applications in pharmaceuticals, agrochemicals, polymer

synthesis, and biofuel production [52, 53, 60, 372, 429, 430]. Despite this established role, broader integration of furfural into commodity chemical sectors still offers significant room for expansion. Unlocking this potential will require the development of innovative production technologies that maximize yields, minimize waste generation, and improve process efficiency. These advances are essential to position furfural as a cornerstone of sustainable chemical manufacturing.

Currently, furfural is produced mainly via the Quaker Oats process and related variants [53, 431-433]. Specifically, lignocellulosic biomass (e.g., oat hulls, corncobs, and sugarcane bagasse) is treated with sulfuric acid. Hemicellulose dehydrates to furfural, which is then steam-stripped into the vapor phase and isolated by distillation. However, this process has two major drawbacks: the acid catalyst is not recyclable, and it generates highly acidic wastewater with high chemical oxygen demand (COD) and biochemical oxygen demand (BOD) levels [59]. This wastewater necessitates the implementation of costly on-site anaerobic digestion systems or other advanced treatment technologies to meet discharge regulations [59, 434, 435]. Solvent-based approaches can mitigate wastewater generation, but process viability hinges on solvent recyclability, biomass-to-solvent loading, and solvent recovery costs. Although many studies focus on maximizing the furfural yield, these factors are often underexamined. For example, the bio-based solvent γ-valerolactone (GVL) has proven effective in achieving high furfural yields, yet key feasibility parameters, such as biomass loading and solvent recyclability, still require further evaluation [357]. Biphasic water/hydrophobic solvent systems have also been widely investigated [53, 436-441], but their industrial applicability remains limited for two main reasons: (1) high furfural yields typically require low biomass loadings [374, 442]; and (2) performance is generally better with xylose or pentose-rich hydrolysates than with raw biomass. For example, Yang et al. reported a ~75% furfural yield from xylose dehydration in a water–THF biphasic system (140 °C, 45–60 min), while yields fell to 29–51% when different raw biomass feedstocks were used (140 °C, 60 min) [442].

Several studies, including ours, show that ionic liquids (ILs) offer clear advantages for synthesizing furan-based chemicals (e.g., HMF and furfural) from sugars, owing to their dual functionality in catalyzing sugar dehydration and stabilizing furans [194, 443-448]. These solvents can also lead to favorable economic outcomes if heat recovery and process integration are in place [419, 449]. However, despite acceptable furfural yields from xylose, IL performance with raw biomass remains limited, even at relatively low biomass loadings (<10 wt%) [446, 447], owing to poor reaction control and severe furfural-consuming side reactions, including self-resinification, condensation with lignin, sugars, and other intermediates, and fragmentation to small molecules [19, 53, 450]. Recently, protic ionic liquids (PILs), synthesized via acid-base neutralization, have emerged as cost-effective alternatives for biomass valorization [36, 144, 145]. Their simple synthesis lowers production costs and allows tailoring to specific applications by tuning the anion–cation pairs [36, 152]. PILs also show superior thermal stability and recyclability [19, 91]. Our previous studies indicated that the PIL *N,N*-dimethylbutylammonium hydrogen sulfate ([DMBA][HSO_4]) is effective for delignification and hemicellulose dissolution during the pretreatment of recalcitrant biomass feedstocks [36, 152]. Meanwhile, employing [DMBA][HSO_4] with polyoxometalates, we obtained an approximately 75% furfural yield directly from sugarcane bagasse, highlighting the promise of PILs, though the biomass loading was still low (5 wt%) and required further optimization. In this study, we developed a recyclable, semi-continuous one-pot process for producing furfural directly from raw biomass (sugarcane bagasse) at high biomass loadings (≥10 wt%). The PIL [DMBA][HSO_4] was chosen as an economical solvent. Our findings demonstrate that, by optimizing the process conditions, this solvent system delivers a high furfural yield at 30 wt% biomass loading with excellent solvent recyclability, competitive with state-of-the-art techniques. A preliminary techno-economic analysis reveals that IL recovery efficiency and processing scale are decisive in determining overall process viability. More broadly, this work establishes a clear connection between PIL-based biomass fractionation (Chapter 3) and hemicellulose valorization, highlighting the importance of integrated upgrading strategies for maximizing the utilization of all biomass

components in PIL-based biorefineries.

4.2 Materials and Methods

4.2.1 Feedstock

Sugarcane bagasse from the São João Mill (Araras, SP, Brazil) was air-dried, sieved into four different particle sizes (<180 μm, 180–850 μm, 850 μm–2 mm, and 2–4 mm), and stored in plastic bags at room temperature in the dark until use. Following the NREL protocols [403, 406], the moisture content of the sugarcane bagasse was determined as 7.23 wt%. The composition of the sugarcane bagasse (on an oven-dried basis) was determined as: glucan (43.77 wt%), xylan (22.26 wt%), galactan (1.79 wt%), arabinan (1.97 wt%), acid soluble lignin (4.33 wt%), acid insoluble lignin (17.69 wt%), ash (1.01 wt%), extractives (5.00 wt%), and others (2.18 wt%).

4.2.2 Synthesis of [DMBA][HSO_4]

The PIL [DMBA][HSO_4] was synthesized under controlled conditions to limit amine volatility and manage the exothermic neutralization. *N,N*-dimethylbutylamine (505.95 g, 5 mol) was placed in a 1 L round-bottom flask cooled in an ice bath. While stirring, 694.73 g of 72 wt% H_2SO_4 (5.1 mol) was added dropwise to the flask to form [DMBA][HSO_4]. The reaction was conducted in a fume hood, and the mixture was stirred overnight to give a colorless IL. The water content of the IL was determined by using a V20 volumetric Karl Fischer Titrator (Mettler-Toledo), and the acid-base ratio was determined by titration with 0.1 M NaOH using a G20S Compact Titrator (Mettler-Toledo). The water content was adjusted to 20 wt% using a rotary evaporator (Büchi), and the acid-base ratio was adjusted to 1.02:1 (mol/mol) by adding either amine or acid. A 2 mol% excess of H_2SO_4 in the IL was retained to catalyze furfural release from the sugarcane bagasse.

4.2.3 Semi-Continuous Furfural Production System

A glass apparatus was used to strip furfural from the mixture of [DMBA][HSO_4] and

sugarcane bagasse (Figure 4.1). A 100 mL three-neck flask served as the reactor. Its center neck was connected to a Dean-Stark–style water estimator topped with a condenser to liquefy the furfural vapor, while a hose from the condenser led to a water-filled bubbler to maintain pressure balance. One side neck held a thermometer, while the other continuously delivered 90 °C deionized water to promote furfural release. Inside the flask, a magnetic stir bar mixed the IL and biomass at 600 rpm. In addition, the flask sat in a heating mantle, and a heating tape wrapped the stem of the water estimator to prevent vapor from condensing there.

In a typical run, 10 g of [DMBA][HSO_4] (20 wt% water content, 1.02:1 (mol/mol) acid-base ratio) was added to the flask. The water pump was operated at varying flow rates, and the IL was heated to 150, 170, or 190 °C. When the target temperatures were reached, the water content of the IL had fallen to 7.4 wt%, 5.0 wt%, and 3.1 wt% at 150, 170, and 190 °C, respectively. Sugarcane bagasse (1–3 g, on an oven-dried basis) was then added through a side neck. During the 120 min run, furfural and water condensed in the right arm of the three-way water estimator, and the condensate was collected in 10 mL vials every 10 min. A Shimadzu HPLC system equipped with an Aminex HPX-87H column (Bio-Rad, 300 × 7.8 mm) was used to measure the furfural concentration in the condensate. The column temperature was 60 °C. The mobile phase was 0.005 M H_2SO_4 at a flow rate of 0.6 mL min^{-1}. Detection was at 254 nm by a UV-Vis detector with 10 µL injections. Calibration was performed using furfural standards at 0.2, 0.4, 0.6, 1.0, and 2.0 mg g^{-1}. Furfural yield was calculated using Equation (4.1). The theoretical maximum mass of furfural was calculated from the xylan and arabinan contents of the sugarcane bagasse, multiplied by 0.7272. The factor 0.7272 is the stoichiometric mass ratio of furfural to anhydropentose [61, 451, 452].

$$\text{Furfural yield (\%)} = \frac{\text{Mass of furfural produced}}{\text{Theoretical maximum mass of furfural}} \times 100 \quad (4.1)$$

4.2.4 Stepwise Biomass Addition

To improve furfural yield at a high biomass loading of 30 wt%, a stepwise biomass addition strategy was used. Specifically, 3 g of the sugarcane bagasse (on an oven-dried basis, 180–850 μm) was split into equal portions according to the planned number of additions (e.g., three 1 g portions for a three-step addition experiment). The first portion was added at the start of the reaction, while the rest were introduced at 20-min intervals (e.g., at 20 and 40 min in the three-step addition run). Series with two-, three-, four-, and five-step additions were evaluated, and a 40-min addition interval was also tested in the two-step addition experiment.

4.2.5 Recovery and Recycling of [DMBA][HSO_4]

After the semi-continuous furfural production run, the [DMBA][HSO_4]/solid residue mixture was transferred to a 50 mL centrifuge tube with 40 mL of deionized water to precipitate lignin from the IL. The suspension stood overnight, and then was centrifuged at 4,000 rpm for 30 min. The supernatant was collected in a pre-weighed 250 mL round-bottom flask. The wash was repeated twice. The solid residue (biochar) was freeze-dried for 48 h and weighed. Its yield was calculated using Equation (4.2):

$$\text{Biochar yield (\%)} = \frac{\text{Mass of freeze dried solid residue}}{\text{Mass of sugarcane bagasse on an oven dried basis}} \times 100 \quad (4.2)$$

Water in the combined liquors was removed via a rotary evaporator. Once most of the water was evaporated, the flask containing the recovered IL was weighed. The water content of the recovered IL was measured by the Karl Fischer Titrator, and its acid-base ratio was determined by the G20S Compact Titrator. The IL recovery rate was calculated using Equation (4.3):

$$\text{IL recovery rate (\%)} = \frac{\text{M dried after}}{\text{M dried before}} \times 100 \quad (4.3)$$

Where M dried before represented the dry mass of [DMBA][HSO_4] before cycle i, and M dried after was the dry mass of the recovered [DMBA][HSO_4] after cycle i.

The acid-base ratio of the recovered IL was readjusted to 1.02:1 (mol/mol) by adding either H_2SO_4 or *N,N*-dimethylbutylamine as needed. The regenerated IL was then

transferred to the 100 mL three-neck flask, combined with fresh air-dried sugarcane bagasse (20 wt% biomass loading relative to the mass of the regenerated IL), and treated under the same conditions as the initial run. Notably, to evaluate the structural integrity, ^{1}H and ^{13}C NMR spectra of fresh and recycled [DMBA][HSO_4] were obtained using a JEOL 400 MHz spectrometer with DMSO-d_6 as the solvent. Chemical shifts (δ) are reported in ppm.

4.2.6 Characterization of Solid Residues from the IL Recycling Process

Elemental analysis (C, H, N, and S) of the solid residue (biochar) was carried out by Medac Limited, UK. The O content was then calculated by difference (Equation (4.4)):

$$O\ (wt\%) = 100\ wt\% - C\ wt\% - H\ wt\% - N\ wt\% - S\ wt\% - Ash\ wt\% \quad (4.4)$$

The elemental retention rate refers to the ratio of the mass of C, H, N, or O retained in the biochar to the mass of the corresponding element in the untreated sugarcane bagasse, which is calculated using Equation (4.5):

$$\text{Retention rate of element i}\ (\%) = \frac{\text{Biochar yield}\ (\%) \times \text{i content in biochar}\ (\%)}{\text{i content in sugarcane bagasse}\ (\%)} \times 100 \quad (4.5)$$

The ash content was measured using a Q500 thermogravimetric analyzer (TA Instruments, USA). The biochar was first heated from room temperature to 110 °C at a rate of 20 °C min^{-1} and held for 5 min, then further heated to 900 °C at the same rate and held for 25 min to remove all organic matter. Throughout the process, the biochar was maintained in an air atmosphere with a gas flow rate of 50 mL min^{-1}. The ash content was calculated using Equation (4.6):

$$\text{Ash content}\ (\%) = \frac{\text{Mass of biochar after heating}}{\text{Mass of biochar before heating}} \times 100 \quad (4.6)$$

The higher heating value (HHV) of the biochar was estimated using the empirical formula (Equation (4.7)) developed by Channiwala et al. [453]:

$$HHV\ (MJ\ kg^{-1}) = 0.3491C + 1.1783H + 0.1005S - 0.1034O - 0.0151N - 0.0211Ash \quad (4.7)$$

For comparison, the HHV of brown coal (lignite) was estimated to be 23.51 MJ kg^{-1} using Equation (4.7), based on the elemental composition and ash content reported by Wang et al. [454].

4.2.7 Sealed-Batch Furfural Production System

For each run, 2 g of the sugarcane bagasse (on an oven-dried basis, 180–850 μm) was mixed with [DMBA][HSO_4] (5.0 wt% water content, acid-base ratio of 1.02:1 (mol/mol)) in a 15 mL pressure tube sealed with a silicone front seal (Ace Glass). The mixture was heated in an oil bath to 170 °C for 5, 10, 20, 30, or 60 min. The IL water content (5.0 wt%) corresponded to its equilibrium value at 170 °C in the semi-continuous system. At this temperature, the reduced IL water content raised the biomass loading in the semi-continuous system from 20.0 wt% (room temperature) to 23.8 wt% (170 °C), and the sealed-batch runs therefore used the same 23.8 wt% biomass loading for consistency. After heating, the tube was cooled to room temperature in a fume hood.

The pretreated mixture was transferred to a 50 mL centrifuge tube, diluted with 40 mL of deionized water, vortexed, and centrifuged at 4,000 rpm for 30 min. The dark-brown supernatant was decanted into a pre-weighed 250 mL round-bottom flask, and the solid residue was washed twice more with 40 mL of deionized water each time. The total mass of the supernatant was obtained by difference. The furfural concentration of the supernatant was measured by HPLC, and the furfural yield was calculated using Equation (4.1).

4.3 Results and Discussion

4.3.1 Reaction Setup

Our initial approach focused on designing a reaction system that limits side reactions consuming furfural. Prior IL-based studies were inefficient because furfural is unstable in acidic media and readily undergoes self-resinification, condensation with lignin and sugars, or fragmentation [19, 53, 450, 455]. Biphasic IL–organic solvent systems can partially suppress these side reactions by extracting furfural from the acidic IL efficiently [374]. Yet the organic phase often becomes acidic because mineral acids (e.g., H_2SO_4) and hemicellulose-derived organic acids (e.g., acetic and formic acids [19, 450]) are

co-extracted from the IL, promoting the acid-catalyzed degradation of furfural. Therefore, our strategy for furfural removal employs water vapor (steam stripping), which we consider more effective than a dry inert gas because it helps maintain moisture in the IL. This moisture moderates the IL's Hammett acidity (H_0) and lowers its viscosity [107, 456, 457], thereby increasing reaction efficiency and suppressing furfural degradation.

For this purpose, we implemented a semi-continuous furfural production setup (Figure 4.1). Water was introduced at 90 °C and, upon contacting the reaction mixture at the set temperature, generated vapor that stripped furfural from the reactive solvent. A bubbler proved essential to preserve sufficient water in [DMBA][HSO_4]. Without it, the drying of the [DMBA][HSO_4] increased acidity and viscosity and led to a sharp drop in furfural productivity. Notably, even with the bubbler, the water content of the IL fell from 7.4 wt% at 150 °C to 3.1 wt% at 190 °C, demonstrating its strong temperature dependence.

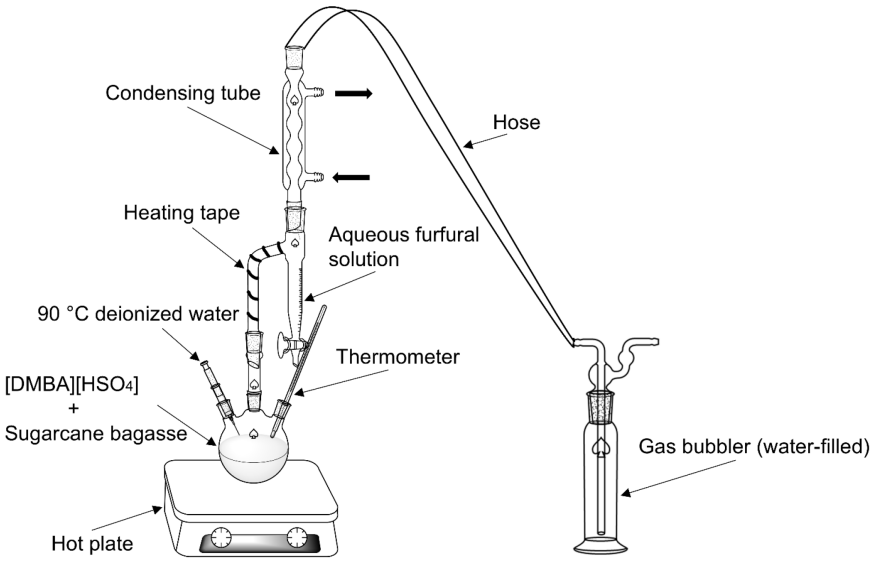


Figure 4.1. Diagram of the apparatus used for furfural production.

To validate the efficacy of this approach, a comparative experiment was conducted

between a sealed-batch reference (170 °C, 23.8 wt% biomass loading) and a semi-continuous run with a 0.50 mL min^{-1} water feed (Figure 4.2). In the semi-continuous run, the initial biomass loading was 20.0 wt% but rose to 23.8 wt% as the system reached 170 °C, owing to a decrease in the PIL water content from 20.0 wt% to 5.0 wt%. In the sealed-batch system, the furfural yield peaked at 51.2% after 10 min and declined to 24.6% by 60 min, indicating furfural degradation in the acidic IL phase. In contrast, the semi-continuous system steadily improved the furfural yield to 66.8% after 120 min, which is 15.6% higher than the maximum attained in the sealed-batch system, confirming that vapor stripping effectively limited side-reaction losses. Notably, in the semi-continuous system, 86% of the furfural was released in the first 20 min, with the remaining 14% released over the subsequent 100 min. This uneven release profile suggests that the overall reaction time could be shortened without significantly sacrificing yield. Furthermore, a sensitivity analysis showed that reducing the water feed from 0.50 to 0.10 mL min^{-1} slowed the early-stage furfural release (the first 40 min) but had little effect on the final yield at 120 min (Figure 4.3). This indicated that vapor injection primarily served as an auxiliary vector, accelerating the furfural removal kinetics rather than altering the final conversion. To facilitate the early-stage furfural release, the water feed was maintained at 0.50 mL min^{-1} for subsequent process optimization.

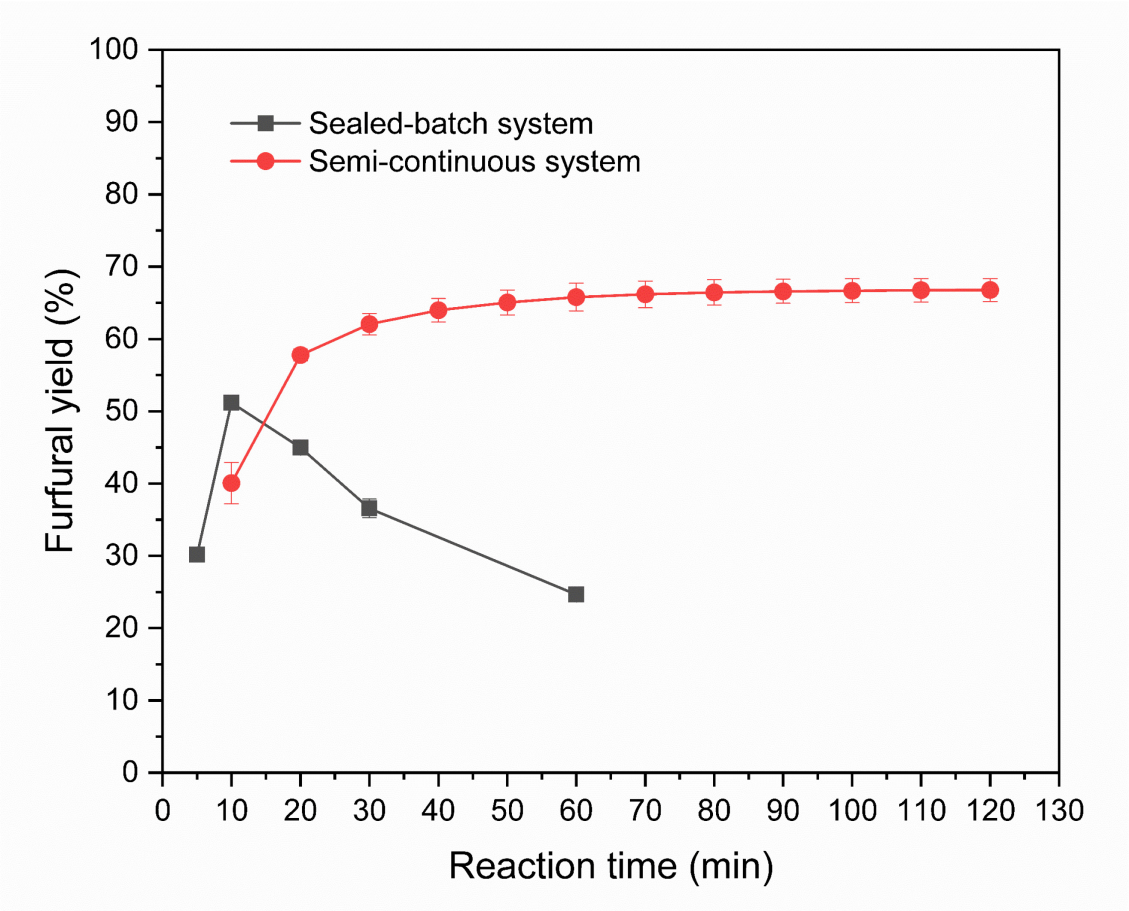


Figure 4.2. Furfural release from the sealed-batch and semi-continuous systems. Sugarcane bagasse (180–850 μm) was treated at 170 °C using [DMBA][HSO_4].

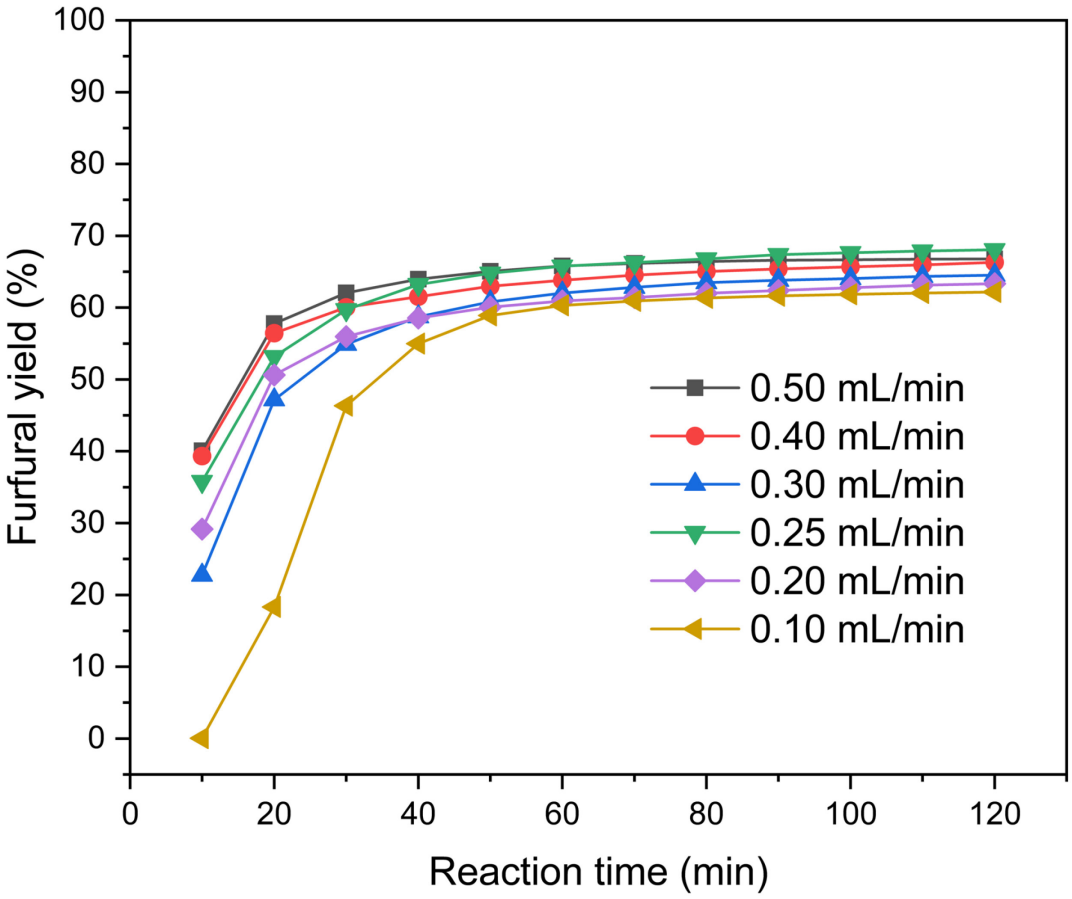


Figure 4.3. Effect of water feed rate on furfural release from the semi-continuous system using [DMBA][HSO_4] at 170 °C with 20 wt% solids loading of sugarcane bagasse (180–850 μm). (The pump used in this study had a minimum setpoint of 0.30 mL min^{-1}. Lower feed rates (0.25, 0.20, and 0.10 mL min^{-1}) were simulated by maintaining the water feed rate at 0.30 mL min^{-1} and proportionally increasing the initial masses of the PIL and sugarcane bagasse to match the target water feed-to-feedstock ratios.)

4.3.2 Effects of Key Process Parameters

To gain a better understanding of the semi-continuous furfural production process, we investigated the effects of reaction temperature, reaction time, and biomass loading on the furfural yield (Figure 4.4). Lower biomass loading resulted in higher furfural yields, which was attributed to suppressed side reactions. Higher temperatures (170 and 190 °C) accelerated furfural release because of faster reaction kinetics and

evaporation. This effect was advantageous at 20 wt% and 30 wt% biomass loadings, allowing for shorter reaction times without a loss of overall furfural yield. At 10 wt% biomass loading, however, a different pattern was observed. Lower temperatures gave higher overall furfural yields, even though the furfural release was slower. These observations suggest that multiple competing phenomena were occurring within the reaction mechanism.

The biomass loadings of 10 wt% and 20 wt% gave higher furfural yields because their biomass–IL slurries were less viscous, improving mass and heat transfer and reducing side-product formation [42, 458]. In contrast, at the high biomass loading of 30 wt%, the lower furfural yields were attributed to the IL's limited wetting capacity. During the first 10–20 min, the IL covered only part of the biomass surface, reducing its effectiveness as a catalytic solvent [458, 459]. Moreover, higher biomass loading increased the slurry concentrations of furfural and potential inhibitors, such as dissolved lignin fragments, cellulose oligomers, and sugar-degradation products, thereby accelerating the side reactions that consume furfural. While an 88.0% furfural yield at 10 wt% biomass loading (150 °C) may represent a competitive result compared with current literature values, this low biomass loading still does not reflect a viable operating condition given the high CAPEX and OPEX involved in the process. Therefore, based on the results obtained so far, strategies to mitigate side reactions at higher biomass loadings need to be implemented.

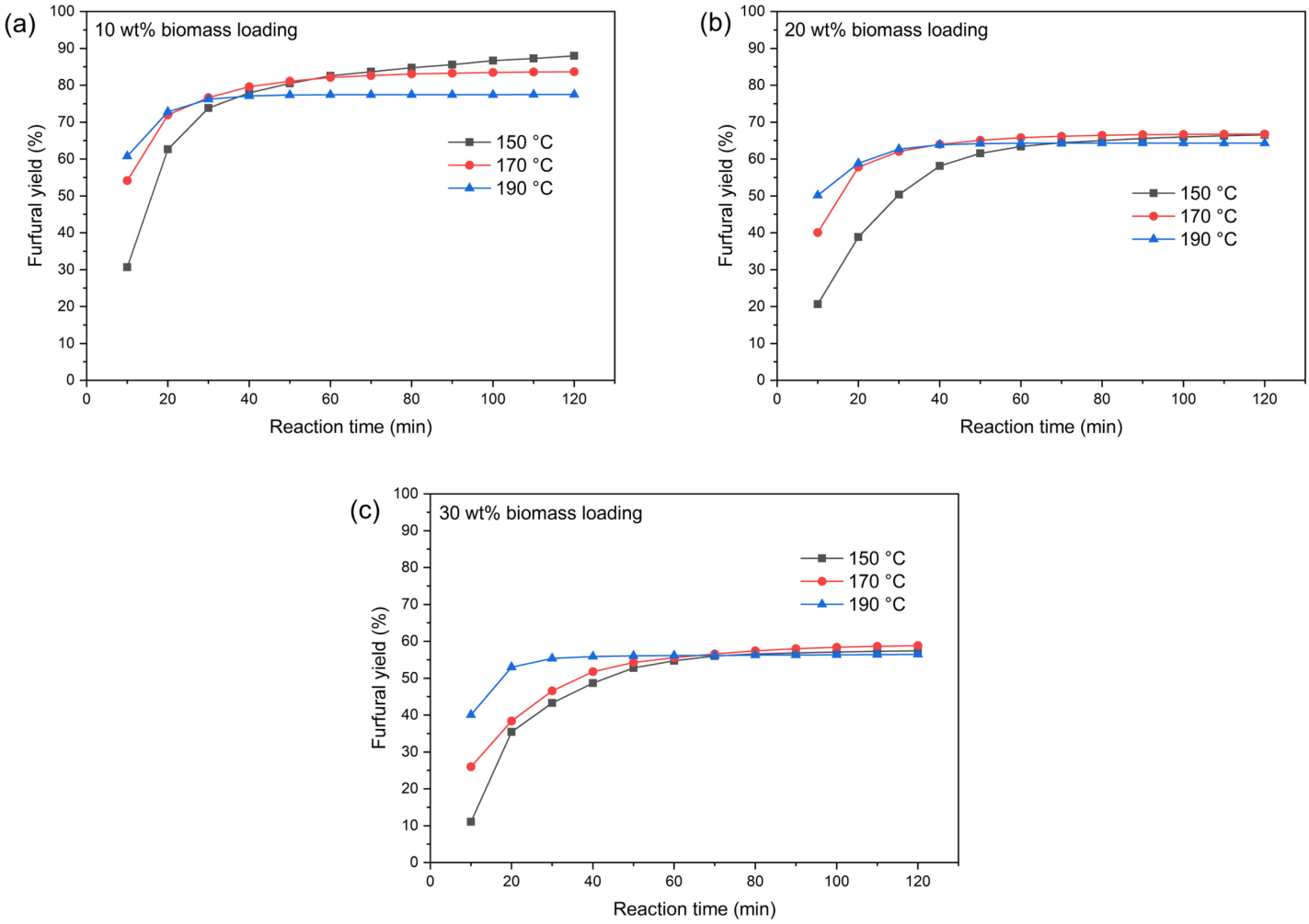


Figure 4.4. Effects of reaction temperature, reaction time, and biomass loading on furfural release from the semi-continuous production system using sugarcane bagasse (180–850 μm) and [DMBA][HSO_4].

4.3.3 Response Surface Methodology (RSM) of Process Parameters

Because of the complex interplay among reaction temperature, reaction time, and biomass loading during furfural production from the semi-continuous system, the response surface methodology (RSM) was applied to enable rigorous statistical analysis rather than relying on simple empirical observation. This facilitated a precise evaluation of the process variables and supported the design of strategies to improve the furfural yield at higher biomass loadings.

The RSM design used three factors: temperature (T), time (t), and solids (biomass) loading (S). The temperature was set at 150, 170, and 190 °C, and the solids loading was set at 10 wt%, 20 wt%, and 30 wt%. The reaction time was split into three ranges to capture stage-specific effects: 10, 20, and 30 min (initial stage); 30, 40, 50, 60, and 70 min (intermediate stage); and 70, 80, 90, 100, and 110 min (final stage). The furfural yield was the response variable, and five center-point replicates were included to measure the experimental error (Figure 4.5). Data fitting, regression modelling, and analysis of variance (ANOVA) were carried out with Design-Expert 12 (Stat-Ease Inc., USA).

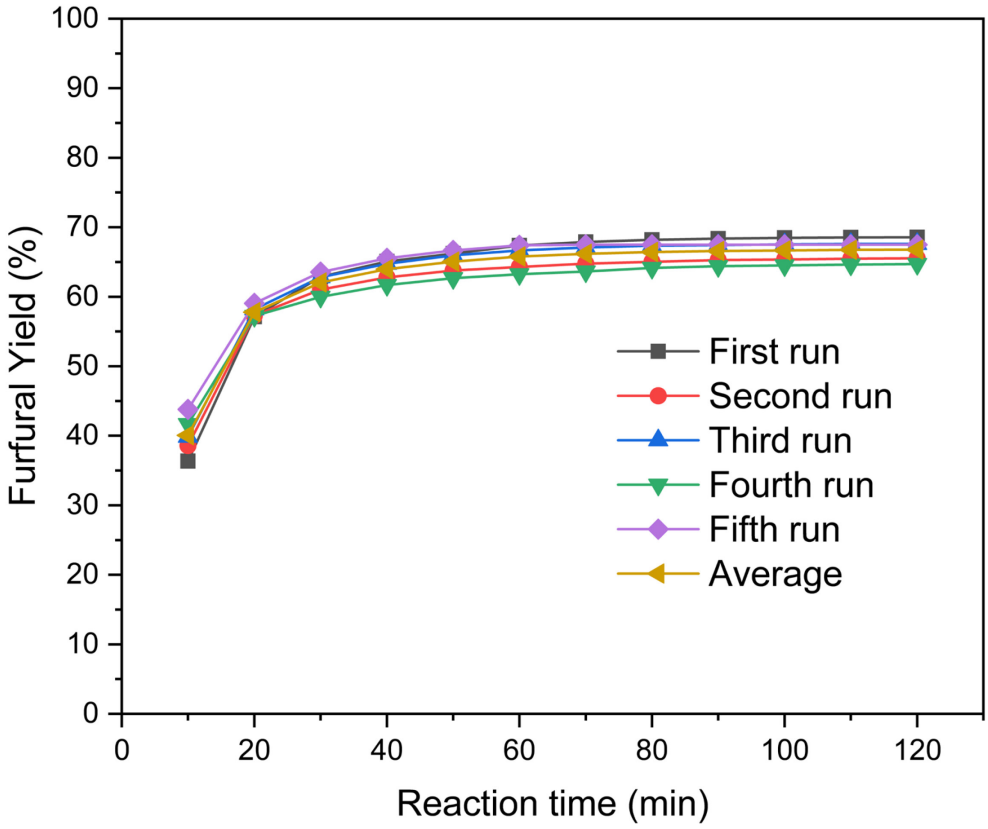


Figure 4.5. Five replicate runs at 170 °C and 20 wt% solids loading of sugarcane bagasse (180–850 µm), representing the center point in the RSM design.

4.3.3.1 Initial Reaction Stage (10–30 min)

During the initial reaction stage, a reduced quadratic model was developed for the furfural yield. Non-significant terms (P-value > 0.05) were removed to improve

predictive accuracy. The mathematical model is as follows:

$$\text{Furfural yield (\%)} = -363.90 + 3.73 \times T + 7.90 \times t - 1.28 \times S - 0.0258 \times T \times t - 0.0081 \times T^2 - 0.0583 \times t^2 \quad (4.8)$$

The fit of the model was strong (R^2 = 0.9649; adjusted R^2 = 0.9561), and the predicted R^2 of 0.9384 confirmed good predictive power despite the high variability in the initial stage of furfural production. As displayed in Table 4.1, the ANOVA gave an F-value of 109.87 (P-value < 0.0001), indicating that the model was highly significant. Although the lack-of-fit test was significant (F-value = 20.38, P-value = 0.0049), diagnostic plots (Figure 4.6) showed that the model was still adequate.

The ANOVA also indicated the importance of each parameter by its F-value. Solids loading was the strongest factor (F-value = 252.84, P-value < 0.0001), followed by reaction time (F-value = 218.78, P-value < 0.0001) and temperature (F-value = 126.58, P-value < 0.0001). Among the interaction terms, only temperature × time (T × t) was significant (F-value = 27.27, P-value < 0.0001), showing that the influence of temperature on the furfural yield depended on the reaction time, and vice versa. This dependency was also demonstrated in the three-dimensional (3D) response surface plot (Figure 4.7 a) and the corresponding contour plot (Figure 4.7 b). Furfural yield rose sharply from 10 to 30 min at 150 °C, while this increase became less pronounced at 190 °C. Furthermore, yield differences among temperatures were the most significant at 10 min but narrowed by 30 min. No significant temperature × solids loading (T × S) or time × solids loading (t × S) interactions were detected, indicating no synergy or antagonism between these pairs under the tested conditions. Meanwhile, although solids loading had the largest effect, its curvature term was not significant, pointing to a linear response over the range studied and allowing predictable scale-up without unexpected yield shifts when the solids loading changes.

Table 4.1. ANOVA results for the reduced quadratic model fitted to the semi-continuous furfural production data from 10 to 30 min.

Source	Sum of Squares	df	Mean Square	F-value	p-value
Model (10-30min)	7702.99	6	1283.83	109.87	< 0.0001
T-Temperature	1479.08	1	1479.08	126.58	< 0.0001
t-Time	2556.35	1	2556.35	218.78	< 0.0001
S-Solids loading	2954.41	1	2954.41	252.84	< 0.0001
Tt	318.63	1	318.63	27.27	< 0.0001
T^2	76.28	1	76.28	6.53	0.0174
t^2	245.50	1	245.50	21.01	0.0001
Residual	280.44	24	11.68		
Lack of Fit	277.71	20	13.89	20.38	0.0049
Pure Error	2.72	4	0.6812		
Cor Total	7983.43	30			

R^2 = 0.9649; Adjusted R^2 = 0.9561; Predicted R^2 = 0.9384

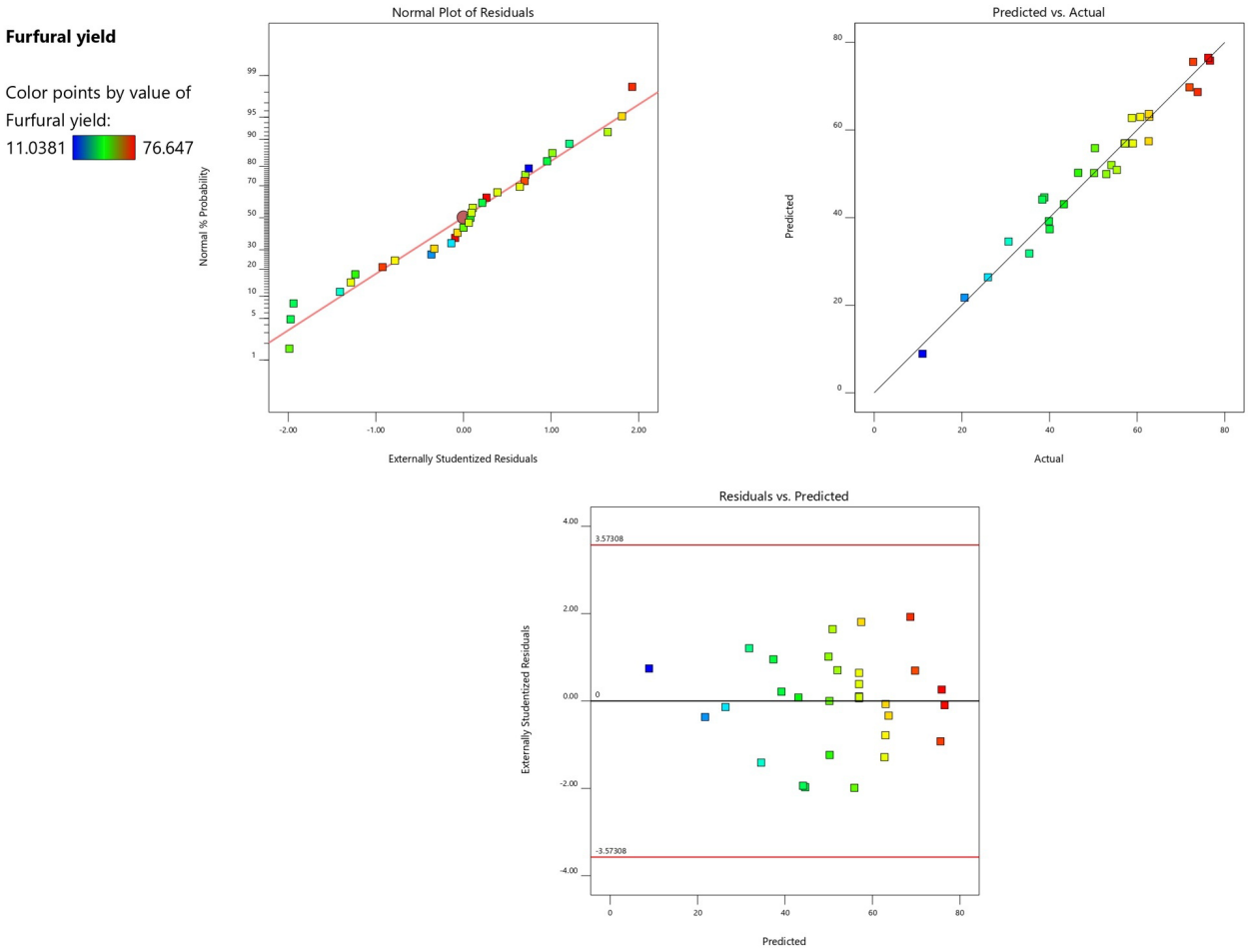


Figure 4.6. Diagnostic plots of the reduced quadratic model fitted to the semi-continuous furfural production data from 10 to 30 min.

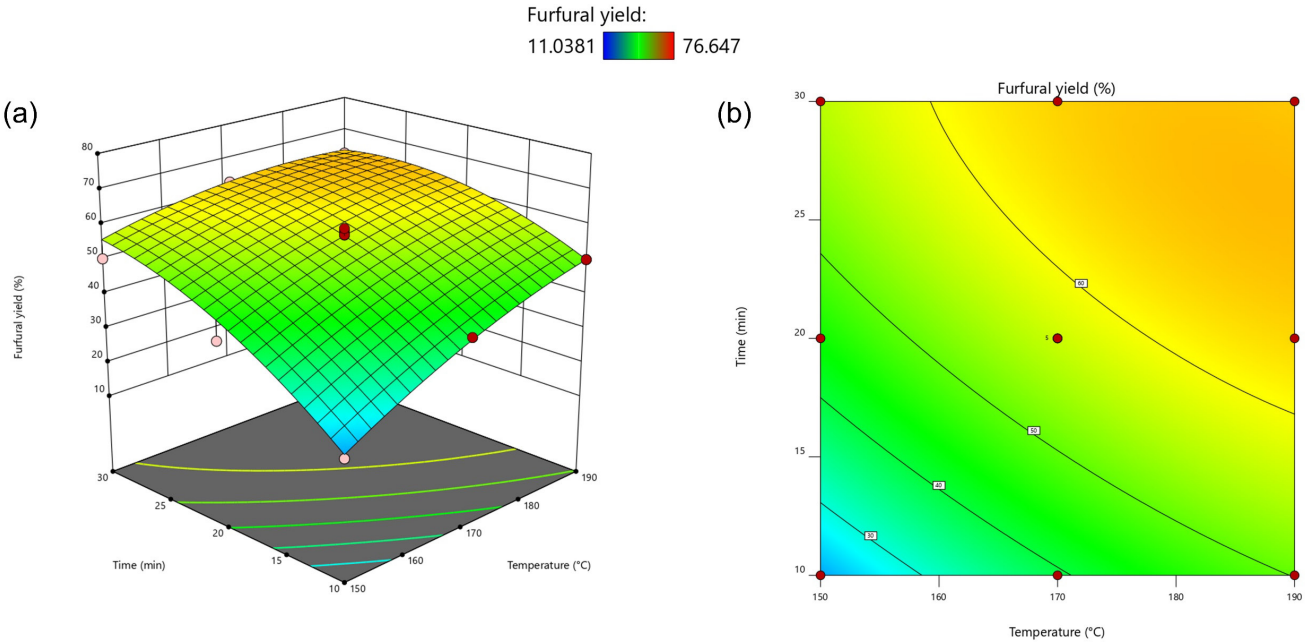


Figure 4.7. (a) 3D response surface plot of furfural yield at the initial reaction stage; and (b) The corresponding contour plot of furfural yield at the initial reaction stage. (Solids loading was fixed at 20 wt%.)

4.3.3.2 Intermediate Reaction Stage (30–70 min)

The reduced quadratic model was developed for the intermediate reaction stage:

$$\text{Furfural yield (\%)} = -72.75 + 1.65 \times T + 1.75 \times t - 4.17 \times S - 0.0068 \times T \times t + 0.0093 \times T \times S - 0.0042 \times T^2 - 0.0044 \times t^2 + 0.0326 \times S^2 \quad (4.9)$$

This model showed better performance than that for the initial stage, with higher R^2 = 0.9845, adjusted R^2 = 0.9814, and predicted R^2 = 0.9760. This improvement is due to the slower and more orderly furfural release during the intermediate stage, resulting in higher model fit and predictability. As shown in Table 4.2, the ANOVA further confirmed the model's reliability (F-value = 697.96, P-value < 0.0001), and the lack-of-fit term was not significant (F-value = 0.7079, P-value = 0.7505).

During this stage, the solids loading remained the key driver of the furfural yield (F-value = 2257.12). Reaction time and temperature also affected the yield, though to a

lesser extent (F-values = 107.53 and 16.10, respectively). Significant interaction terms were the temperature × time (T × t) and temperature × solids loading (T × S). Curvature was evident, as the quadratic terms for temperature (T^2), time (t^2), and solids loading (S^2) were all significant—for example, S^2 showed an F-value = 54.51 and a P-value < 0.0001.

Table 4.2. ANOVA results for the reduced quadratic model fitted to the semi-continuous furfural production data from 30 to 70 min.

Source	Sum of Squares	df	Mean Square	F-value	p-value
Model (30-70min)	5583.65	8	697.96	316.72	< 0.0001
T-Temperature	35.47	1	35.47	16.10	0.0003
t-Time	236.95	1	236.95	107.53	< 0.0001
S-Solids loading	4973.94	1	4973.94	2257.12	< 0.0001
Tt	109.34	1	109.34	49.62	< 0.0001
TS	68.55	1	68.55	31.11	< 0.0001
T^2	32.31	1	32.31	14.66	0.0004
t^2	26.22	1	26.22	11.90	0.0013
S^2	120.11	1	120.11	54.51	< 0.0001
Residual	88.15	40	2.20		
Lack of Fit	76.19	36	2.12	0.7079	0.7505
Pure Error	11.96	4	2.99		
Cor Total	5671.80	48			

R^2 = 0.9845; Adjusted R^2 = 0.9814; Predicted R^2 = 0.9760

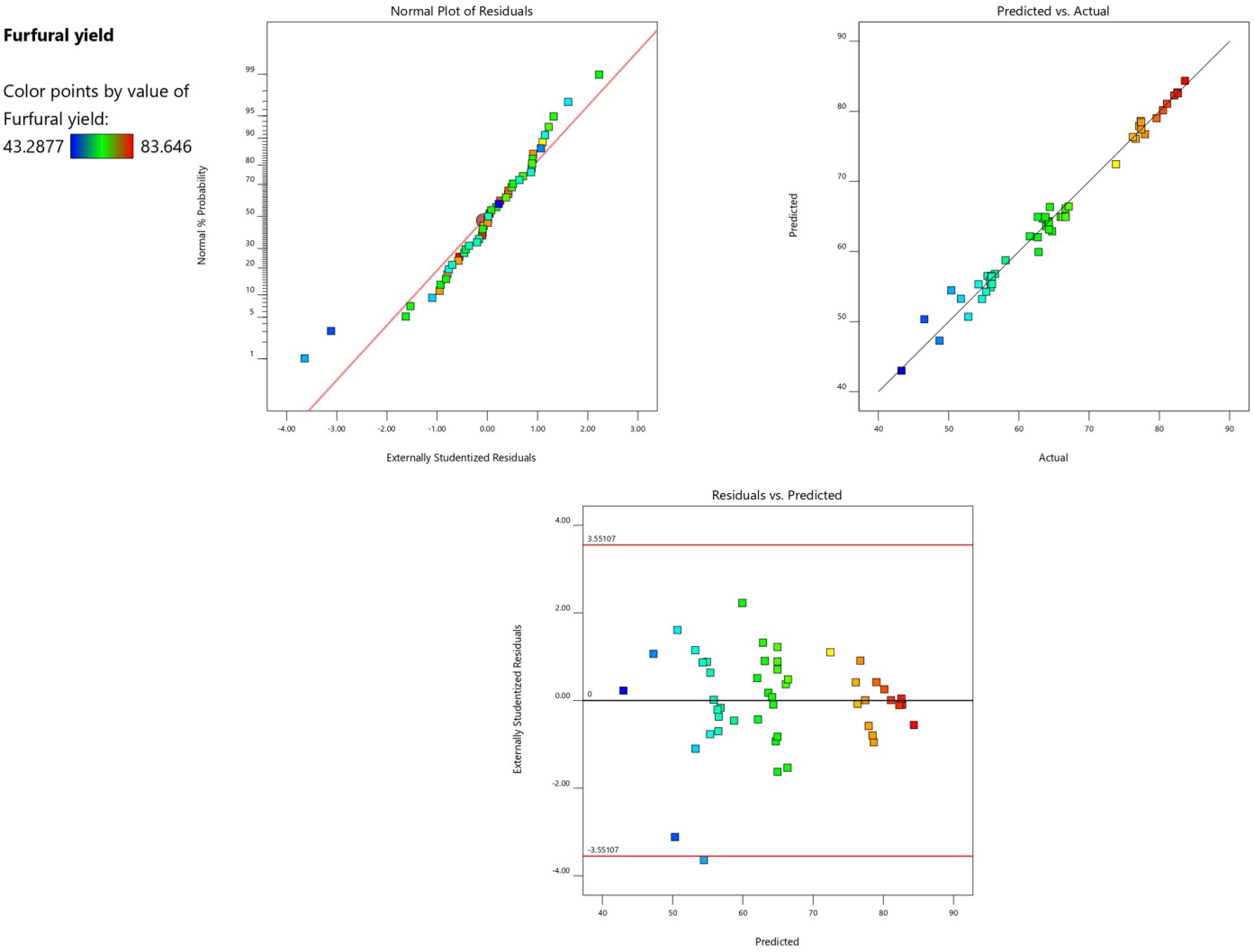


Figure 4.8. Diagnostic plots of the reduced quadratic model fitted to the semi-continuous furfural production data from 30 to 70 min.

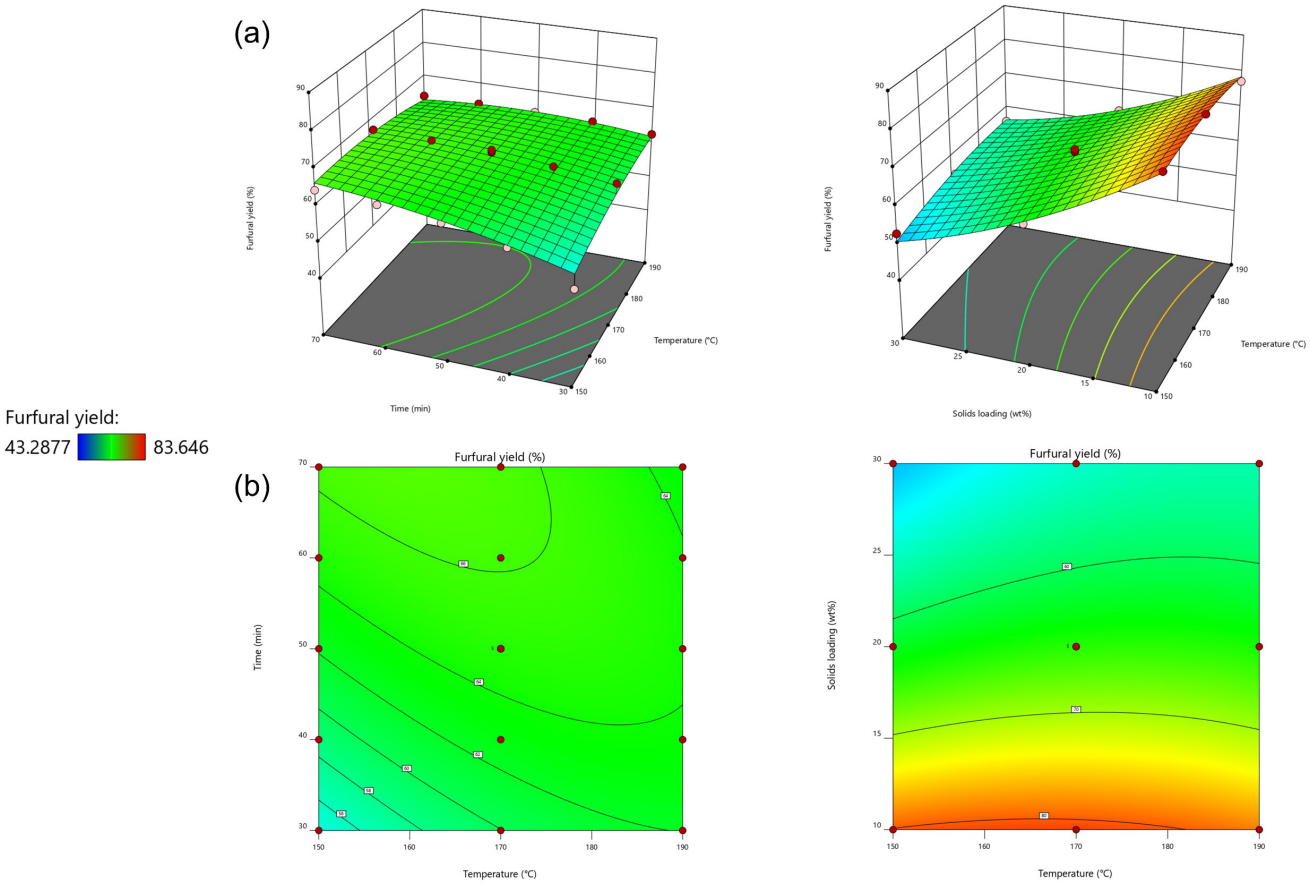


Figure 4.9. (a) 3D response surface plots of furfural yield at the intermediate reaction stage; and (b) The corresponding contour plots of furfural yield at the intermediate reaction stage. (Solids loading was fixed at 20 wt% when temperature and time were taken as the variables, while time was fixed at 50 min when temperature and solids loading were taken as the variables.)

4.3.3.3 Final Reaction Stage (70–110 min)

The reduced quadratic model for the furfural yield in the final reaction stage was established:

$$\text{Furfural yield (\%)} = 5.72 + 1.32 \times T + 0.2611 \times t - 4.44 \times S - 0.0014 \times T \times t + 0.0096 \times T \times S - 0.0043 \times T^2 + 0.0390 \times S^2 \quad (4.10)$$

This model showed the strongest statistical fit, with the highest adjusted R^2 of 0.9923 and predicted R^2 of 0.9909. Because furfural release was nearly complete in this stage, its yield varied little with time, enhancing the model's predictability. As displayed in

Table 4.3, the ANOVA confirmed the model's strength (F-value = 888.43, P-value < 0.0001) and showed an insignificant lack of fit (F-value = 0.2183, P-value = 0.9958).

Solids loading was still the strongest linear factor affecting the furfural yield (F-value = 5784.36, P-value < 0.0001), followed by temperature (F-value = 97.43, P-value < 0.0001). Their interaction was also significant (F-value = 90.01, P-value < 0.0001). At 10 wt% solids loading, higher temperatures lowered the furfural yield, whereas yields at 20 wt% and 30 wt% were largely temperature-independent. At 150 °C, raising the solids loading from 10 wt% to 30 wt% markedly reduced the yield, while this effect was less pronounced at 170–190 °C. Reaction time had only a minor influence (F-value = 9.53, P-value = 0.0036) because most hemicellulose hydrolysis was complete. Significant curvature terms for the solids loading (S^2, F-value = 212.47, P-value < 0.0001) and temperature (T^2, F-value = 41.56, P-value < 0.0001) underlined the system's nonlinear behavior.

Table 4.3. ANOVA results for the reduced quadratic model fitted to the semi-continuous furfural production data from 70 to 110 min.

Source	Sum of Squares	df	Mean Square	F-value	p-value
Model (70-110min)	5088.67	7	726.95	888.43	< 0.0001
T-Temperature	79.72	1	79.72	97.43	< 0.0001
t-Time	7.80	1	7.80	9.53	0.0036
S-Solids loading	4733.02	1	4733.02	5784.36	< 0.0001
Tt	4.46	1	4.46	5.45	0.0246
TS	73.65	1	73.65	90.01	< 0.0001
T^2	34.01	1	34.01	41.56	< 0.0001
S^2	173.86	1	173.86	212.47	< 0.0001
Residual	33.55	41	0.8182		
Lack of Fit	22.44	37	0.6064	0.2183	0.9958

Pure Error	11.11	4	2.78
Cor Total	5122.21	48	

R^2 = 0.9935; Adjusted R^2 = 0.9923; Predicted R^2 = 0.9909

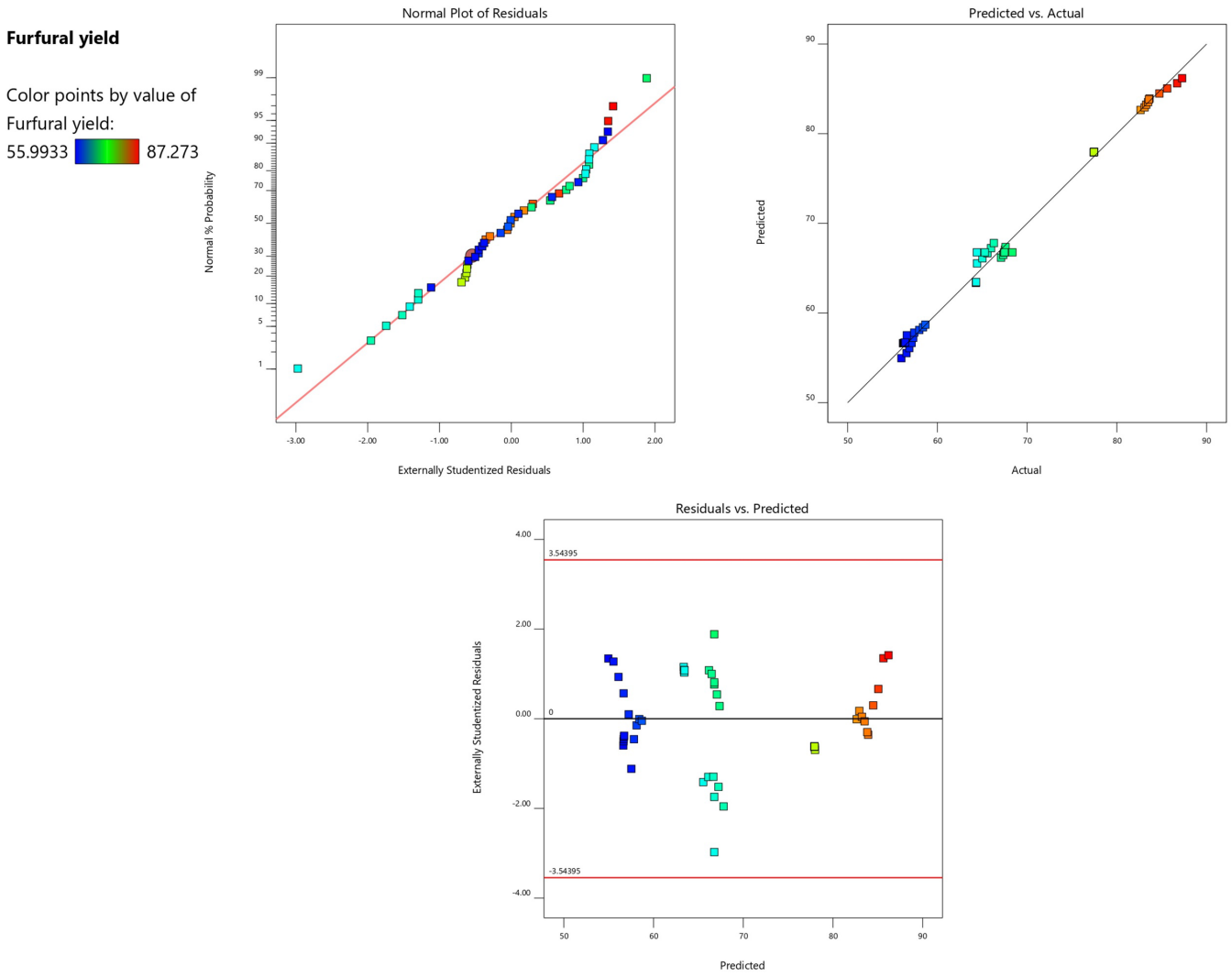


Figure 4.10. Diagnostic plots of the reduced quadratic model fitted to the semi-continuous furfural production data from 70 to 110 min.

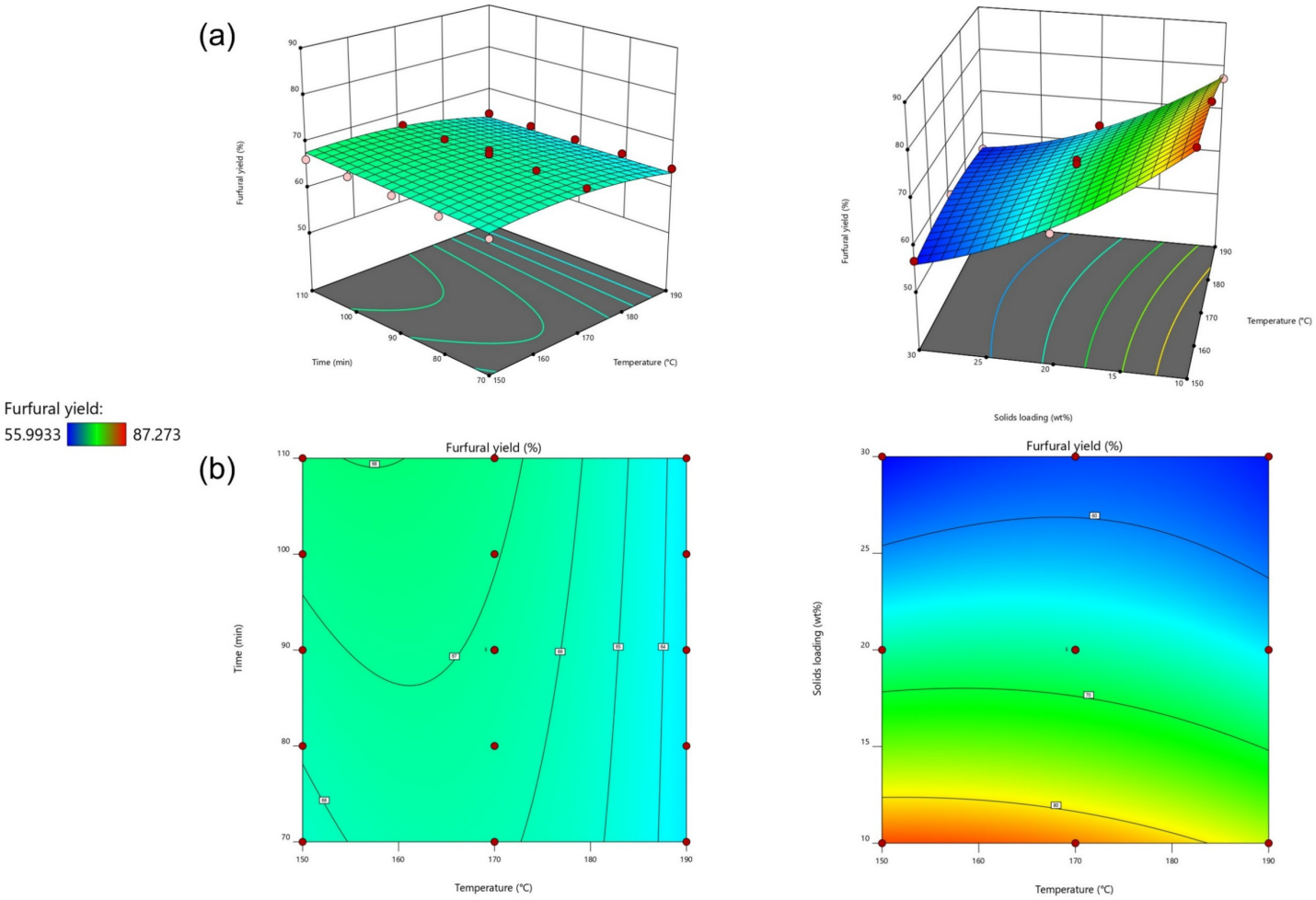


Figure 4.11. (a) 3D response surface plots of furfural yield at the final reaction stage; and (b) The corresponding contour plots of furfural yield at the final reaction stage. (Solids loading was fixed at 20 wt% when temperature and time were taken as the variables, while time was fixed at 90 min when temperature and solids loading were taken as the variables.)

4.3.3.4 Overall Reaction (10–110 min)

A single reduced quadratic model was fitted to all data collected from 10 min to 110 min:

$$\text{Furfural yield (\%)} = -130.85 + 2.10 \times T + 1.96 \times t - 4.20 \times S - 0.0065 \times T \times t + 0.0086 \times T \times S - 0.0052 \times T^2 - 0.0053 \times t^2 + 0.0370 \times S^2 \quad (4.11)$$

Using one model to describe the entire reaction process reduced the fit quality, with an adjusted $R^2 = 0.9117$ and a predicted $R^2 = 0.8958$, which are lower than the values

achieved with the stage-specific models. This result underscores the process's complexity and variability, which the stage-specific models capture more effectively. Even so, the unified model's adjusted and predicted R^2 values are still high enough to represent the overall furfural production profile.

As summarized in Table 4.4, the solids loading was still the most influential factor, with an F-value of 575.83, more than twice that of the reaction time (F-value = 259.39). The temperature was the weakest linear term but still significant (F-value = 15.25, P-value = 0.0002). The interactions of the solids loading with temperature (F-value = 7.00, P-value = 0.0096) and with time (F-value < 0.001, P-value $\gg$ 0.05) were far less important, suggesting that the strong main effect of the solids loading may mask these interaction effects. In contrast, the temperature × time interaction was pronounced (T × t, F-value = 60.64, P-value < 0.0001), consistent with the diminishing influence of temperature on the yield as the reaction progressed. The quadratic term for the reaction time (t^2) was also significant (F-value = 123.24), matching the observed gradual decrease in the furfural release rate from 10 to 110 min.

Table 4.4. ANOVA results for the reduced quadratic model fitted to the semi-continuous furfural production data from 10 to 110 min.

Source	Sum of Squares	df	Mean Square	F-value	p-value
Model (10-110 min)	19579.83	8	2447.48	132.69	< 0.0001
T-Temperature	281.22	1	281.22	15.25	0.0002
t-Time	4784.47	1	4784.47	259.39	< 0.0001
S-Solids loading	10621.18	1	10621.18	575.83	< 0.0001
Tt	1118.43	1	1118.43	60.64	< 0.0001
TS	129.03	1	129.03	7.00	0.0096
T^2	102.40	1	102.40	5.55	0.0205
t^2	2273.16	1	2273.16	123.24	< 0.0001

S^2	322.23	1	322.23	17.47	< 0.0001
Residual	1733.84	94	18.45		
Lack of Fit	1719.25	90	19.10	5.24	0.0574
Pure Error	14.59	4	3.65		
Cor Total	21313.66	102			

R^2 = 0.9187; Adjusted R^2 = 0.9117; Predicted R^2 = 0.8958

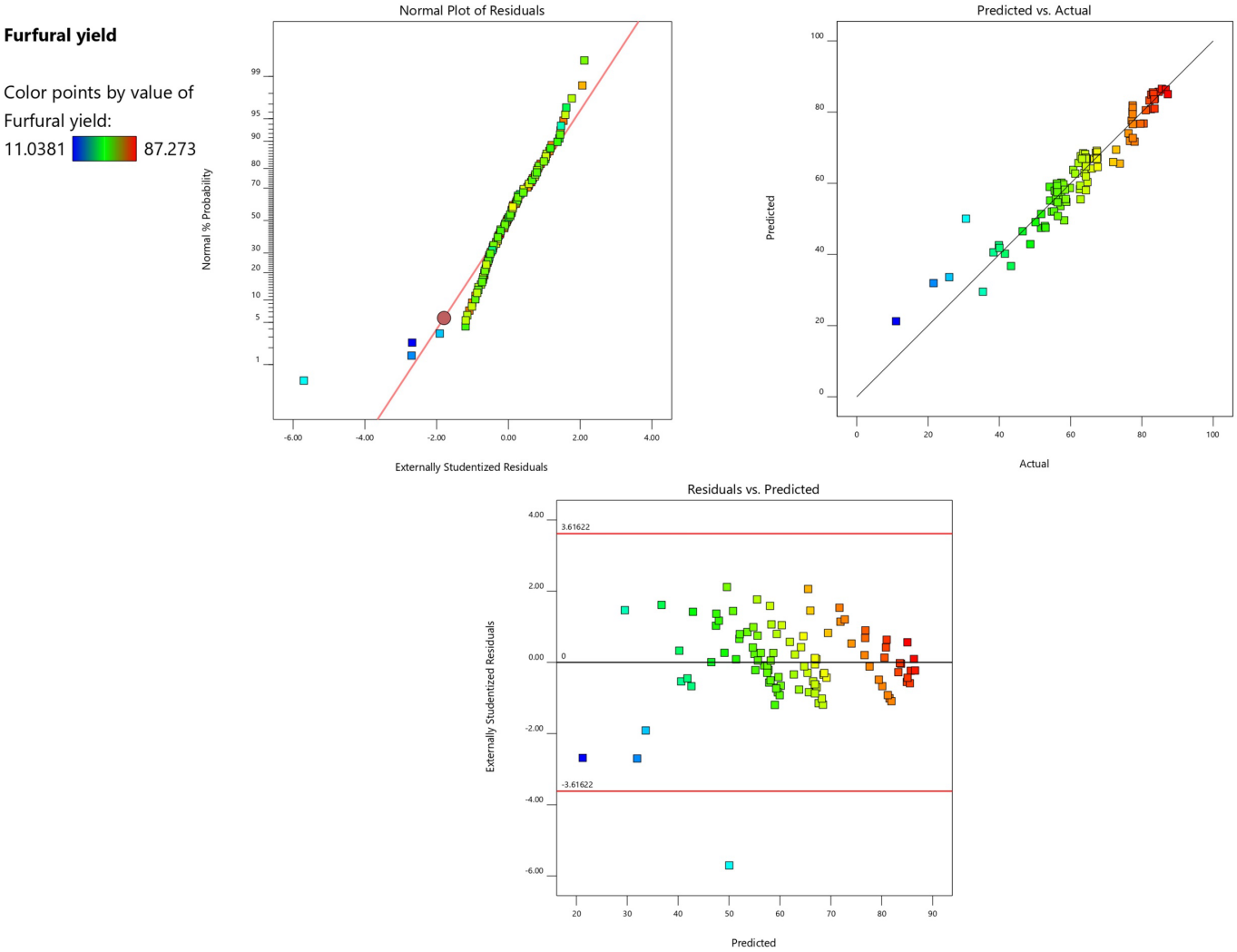


Figure 4.12. Diagnostic plots of the reduced quadratic model fitted to the semi-continuous furfural production data from 10 to 110 min.

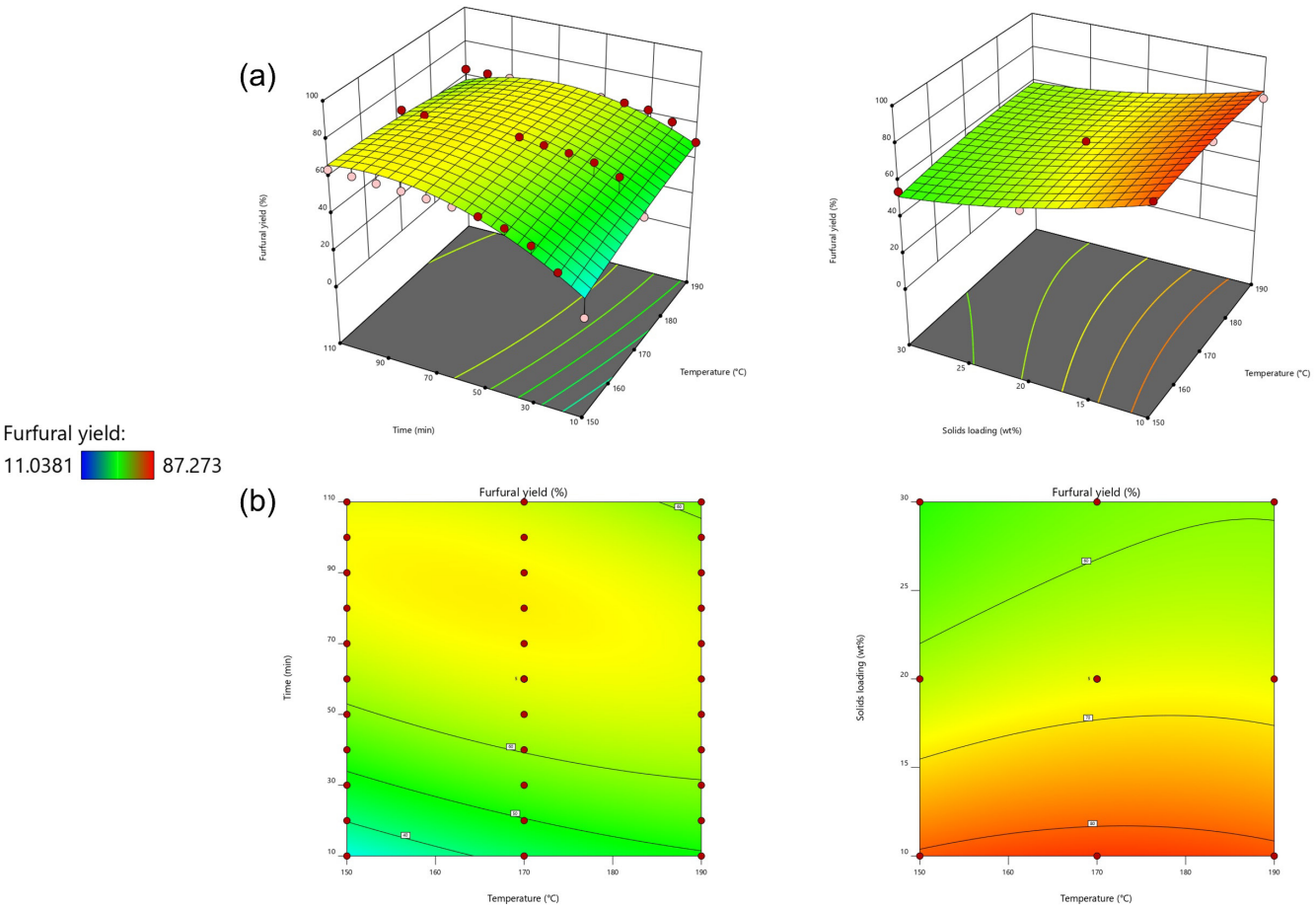


Figure 4.13. (a) 3D response surface plots of furfural yield for the whole production process; and (b) The corresponding contour plots of furfural yield for the whole production process. (Solids loading was fixed at 20 wt% when temperature and time were taken as the variables, while time was fixed at 60 min when temperature and solids loading were taken as the variables.)

In conclusion, the RSM quantified how temperature, time, and solids loading shape furfural production. Dividing the production process into initial, intermediate, and final stages improved the model fit, as confirmed by the higher adjusted and predicted R^2 values. Solids loading was the most influential parameter throughout. Lower loadings produced higher yields, largely regardless of temperature or time. Reaction time strongly influenced the yields in the initial and intermediate stages but had little effect in the final stage. Higher temperatures sped up the furfural release early on yet did not change the final yields at 20 wt% and 30 wt% solids loadings. Because the solids

loading was the dominant factor and interacted only weakly with temperature and time, adjusting either offered little scope to improve furfural yields at high loadings. Therefore, new strategies are required to raise furfural yields at 30 wt% solids loading and above.

4.3.4 Optimization of Furfural Yield at High Biomass Loading (30 wt%)

4.3.4.1 Stepwise Biomass Addition

According to our observations, keeping the biomass loading as low as possible can maximize the furfural yield. When a high loading of 30 wt% is required, adding the biomass stepwise rather than in a single charge may help. This approach restricts the amount of biomass added at each step, allows the IL to wet and dissolve the biomass more efficiently, keeps the slurry viscosity lower in the early reaction stage, and thereby suppresses the side reactions that consume furfural. An effective addition protocol should leave sufficient time to convert the hemicellulose fraction into furfural and strip the product out, without excessively prolonging the overall run. In this section, the efficacy of the multi-step biomass addition strategy was evaluated.

As shown in Figure 4.14 a, a two-step biomass addition with a 20-min interval produced only a modest 3.4% increase in the furfural yield compared with a single addition. Specifically, the yield reached 30.6% in the first 20 min after the initial addition but fell to 26.0% in the 20–40 min period following the second addition, indicating that the reaction environment had deteriorated. This drop stemmed mainly from the more viscous biomass–IL slurry after the second addition, where the higher substrate concentration promoted side reactions that consumed furfural. Extending the interval to 40 min gave a similar result, improving the overall yield by just 2.0% over the single addition. These findings suggest that adding biomass more frequently, in smaller portions, may relieve the adverse effects of sudden jumps in the substrate concentration.

Indeed, adding biomass in three equal portions, with a 20-min interval, greatly raised the furfural yield to 72.8% (Figure 4.14 b). Yields for 0–20, 20–40, and 40–60 min were

23.2%, 22.7%, and 20.4%, respectively, indicating that three additions maintained a stable reaction environment. Smaller, staggered additions slowed the build-up of the substrate concentration and therefore limited furfural loss to side reactions with lignin and other hydrolysates. Further increasing the number of additions to four and five produced furfural yields of 75.1% and 72.2%, respectively, with only marginal variation. These results demonstrate that three to four additions already allow the IL to dissolve biomass effectively, maintain catalytic activity, and keep the transient furfural concentration low enough to suppress concentration-driven side reactions. Splitting the addition any further has very little effect on that concentration, so the overall yield no longer improves.

In conclusion, the stepwise biomass addition is an effective way to boost furfural production at the high biomass loading of 30 wt%. The four-step addition delivered the best result, a 16.3% increase over the single addition, whereas further subdivision showed no extra benefit. This optimal addition pattern streamlines the process and improves the overall efficiency.

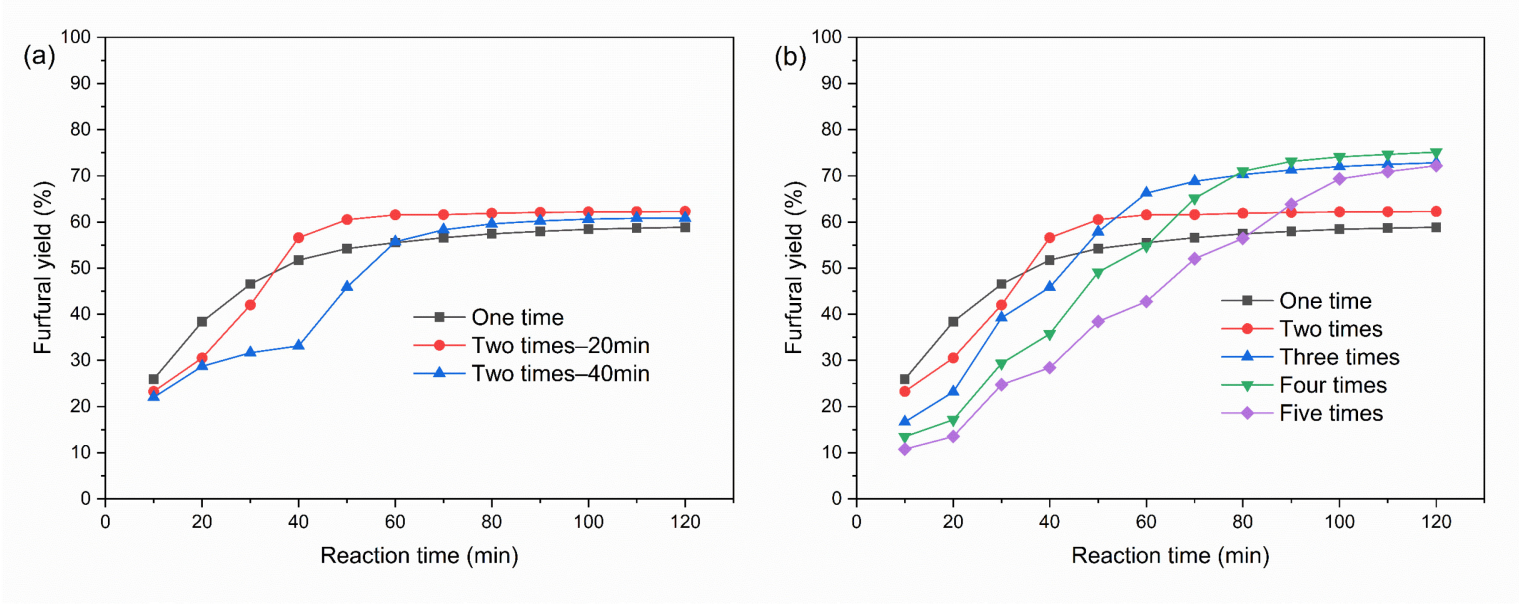


Figure 4.14. Effect of stepwise biomass addition on furfural release from the semi-continuous production system at 170 °C for 120 min with 30 wt% solids loading of sugarcane bagasse (180–850 μm). (a) Two-step biomass addition with an addition

interval of 20 or 40 min; and (b) Multi-step biomass additions with an addition interval of 20 min.

4.3.4.2 Particle Size Screening

The biomass-dissolving capacity of the IL highly depends on the particle size of the biomass. Finer particles accelerate the hydrolysis and dehydration of the hemicellulose fraction to furfural by providing a higher available surface area, yet this also sharply raises the instantaneous substrate concentration in the IL, which can in turn trigger concentration-driven side reactions. To boost the furfural yield at 30 wt% biomass loading, we conducted a particle size analysis (<180 μm, 180–850 μm, 850 μm–2 mm, and 2–4 mm) to assess whether faster biomass dissolution could favor the main hydrolysis pathway over these side reactions.

Unexpectedly, Figure 4.15 shows that larger particle sizes were more favorable for furfural release. Specifically, the 2–4 mm and 850 μm–2 mm fractions achieved yields of 63.5% and 64.6%, respectively, whereas the 180–850 μm fraction fell slightly to 58.9%. The finest size fraction (<180 μm) produced the lowest yield of only 46.1%. Although the powder-like <180 μm fraction offered a much larger surface area that facilitated the rapid biomass wetting and dissolution in the IL, the resulting high concentrations of furfural and potential inhibitors (e.g., sugar degradation products and lignin fragments) that accumulated in the IL appeared to accelerate liquid-phase side reactions. As the particle size increased to a more fibrous form, the IL penetration slowed, leading to a more controlled and even biomass dissolution and hydrolysis. The concentrations of furfural and potential inhibitors built up more slowly in the IL, relieving the intensity of side reactions compared with the powder-like fraction. Consequently, furfural had enough time to leave the reaction system, an advantage similar to that achieved with the stepwise biomass addition. Notably, although the yield gains for the 850 μm–2 mm and 2–4 mm fractions over the 180–850 μm fraction were modest (4.6–5.7%), using coarser material could significantly reduce energy-intensive grinding costs, as biomass comminution can account for up to 60% of pretreatment energy use

and about 10% of overall costs [42, 460]. These findings support the feasibility of reducing biomass comminution in the semi-continuous system at a high biomass loading of 30 wt%, offering significant economic benefits through energy savings.

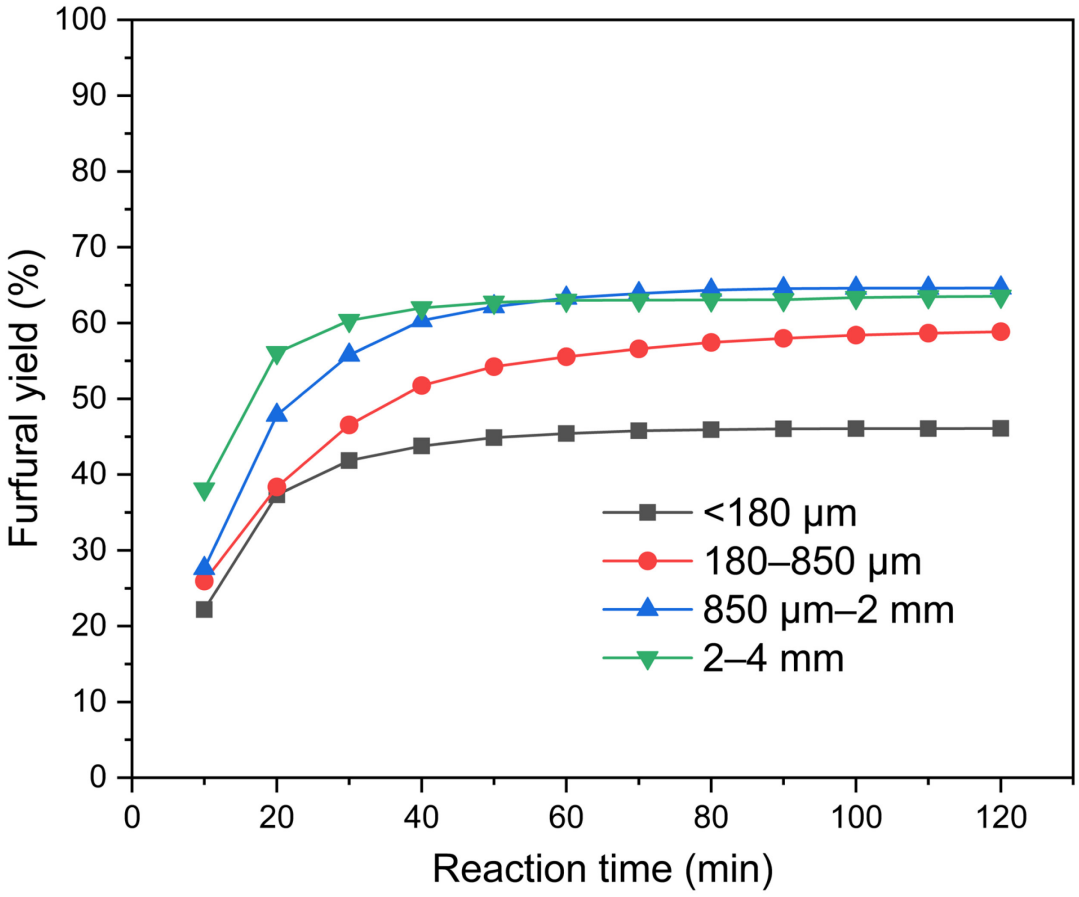


Figure 4.15. Effect of particle size on furfural release from the semi-continuous production system at 170 °C for 120 min with 30 wt% biomass loading.

4.3.5 Recyclability Evaluation of [DMBA][HSO_4]

The recyclability of [DMBA][HSO_4] is critical for large-scale viability. To assess this, five treatment cycles were conducted at 170 °C for 1 h with 20 wt% biomass loading, employing a two-step biomass addition protocol. The IL recovery rates for cycles 1–5 were 100%, 98.16%, 96.95%, 97.91%, and 97.60%, respectively, indicating that very little make-up solvent was required. Techno-economic models have shown that maintaining recovery rates above 96% is essential for profitability, even with low-cost ILs [19, 461, 462]. Moreover, Figure 4.16 shows that the furfural yields during recycling

remained within 69.4–74.5% (except for cycle 3), consistent with the inherent variability of the system. The lower yield observed in cycle 3 (65.4%) was likely attributable to operational uncertainty in the experimental setup, rather than indicating a systematic deterioration of the IL recycling performance. These results suggest that [DMBA][HSO_4] can maintain its efficiency over at least five reuse cycles owing to its high thermal stability. ^{1}H and ^{13}C NMR spectra of the fresh and recycled [DMBA][HSO_4] further confirmed the absence of detectable IL degradation after five cycles (Figures 4.17–4.20).

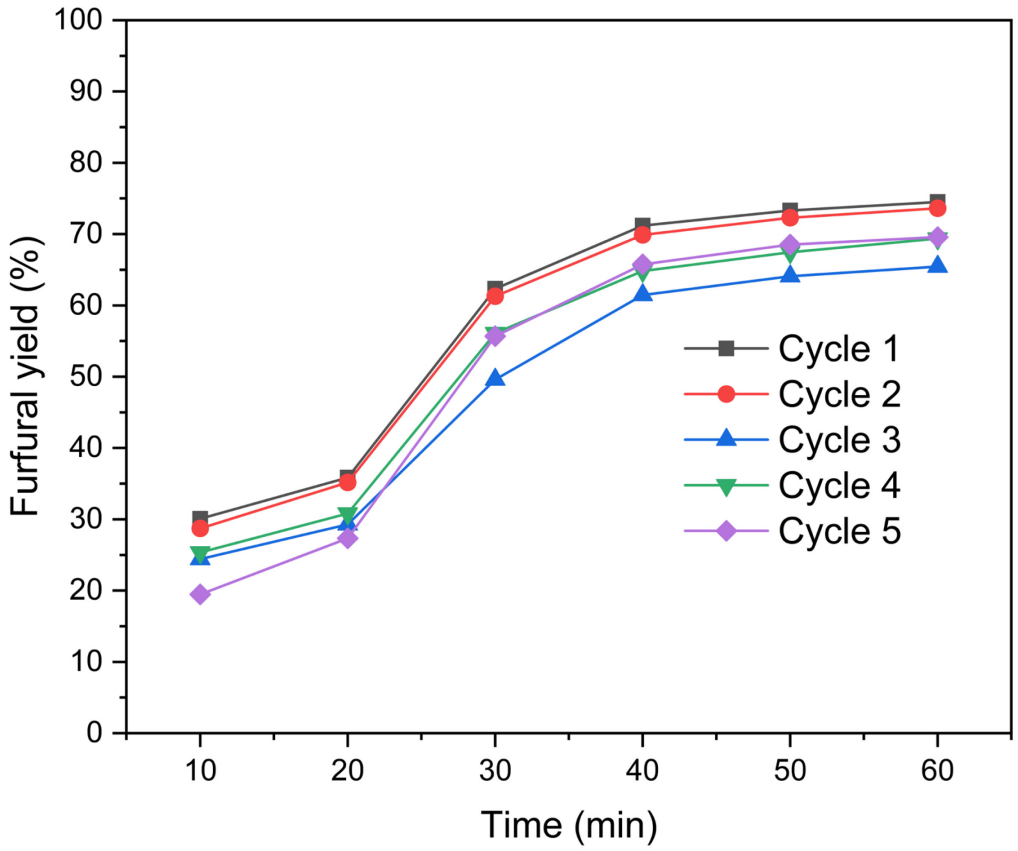


Figure 4.16. Recyclability evaluation of [DMBA][HSO_4] at 170 °C for 60 min with 20 wt% solids loading of sugarcane bagasse (180–850 μm), using a two-step biomass addition protocol with a 20-min addition interval.

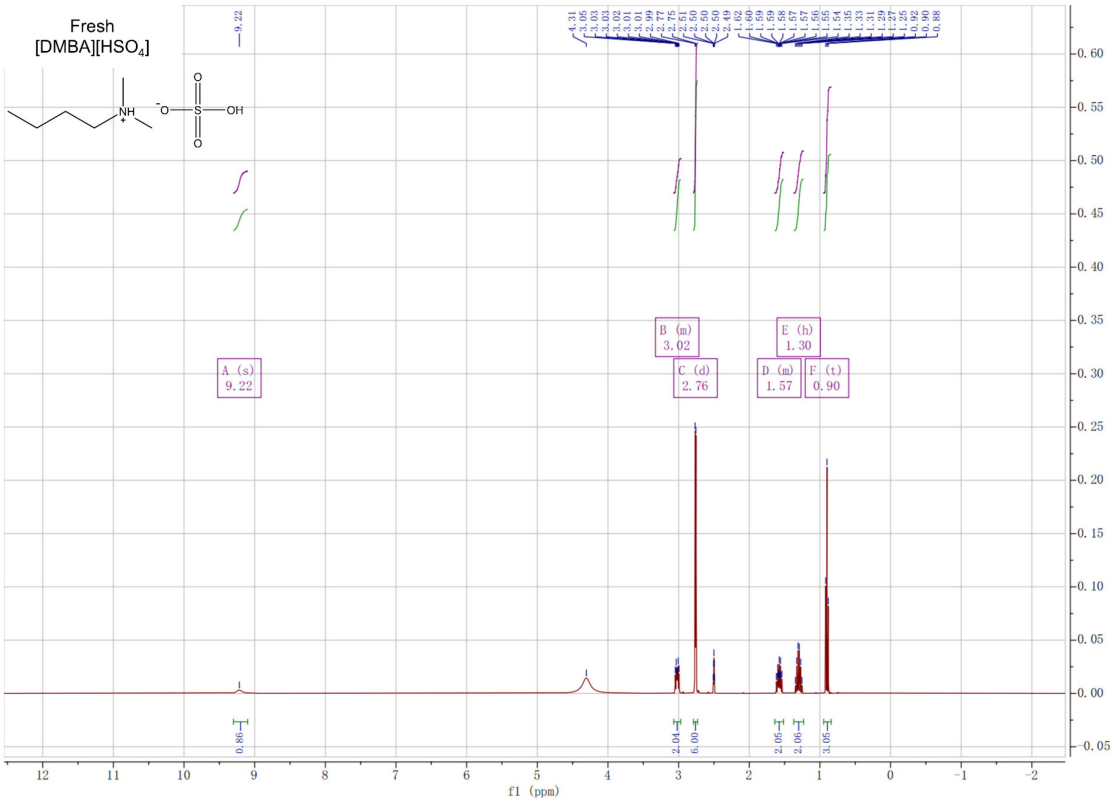


Figure 4.17. ^{1}H NMR of fresh [DMBA][HSO_4]: δ_H (400 MHz, DMSO-d_6)/ppm: 9.22 (s, 1H, N–*H*), 3.07–2.97 (m, 2H, N–CH_2), 2.76 (d, *J* = 4.9 Hz, 6H, N–(CH_3)$_2$), 1.64–1.52 (m, 2H, N–CH_2–CH_2), 1.30 (h, *J* = 7.3 Hz, 2H, N–CH_2–CH_2–CH_2), 0.90 (t, *J* = 7.4 Hz, 3H, N–CH_2–CH_2–CH_2–CH_3).

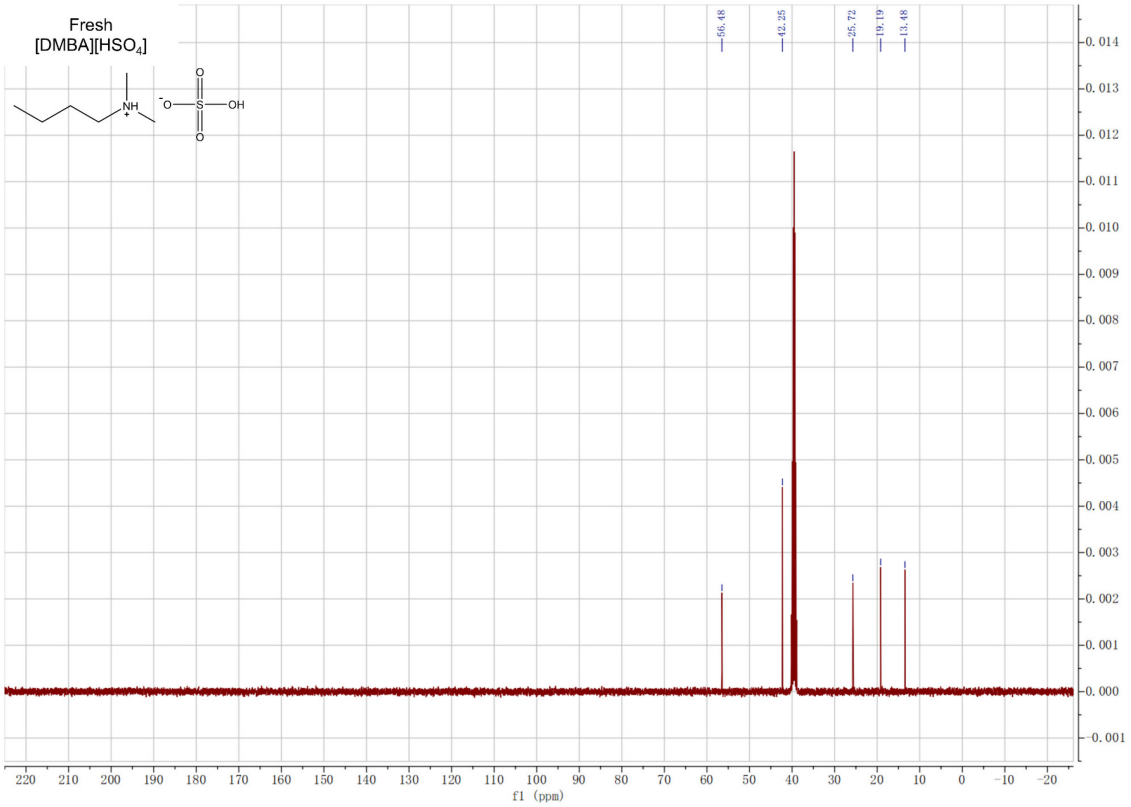


Figure 4.18. ^{13}C NMR of fresh [DMBA][HSO_4]: δ_C (101 MHz, DMSO-d_6)/ppm: 56.48 (N–*C*H_2), 42.25 (N–(*C*H_3)$_2$), 25.72 (N–CH_2–*C*H_2), 19.19 (N–CH_2–CH_2–*C*H_2), 13.48 (N–CH_2–CH_2–CH_2–*C*H_3).

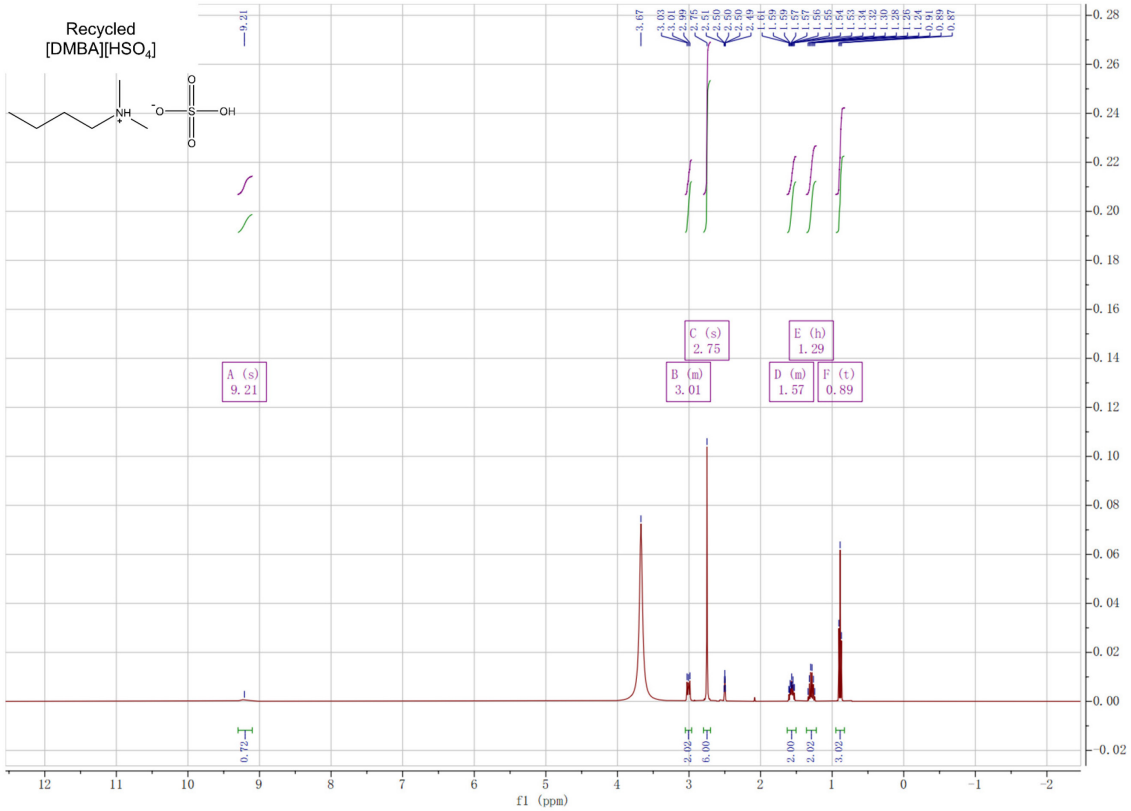


Figure 4.19. ^{1}H NMR of [DMBA][HSO_4] recovered from cycle 5: δ_H (400 MHz, DMSO-d_6)/ppm: 9.21 (s, 1H, N–*H*), 3.05–2.96 (m, 2H, N–CH_2), 2.75 (s, 6H, N–(CH_3)$_2$), 1.63–1.51 (m, 2H, N–CH_2–CH_2), 1.29 (h, *J* = 7.3 Hz, 2H, N–CH_2–CH_2–CH_2), 0.89 (t, *J* = 7.4 Hz, 3H, N–CH_2–CH_2–CH_2–CH_3).

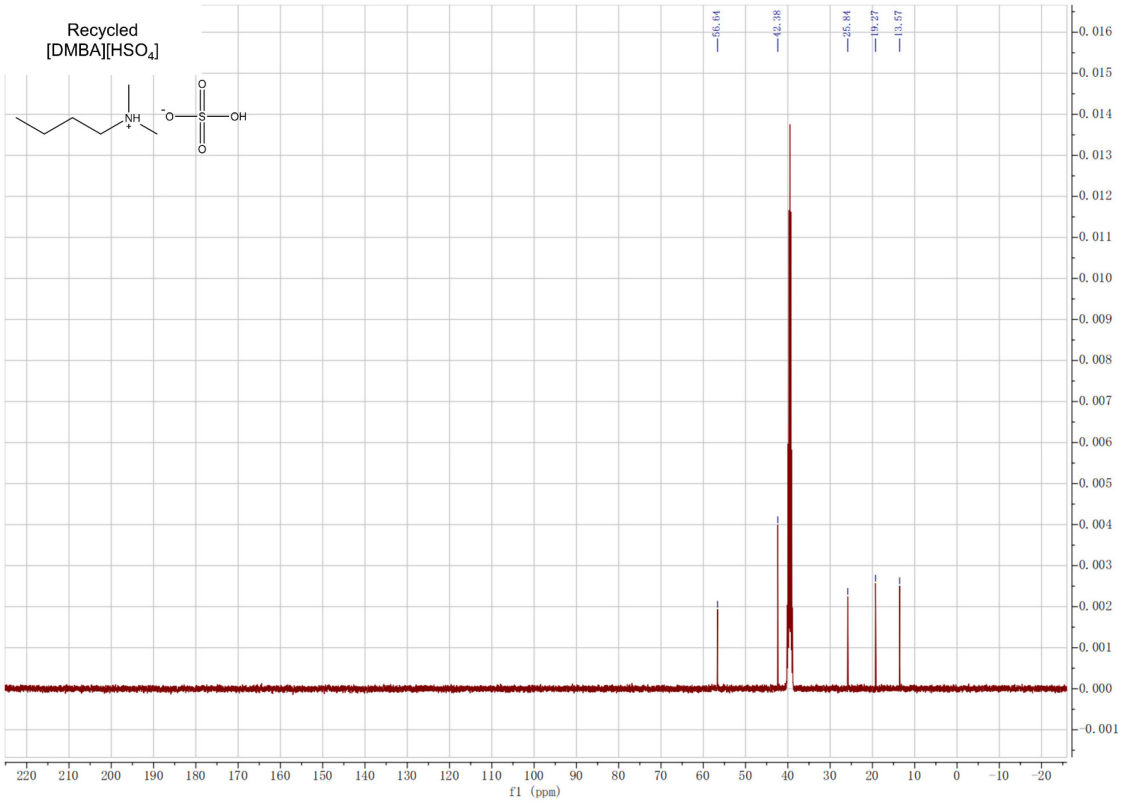


Figure 4.20. ^{13}C NMR of [DMBA][HSO_4] recovered from cycle 5: δ_C (101 MHz, DMSO-d_6)/ppm: 56.64 (N–*C*H_2), 42.38 (N–(*C*H_3)$_2$), 25.84 (N–CH_2–*C*H_2), 19.27 (N–CH_2–CH_2–*C*H_2), 13.57 (N–CH_2–CH_2–CH_2–*C*H_3).

4.3.6 Characterization of Solid Residues from the IL Recycling Process

The valorization of solid residues (biochars) is important for biorefinery profitability. Therefore, biochar samples were collected after each IL recycling run for detailed analysis (Table 4.5). The yields of the recovered biochars fluctuated between 42.88% and 57.45%. The conversion of raw biomass to biochars markedly increased the carbon (C) content from 41.25% to 58.15–63.20% and reduced the hydrogen (H) and oxygen (O) contents from 5.74% and 48.59% to 4.64–4.92% and 27.15–30.73%, respectively. This carbon enrichment, driven by dehydration and C–C condensation reactions, produced energy-dense materials suitable for bioenergy applications [37]. Interestingly, the sulfur (S) content, undetected in the raw biomass, was present in the biochars at 1.14–1.95% after IL treatment, probably from residual $[HSO_4]^-$. The

nitrogen (N) content also increased from 0.46% (raw biomass) to 0.50–0.86%. Elevated S and N contents in the biochars can generate pollutant emissions during combustion (e.g., SO_2, NO_x, and NH_3), limiting their suitability as value-added fuels [463, 464]. To address this, the biochars were Soxhlet-washed with water overnight. As shown in Table 4.5, the C content of the biochars from cycles 1 and 5 remained stable after washing, preserving their energy value. In contrast, the S content decreased to 0.59% (cycle 1) and 0.72% (cycle 5) after washing, supporting the removal of $[HSO_4]^-$. The N content showed a similar pattern, dropping to 0.25% (cycle 1) and 0.69% (cycle 5), attributable to the removal of residual $[DMBA]^+$. Notably, after washing, the N content was significantly lower than that of lignite (1.03%) and anthracite (1.13–1.98%), while the S content was comparable to lignite (0.73%) and close to anthracite (0.39–0.44%) [454, 465]. The lower S and N levels contribute to cleaner fuel performance during the biochar combustion [463, 464].

The study also examined the evolution of H/C and O/C atomic ratios in the biochars, as shown on the Van Krevelen diagram (Figure 4.21), to illustrate their degree of coalification [466, 467]. It can be observed that biochar formation was driven mainly by dehydration, which markedly reduced the H/C and O/C ratios compared with the raw biomass and produced more chemically stable and durable structures. This down-left shift on the Van Krevelen diagram is consistent with trends widely reported for biochars produced by slow pyrolysis and hydrothermal carbonization [466, 468-471]. According to the guidelines proposed by Spokas et al., the biochars generated in this process, with O/C ratios of 0.32–0.40, were estimated to have half-lives of 100–1,000 years, far longer than that of raw biomass (<100 years) [472]. These extended half-lives make the biochars attractive for carbon sequestration and confer carbon-negative credentials on a wide range of biochar-derived products. Moreover, on the Van Krevelen diagram, the migration of the biochars' positions toward the lignite zone highlighted their potential as an alternative to traditional coal. Their higher heating values (HHVs) climbed from 16.05 MJ kg^{-1} for the raw biomass to 22.94–24.88 MJ kg^{-1} after the IL treatment, a gain attributable to the transformation of low-energy C–H

and C–O bonds into higher-energy C–C bonds [473, 474]. Although the HHVs of the biochars are close to that of lignite (23.51 MJ kg^{-1}), their much lower ash contents (2.27–3.69% versus lignite's 13.14%) offer additional advantages, including reduced slagging in boilers, enhanced combustion efficiency, lower particulate emissions, and lower ash disposal demands [454, 475, 476].

In summary, the biochars obtained from furfural production represent stable, energy-rich solid fuels with a smaller environmental footprint, which are beneficial for enhancing the sustainability and economic viability of the overall biorefinery process.

Table 4.5. Characterization of sugarcane bagasse (SB) and biochars on an oven-dried basis.

Sample	biochar yield (%)	Element and ash contents (wt%)					
		C	H	O	N	S	Ash
SB	–	41.25	5.74	48.59	0.46	0.00	3.97
Cycle 1	42.88	62.52	4.64	28.04	0.50	1.14	3.17
Cycle 2	57.45	58.51	4.75	30.61	0.74	1.71	3.69
Cycle 3	56.25	58.15	4.92	30.73	0.86	1.95	3.40
Cycle 4	52.56	61.21	4.75	28.16	0.74	1.52	3.63
Cycle 5	47.36	63.29	4.64	27.15	0.83	1.83	2.27
Washed cycle 1	–	61.57	4.73	29.32	0.25	0.59	3.56
Washed cycle 5	–	63.11	4.78	27.34	0.69	0.72	3.37

Sample	Retention rate (%)				Atomic ratio		HHV
	C	H	O	N	H/C	O/C	(MJ kg^{-1})
SB	–	–	–	–	1.67	0.88	16.05
Cycle 1	65.00	34.63	24.75	47.12	0.89	0.34	24.43
Cycle 2	81.50	47.55	36.19	93.44	0.97	0.39	22.94

Cycle 3	79.29	48.21	35.57	106.31	1.02	0.40	23.03
Cycle 4	78.00	43.45	30.46	84.90	0.93	0.35	24.11
Cycle 5	72.68	38.29	26.46	85.88	0.88	0.32	24.88
Washed cycle 1	–	–	–	–	0.92	0.36	24.01
Washed cycle 5	–	–	–	–	0.91	0.32	24.82

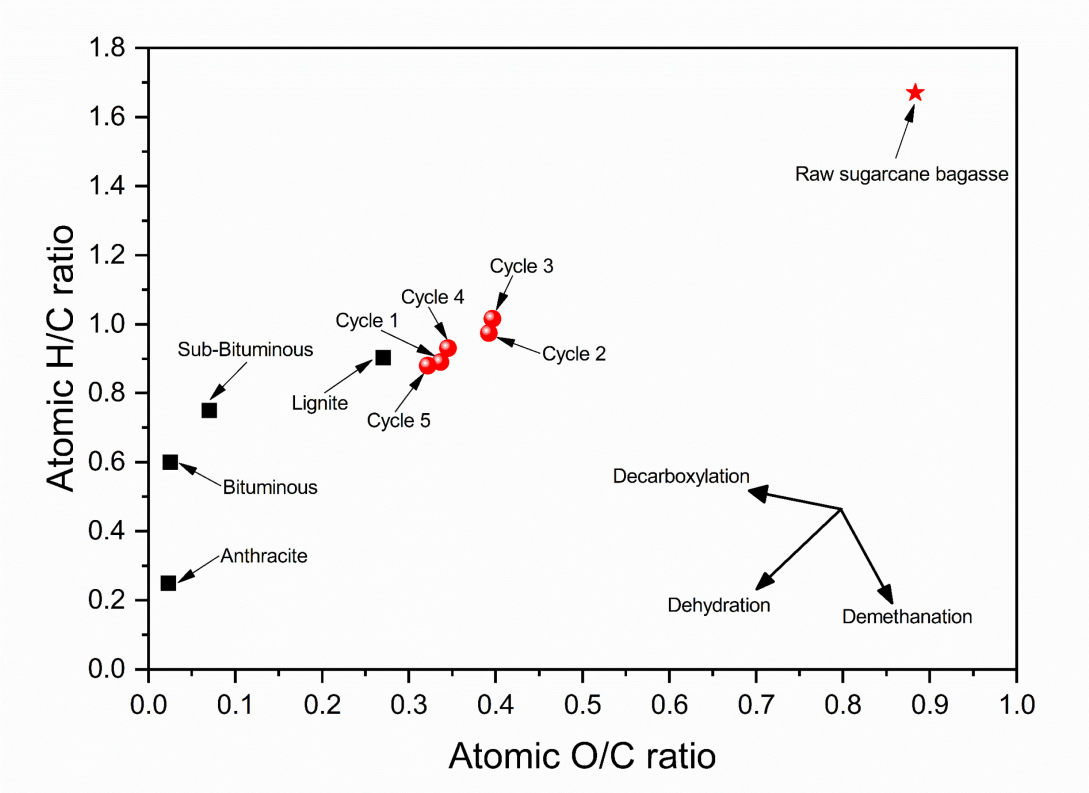


Figure 4.21. Van Krevelen diagram of sugarcane bagasse and its derived biochars (cycles 1–5).

4.3.7 Preliminary Techno-Economic Analysis

Aspen Plus v11 was employed for large-scale process simulation and cost estimation based on the experimental process developed in this work (Figure 4.22). The IL was mixed in the desired ratio with the feedstock (defined as a mixture of cellulose, xylan, galactan, arabinan, and lignin, with proportions based on the experimental composition of the sugarcane bagasse), heated to the treatment temperature using a Heater module, and then fed to an RStoic reactor module. The desired amount of steam was

also fed to the reactor. Reactions of pentoses (xylan and arabinan) to furfural were defined, and the fractional conversions were set according to the experimental data for each set of reaction conditions simulated. Two outlet streams were obtained: a vapor stream containing water and furfural, and a slurry stream mainly composed of biochar and IL. The furfural–water mixture was compressed to 1.65 bar using a Compr module to increase the temperature to allow for heat integration. The mixture was then cooled (with this heat integrated to produce the steam fed into the reactor) and fed into an Extract column using ethyl acetate as an entrainer to extract furfural from water. The ethyl acetate–furfural mixture was then separated using a RadFrac distillation column, and furfural was obtained with a 98% recovery. The slurry was filtered and washed with 3.75 kg of water per kg of pure IL using a Filter module, and a biochar stream was obtained. According to our previous work, a multi-effect evaporator consisting of four evaporating stages (Flash2 module) was used to evaporate water from the IL–water mixture, allowing the IL to be recovered and recycled [477, 478]. Every required temperature change was simulated using the Heater module, and Pump modules were used where necessary to meet pressure needs. In addition, a combined heat and power (CHP) cycle was simulated to produce heat and electricity from burning the produced biochar to meet the energy demands of the process.

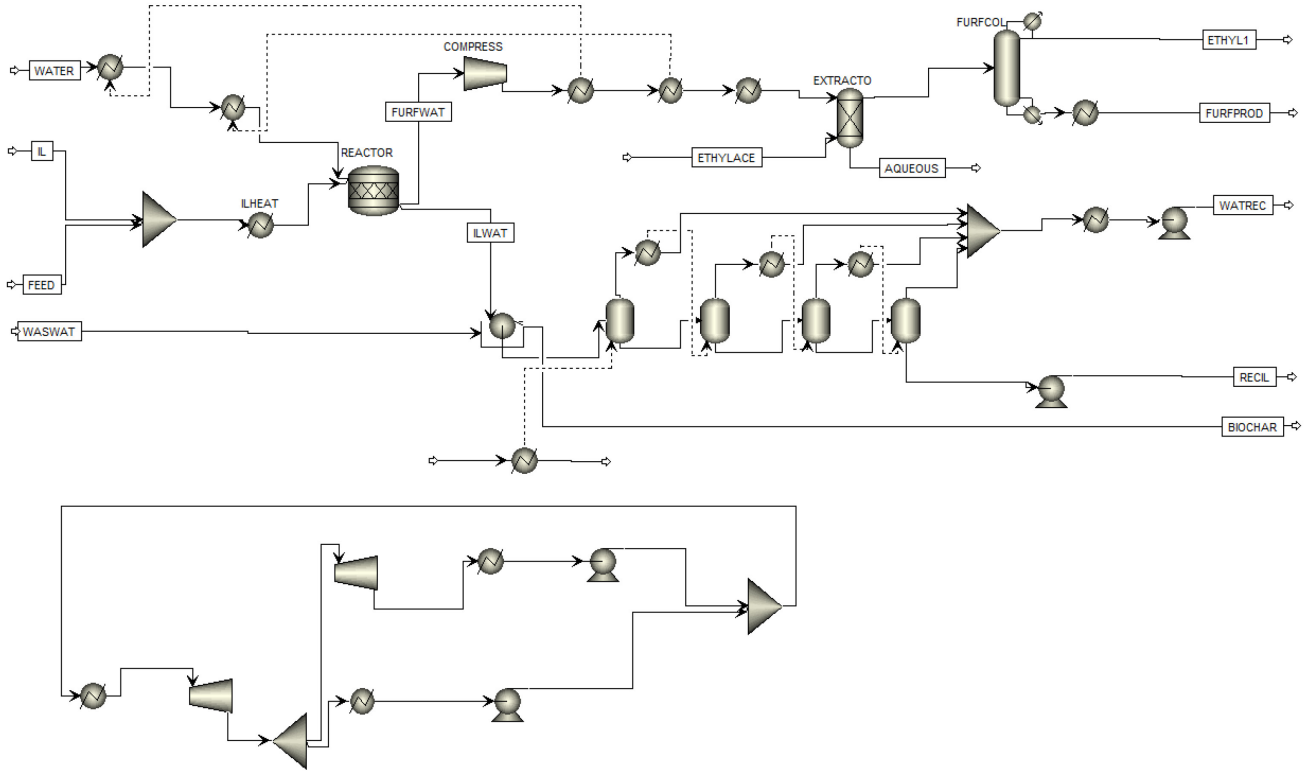


Figure 4.22. Aspen Plus flowsheet for the simulation of the proposed furfural production process, including the CHP cycle used for energy generation (shown at the bottom).

Properties of the main components were obtained from the National Renewable Energy Laboratory biorefinery Aspen models [249]. The Non-Random Two-Liquid (NRTL) thermodynamic model was employed in cases where information about the mixtures was available. In cases where the IL was present and no information was available, the IL was introduced in Aspen Plus as a pseudocomponent, defining the molecular weight, density, and normal boiling point. The COSMO-SAC model was selected for these cases, following our previous publication [478]. The COSMO volume was specified as CSACVL, and the sigma profiles as SGPRF1–5.

The parameters employed for cost calculations can be found in the Appendices (Tables S2–S4), which follow the methodology outlined in our previous work [416]. A plant lifetime of 20 years and a discount rate of 10% were assumed when annualizing the

CAPEX. For the current preliminary evaluation, ethyl acetate was assumed to be fully recovered and recycled (100%). The feedstock and PIL prices were estimated as \$0.01875 kg^{-1} [479, 480] and \$1.24 kg^{-1} [24, 144], respectively.

As shown in Figure 4.22 (the Aspen Plus flowsheet) and Figure 4.23 (the process mass balance), this industrial process can be simplified into five main sections: (1) biomass and IL pre-mixing, (2) furfural and biochar production, (3) furfural purification, (4) combined heat and power production, and (5) IL recovery. Efficient wastewater recovery and reuse in this simulation greatly reduce effluent disposal requirements, mitigating a key drawback of current acid-hydrolysis-based furfural production [59].

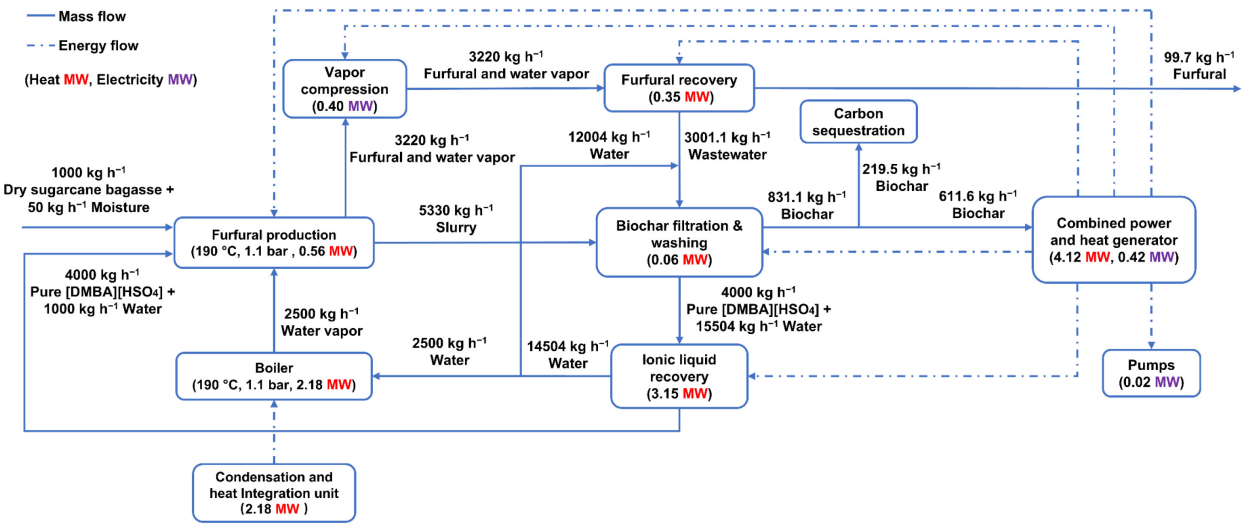


Figure 4.23. Mass balance of the optimized furfural production process at 190 °C and 20 wt% biomass loading (Case 3). Approximately 120 kg h^{-1} of water is unaccounted for after the furfural recovery block because this portion leaves with the ethyl acetate during furfural extraction, a step not shown here.

The simulated minimum selling prices (MSPs) of furfural under five production cases are summarized in Table 4.6. As expected, Case 4 (170 °C, 10 wt% biomass loading), in which our experimental work delivered the highest yield among these cases, exhibited the highest MSP because the lower biomass loading generated insufficient

biochar to supply the high energy duty needed for IL regeneration. In all other cases, the heat and electricity produced by the biochar fully met the process demand, making these operating conditions carbon-neutral with no additional CO_2 emissions. Cases 3 and 5 showed the lowest MSPs. Case 3 benefited from higher furfural productivity at 190 °C, where furfural release was faster (based on experimental data), whereas Case 5 reduced IL make-up costs by operating at a higher biomass loading (30 wt%), which lowered the required IL inventory. The percentage contributions to the MSPs for these two cases are shown in Figure 4.24. Fixed costs accounted for the largest share of the MSPs, at 68.5% in Case 3 and 72.2% in Case 5, indicating that a biomass processing scale of 1,000 kg h^{-1} was not sufficient for process viability. Expanding capacity to exploit economies of scale therefore offers a practical route to further reduce MSPs. Annualized CAPEX was the second largest contributor, highlighting the high capital intensity of the PIL-based biorefinery process. Additionally, the influence of the IL and its make-up costs was significant, representing 11.1% for Case 3 and 7.8% for Case 5, emphasizing the need for improved IL recovery. Notably, although laboratory-scale experiments achieved an average IL recovery rate of 98.1%, this performance may not be fully representative on an industrial scale because higher IL losses commonly occur during sample transfers in laboratory setups.

The variations in the MSPs of furfural at different biomass processing scales and IL recovery rates are shown in Figure 4.25. Biomass input is one of the key factors influencing MSPs, with costs falling sharply as the processing scale increased from 50 to 30,000 kg h^{-1}. Meanwhile, across all processing scales, each 1% improvement in the IL recovery rate reduced MSPs by \$0.50 kg^{-1} (Case 3) and \$0.34 kg^{-1} (Case 5). Using a typical large-scale plant processing 30,000 kg h^{-1} of biomass as a reference and assuming a 99.9% IL recovery rate in an industrial continuous process, the MSPs would drop to \$1.62 kg^{-1} (Case 3) and \$1.54 kg^{-1} (Case 5), with furfural productivities of 2,992 kg h^{-1} (Case 3) and 2,876 kg h^{-1} (Case 5). These MSPs are still not competitive with current furfural market prices, which are in the range of \$1.016–1.479 kg^{-1} [481, 482]. The reason for such inefficiency is related to the impact of fixed costs,

which drops significantly as the biomass processing scale increases to 30,000 kg h^{-1}, but still accounts for 43.2% (Case 3) and 47.2% (Case 5) of the MSPs, because the plant needs to process roughly ten times more biomass than the furfural it produces.

Table 4.6. Furfural productivities, purities, and MSPs under various process conditions.

Label	Process condition [a]		Furfural productivity	Furfural purity	MSP of furfural
	Temperature (°C)	Biomass loading (wt%)	(kg h^{-1})	(%)	($ kg^{-1})
Case 1	150	20	84.21	99.80	10.13
Case 2	170	20	97.82	98.97	8.72
Case 3	190	20	99.74	98.88	8.57
Case 4	170	10	114.15	99.16	12.36
Case 5	170	30	95.86	98.95	8.46

[a] sugarcane bagasse (180–850 μm) processing scale: 1,000 kg h^{-1}; IL recovery rate (experimental average): 98.1%

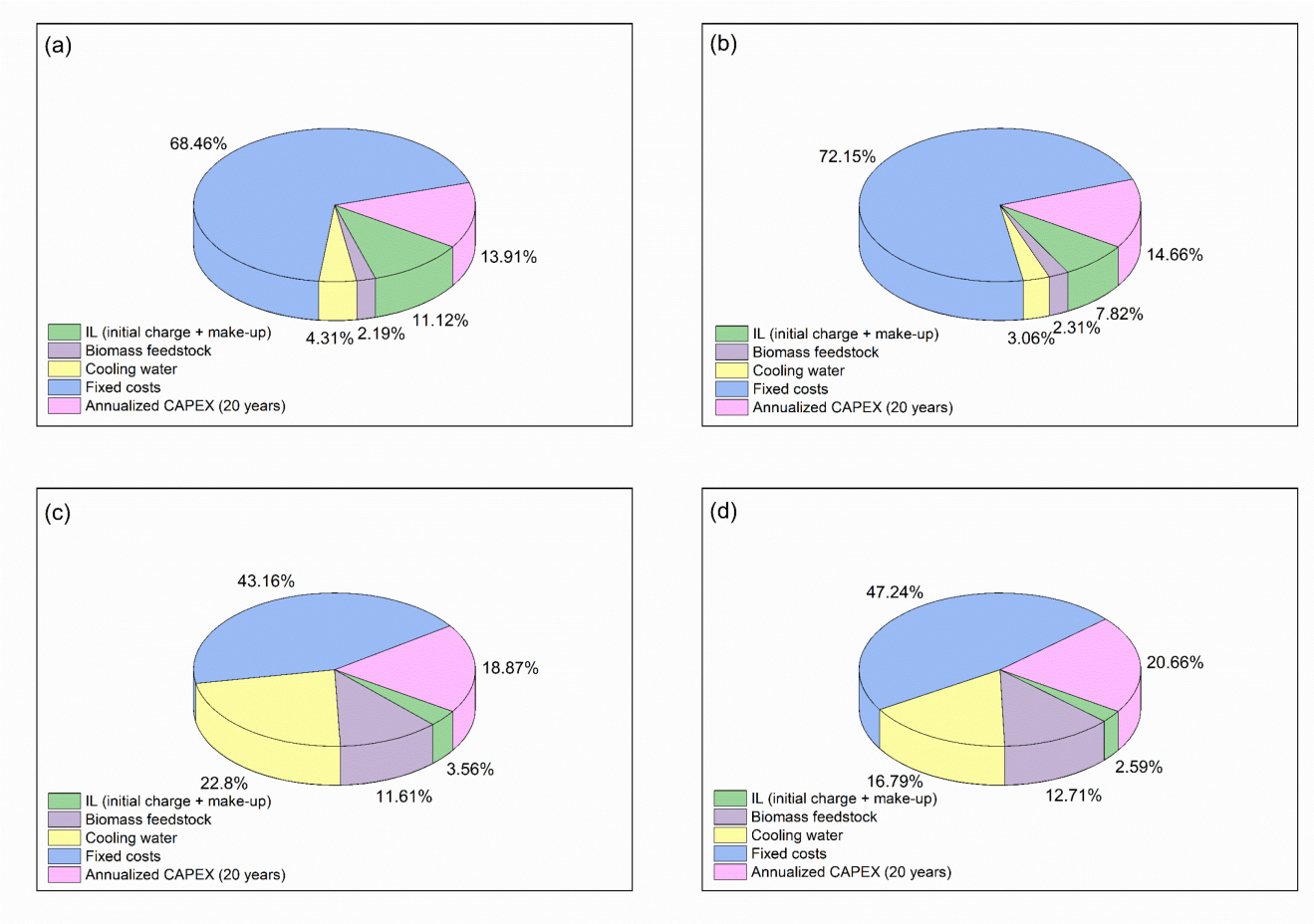


Figure 4.24. Contributions to MSPs of furfural under different operating conditions. (a) Case 3: biomass processing scale of 1,000 kg h^{-1} and IL recovery rate of 98.1%; (b) Case 5: biomass processing scale of 1,000 kg h^{-1} and IL recovery rate of 98.1%; (c) Case 3: biomass processing scale of 30,000 kg h^{-1} and IL recovery rate of 99.9%; and (d) Case 5: biomass processing scale of 30,000 kg h^{-1} and IL recovery rate of 99.9%.

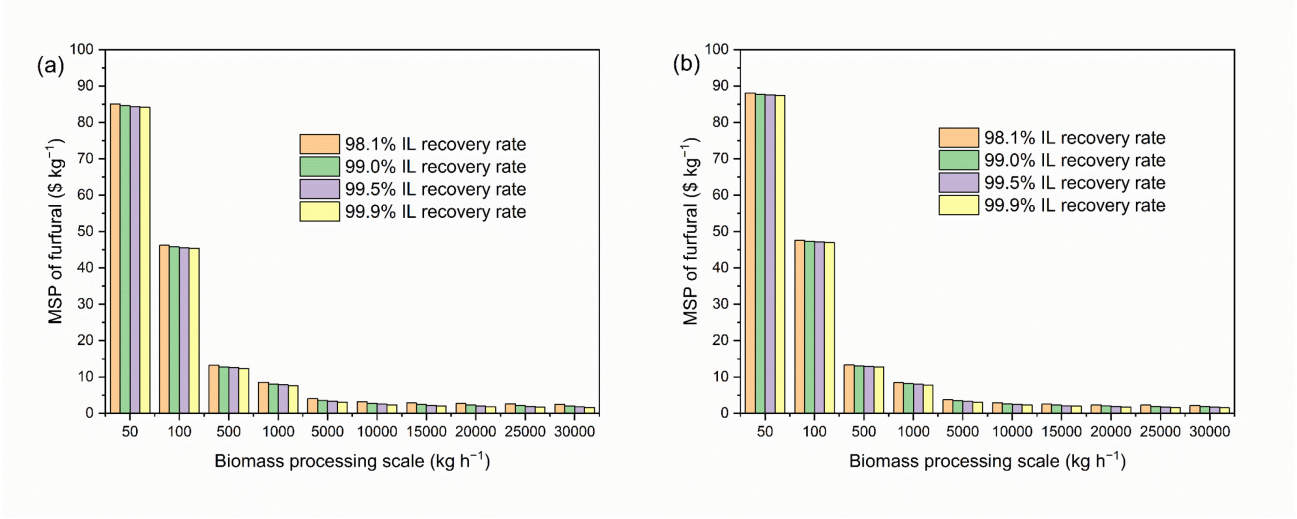


Figure 4.25. Sensitivity analysis of biomass processing scale and IL recovery rate on MSPs of furfural. (a) Case 3; and (b) Case 5.

4.3.8 Future Outlook

Our techno-economic analysis indicates that producing only furfural in a PIL-based biorefinery sits at the edge of economic viability on a large scale. The relatively low product output cannot offset the high CAPEX and the large biomass throughput required. To improve profitability, the PIL-based biorefinery should target multiple products and valorize additional biomass fractions. For instance, rather than converting cellulose to biochar, preserving it as pulp for higher-value applications would strengthen the process economics. Ongoing work in our laboratory focuses on developing such multi-product strategies to achieve a sustainable and commercially robust PIL-based biorefinery.

4.4. Conclusion

This study demonstrates that the PIL [DMBA][HSO_4] is an efficient and recyclable solvent for furfural production, increasing yields and reducing wastewater generation. Employing vapor stripping for furfural removal, a promising yield of 88.0% was obtained at 150 °C and 10 wt% biomass loading. More importantly, combining this technique with the stepwise biomass addition strategy gave a 75.1% yield at 30 wt% biomass loading (170 °C), a level not previously reported at such a high biomass

loading. Although this approach holds strong potential for process intensification, attention should be paid to solvent recovery and plant scale-up, which significantly influence the overall economic viability. With an appropriate strategy, PIL-mediated hydrolysis can match the efficiency of sulfuric acid hydrolysis while offering additional operational benefits. Commercial success, however, depends on integrating multi-component valorization within a biorefinery—a challenge common to all furfural production technologies.

4.5 External Contributions

Dr. Antonio Ovejero-Pérez contributed to the Aspen Plus process modelling and CAPEX/OPEX calculations for the techno-economic analysis of the large-scale furfural production biorefinery process.

Chapter 5: High-Pressure Continuous-Flow Aerobic Oxidation of Furfural to Furoic Acid over Robust Ru/C

5.1 Introduction

Furfural, derived from the depolymerization and dehydration of hemicellulosic pentosans, is listed by the U.S. Department of Energy among its top 30 bio-based platform chemicals [51, 346]. Meanwhile, furfural represents a key intermediate linking lignocellulosic biomass fractionation to downstream furan-based chemicals. In Chapter 4, a semi-continuous protic ionic liquid (PIL)-based process was developed to intensify furfural production from sugarcane bagasse at high solids loadings, providing a renewable furfural stream suitable for further upgrading.

Building on this upstream production platform, Chapter 5 focuses on the selective oxidation of furfural to furoic acid, a value-added furan derivative with growing relevance in bio-based materials and specialty chemicals. For instance, furoic acid can serve as a precursor for 2,5-furandicarboxylic acid (FDCA) via carboxylation with CO_2, offering an alternative to the more widely studied route via 5-hydroxymethylfurfural (HMF) [63, 64]. More recently, our group has also identified furoic acid as a key precursor for a new bio-based surfactant, sulfonated alkyl furoate (SAF), produced via simple esterification with fatty alcohols [68].

Industrially, furoic acid is produced via the Cannizzaro disproportionation of furfural in a strong alkaline (NaOH) environment [64, 380]. This route demands precise temperature control to suppress side reactions such as furfural oligomerization [64, 379]. Meanwhile, the maximum furoic acid selectivity in the Cannizzaro reaction is capped at 50% because an equimolar amount of furfuryl alcohol is formed [65]. To obtain higher furfural conversion and furoic acid selectivity, researchers have turned to the direct catalytic oxidation of furfural with oxidants such as O_2 and H_2O_2. O_2 (or air)

is preferred because it is greener, safer, and cheaper. By contrast, H_2O_2 is costly and non-recyclable. Its highly exothermic decomposition raises the risk of explosion, and its strong oxidizing power promotes side reactions that generate maleic and formic acids [64, 379].

Efficient aerobic oxidation of furfural to furoic acid is widely reported using heterogeneous catalysts based on noble or rare metals. Gold (Au) is one of the most studied ones. Its primary role is to activate O_2 on Au nanoparticle surfaces, generating reactive oxygen species (e.g., OH* and OOH*; * denotes surface adsorption) via O═O bond cleavage in the presence of water [384-386]. These species react with chemisorbed furfural, oxidizing the aldehyde to a carboxylic acid by abstracting the aldehydic hydrogen and adding an OH group to the carbon [384]. This direct pathway typically proceeds under a truly base-free environment (without any external or in situ base), but its efficiency is limited. For instance, Rawas et al. examined base-free furfural oxidation using 2 wt% Au nanoparticles supported on acidic TiO_2 [483]. Although the reaction gave 92% selectivity for furoic acid, furfural conversion reached only 44% after 2 h at 110 °C. Further extending the reaction to 8 h raised the furoic acid yield to 79%. Ferraz et al. likewise reported low catalytic activity with Au/TiO_2 or Au/MgF_2, but obtained a 100% furoic acid yield when the support was switched to basic MgO [69]. The high yield is because MgO can react with water to form $Mg(OH)_2$, acting as a weak base. Under this “pseudo” base-free environment, furfural likely follows an indirect conversion route similar to that in the presence of external bases (e.g., NaOH and Na_2CO_3). Specifically, furfural undergoes reversible hydration through the nucleophilic attack of OH^-, forming a geminal diol. This intermediate is then oxidatively dehydrogenated to furoic acid [71, 387, 388]. Notably, under basic conditions, furoic acid is present as its furoate salt and must be protonated in a separate acidification step [379, 484]. Because the geminal diol has a much lower oxidation barrier than furfural itself, this indirect pathway enables higher efficiency [389]. In fact, most heterogeneous catalysts require the co-presence of an external base to achieve high furoic acid yields. For example, Sadier et al. used the less expensive noble metal silver

(Ag) as the catalyst with TiO_2 as the support and achieved a 96% furoic acid yield with 100% selectivity at room temperature (25 °C) after 3 h in the presence of NaOH, whereas negligible furfural oxidation occurred with weaker bases (Na_2CO_3 or $NaHCO_3$) or without a base [71]. However, significant deactivation of Ag/TiO_2 was observed during catalyst recycling due to the severe aggregation of Ag particles.

The catalytic performance of non-noble metals, such as copper (Cu) and manganese (Mn), has also been studied [70, 383]. Rather than the pure metals, their oxides are used as the active phase. In these systems, the metal oxides, instead of molecular oxygen, act as the immediate oxidants, supplying lattice oxygen to furfural to form furoic acid while being reduced to a lower-valence state. The reduced oxides are then reoxidized by O_2, completing a redox cycle. For example, Tian et al. reported an 86.6% furoic acid yield using 150 nm CuO nanoparticles [70]. X-ray diffraction (XRD) confirmed the formation of Cu_2O/Cu after catalytic reactions. As with the Ag-based catalysts, a strong base (NaOH) was required to maintain the optimal pH of 13. Catalyst deactivation again occurred due to nanoparticle aggregation.

Although numerous heterogeneous catalyst systems have achieved high furoic acid yields in laboratory batch tests, scaling them up to continuous industrial operation remains challenging. Several factors that matter little at the bench scale become decisive at larger scales. Catalyst cost is a primary concern. For example, although Au-based catalysts deliver outstanding activity and selectivity, their high prices limit economic viability at scale. Catalyst stability is equally critical, especially in a flow system where a furfural solution and air continuously pass through a reactor packed with a catalyst to produce furoic acid in situ. In such settings, the catalyst must operate for extended periods without obvious deactivation or metal leaching under high flow conditions. Therefore, Ag-based and metal oxide-based catalysts, which tend to undergo particle aggregation or morphological changes during furfural oxidation, are generally unsuitable. Finally, according to the principles of green chemistry, the use of milder bases is preferred to minimize equipment corrosion and simplify downstream

wastewater treatment.

To overcome these limitations, we were inspired by the work of Lokhande et al. and selected ruthenium on carbon (Ru/C) as a cost-effective and structurally stable alternative [379]. Ruthenium (Ru) is far less expensive than Au, platinum (Pt), or palladium (Pd). More importantly, Lokhande's work showed that Ru remained uniformly dispersed on the carbon support after furfural oxidation, with minimal leaching. Negligible variation in the size of the spherical Ru particles was also observed, indicating a low risk of catalyst aggregation. Although their study recommended a hydrogen reduction step at 150 °C before catalyst reuse, our current results show that a simple acetonitrile/water wash can restore the activity of Ru/C. Additionally, Lokhande's study indicated that Ru/C was more active with Na_2CO_3 than with NaOH, achieving optimal conversion at pH 8–11 and allowing the use of a milder, more environmentally benign base. Building on these advantages, we report, for the first time, the design and operation of a high-pressure continuous-flow system for the stable and scalable aerobic oxidation of furfural to furoic acid using Ru/C and the benign base $NaHCO_3$. This system successfully scales previous milliliter-scale batch production up to a liter-scale continuous operation, providing valuable insights for the development of a cost-effective downstream upgrading step that complements the PIL-based furfural production platform established in Chapter 4.

5.2 Materials and Methods

5.2.1 Feedstock

Furfural (ACS reagent grade, 99% purity) was purchased from Sigma-Aldrich. Sodium bicarbonate ($NaHCO_3$, ≥99% purity) was purchased from VWR Chemicals. The 10 wt% Ru/C catalyst (40–60 mesh) was custom-manufactured and supplied by Henan Yetan Environmental Protection Material Co., Ltd.

5.2.2 High-Pressure Continuous-Flow System

A high-pressure continuous-flow system was designed and used in this study to investigate the oxidation of furfural to furoic acid under an air atmosphere, using 10 wt% Ru/C as the catalyst (Figure 5.1). Pure O_2 was replaced by air for safety reasons. The aqueous solution, with a volume of approximately 0.5–5 L and a furfural concentration of 1–3 wt%, was premixed with $NaHCO_3$ at a base-to-furfural molar ratio of 0.9:1–1.1:1. An HPLC pump was used to deliver the aqueous solution at a constant flow rate of 2.5–10 mL min^{-1}. Simultaneously, air was introduced at a flow rate of 25–500 mL min^{-1}, regulated by a flowmeter, and combined with the furfural solution in a sealed mixing unit equipped with a micro-stirrer to enhance gas–liquid mixing. The mixed stream subsequently entered a fixed-bed reactor packed with 10 g of 10 wt% Ru/C. Larger catalyst particles (40–60 mesh) were used instead of fine powders to improve packing and prevent catalyst washout at high flow rates. The reactor was wrapped in a heating jacket, through which hot silicone oil was continuously circulated by a pump to maintain the required reaction temperature. A thermocouple was installed at the reactor outlet to monitor the temperature of the product stream in real time. Notably, all reaction temperatures reported below refer to the outlet fluid temperature rather than the silicone oil temperature, with a typical difference of 12–15 °C owing to heat transfer limitations. Catalytic oxidation occurred as the reactant stream passed through the catalyst bed, and the product stream was then cooled in a condenser (coolant set to 1.5 °C) before passing through a back-pressure regulator (BPR) to control the system pressure. Nitrogen was used to maintain the system pressure at 10–40 bar, enabling smooth, high-pressure continuous-flow operation. A continuous furoic acid production process generally lasted for 2–10 h, depending on specific requirements.

During the experiment, products were sampled periodically at predetermined time intervals (0.5 or 1 h) to monitor furfural conversion and furoic acid formation. After the reaction, the entire collected solution was also analyzed to assess the overall reaction efficiency. A Shimadzu HPLC system equipped with an Aminex HPX-87H column (Bio-

Rad, 300 × 7.8 mm) was used to determine the furfural and furoic acid molar concentrations in the products. The column temperature was 60 °C. The mobile phase was 0.005 M H_2SO_4 at a flow rate of 0.6 mL min^{-1}. Detection was performed at 254 nm using a UV-Vis detector with 10 μL injections. Furfural and furoic acid molar concentrations were calculated based on calibrated standard solutions. Catalytic performance metrics—including furfural conversion, furoic acid yield, and furoic acid selectivity—were calculated as follows:

$$\text{Furfural conversion (\%)} = \left(1 - \frac{\text{Furfural molar concentration in the solution after oxidation}}{\text{Furfural molar concentration in the solution before oxidation}}\right) \times 100 \quad (5.1)$$

$$\text{Furoic acid yield (\%)} = \frac{\text{Furoic acid molar concentration in the solution after oxidation}}{\text{Theoretical maximum furoic acid molar concentration based on complete furfural oxidation}} \times 100 \quad (5.2)$$

$$\text{Furoic acid selectivity (\%)} = \frac{\text{Furoic acid molar concentration in the solution after oxidation}}{\text{Molar concentration of converted furfural after oxidation}} \times 100 \quad (5.3)$$

To improve operational safety, all system components were made of corrosion-resistant stainless steel, and all connectors and fittings were sourced from *Swagelok* to ensure seal integrity and pressure resistance.

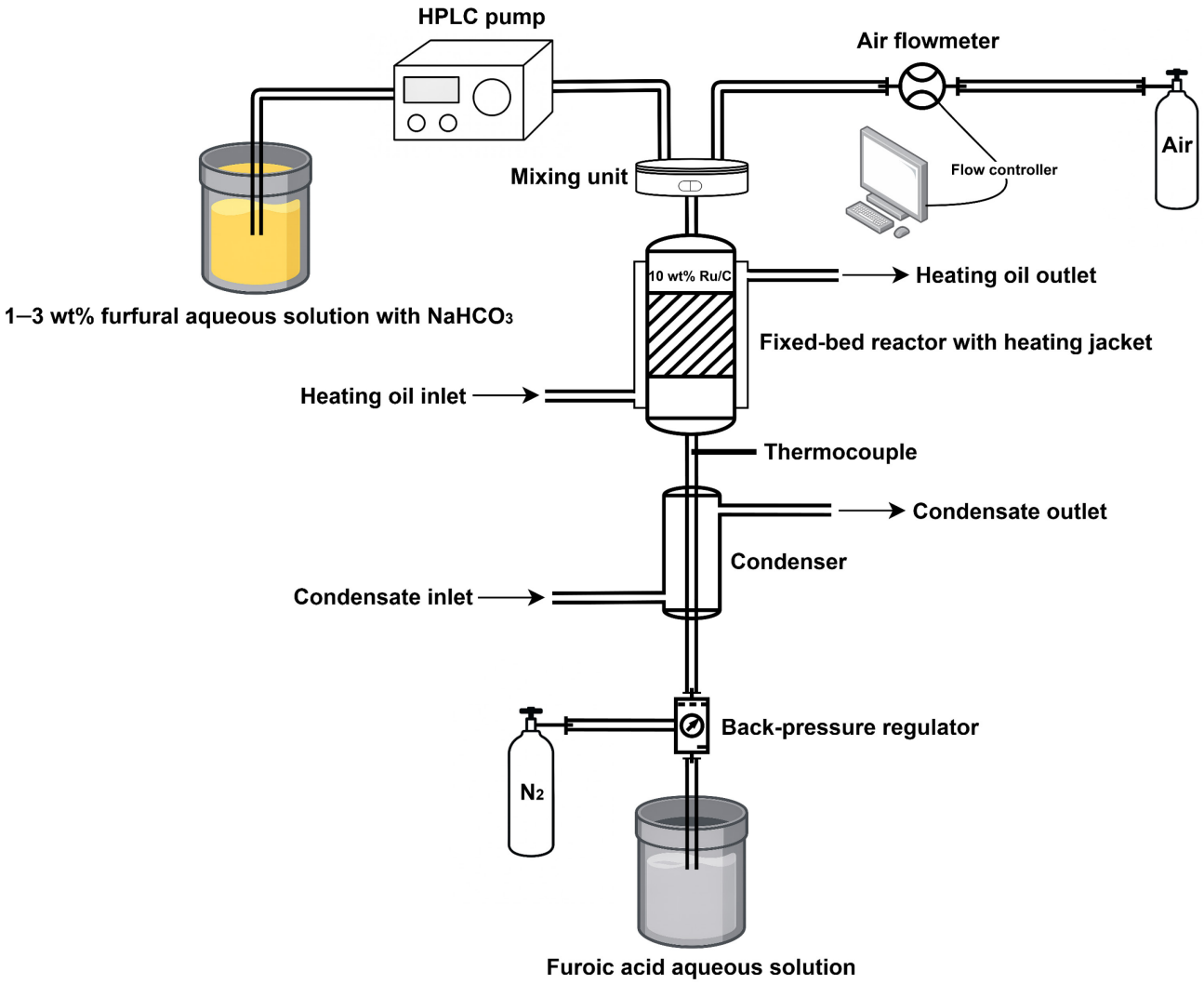


Figure 5.1. High-pressure continuous-flow system for 10 wt% Ru/C-catalyzed aerobic oxidation of furfural to furoic acid.

5.2.3 Catalyst Characterization

X-ray Diffraction (XRD)

Powder XRD (Malvern Panalytical) was used to characterize the crystalline phases of the fresh and spent 10 wt% Ru/C catalysts. Patterns were collected using Cu Kα radiation at 40 kV and 15 mA over a 2θ range of 5–80°.

X-ray Photoelectron Spectroscopy (XPS)

XPS (K-Alpha$^+$, Thermo Scientific), equipped with a monochromatic, micro-focused Al

Kα X-ray source, was used to measure the oxidation state of ruthenium in the fresh and spent 10 wt% Ru/C catalysts. Binding energies were calibrated with respect to the C 1s peak at 284.8 eV.

Inductively Coupled Plasma-Mass Spectrometry (ICP-MS)

The total Ru content in the fresh and spent 10 wt% Ru/C catalysts was measured by ICP-MS (Agilent 7900). Approximately 10 mg of catalyst was pre-digested in 5 mL of aqua regia in a PTFE digestion container for 3 h. Subsequently, an additional 5 mL of aqua regia was added. The PTFE container was sealed and placed in a microwave digester (CEM Corporation) for programmed digestion. Specifically, the temperature was ramped to 80 °C over 5 min and held for 15 min, then increased to 180 °C over 10 min and held for 120 min. After the program, the solid catalyst was fully dissolved. The solution was cooled to room temperature, filtered through a 0.22 μm membrane, and diluted 500-fold for ICP-MS analysis.

Nitrogen Physisorption

The surface area, pore volume, and pore size of the fresh and spent 10 wt% Ru/C catalysts were measured by N_2 adsorption–desorption isotherms at 77 K on a Micromeritics 3Flex physisorption analyzer. Samples were degassed under vacuum at 180 °C for 18 h prior to analysis. The specific surface area was determined by the Brunauer-Emmett-Teller (BET) method. The total pore volume was obtained from the single-point adsorption at P/P_0 = 0.973, and the average pore diameter was derived using the Barrett-Joyner-Halenda (BJH) method (from the adsorption branch, 4V/A).

Scanning Electron Microscopy with Energy-Dispersive X-ray Spectroscopy (SEM-EDX)

The morphology and elemental distribution (C, O, and Ru) of the fresh and spent 10 wt% Ru/C catalysts were examined by SEM equipped with an EDX detector (LEO Gemini 1525, Zeiss).

Transmission Electron Microscopy (TEM)

The morphology and size of the Ru nanoparticles on the fresh and spent 10 wt% Ru/C catalysts were characterized by TEM (JEOL 2100Plus).

5.3 Results and Discussion

5.3.1 Preliminary Batch Oxidation of Furfural to Furoic Acid

Bioataraxis Ltd, a start-up company from our group [485], completed a preliminary catalyst (5 wt% Ru/C, powder form) validation in a batch reactor at 130 °C for 1 h, using a 1:1 base-to-furfural molar ratio under 10 bar O_2. Unlike the work of Lokhande et al., which employed Na_2CO_3, this study used the more environmentally benign $NaHCO_3$, maintaining a milder alkaline environment (starting pH 8.8–9.1) than that of Na_2CO_3 (starting pH 11–11.5) [379]. This pH range, together with the buffering capacity of $NaHCO_3$, suppressed side reactions promoted by strong bases (e.g., the Cannizzaro reaction [64, 380]) and stabilized the reaction medium. Fresh 5 wt% Ru/C achieved complete furfural conversion (100%) with an 83.2% furoic acid yield. The catalyst was recovered by a simple water/acetonitrile washing step and showed stable performance over four recycles, maintaining high furoic acid yields of 73.8–80.3%, thereby confirming the robustness of Ru/C. As these results remain unpublished by Bioataraxis Ltd, further details are not discussed in this thesis (Copyright © Dr. Amir Al Ghatta, CEO, Bioataraxis Ltd; used with permission).

5.3.2 Continuous Oxidation of Furfural to Furoic Acid

5.3.2.1 Process Parameter Optimization Using a 1 wt% Furfural Aqueous Solution

Effect of Temperature

Following the successful demonstration of the effectiveness and durability of Ru/C in the batch reactor, we further evaluated the performance of 10 wt% Ru/C (40–60 mesh) for furfural oxidation in the high-pressure continuous-flow system. Preliminary testing at 130 °C used a 1 wt% furfural aqueous solution, a 1:1 $NaHCO_3$-to-furfural molar ratio,

a liquid flow rate of 8 mL min^{-1}, a gas flow rate of 125 mL min^{-1}, and an air pressure of 10 bar (Figure 5.2). Although the furfural conversion (33.5–39.6%) and furoic acid yield (26.5–30.5%) were steady over the run, both were significantly lower than those in batch operation. This shortfall was attributed to the reduced residence time on the catalytic sites under flow conditions, allowing a considerable fraction of furfural to exit unoxidized. To address this kinetic limitation, the temperature was raised to 150 °C and then to 160 °C with all other parameters unchanged. At 150 °C, both the furfural conversion (72.9–81.7%) and furoic acid yield (66.2–73.3%) increased substantially. In addition, the higher temperature suppressed low-temperature side reactions, improving the selectivity for furoic acid (83.7–92.4%). Further improvements in the furfural conversion (92.1–97.7%) and furoic acid yield (81.2–86.2%) were achieved at 160 °C, despite a negligible additional gain in furoic acid selectivity (85.8–91.0%) relative to that at 150 °C. More importantly, stable operation was maintained at 160 °C for at least 10 h, cumulatively processing approximately 5 L of feed and producing a uniform furoic acid solution, indicating negligible catalyst deactivation. Previous studies on furfural oxidation have shown that one cause of metal catalyst deactivation is the blockage of active sites by insoluble, resinous by-products [486, 487]. In our continuous-flow system, the high selectivity for furoic acid suppressed the formation of these species, thereby maintaining catalyst performance over extended operation.

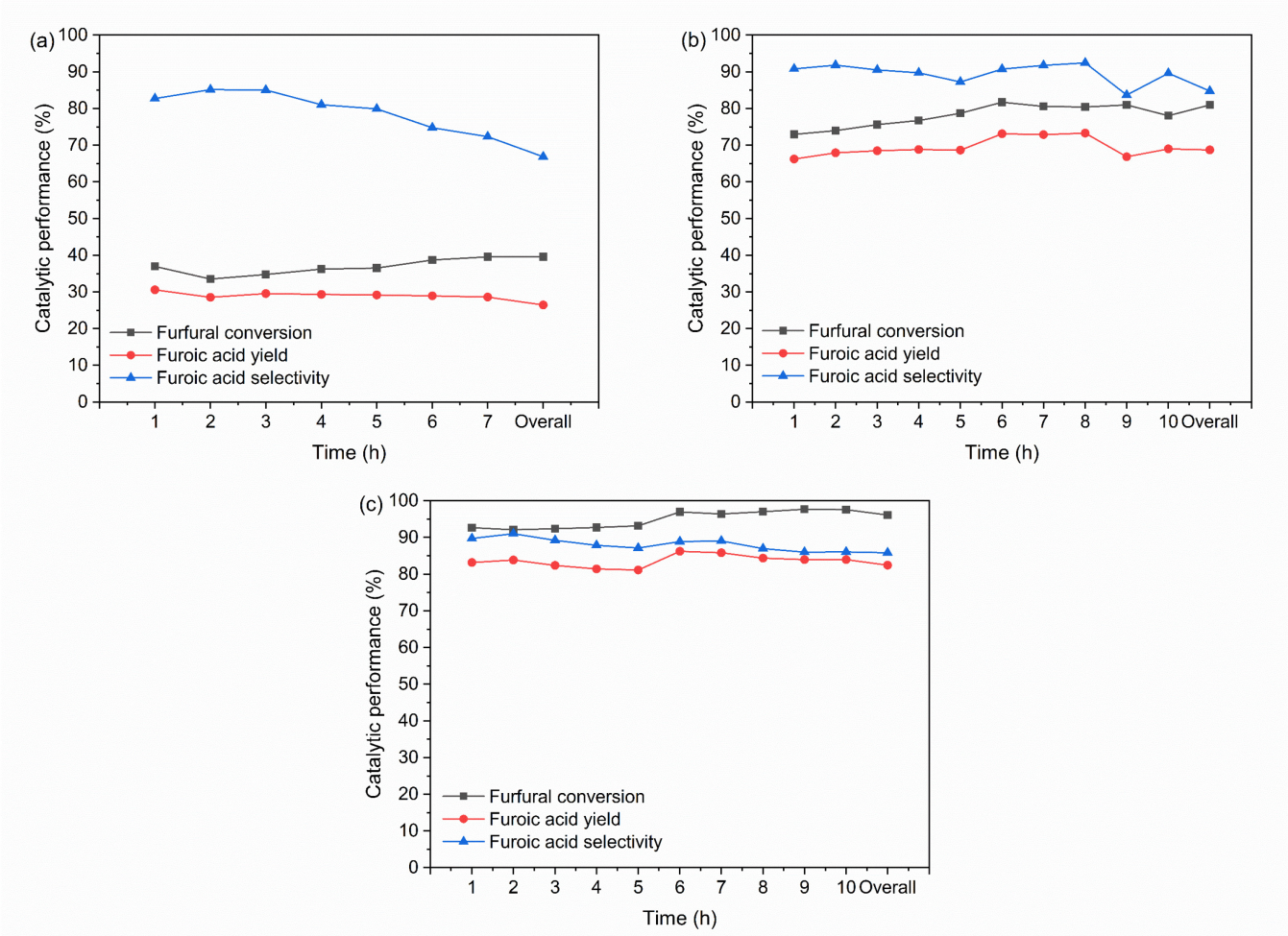


Figure 5.2. Effect of temperature on the continuous oxidation of furfural to furoic acid over 10 wt% Ru/C. Conditions: 1 wt% furfural aqueous solution; air pressure of 10 bar; 1:1 $NaHCO_3$-to-furfural molar ratio; liquid flow rate of 8 mL min^{-1}; and air flow rate of 125 mL min^{-1}. Temperatures: (a) 130 °C; (b) 150 °C; and (c) 160 °C.

Effect of Air Pressure

Air pressure is an important parameter because it controls the dissolved O_2 concentration in the liquid phase. At least stoichiometric amounts of O_2 need to be activated on the catalytic sites to oxidize furfural to furoic acid (0.5 mol O_2 per mol of furfural), whereas an excess of O_2 can promote over-oxidation to undesired by-products. We therefore examined the effect of air pressure. As shown in Figure 5.3, increasing the air pressure from 10 to 20 bar produced negligible changes in performance. At 20 bar, the furfural conversion and furoic acid yield remained at 89.6–

94.1% and 81.4–86.4%, respectively. The selectivity for furoic acid was 90.5–93.6%, indicating limited formation of by-products. Further increasing the air pressure to 40 bar achieved near-quantitative furfural conversion (93.2–97.0%) but reduced the furoic acid yield and selectivity to approximately 75%, indicating over-oxidation. A similar trend was reported by Lokhande et al., who observed a decrease in furoic acid yield as O_2 pressure increased from 15 to 20 bar in a batch reactor, alongside greater formation of low-molecular-weight organic acids (e.g., formic and acetic acids) and maleic anhydride [379]. These results showed that pressures above 10 bar were unnecessary for achieving a high furoic acid yield in our continuous-flow system. This is advantageous, as operation at higher pressures would require higher pressure ratings for vessels and auxiliaries, markedly increasing equipment costs and complicating scale-up. Notably, a further reduction to 5 bar or atmospheric pressure was not feasible because sufficient pressure was required to maintain the liquid phase and stable flow at 160 °C.

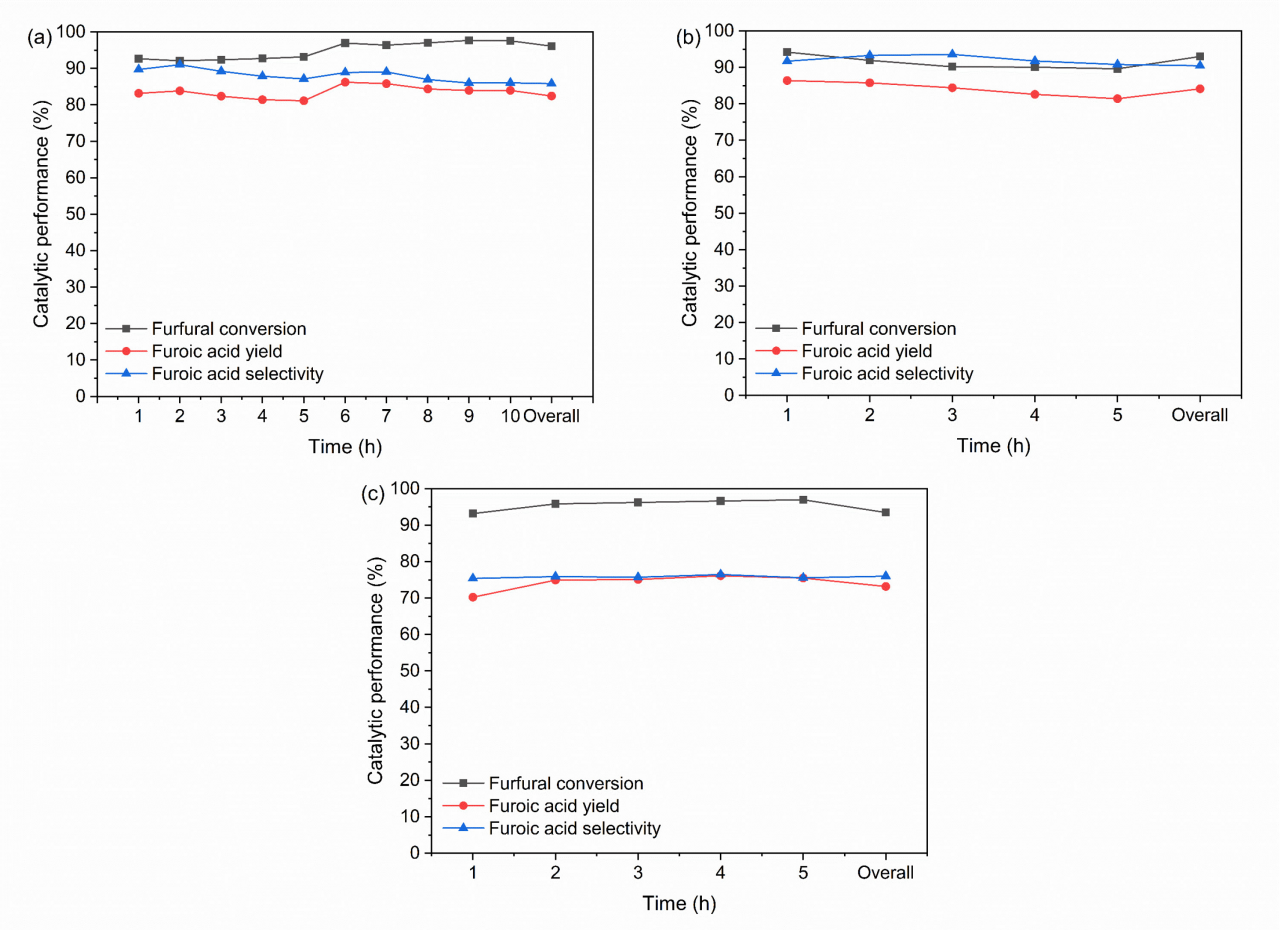


Figure 5.3. Effect of air pressure on the continuous oxidation of furfural to furoic acid over 10 wt% Ru/C. Conditions: 1 wt% furfural aqueous solution; 160 °C; 1:1 $NaHCO_3$-to-furfural molar ratio; liquid flow rate of 8 mL min^{-1}; and air flow rate of 125 mL min^{-1}. Air pressures: (a) 10 bar; (b) 20 bar; and (c) 40 bar.

Effect of the Base-to-Furfural Molar Ratio

An appropriate base-to-furfural molar ratio is essential. Sufficient base is required to promote the hydration of furfural to the geminal diol, which can be readily oxidized to furoic acid via dehydrogenation [67, 71]. Excess base, however, elevates the pH and promotes the Cannizzaro disproportionation (side reaction) of furfural into furfuryl alcohol and furoic acid [379]. Meanwhile, the overuse of base complicates downstream neutralization and increases economic and environmental burdens. To balance these factors, we examined $NaHCO_3$-to-furfural molar ratios from 0.9:1 to 1.1:1 in the

continuous-flow system (Figure 5.4). At the base ratio of 0.9, the furfural conversion was 73.3–77.1% with a 70.5–72.1% furoic acid yield—both significantly lower than those at the stoichiometric ratio of 1.0—whereas the selectivity for furoic acid was near-quantitative (93.1–97.9%) and slightly higher than that at 1.0. This suggests that, at a lower base ratio, the reversible hydration of furfural to the geminal diol was kinetically limited by reduced OH^- availability, decreasing the effective substrate (geminal diol) concentration for the Ru-catalyzed oxidation. Increasing the base ratio to 1.1 resulted in complete furfural conversion (100%) and a promising 92.4–94.9% furoic acid yield over the entire 5 h of operation, with no loss of selectivity relative to the lower base ratio. The resulting product solution was clear and colorless compared with the brown furfural feed. The quantitative furfural conversion at the base ratio of 1.1 was attributed to greater OH^- availability, which shifted the aldehyde–hydrate equilibrium toward the geminal diol. In addition, high furoic acid selectivity was maintained across the base ratios of 0.9–1.1 because the buffering capacity of $NaHCO_3$ limited pH fluctuations, thereby suppressing the undesired Cannizzaro reaction, which occurs under strongly basic conditions [64, 380], and keeping the furfural oxidation pathway to furoic acid highly selective.

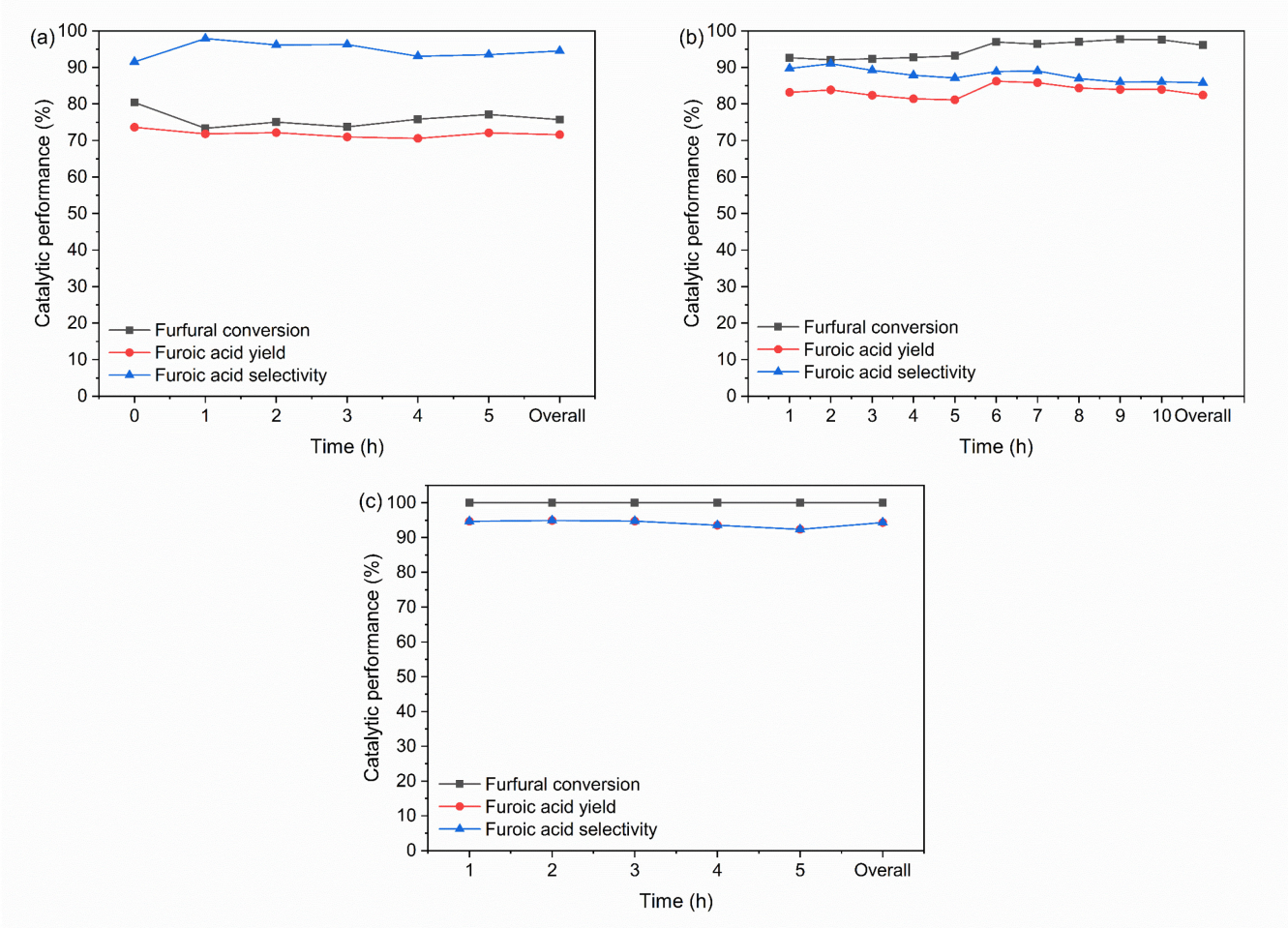


Figure 5.4. Effect of $NaHCO_3$-to-furfural molar ratio on the continuous oxidation of furfural to furoic acid over 10 wt% Ru/C. Conditions: 1 wt% furfural aqueous solution; 160 °C; air pressure of 10 bar; liquid flow rate of 8 mL min^{-1}; and air flow rate of 125 mL min^{-1}. $NaHCO_3$-to-furfural molar ratios: (a) 0.9:1; (b) 1:1; and (c) 1.1:1.

Effect of Liquid and Air Flow Rates

Higher liquid flow rates increase processing capacity per unit time and help sweep resinous by-products from the catalyst surface, thereby mitigating active-site blockage. However, higher liquid flow rates reduce the residence time of furfural over the Ru/C catalyst, leading to incomplete oxidation. In our previous tests, complete furfural conversion was achieved at an 8 mL min^{-1} liquid flow (160 °C, 1.1 base ratio, and 125 mL min^{-1} air flow). Therefore, a higher liquid flow rate is worth further exploration. As shown in Figure 5.5, raising the liquid flow rate to 10 mL min^{-1} likewise gave near-

quantitative furfural conversion (97.5–98.7%) with negligible changes in the furoic acid yield (91.2–93.4%) and selectivity (93.0–95.0%) relative to the results at 8 mL min^{-1}, indicating sufficient catalytic capacity at this rate and enabling higher throughput. Because 10 mL min^{-1} is the maximum capacity of the HPLC pump, higher flow rates were not evaluated. Subsequent optimization therefore used a 10 mL min^{-1} liquid flow rate.

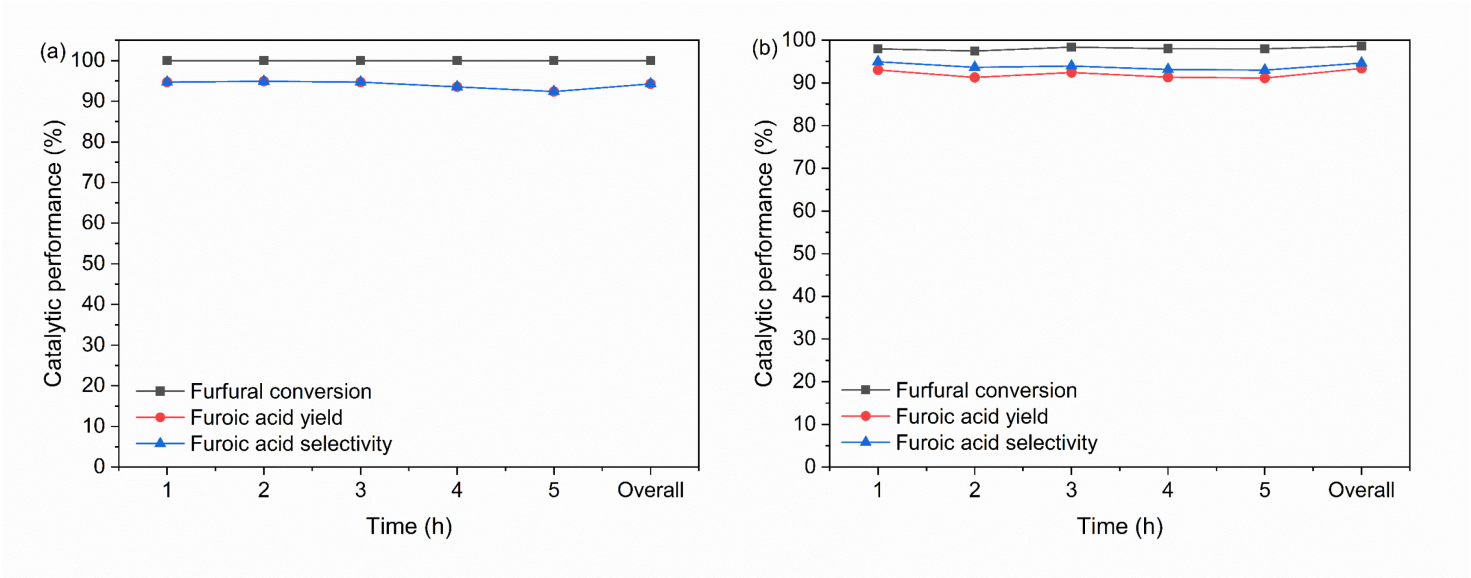


Figure 5.5. Effect of liquid flow rate on the continuous oxidation of furfural to furoic acid over 10 wt% Ru/C. Conditions: 1 wt% furfural aqueous solution; 160 °C; air pressure of 10 bar; 1.1:1 $NaHCO_3$-to-furfural molar ratio; and air flow rate of 125 mL min^{-1}. Liquid flow rates: (a) 8 mL min^{-1}; and (b) 10 mL min^{-1}.

The air flow rate is a critical parameter that controls oxygen delivery. Appropriate air flow ensures the efficient oxidation of furfural while minimizing oxygen wastage. Optimizing this parameter can improve economic viability, especially on an industrial scale, because compressed air is typically supplied by compressors rather than the gas cylinders used on a laboratory scale. Higher air flow rates require greater compression power, significantly increasing energy consumption and operating costs. Since a furoic acid yield of over 90% was achieved at a 125 mL min^{-1} air flow rate, lower air flow rates (75 and 25 mL min^{-1}) were investigated to assess whether reduced

air usage could maintain comparable process efficiency. As shown in Figure 5.6, reducing the flow rate to 75 mL min^{-1} caused only a marginal decrease in the furoic acid yield to 84.9–88.6% (after 1 h of operation), whereas a further decrease to 25 mL min^{-1} significantly lowered the yield to 36.8–42.6%. At 25 mL min^{-1}, the low furoic acid yield was mainly due to limited furfural conversion (39.7–47.5%), while selectivity remained high at approximately 90%. This indicates that oxygen-independent side reactions (e.g., Cannizzaro disproportionation) remained suppressed under these conditions. Although the maximum furoic acid yield was obtained at 125 mL min^{-1}, the modest reduction at 75 mL min^{-1} might also be acceptable from an economic standpoint.

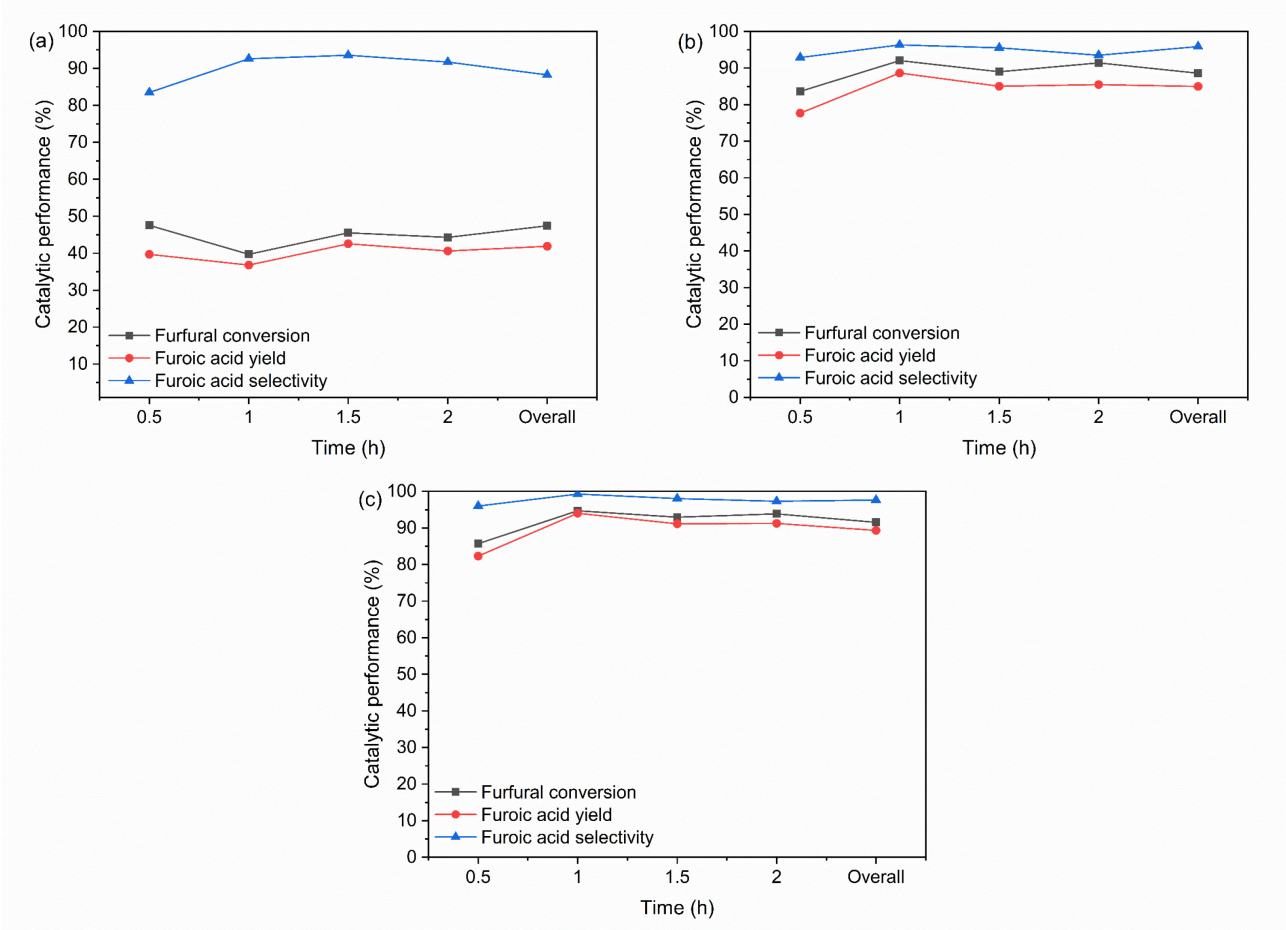


Figure 5.6. Effect of air flow rate on the continuous oxidation of furfural to furoic acid over 10 wt% Ru/C. Conditions: 1 wt% furfural aqueous solution; 160 °C; air pressure of 10 bar; 1.1:1 $NaHCO_3$-to-furfural molar ratio; and liquid flow rate of 10 mL min^{-1}. Air flow rates: (a) 25 mL min^{-1}; (b) 75 mL min^{-1}; and (c) 125 mL min^{-1}.

5.3.2.2 Process Parameter Optimization Using 2–3 wt% Furfural Aqueous Solutions

To develop a techno-economically viable process and fully leverage the capability of the catalytic system, operating at higher substrate concentrations is preferred: it raises volumetric productivity, simplifies product isolation by increasing product concentration, and reduces wastewater. Accordingly, furfural oxidation was tested at a 2 wt% concentration using the same optimized conditions as those used for 1 wt% (160 °C, 1.1 base ratio, 10 mL min^{-1} liquid flow, and 125 mL min^{-1} air flow). As shown in Figure 5.7, the 1 wt% optimum did not translate to 2 wt%. Furfural conversion and furoic acid yield dropped significantly to 61.9–68.3% and 57.4–62.7%, respectively, although selectivity remained over 90%. Guided by the air-flow experiments above, we attributed the lower furfural conversion at 2 wt% to insufficient oxidant. Therefore, we increased the air flow rate to 250 and 500 mL min^{-1} (the system maximum) and observed a clear catalytic performance improvement with higher flow rates. Furfural conversion increased without compromising furoic acid selectivity (>90%). At 500 mL min^{-1}, furfural conversion and furoic acid yield were 84.6–87.8% and 76.6–80.7%, respectively. This raised furoic acid productivity to approximately 1.7 times that of the optimized 1 wt% case.

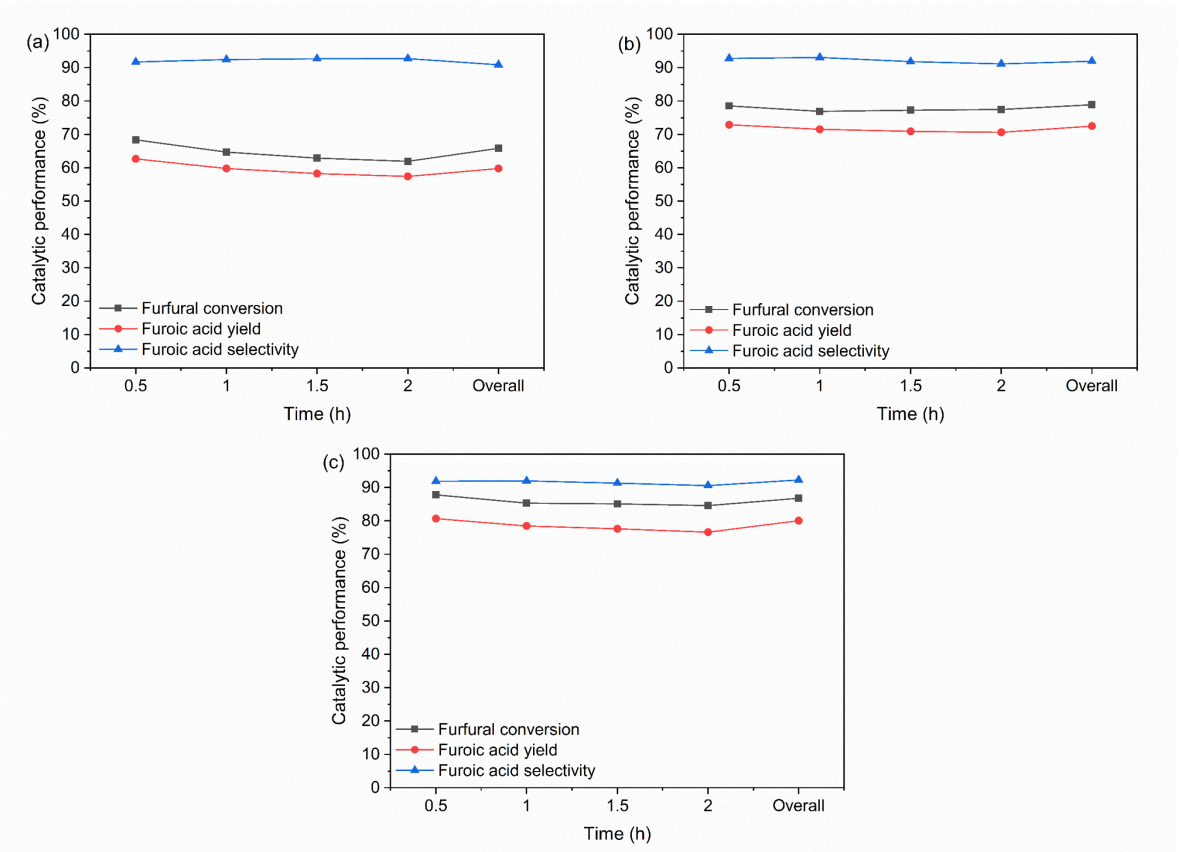


Figure 5.7. Continuous oxidation of furfural to furoic acid over 10 wt% Ru/C using a 2 wt% furfural aqueous solution. Conditions: 160 °C; air pressure of 10 bar; 1.1:1 $NaHCO_3$-to-furfural molar ratio; and liquid flow rate of 10 mL min^{-1}. Air flow rates: (a) 125 mL min^{-1}; (b) 250 mL min^{-1}; and (c) 500 mL min^{-1}.

At a 3 wt% furfural concentration and the maximum air flow rate of 500 mL min^{-1}, furfural conversion and furoic acid yield were limited to 25.7–27.9% and 24.7–25.4%, respectively, while selectivity remained high at 90.9–95.9%. This outcome is consistent with oxygen supply limitations. Since further increasing the air flow rate was not available, two compensating strategies were tested: (1) a second-pass oxidation of the collected effluent (Figure 5.8), and (2) lowering the liquid flow rate (Figure 5.9). Firstly, the second pass reproduced the first-pass performance, giving a cumulative furfural conversion and furoic acid yield of 52.5–54.2% and 46.6–47.2%, respectively. Secondly, reducing the liquid flow rate from 10 to 5 mL min^{-1} delivered a similar cumulative outcome to that of the second-pass method. Further reducing the flow rate

to 2.5 mL min^{-1} increased furfural conversion to 84.0–87.3% and furoic acid yield to 73.9–76.9%, with a selectivity of 87.3–88.4%. These results indicate that extending the residence time of furfural over Ru/C (or improving O_2 availability per mole of substrate) increased furfural conversion with only a slight loss in selectivity. However, both strategies prolonged the operation and lowered volumetric productivity. For industrial applications, a more scalable approach is to extend the furfural residence time by increasing the length-to-diameter ratio of the fixed-bed reactor, so that high liquid throughput can be maintained without sacrificing furfural conversion.

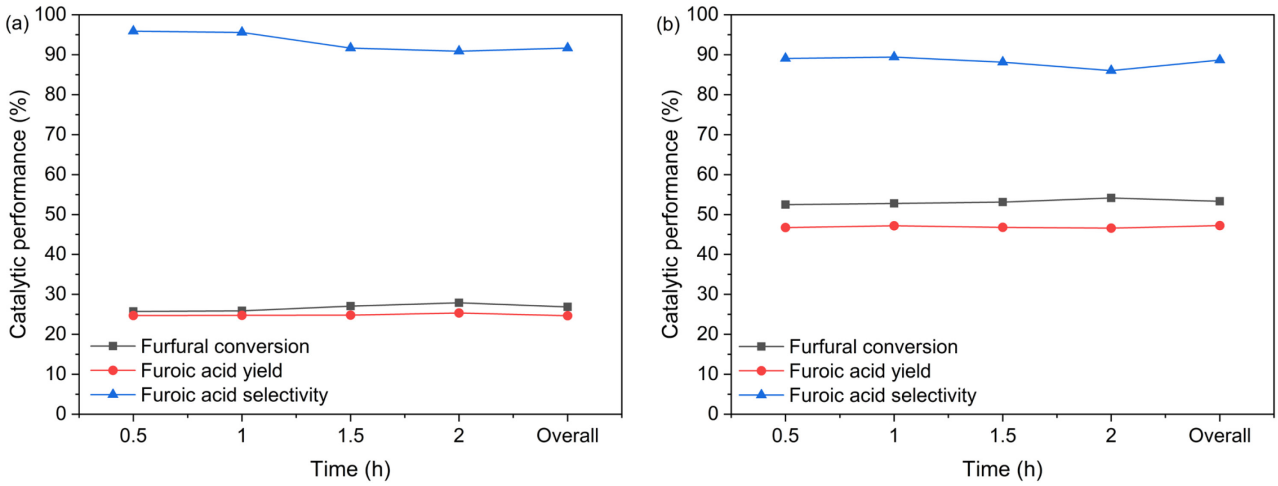


Figure 5.8. Continuous oxidation of furfural to furoic acid over 10 wt% Ru/C using a 3 wt% furfural aqueous solution. Conditions: 160 °C; air pressure of 10 bar; 1.1:1 $NaHCO_3$-to-furfural molar ratio; liquid flow rate of 10 mL min^{-1}; and air flow rate of 500 mL min^{-1}. (a) First-pass oxidation; and (b) Second-pass oxidation.

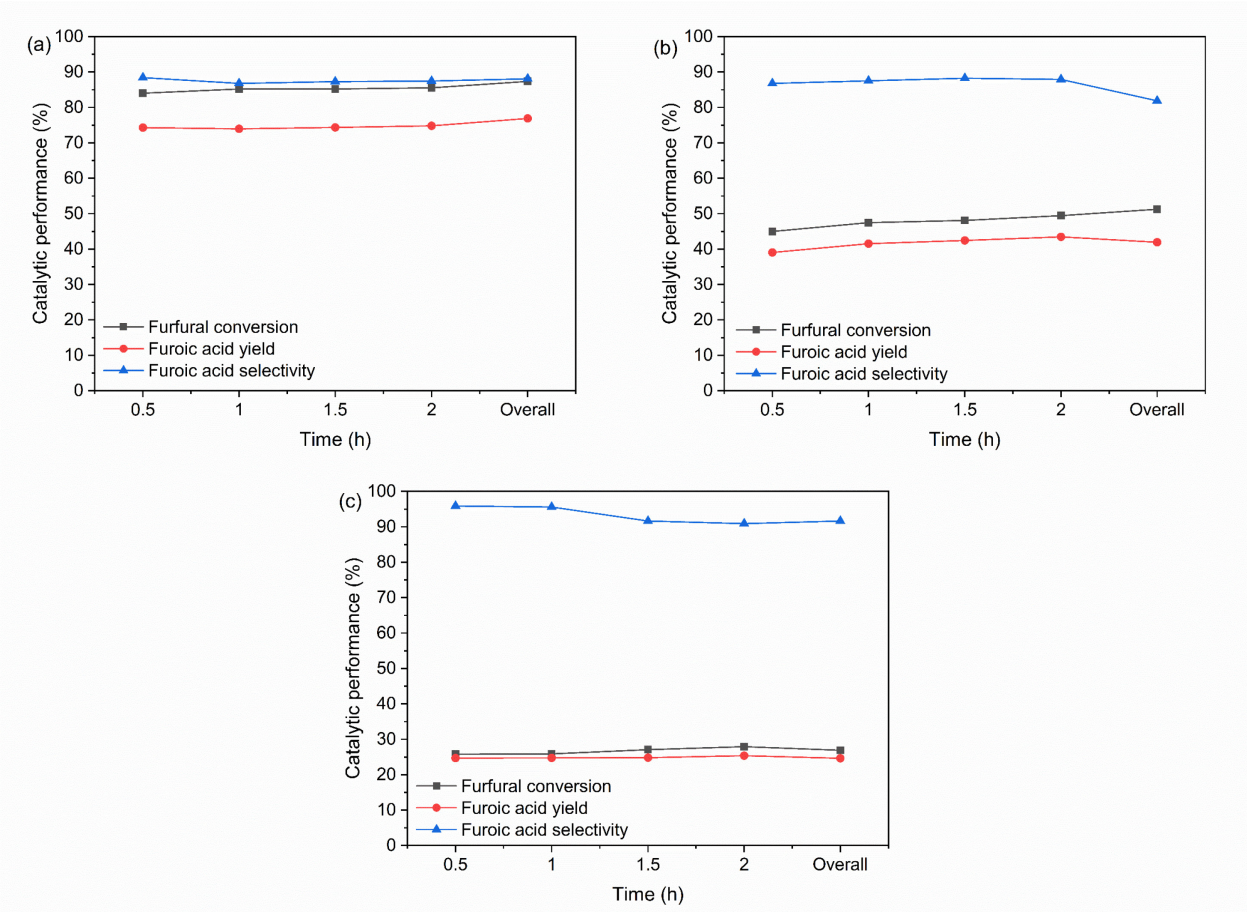


Figure 5.9. Continuous oxidation of furfural to furoic acid over 10 wt% Ru/C using a 3 wt% furfural aqueous solution. Conditions: 160 °C; air pressure of 10 bar; 1.1:1 $NaHCO_3$-to-furfural molar ratio; air flow rate of 500 mL min^{-1}; and single-pass oxidation. Liquid flow rates: (a) 2.5 mL min^{-1}; (b) 5 mL min^{-1}; and (c) 10 mL min^{-1}.

5.3.3 Characterization of Fresh and Spent 10 wt% Ru/C Catalysts

To elucidate changes in the physicochemical properties of the catalyst after furfural oxidation in the high-pressure continuous-flow system, fresh and spent 10 wt% Ru/C were characterized by XRD, XPS, N_2 physisorption, SEM-EDX, and TEM. Notably, the catalyst was operated under the optimal conditions—a 1 wt% furfural aqueous solution, 160 °C, a 1.1:1 $NaHCO_3$-to-furfural molar ratio, an air flow rate of 125 mL min^{-1}, and a liquid flow rate of 8–10 mL min^{-1}—and then recovered as the spent sample. No discernible decline in its catalytic performance was observed during over 20 h of operation.

The XRD patterns (Figure 5.10) showed two broad reflections at 2θ = 23.5–24.5° and 43.5–43.7°, attributable to the disordered/graphitic carbon of the support [379, 488]. The similarity of the profiles before and after furfural oxidation indicated no XRD-detectable change in the bulk structure of the carbon support. Moreover, no reflections assignable to Ru or RuO_2 were observed, consistent with nanoscale, highly dispersed Ru on the carbon support being below the XRD detection limit [379, 488].

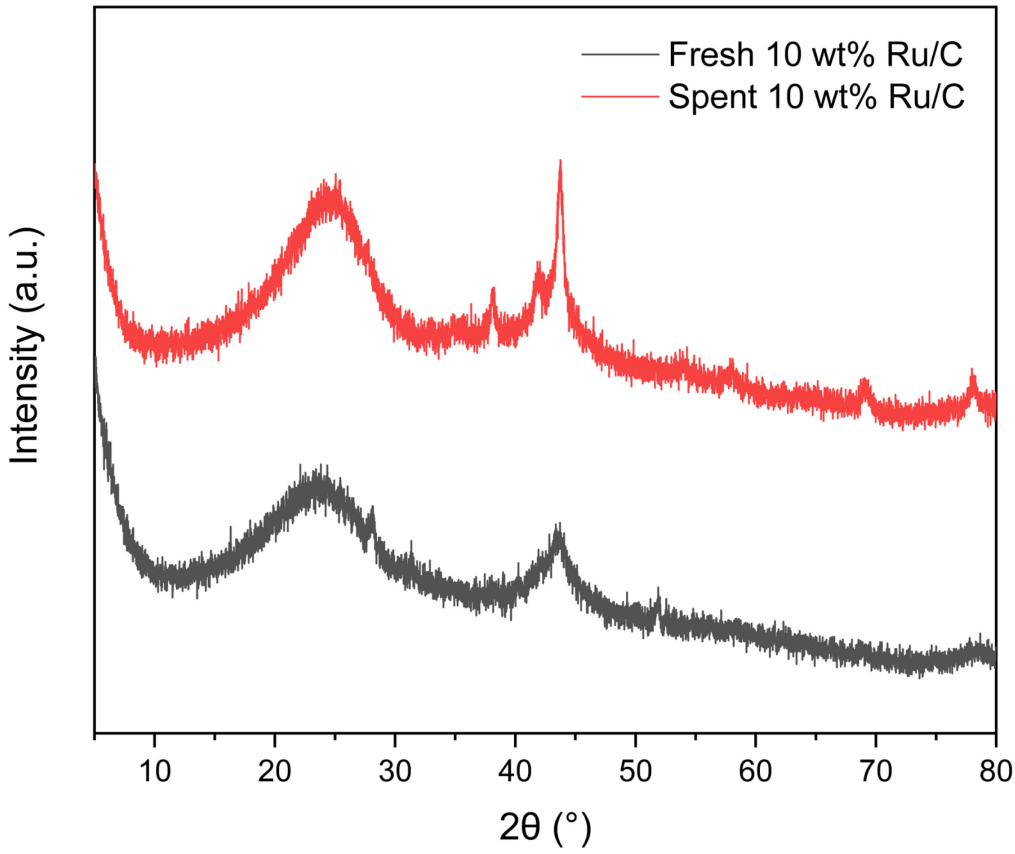


Figure 5.10. XRD patterns of fresh and spent 10 wt% Ru/C catalysts.

XPS was carried out to investigate changes in the chemical state of Ru before and after furfural oxidation. In the Ru 3p region (Figure 5.11), the Ru/C catalyst showed peaks at binding energies (B.E.) of 461.9–462.0 and 484.1–484.2 eV, assigned to the $3p_{3/2}$ and $3p_{1/2}$ of metallic Ru (0), and peaks at 465.1–465.7 and 487.0–487.8 eV

attributed to Ru (IV) (RuO_2). These assignments are consistent with literature reports for Ru and RuO_2 in the 3p region [379, 489], indicating the coexistence of metallic and oxidized Ru species in the Ru/C catalyst. The Ru (0)/Ru (IV) atomic ratio remained stable at 3.14 (fresh Ru/C) and 3.09 (spent Ru/C), suggesting little shift in the surface Ru oxidation state under aerobic operation. XPS also provided surface atomic percentages (at%) of C, O, and Ru (Table 5.1). The Ru fraction was similar for the fresh (5.19 at%) and spent (6.42 at%) catalysts, indicating, within the method's uncertainty, no clear evidence of surface Ru leaching after continuous furfural oxidation. Because XPS probes only the top few nanometers of the catalyst and reports atomic fractions, these values do not represent the bulk Ru loading (wt%). Therefore, the bulk Ru content of the catalysts was further verified by ICP-MS. The results indicated 9.55 ± 0.21 wt% Ru in the fresh Ru/C and 12.55 ± 0.52 wt% in the spent Ru/C after more than 20 h of furfural oxidation. This increase in Ru content likely reflects the loss of the carbon support under high liquid flow operation, which is consistent with the XPS finding that the surface C atomic percentage decreased from 67.24 at% to 63.32 at% after furfural oxidation.

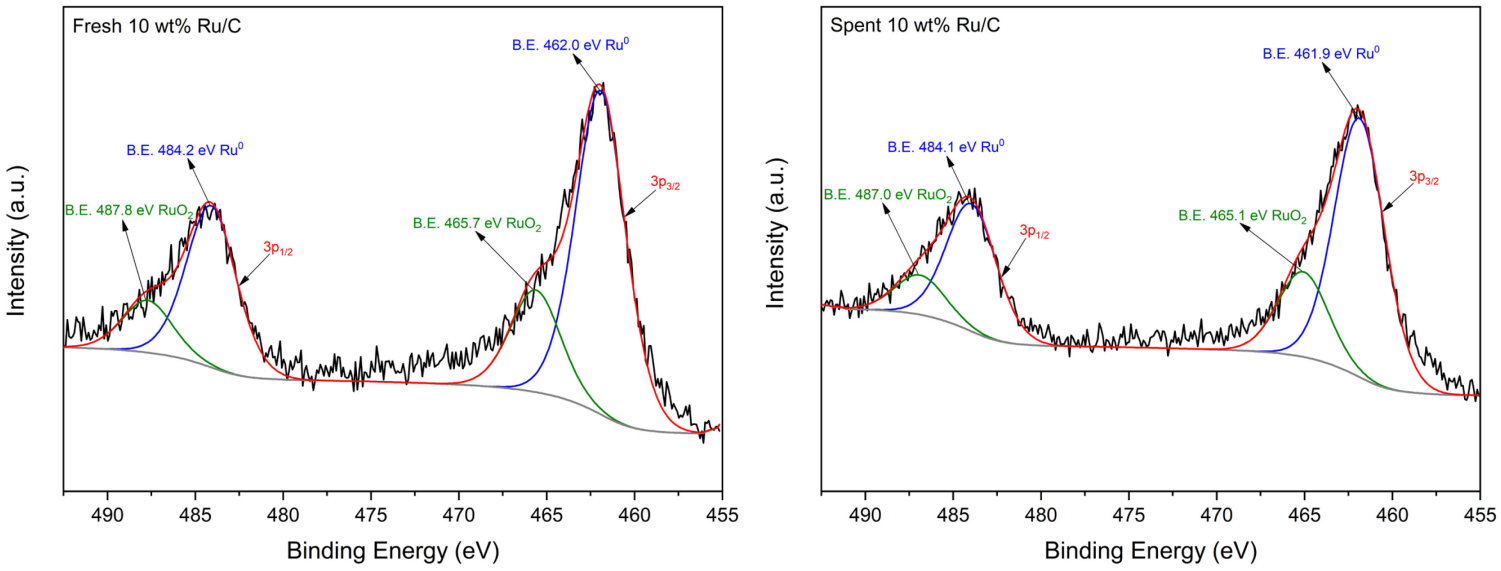


Figure 5.11. XPS spectra in the Ru 3p region for fresh and spent 10 wt% Ru/C catalysts.

Table 5.1. XPS surface elemental composition and Ru chemical-state distribution of fresh and spent Ru/C catalysts.

Catalyst	Ru chemical-state distribution (at%) [a]				Surface elemental composition (at%)		
	Ru (0) $3p_{3/2}$	Ru (IV) $3p_{3/2}$	Ru (0) $3p_{1/2}$	Ru (IV) $3p_{1/2}$	C	O	Ru
Fresh Ru/C	50.29	15.91	25.54	8.26	67.24	27.57	5.19
Spent Ru/C	50.34	16.60	25.22	7.84	63.32	30.26	6.42

[a] The atomic percentage of each Ru chemical state is calculated relative to the total Ru on the Ru/C surface.

The BET surface area, total pore volume, and average pore diameter were measured. Fresh Ru/C had a high surface area (585.24 $m^2\ g^{-1}$), favoring good Ru dispersion on the carbon support and providing abundant accessible sites for furfural oxidation. Its relatively large pore volume (0.28 $cm^3\ g^{-1}$) and suitable average pore diameter (4.46 nm) facilitate the diffusion of furfural and furoic acid, reducing internal mass-transfer limitations. After continuous operation, these values decreased modestly to 477.36 $m^2\ g^{-1}$, 0.23 $cm^3\ g^{-1}$, and 3.42 nm, respectively, which can be attributed to pore collapse, the loss of the carbon support under pressurized liquid flow, and/or partial pore blockage by organic deposits. Nevertheless, the spent catalyst retained a sufficiently high surface area, and the furfural conversion and furoic acid selectivity remained essentially unchanged over the run.

SEM-EDX elemental maps (C, O, and Ru) were acquired for the fresh and spent Ru/C catalysts (Figure 5.12). The fresh catalyst showed a uniform pore network with an intact framework, whereas the spent sample exhibited local pore collapse and coarsening, consistent with the lower BET surface area. Within the resolution of EDX, the C and O distributions did not change appreciably. In contrast, Ru was uniformly dispersed on the fresh catalyst support but formed locally enriched regions after the

reaction, indicating small-scale agglomeration. TEM images (Figure 5.13) revealed this more clearly: the fresh Ru/C contained well-separated Ru nanoparticles (particle size: 10–15 nm) with clear boundaries. However, after the reaction, the Ru particles coalesced into larger aggregates (particle size: 20–50 nm) with blurred boundaries. These observations differ from those of Lokhande et al., who reported that Ru remained uniformly distributed on the carbon support after batch furfural oxidation [379].

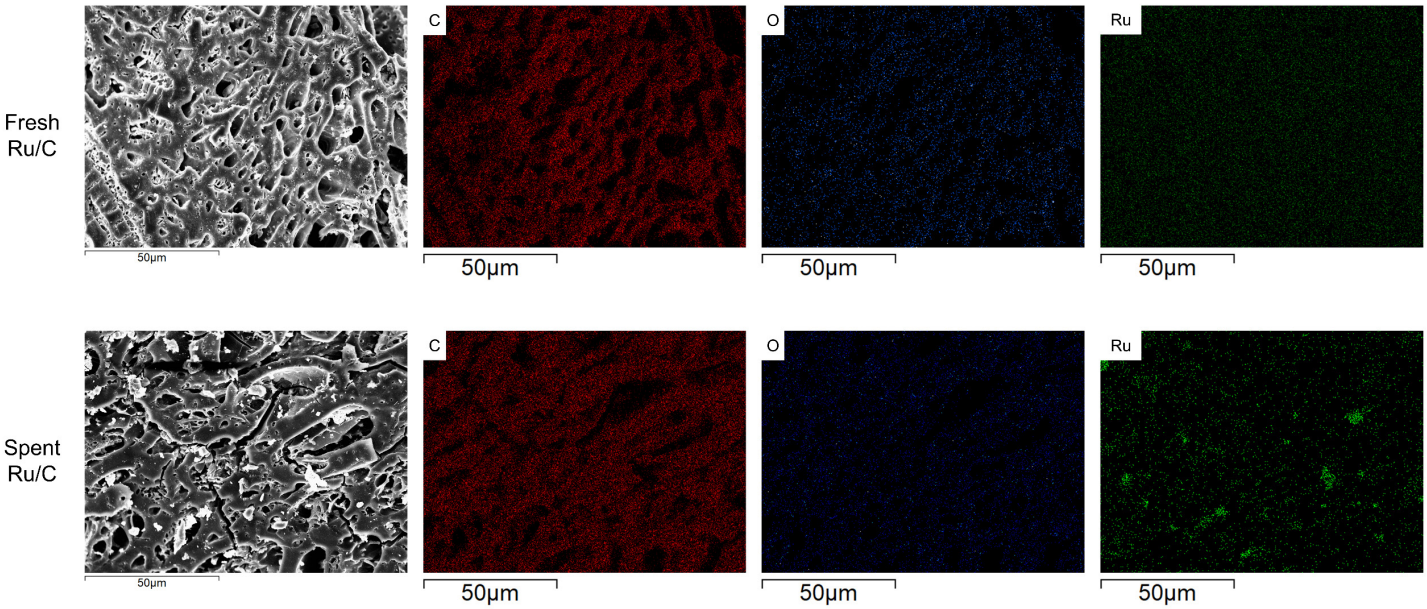


Figure 5.12. SEM images and the corresponding EDX elemental maps (C, O, and Ru) of fresh and spent 10 wt% Ru/C catalysts.

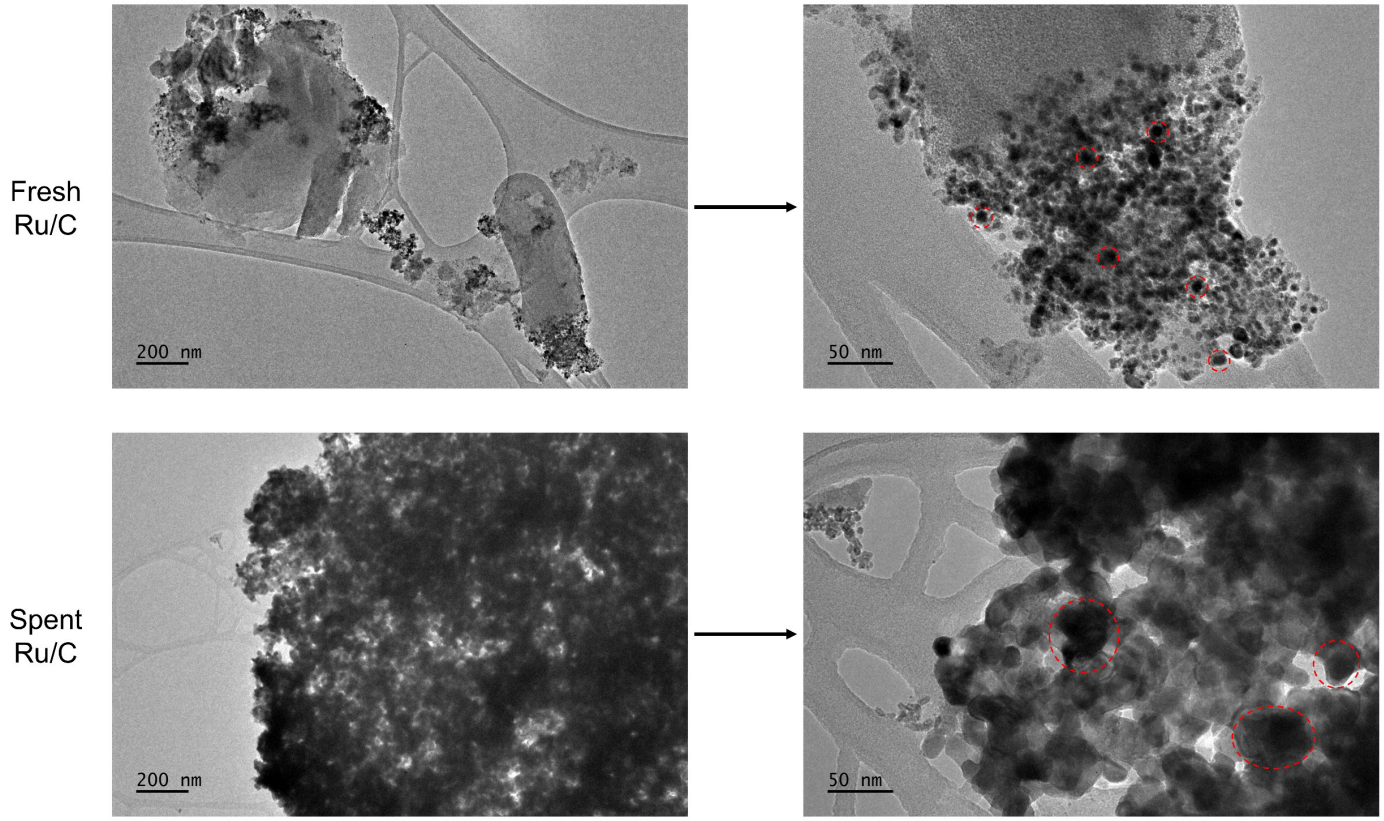


Figure 5.13. TEM images of fresh and spent 10 wt% Ru/C catalysts.

Overall, although the spent Ru/C catalyst showed a collapse of the pore structure and the aggregation of the Ru nanoparticles, neither the surface Ru abundance nor the catalytic performance declined after more than 20 h of continuous furfural oxidation.

5.3.4 Proposed Mechanisms for the Oxidation of Furfural to Furoic Acid over 10 wt% Ru/C

Because of the coexistence of Ru^0 and Ru^{4+} (RuO_2) on the catalyst, two possible pathways for furfural oxidation to furoic acid over 10 wt% Ru/C are proposed (Figure 5.14):

(1) The Ru^0-dominated O_2-activation route [384, 387]. Molecular O_2 is activated on metallic Ru into adsorbed reactive oxygen species (O*, OH*, OOH*; * denotes

adsorption on Ru^0) that act as hydrogen/electron acceptors. In alkaline water, furfural hydrates to the geminal diol and can further deprotonate to the geminal diol monoanion [71]. This intermediate is dehydrogenated on the Ru^0 surface, with adsorbed oxygen species accepting the H to form H_2O, which further desorbs and regenerates vacant Ru^0 sites for subsequent turnovers. The product is predominantly furoate, which is protonated to furoic acid upon acidification.

(2) The RuO_2-mediated (Mars–Van Krevelen) cycle [383]. Lattice oxygen from RuO_2 serves as the direct oxidant that converts the geminal diol/geminal diol monoanion to furoate (protonated to furoic acid upon acidification). In this step, Ru^{4+} is transiently reduced to lower-valent Ru^{3+} or Ru^{2+}. Molecular O_2 then reoxidizes these catalytic sites, regenerating RuO_2 and closing the redox cycle.

Due to the greater exposed fraction of Ru^0 on the catalyst surface (as indicated by XPS), the Ru^0-dominated route likely predominates under our conditions, though both pathways may proceed in parallel. Notably, high liquid flow rates over the catalyst surface, together with repeated $Ru^{4+}/Ru^{3+}/Ru^{2+}$ redox cycling in aqueous media, may drive particle growth via particle migration and coalescence (PMC) and/or Ostwald ripening [490, 491], which is consistent with the Ru nanoparticle aggregation observed in the spent 10 wt% Ru/C.

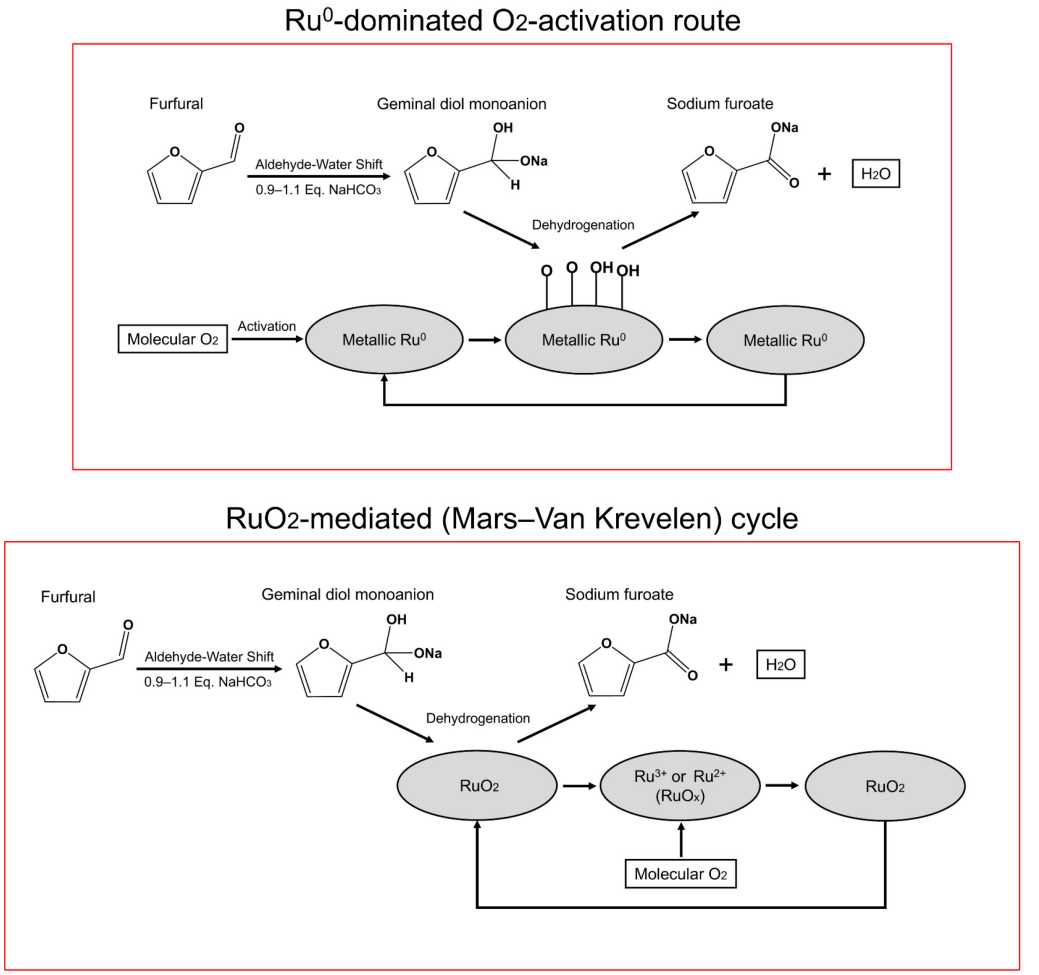


Figure 5.14. Two proposed mechanisms for the oxidation of furfural to furoic acid over 10 wt% Ru/C.

5.4 Conclusion

A high-pressure continuous-flow system was developed and, when coupled with a robust 10 wt% Ru/C catalyst, enabled the continuous oxidation of furfural to furoic acid. Key operating parameters at a 1 wt% furfural aqueous solution were the temperature, pressure, base ratio, and liquid/air flow rates. After optimization, (near)-quantitative furfural conversion and a ~95% furoic acid yield were achieved at 160 °C under 10 bar air with a 1.1:1 $NaHCO_3$-to-furfural molar ratio, using a 125 mL min^{-1} air flow and an 8–10 mL min^{-1} liquid flow. Catalytic performance remained stable over extended operation.

At higher furfural concentrations (2–3 wt%), the furoic acid selectivity remained ~90%, but furfural oxidation became limited by insufficient residence time and O_2 availability. Increasing the air flow rate from 125 to 500 mL min^{-1} improved the furoic acid yield to ~80% at 2 wt%, whereas the same air flow increase was ineffective at 3 wt% (~25% furoic acid yield). Lowering the liquid flow rate from 10 to 2.5 mL min^{-1} at 3 wt% effectively raised the furoic acid yield to ~75%, but at the expense of volumetric productivity. A practical remedy is to raise the fixed-bed length-to-diameter ratio to extend the furfural residence time over the catalyst while maintaining a high liquid throughput.

Additionally, various characterization techniques were used to compare the fresh and spent 10 wt% Ru/C catalysts. Although the spent catalyst exhibited a collapse of the pore structure on the carbon support and the aggregation of Ru nanoparticles, its surface Ru abundance and catalytic performance remained stable for more than 20 h of continuous furfural oxidation to furoic acid. Based on the XPS data, two possible catalytic pathways are proposed, including a Ru^0-dominated O_2-activation route and a RuO_2-mediated (Mars–Van Krevelen) cycle. Both of them require further validation.

Overall, these findings offer guidance for catalyst and process design toward the commercial-scale continuous furoic acid production.

5.5 External Contributions

Dr. Amir Al Ghatta (CEO, Bioataraxis Ltd) provided preliminary batch-reactor data on the oxidation of furfural to furoic acid. Bioataraxis Ltd provided external funding for the high-pressure continuous-flow setup. Boyuan Hao (Ph.D.), Yongze Chen (Ph.D.), Ruihua Luo (Ph.D.), and Dr. Mengjiao Zhai assisted with the XPS, BET, SEM, and SEM-EDX measurements, respectively.

Chapter 6: Conclusions and Future Work

6.1 Thesis Conclusions

This Ph.D. thesis focuses on developing an integrated protic ionic liquid-based biorefinery and investigates the utilization pathways of cellulose and hemicellulose in lignocellulosic biomass. The valorization approach is based on our group's ionoSolv process, modified for specific objectives. The main product streams are a cellulose-rich pulp, furfural, and furoic acid. In this context, Chapters 3–5 address the value-chain steps from fractionation to upgrading: Chapter 3 intensifies ionoSolv fractionation via sonication; Chapter 4 enables furfural production at high solids loadings with rapid vapor stripping and PIL recycling; and Chapter 5 upgrades furfural to furoic acid in a high-pressure continuous-flow system. The methodology in Chapter 3 is scientifically valuable for elucidating sonication mechanisms for ionoSolv intensification but, at this stage, is less attractive for industrial deployment due to the high cost of sonication equipment. By contrast, the process configurations developed in Chapters 4 and 5 show stronger near-term potential for industrial application. Further optimization should prioritize: (1) the co-valorization of cellulose and lignin streams during furfural production to improve economic viability; and (2) achieving a high furfural conversion and furoic acid yield at higher furfural concentrations (>3 wt%) and at high flow rates to increase productivity. Detailed conclusions for each chapter are summarized below:

Chapter 3: Sonication was applied to ionoSolv pretreatment with the PIL [DMBA][HSO_4] for different feedstocks. Its benefit was feedstock- and temperature-dependent. For *Miscanthus*, acceleration was notable only in the first hour and largely vanished by 2 h at 110 and 130 °C. For spruce, the effect was pronounced and durable. At 130 °C, 0.5 h with sonication matched the saccharification yield of 4 h of conventional ionoSolv. Lower temperatures produced stronger acceleration.

Sonication generated two pulp layers of different particle sizes. In spruce, the finer upper layer had a lower pulp yield but much higher glucan digestibility than the coarse

lower layer. Lowering solids loading or increasing ultrasonic power may improve homogeneity. The dominant macroscopic effects of sonication were heating and mass transfer enhancement. Quantitative analysis showed that the temperature rise contributed most to the increase in glucose release, with its share declining over time (*Miscanthus*: 89.8% to 73.5% from 0.25 to 0.5 h; spruce: 72.2% to 61.3% from 0.5 to 1 h).

A preliminary techno-economic analysis indicated that applying sonication during spruce fractionation could reduce the MSP of spruce-derived ethanol relative to the conventional ionoSolv route, although the magnitude of the benefit depends on the extent to which the sonication-induced, laboratory-scale temperature increase can be maintained at an industrial scale. Meanwhile, the economic feasibility of the (sonication-assisted) ionoSolv process requires the further valorization of additional biomass fractions.

Chapter 4: Furfural, a key platform chemical for pharmaceuticals, agrochemicals, fuel additives, and flavoring agents, was efficiently produced from sugarcane bagasse using a customized semi-continuous system integrating steam stripping with the low-cost PIL [DMBA][HSO_4]. Compared with a sealed system, the process achieved higher efficiency by suppressing furfural-consuming side reactions, delivering an 88% yield at 150 °C and 10 wt% biomass loading.

Solids loading had the greatest influence on the furfural yield, which dropped sharply when increased from 10 wt% to 30 wt%. To overcome this limitation, two strategies were tested under high loading conditions. Stepwise biomass addition successfully increased the yield to over 75% at 30 wt% biomass loading, while using larger biomass particles provided a slight improvement. However, the latter result suggests that energy-intensive comminution could potentially be avoided, offering economic advantages.

The [DMBA][HSO_4] can retain its catalytic activity over five reuse cycles, with an average recovery rate of 98.12%. The biochar co-produced in the process exhibited properties suitable for premium-grade solid fuel. A techno-economic analysis indicated that the production scale is the primary factor affecting the minimum selling price of furfural, largely due to high capital expenditures and fixed costs. The analysis also recommended upgrading the solid residue into higher-value cellulose products rather than converting it to biochar, thereby improving overall economics.

Chapter 5: Furoic acid is a higher-value derivative of furfural with promising applications in biopolymers and bio-based surfactants. To enable efficient, scalable production, we designed a high-pressure continuous-flow system packed with a 10 wt% Ru/C catalyst. Compared with the batch operation reported previously, the continuous system offers tighter control of temperature, pressure, and residence time, and it operated stably with negligible loss of catalytic activity over extended runs.

Under dilute conditions (1 wt% furfural in water), a ~95% furoic acid yield was achieved at 160 °C and 10 bar air with a $NaHCO_3$:furfural molar ratio of 1.1:1. The air and liquid flow rates were 125 and 8–10 mL min^{-1}, respectively. Increasing the furfural concentration to 2 wt% at otherwise similar conditions led to a marked drop in furfural conversion, while furoic acid selectivity remained high (≥90%). This indicates a bottleneck in gas–liquid–solid mass transfer and/or insufficient furfural residence time on the catalyst surface, rather than side reactions. Raising the air flow from 125 to 500 mL min^{-1} partially alleviated the oxygen supply limitation, increasing the furoic acid yield to ~80%. Similarly, at 3 wt% furfural, a liquid flow of 10 mL min^{-1} resulted in insufficient residence time. Furfural conversion fell to ~25% even with an air flow rate of 500 mL min^{-1}, while furoic acid selectivity remained ~90%. Recycling the effluent for multiple passes or reducing the liquid flow improved conversion. For example, a ~75% furoic acid yield was achieved at 2.5 mL min^{-1} liquid flow, albeit at the expense of space–time yield (productivity).

Collectively, these results identify oxygen availability and catalyst–substrate contact time as the primary levers for process intensification at elevated feed concentrations. Future work should increase residence time without sacrificing throughput—for example, by (1) lengthening the packed bed (greater bed volume/length-to-diameter ratio) and (2) modestly increasing catalyst inventory or packing density. These changes are expected to preserve high furoic acid selectivity while restoring high furfural conversion at ≥3 wt% furfural concentration and elevated flow rates.

Catalyst characterization revealed pore collapse and Ru nanoparticle aggregation in the spent Ru/C after more than 20 h of furfural oxidation. Despite these structural changes, its catalytic performance remained stable over the entire run. Based on the XPS results, two catalytic pathways are proposed—a Ru^0-dominated O_2-activation route and a RuO_2-mediated (Mars–Van Krevelen) redox cycle—both requiring further validation.

6.2 Suggestions for Future Work

While the results of this thesis are encouraging and point to the potential of a PIL-based biorefinery, full commercial deployment remains some distance away. Crucially, the future of biorefineries should not rest on bioethanol alone. Energy sources such as wind, solar, and nuclear are already integrated into power grids and supply low-carbon electricity, and the rapid development of electric vehicles is decarbonizing road transport. These trends reduce the role of bioethanol as a fuel. Nevertheless, biorefineries remain important because they can supply a broad range of bio-based chemicals and materials that progressively displace petrochemical products. Compared with other clean energy pathways, the competitiveness of biorefineries depends on a multi-product strategy that valorizes cellulose, hemicellulose, and lignin rather than an energy-only model. To consolidate the findings of this thesis, future work for each chapter is outlined below:

Chapter 3: Although we have quantified the mechanism of sonication-induced acceleration in the ionoSolv process using temperature measurements, our averaging method was limited. We estimated the system's average temperature as the arithmetic mean of the measured maximum and minimum, which implicitly assumed a linear spatial temperature profile. In acoustically driven systems, temperature distributions are typically nonlinear, which may misrepresent the true volume-averaged temperature [47]. A better approach would be to place multiple sensors (radial and axial) in the sonication-assisted ionoSolv setup or use synchronized infrared thermography to capture a more comprehensive temperature map and obtain a more reliable estimate of the system's average temperature. This would allow for a more accurate separation of effects arising from sonication-driven heating versus mass transfer enhancement.

Our analysis considered only macroscopic physical effects. Chemical effects associated with cavitation, particularly transient free radical formation [492], were not evaluated and may have contributed to the observed acceleration of biomass fractionation. Future studies should incorporate control measures, such as the use of free radical scavengers, to isolate and assess these contributions.

The heterogeneous particle sizes generated during the sonication-assisted ionoSolv remain problematic, especially when homogeneous material is required for downstream applications. In a viscous, high-biomass-loading ionic liquid medium, ultrasound is strongly damped, and effective cavitation is confined to the vicinity of the sonication probe [492]. Therefore, material farther from the probe experiences little disruption. Future work should evaluate higher-power transmitters, multiple probes, lower biomass loadings, and integration with mechanical agitation to improve biomass disruption uniformity and ensure consistent product quality.

The main bottleneck for current sonication technology is scaling up from laboratory-scale to industrial-scale operation. Our preliminary techno-economic analysis indicated that sonication-assisted ionoSolv could reduce the production cost of spruce-derived

ethanol relative to the conventional ionoSolv process. However, even at a biomass processing capacity of 2,000 tons per day, the estimated MSP of ethanol remained substantially higher than recently reported ethanol market prices. A priority for further work is a detailed techno-economic analysis to identify the key drivers of sonication-related CAPEX and OPEX at scale and to define approaches for reducing these costs. Meanwhile, shifting the product structure from bioethanol to higher-value co-products (e.g., nanocellulose, furan-based intermediates, and lignin-derived nanofibers) could improve the economics of large-scale biorefineries.

Chapter 4: Although the semi-continuous furfural production process is technically effective, the minimum selling price of furfural from this route remains uncompetitive in the current market, even on a full industrial scale (30,000 kg h^{-1}) with a high recyclability (99.9%) of the PIL [DMBA][HSO_4]. The main limitation is the single-product model: hemicellulose is converted to furfural, while cellulose and lignin are largely carbonized to biochar to meet process heat demand. This supports a near-carbon-neutral energy balance but leaves much of the PIL-based biorefinery potential unrealized.

Operationally, a low water content in the PIL promotes biochar formation. Even with a bubbler, the PIL's water content fell below 10 wt% during furfural production, and its high acidity drove the rapid dehydration of the solids rather than the effective fractionation of cellulose and lignin. To suppress charring and enable ionoSolv fractionation, the system should maintain roughly 20–25 wt% water in the PIL. Therefore, we propose a pressurized steam-assisted ionoSolv setup for future study (Figure 6.1). This system uses an HPLC metering pump to feed water to a steam generator. Steam is sent to a high-pressure reactor containing biomass and the PIL, where it continuously strips furfural from the solvent. The vapors are then condensed into a furfural–water stream. A back-pressure regulator located between the reactor and condenser maintains the set pressure and stabilizes the PIL's water content.

Under these conditions, biomass fractionation proceeds as intended, avoiding biochar formation in the residual solids. A cellulose-rich pulp can be obtained for fermentation or material upgrading. Lignin can be precipitated by water addition and directed to higher-value applications such as carbon fibers. The furfural–water condensate is purified to the platform product. The timely removal of furfural also limits condensation between furfural, sugars, and lignin, reducing pseudo-lignin formation and improving pulp quality. In this way, the process moves from a furfural-only route to a true multi-product biorefinery that fully utilizes cellulose, hemicellulose, and lignin, improving overall economic viability.

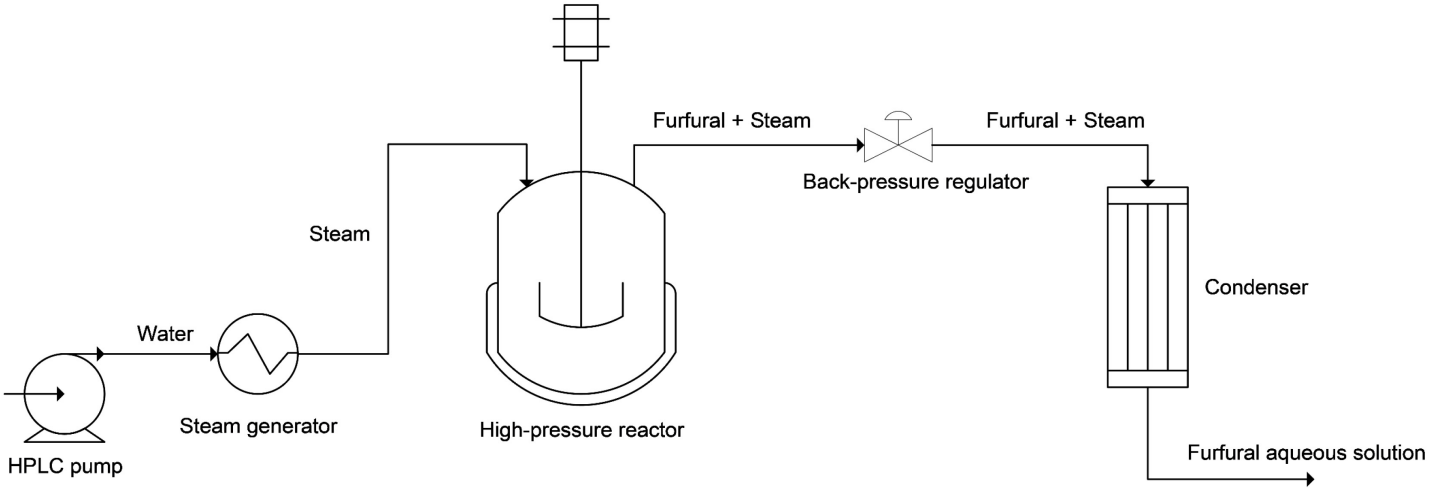


Figure 6.1. Pressurized steam-assisted ionoSolv setup.

Chapter 5. The high-pressure continuous-flow system with a 10 wt% Ru/C catalyst effectively oxidized 1–2 wt% furfural aqueous solutions to furoic acid under optimized conditions. At a 3 wt% feed, however, furfural conversion fell because the residence time over the catalyst (or O_2 availability per mole of substrate) was insufficient for complete oxidation. Reducing the liquid flow would promote furfural conversion but at the expense of volumetric productivity, which is unfavorable for scale-up. Because furoic acid selectivity did not decline at higher furfural concentrations, the rational design change is to increase the fixed-bed length-to-diameter ratio, extending the

furfural residence time at the same throughput to achieve full conversion of the more concentrated feed. Additionally, the experiments should be replicated to enhance the accuracy and reliability of the findings.

To clarify the underlying mechanism in continuous furfural oxidation, the gas–liquid flow regime (e.g., trickle, pulse, or dispersed-bubble) in the fixed-bed reactor should be identified experimentally or with validated models, because the flow regime governs catalyst wetting and the interfacial area, thus influencing oxygen–furfural mass transfer, heat transfer, and final furfural oxidation.

Further catalyst-design optimization is needed to mitigate carbon-support morphological changes and to limit Ru surface enrichment and nanoparticle aggregation. The proposed mechanisms, the Ru^0-dominated O_2-activation route and the RuO_2-mediated (Mars–Van Krevelen) cycle, require targeted experimental validation.

Before pilot-scale demonstration, a detailed techno-economic analysis is needed to estimate the minimum selling price of furoic acid and to test its sensitivity to feed concentration, volumetric productivity, oxygen utilization, and wastewater management. Downstream integration should also be evaluated—for example, upgrading furoic acid to FDCA and then to PEF, or pursuing routes to bio-based surfactants—to capture additional value and strengthen overall viability.

Appendices

Chapter 2:

Physical Pretreatment—Extrusion

Extrusion pretreatment is a thermo-mechanical method that combines shearing, heating, and mixing [493]. During the extrusion process, biomass is continuously fed into a single-screw or twin-screw extruder, where a rotating screw pushes the material through a tight barrel at elevated temperatures and pressures while subjecting it to intense mechanical shear forces [278, 494]. Under these thermal and mechanical stresses, extrusion disrupts the lignin–carbohydrate matrix, reducing particle size and increasing the surface area and fibrillation of the biomass [493]. As a result, enzyme accessibility during subsequent saccharification increases markedly [493, 495]. Heredia-Olea et al. investigated the effects of various extrusion parameters (e.g., barrel temperature, screw speed, and feedstock moisture) on sweet sorghum bagasse [496]. The results indicated that, under optimal conditions (100 °C, 200 rpm screw speed, and 30 wt% moisture content), up to 70% of total sugars were released from the pretreated fiber matrix during the subsequent enzymatic hydrolysis. Meanwhile, no inhibitory compounds (e.g., acetic acid, furfural, and HMF) were detected in the enzymatic hydrolysate, which could be fermented by yeast to about 200 mL ethanol per kg of extruded biomass. As with milling, large-scale extrusion faces high capital costs and high operating energy demands. Wahid et al. reported a specific energy consumption of 226–324 kWh t^{-1} for the extrusion pretreatment of wheat straw and deep litter [497]. Lamsal et al. also showed that the extrusion pretreatment of wheat bran yielded high levels of reducing sugars, but required a mechanical energy input of about 1,500 kJ kg^{-1} (417 kWh t^{-1}) [498]. To cut the energy demand of extrusion and improve its economic feasibility, extruder designs with efficient heat recovery and process integration are required.

Chemical Pretreatment—Oxidative Pretreatment

Oxidative pretreatment introduces oxidants, such as H_2O_2 and O_3 (ozonolysis), to

delignify lignocellulosic biomass [32, 499]. Under basic conditions, H_2O_2 generates highly reactive radical species that attack lignin (side chains and ester/ether linkages), fragmenting the macromolecules into low-molecular-weight compounds [32, 499, 500]. Additionally, a large fraction of hemicellulose is degraded by H_2O_2, whereas most cellulose remains and shows higher enzymatic digestibility [499]. After H_2O_2 pretreatment, the solids often turn white, which is why this method is widely used in pulp bleaching [501, 502]. Ozone can also disrupt the conjugated regions of lignin, enabling effective delignification, while its reactivity toward carbohydrates is low [499]. Consequently, ozonolysis pretreatment forms very low levels of fermentation inhibitors (e.g., furfural and HMF) [292, 499]. For instance, García-Cubero et al. treated wheat and rye straw with ozone at room temperature in a fixed-bed reactor [503]. Significant lignin removal occurred with only slight hemicellulose degradation and negligible cellulose loss. Enzymatic hydrolysis then released 89% glucose from wheat straw and 57% from rye straw, compared with only 29% and 16% for the non-ozonated controls. One advantage of O_3 and H_2O_2 is their high selectivity for lignin, which allows for milder operating conditions [499]. However, these oxidants are still costly and difficult to recover, limiting their large-scale application [32, 266, 499]. Therefore, oxidative pretreatment is often used as an adjunct to other methods to improve lignin removal. For example, Ummalyma et al. reported that treating bamboo with 1% (w/v) H_2O_2 at 121 °C for 1 h raised cellulose digestibility to 75%, while a combined 1% (w/v) NaOH–H_2O_2 treatment boosted lignin removal further, yielding 83% digestibility [504]. Furthermore, the “Milox” pulping process also combines formic acid with H_2O_2 to generate peroxyformic acid, a strong oxidant that removes lignin and hydrolyzes hemicellulose efficiently [505].

Chemical Pretreatment—Organosolv Pretreatment

Organosolv pretreatment refers to the use of organic solvents, such as methanol, ethanol, acetone, and ethylene glycol, to fractionate biomass components [278, 506]. These solvents can penetrate the cell wall and cleave the β-O-4′ ether and 4-O-methylglucuronic acid ester bonds linking hemicellulose and lignin, dissolving most

lignin and part of the hemicellulose while leaving a cellulose-rich pulp with higher enzyme accessibility [16, 507, 508]. Lignin dissolved in the liquor can be regenerated as a high-purity (sulfur-free, low-carbohydrate), low-molecular-weight product with a narrow molecular weight distribution, suitable for use in carbon fibers, antioxidants, and epoxy resins [16, 32, 509, 510]. The organic solvent can be recovered through distillation [278]. Optimal operating conditions often depend on the recalcitrance of the feedstock. For example, grass biomass can be treated at 90–120 °C in ethanol-based organosolv, whereas hardwood and softwood require 150–220 °C [511]. Other reaction parameters, including solvent types, reaction times, solvent–water ratios, and solvent-to-biomass ratios, should also be adjusted on a case-by-case basis. Additionally, small amounts of acids (e.g., HCl and H_2SO_4) or alkalis (e.g., NaOH and lime) are often added during organosolv pretreatment to improve delignification or reduce operating temperatures [278, 512]. Park et al. studied ethanol-based organosolv pretreatment of pitch pine from 150 to 210 °C with 1% (w/v) catalysts [513]. Both H_2SO_4 and $MgCl_2$ raised digestibility to 50–60% under optimal conditions, whereas NaOH had little effect, giving about 10% digestibility across all conditions. Huijgen et al. also examined organosolv pretreatment of willow wood and wheat straw at 190 °C using HCl, H_2SO_4, or $MgCl_2$ as catalysts [514]. With 0.01 mol/L H_2SO_4, the authors obtained 87% enzymatic cellulose conversion for willow wood, whereas with 0.02 mol/L HCl, they obtained 99% conversion for wheat straw. These values were far higher than those achieved with non-catalytic organosolv treatment under the same conditions. In contrast, $MgCl_2$ produced only a modest improvement in biomass fractionation and enzymatic digestibility compared with the acid catalysts. The main advantages of organosolv pretreatment are straightforward solvent recovery by distillation and the opportunity to valorize high-purity lignin [278]. However, solvent costs make the economics highly sensitive to recovery efficiency [278, 515], placing strict demands on recovery equipment. The solvents' volatility and flammability also raise safety concerns, requiring robust reactors [138, 512], especially at the elevated temperatures and pressures used during pretreatment.

Physicochemical Pretreatment—Supercritical CO_2 Explosion

Compared with toxic ammonia [331], supercritical CO_2 explosion has emerged as a greener alternative owing to the non-toxicity and non-flammability of CO_2 [516]. Supercritical CO_2 pretreatment exploits CO_2 above its critical point (31.1 °C, 73.8 bar) [517], where it combines gas-like diffusivity with liquid-like solvating power [516]. Under high pressure, CO_2 penetrates the biomass matrix, and rapid depressurization then causes explosive CO_2 expansion, physically disrupting cell walls, increasing porosity, and enlarging the enzyme-accessible surface area [228, 518]. The moisture content of biomass strongly influences pretreatment effectiveness, since dissolved CO_2 can form carbonic acid, which accelerates hemicellulose hydrolysis [32, 278]. Narayanswamy et al. treated corn stover with supercritical CO_2 at 100–150 °C and 2,500–3,500 psi (172–241 bar) for 1 h, observing that glucose release rose from 13 g glucose/100g corn stover (0 wt% moisture) to 24 g/100 g (75 wt% moisture) [519]. Additionally, under optimal conditions (3,500 psi (241 bar), 150 °C, and 60 min), they obtained 30 g glucose per 100 g corn stover, 2.5 times higher than that of native corn stover, which was attributed to increased porosity after pretreatment. However, for more recalcitrant switchgrass, the effect of supercritical CO_2 is very limited. Because supercritical CO_2 alone removes little lignin [32], it is often combined with co-solvents. For instance, Lv et al. paired supercritical CO_2 with a water–ethanol mixture as a co-solvent for corn stover pretreatment [520]. Superior delignification efficiency can be obtained due to enhanced ether-bond cleavage and high lignin solubility in the water–ethanol co-solvent, which further boosted enzymatic hydrolysis. Supercritical CO_2 explosion has been shown to be more cost-effective than AFEX and, unlike steam explosion, generates no fermentation inhibitors [521]. However, saccharification yields are lower than those achieved with AFEX or steam explosion [228, 279]. Currently, the principal barrier to the industrial adoption of supercritical CO_2 pretreatment remains the high capital cost of pressure-rated equipment [32, 228, 278].

Table S1. Effects of different pretreatment methods on the composition and structure of lignocellulosic biomass.

Pretreatment	Delignification	Lignin structure alteration	Hemicellulose removal
Milling	L [a]	M [a]	L
Extrusion	L	H	L
Ultrasound (alone)	L	L	L
Biological (White rot)	H [a]	H	L-M
Dilute Acid	L	M-H	H
Alkaline	H	H	M
Oxidative (H_2O_2)	H	H	M-H
Oxidative (ozonolysis)	H	H	L
Organosolv	H	H	M
IonoSolv	H	H	H
Steam explosion	L	M	M-H
AFEX	L	M	L
CO_2 explosion	L	L	M

Pretreatment	Increasing cellulose-accessible surface area	Generation of inhibitors	Reference
Milling	H	L	[32, 494, 522, 523]
Extrusion	H	L	[493, 524]
Ultrasound	M	L	[301]
Biological (White rot)	H	L	[278, 279, 292, 525]
Dilute Acid	H	H	[292, 526]
Alkaline	H	L	[32, 301]
Oxidative (H_2O_2)	H	L	[499]
Oxidative (ozonolysis)	H	L	[499]

Organosolv	H	L	[508]
IonoSolv	H	M	[19, 36]
Steam explosion	H	H	[32, 527]
AFEX	H	L	[32, 327]
CO_2 explosion	H	L	[32, 279, 528]

[a] H: high effect; M: medium effect; L: low effect

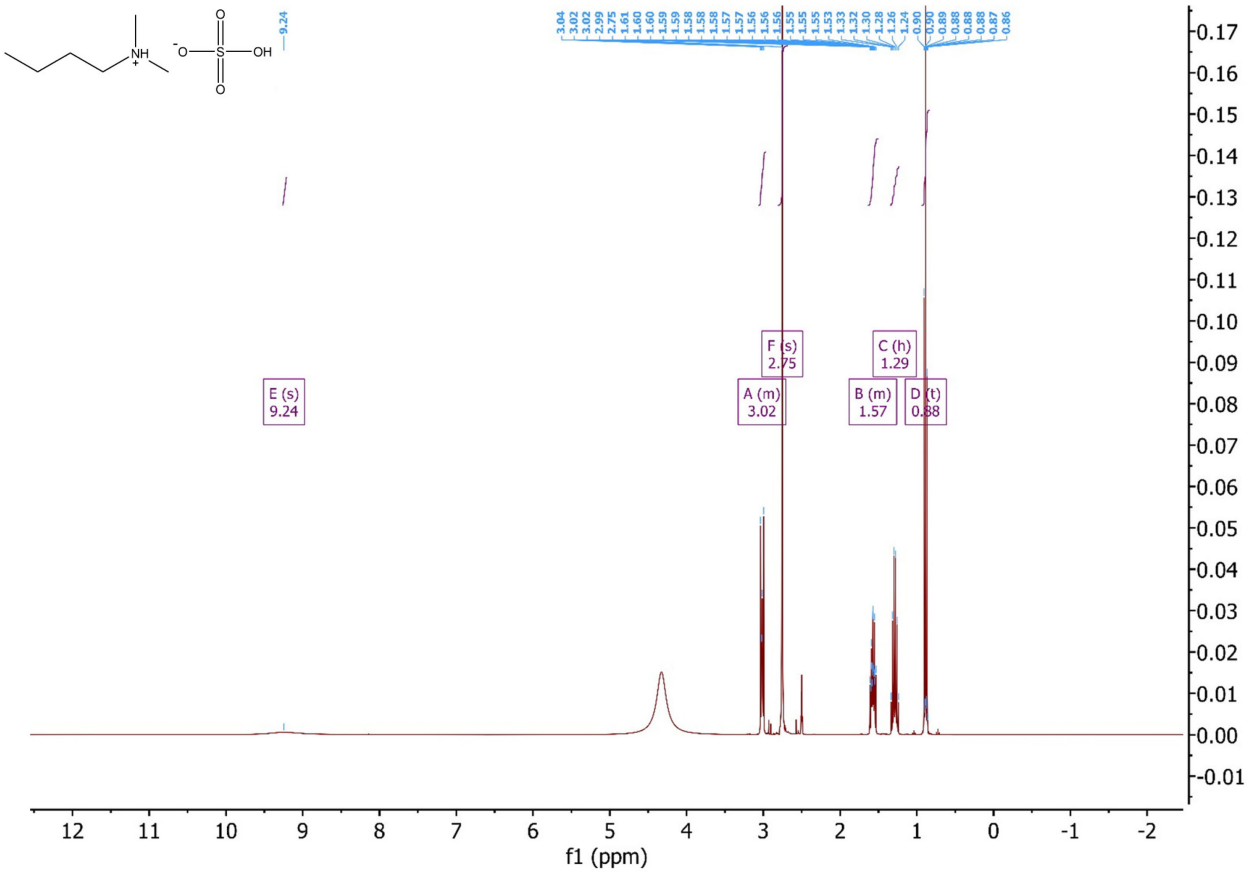


Figure S1. ^{1}H NMR of fresh [DMBA][HSO_4] for the ionoSolv process: δ_H (400 MHz, DMSO-d_6)/ppm: 9.24 (s, 1H, N–*H*), 3.06–2.97 (m, 2H, N–CH_2), 2.75 (s, 6H, N–(CH_3)$_2$), 1.63–1.51 (m, 2H, N–CH_2–CH_2), 1.29 (h, J = 7.4 Hz, 2H, N–CH_2–CH_2–CH_2), 0.88 (t, J = 7.4 Hz, 3H, N–CH_2–CH_2–CH_2–CH_3).

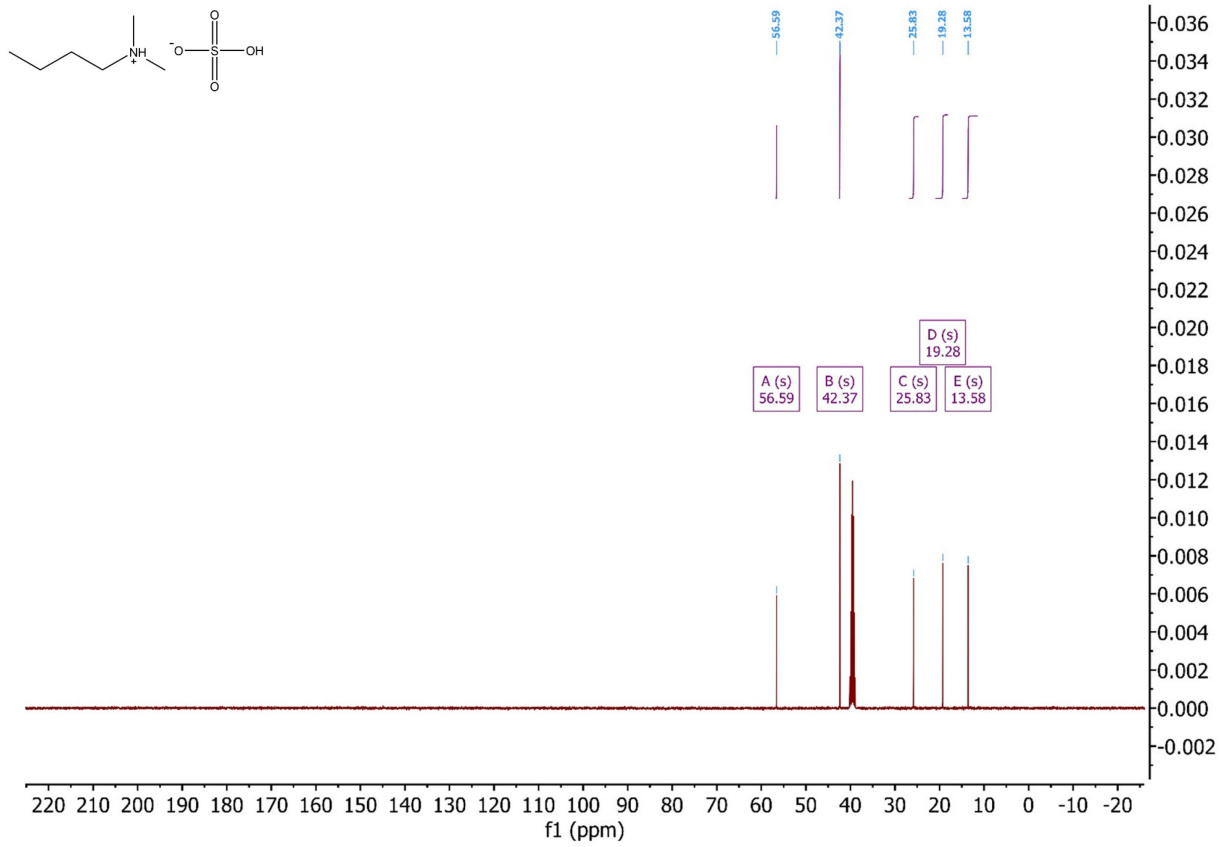


Figure S2. ^{13}C NMR of fresh [DMBA][HSO_4] for the ionoSolv process: δ_C (101 MHz, DMSO-d_6)/ppm: 56.59 (N–CH_2), 42.37 (N–(CH_3)$_2$), 25.83 (N–CH_2–CH_2), 19.28 (N–CH_2–CH_2–CH_2), 13.58 (N–CH_2–CH_2–CH_2–CH_3).

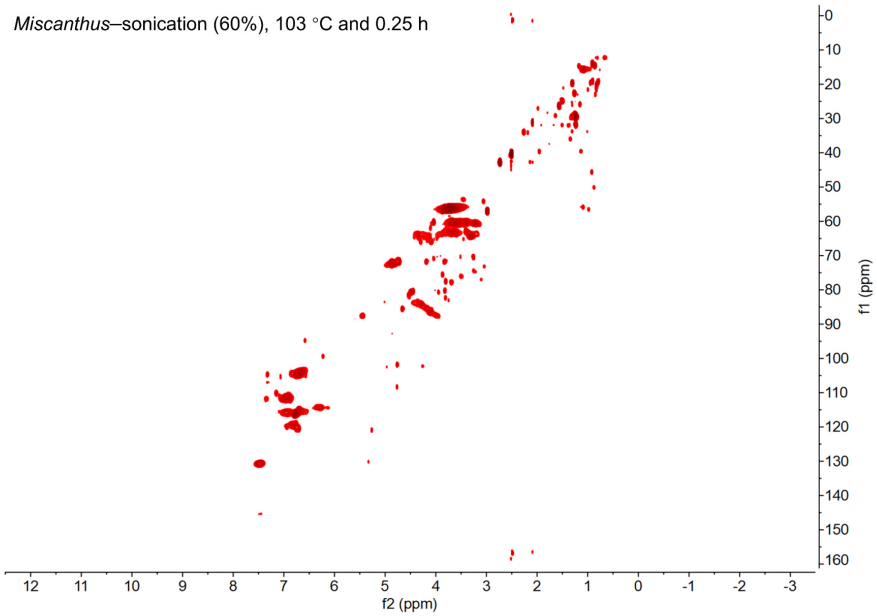


Figure S3. HSQC NMR spectrum of *Miscanthus* lignin isolated after the sonication-assisted ionoSolv process at 103 °C and 0.25 h.

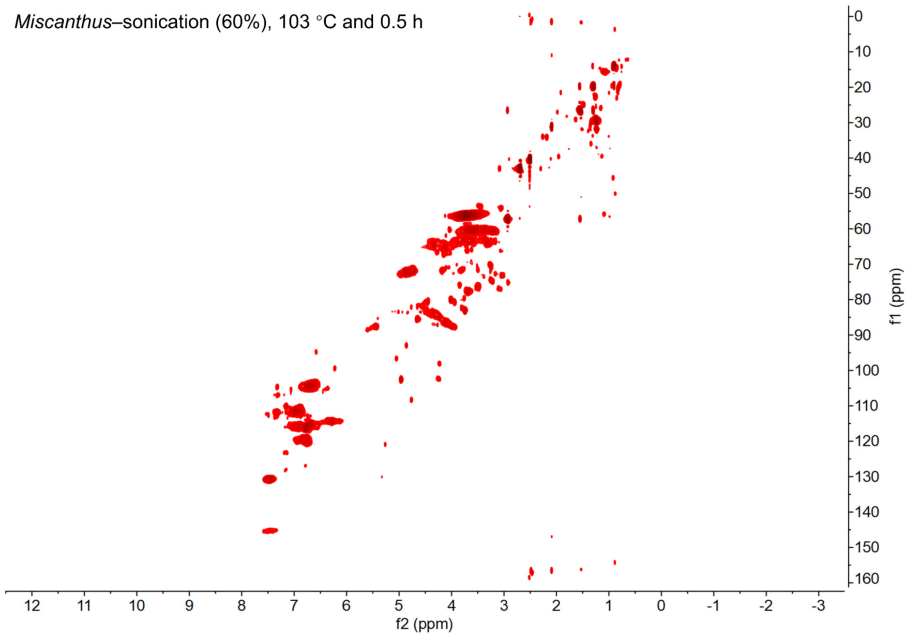


Figure S4. HSQC NMR spectrum of *Miscanthus* lignin isolated after the sonication-assisted ionoSolv process at 103 °C and 0.5 h.

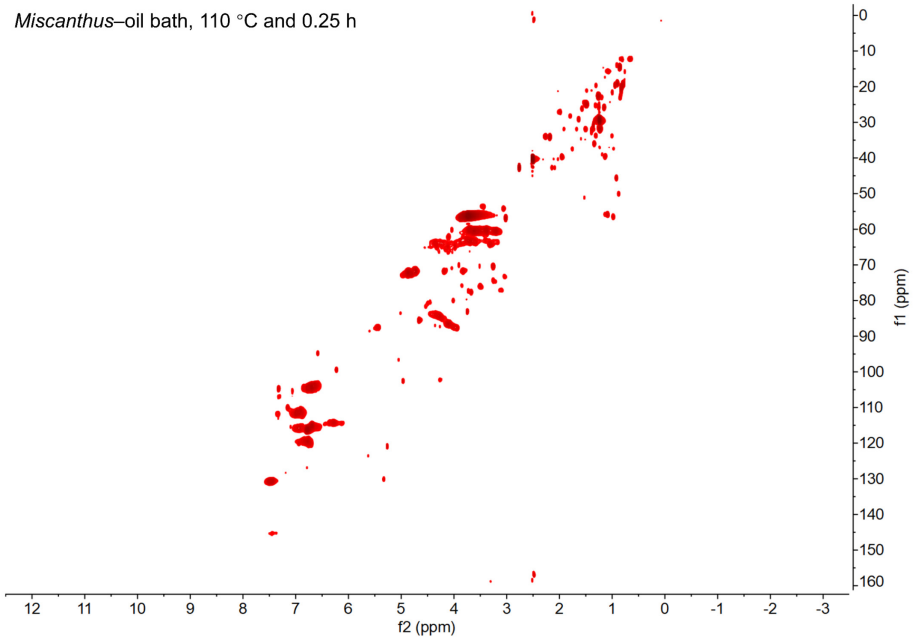


Figure S5. HSQC NMR spectrum of *Miscanthus* lignin isolated after the oil-bath heating ionoSolv process at 110 °C and 0.25 h.

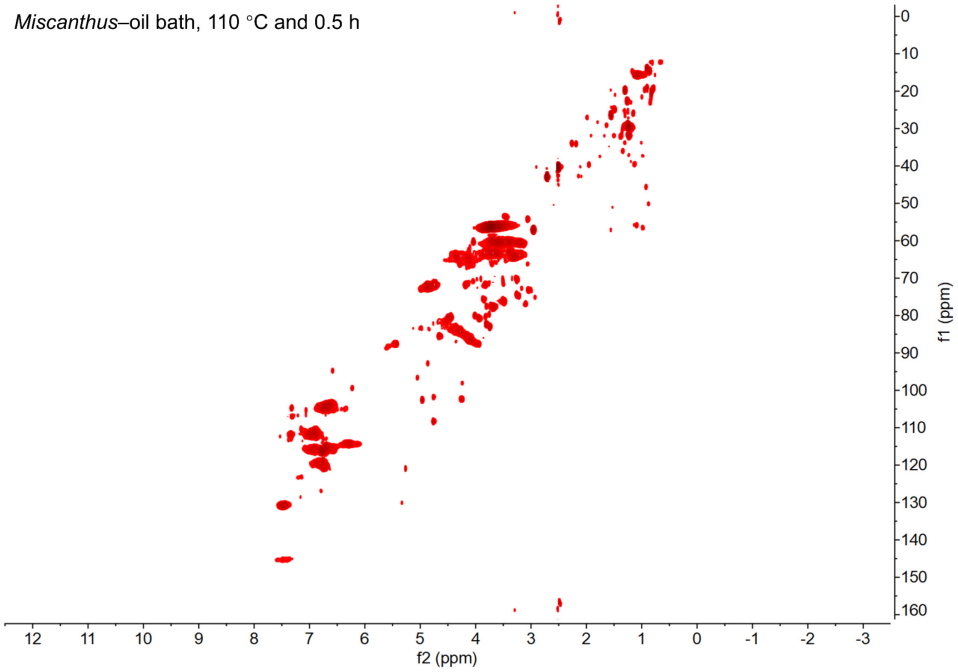


Figure S6. HSQC NMR spectrum of *Miscanthus* lignin isolated after the oil-bath heating ionoSolv process at 110 °C and 0.5 h.

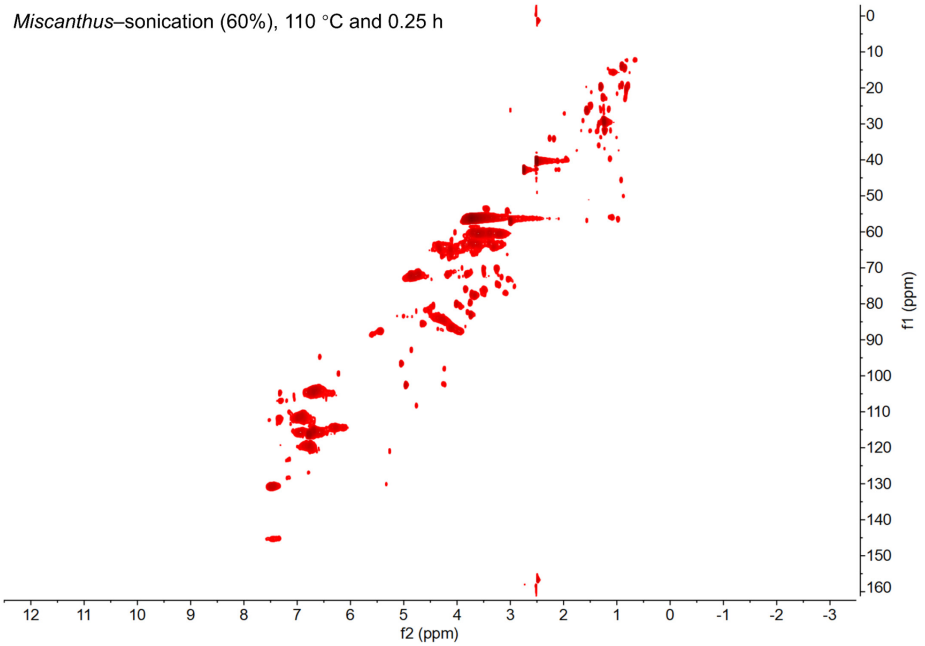


Figure S7. HSQC NMR spectrum of *Miscanthus* lignin isolated after the sonication-assisted ionoSolv process at 110 °C and 0.25 h.

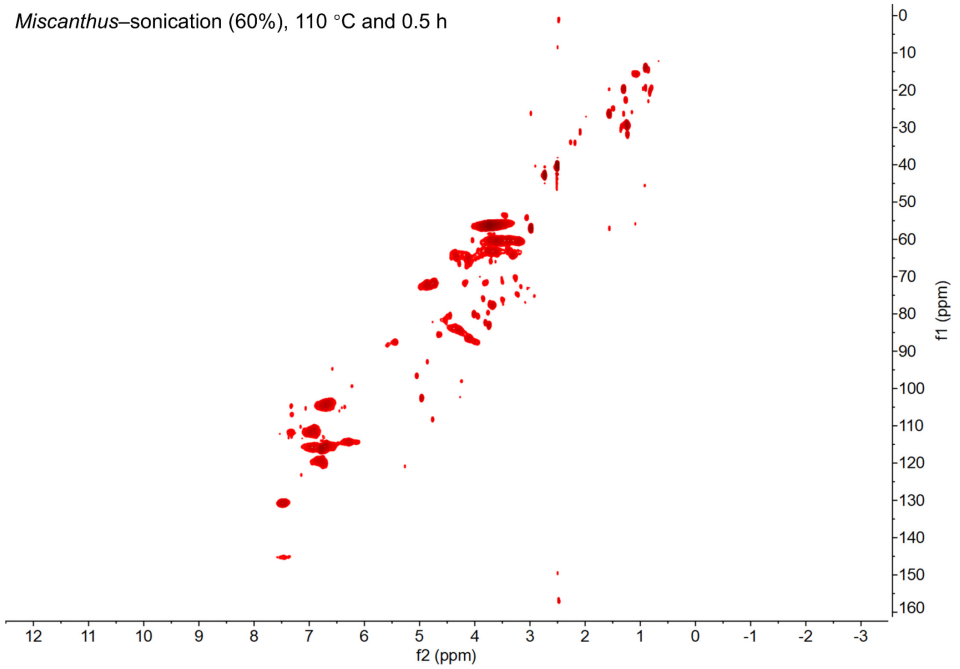


Figure S8. HSQC NMR spectrum of *Miscanthus* lignin isolated after the sonication-assisted ionoSolv process at 110 °C and 0.5 h.

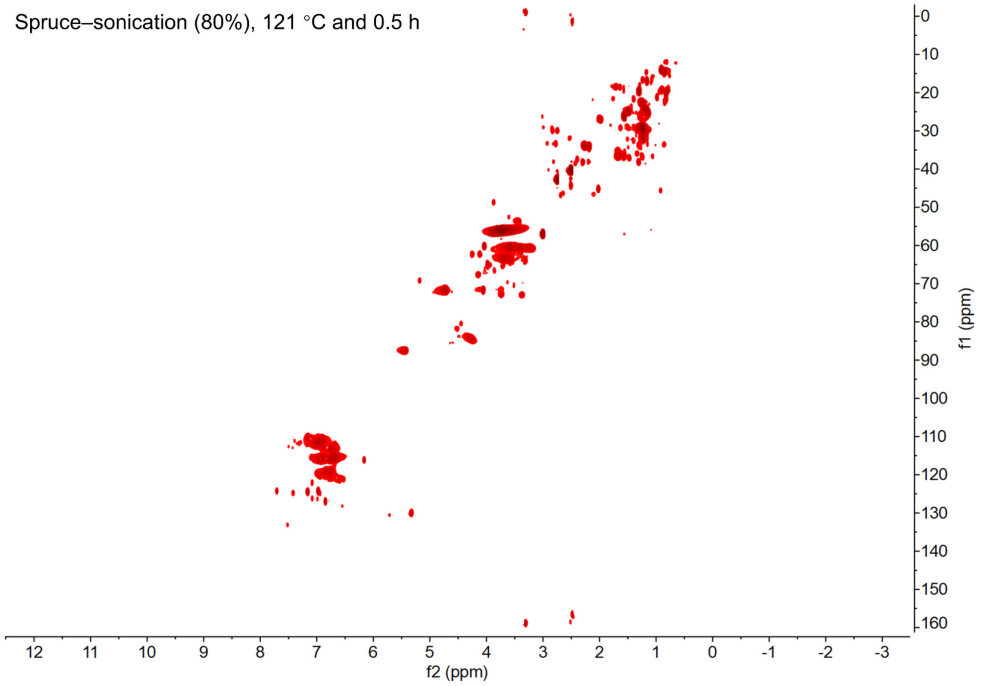


Figure S9. HSQC NMR spectrum of spruce lignin isolated after the sonication-assisted ionoSolv process at 121 °C and 0.5 h.

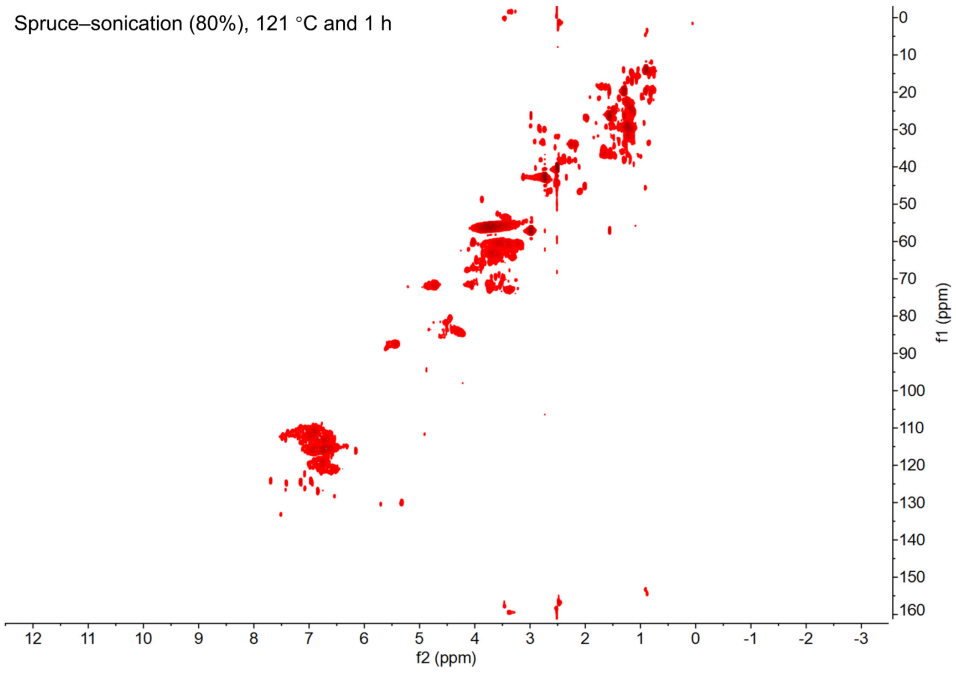


Figure S10. HSQC NMR spectrum of spruce lignin isolated after the sonication-assisted ionoSolv process at 121 °C and 1 h.

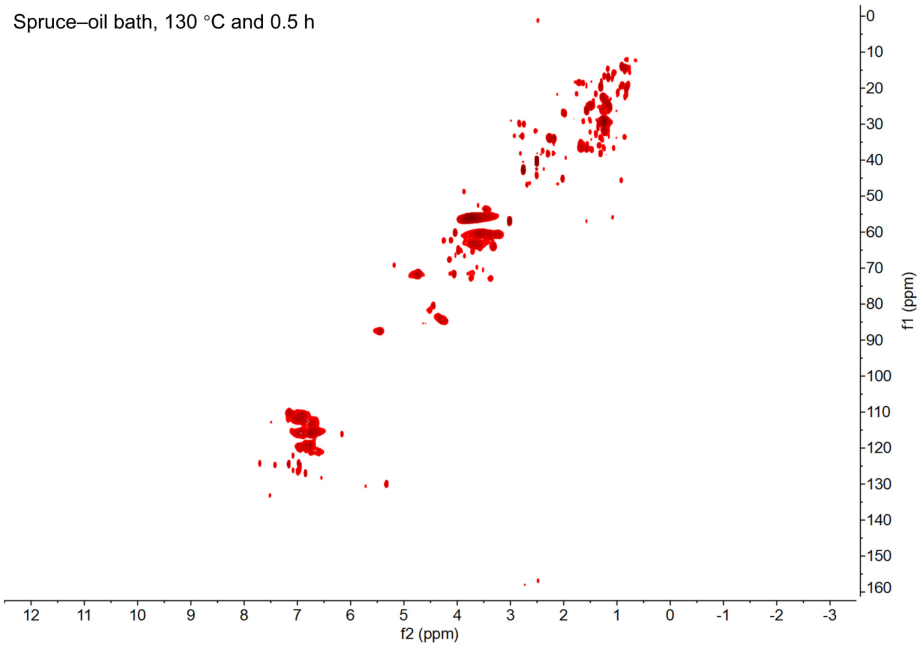


Figure S11. HSQC NMR spectrum of spruce lignin isolated after the oil-bath heating ionoSolv process at 130 °C and 0.5 h.

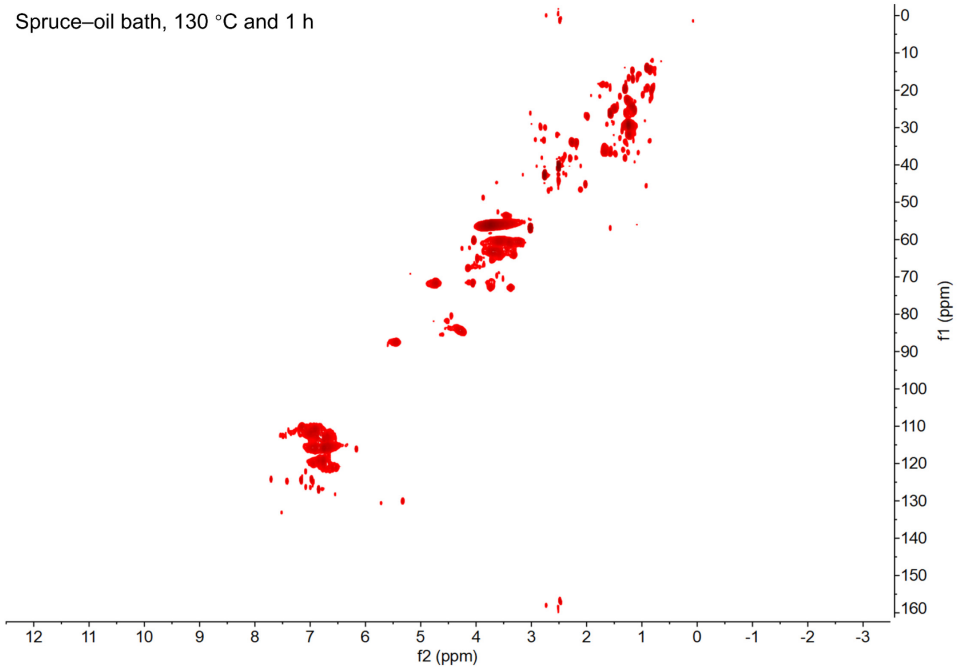


Figure S12. HSQC NMR spectrum of spruce lignin isolated after the oil-bath heating ionoSolv process at 130 °C and 1 h.

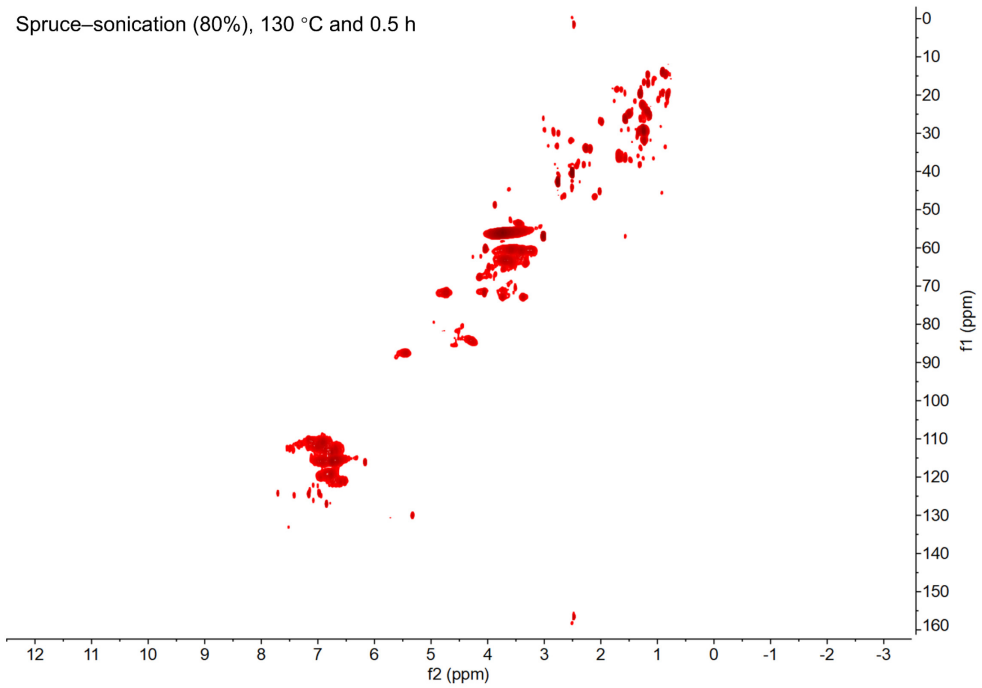


Figure S13. HSQC NMR spectrum of spruce lignin isolated after the sonication-assisted ionoSolv process at 130 °C and 0.5 h.

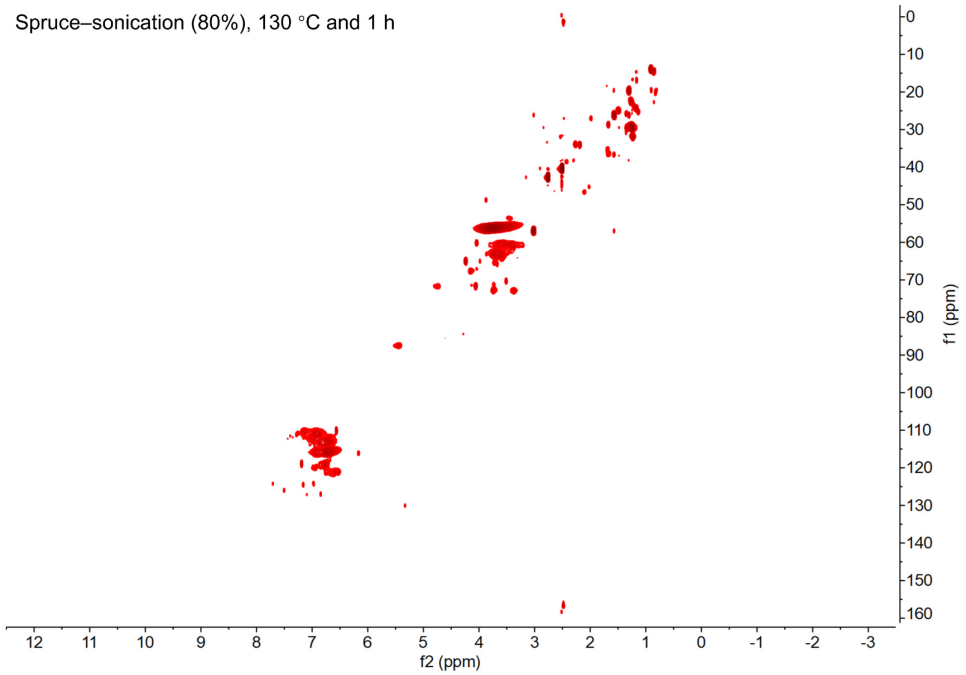


Figure S14. HSQC NMR spectrum of spruce lignin isolated after the sonication-assisted ionoSolv process at 130 °C and 1 h.

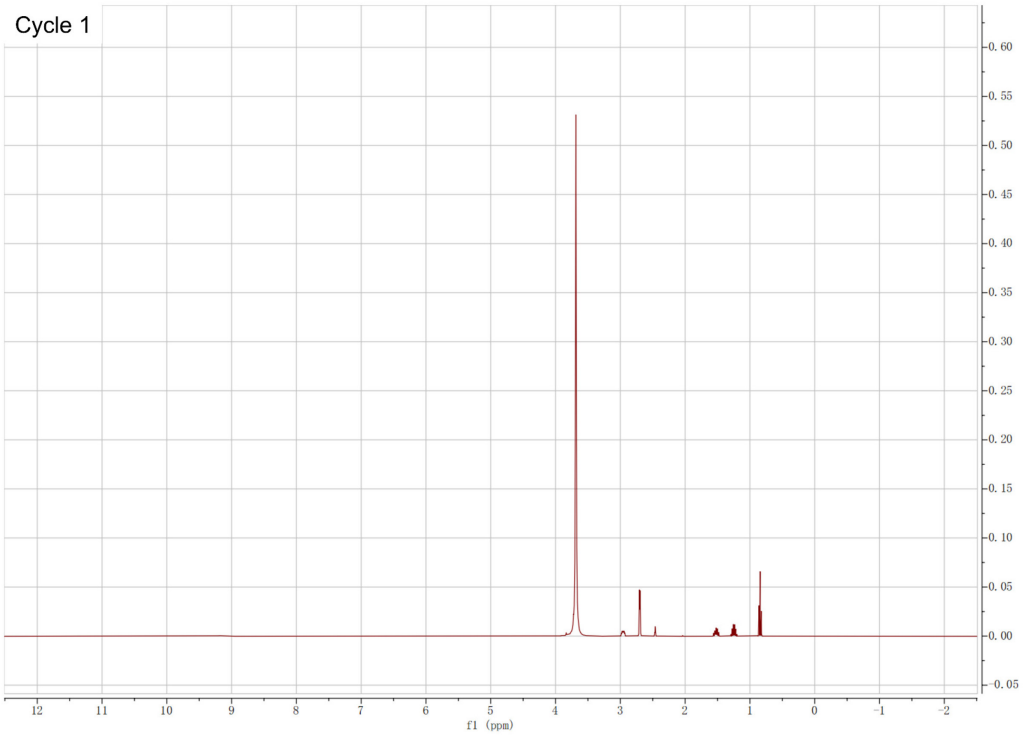


Figure S15. ^{1}H NMR of [DMBA][HSO_4] recovered after cycle 1.

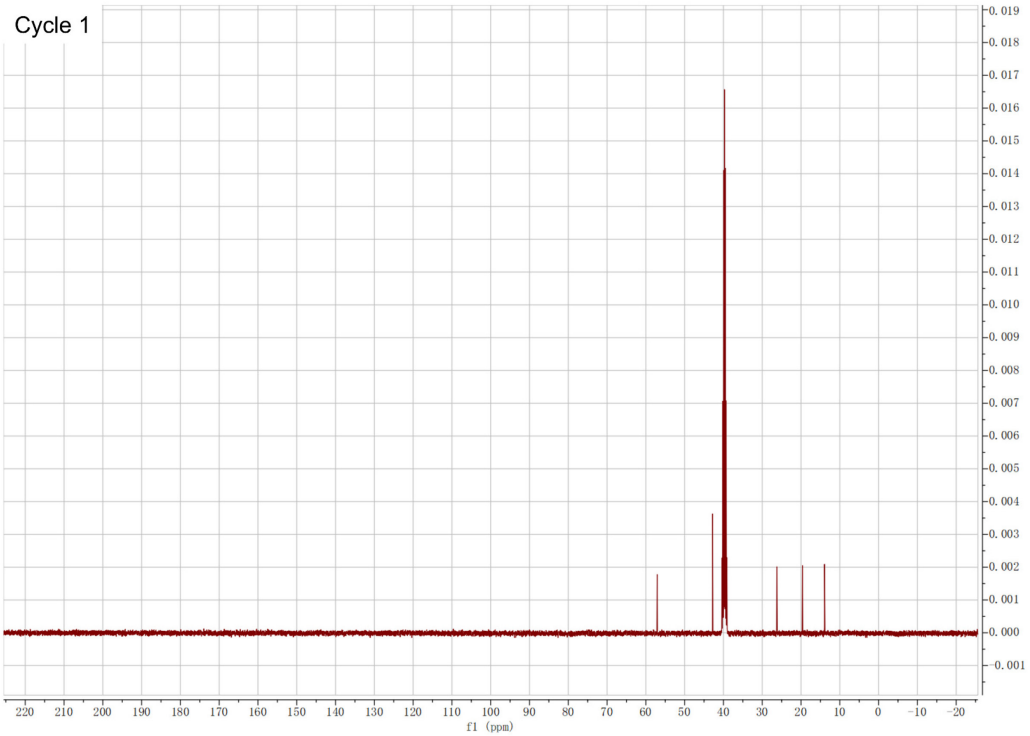


Figure S16. ^{13}C NMR of [DMBA][HSO_4] recovered after cycle 1.

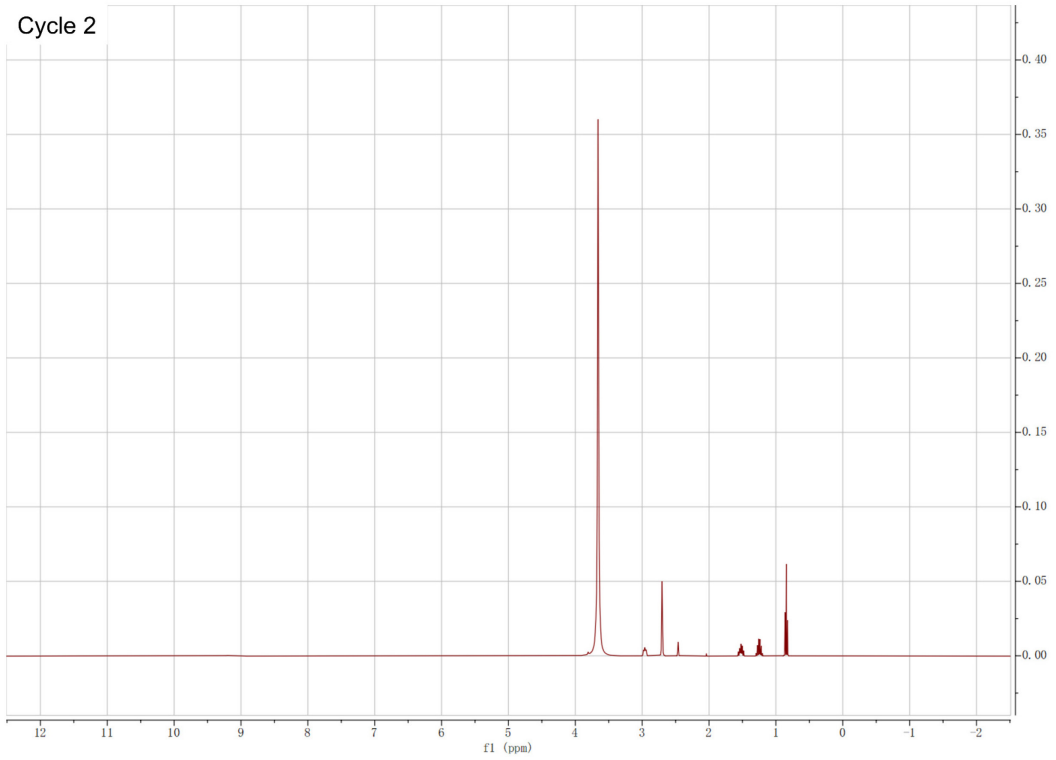


Figure S17. ^{1}H NMR of [DMBA][HSO_4] recovered after cycle 2.

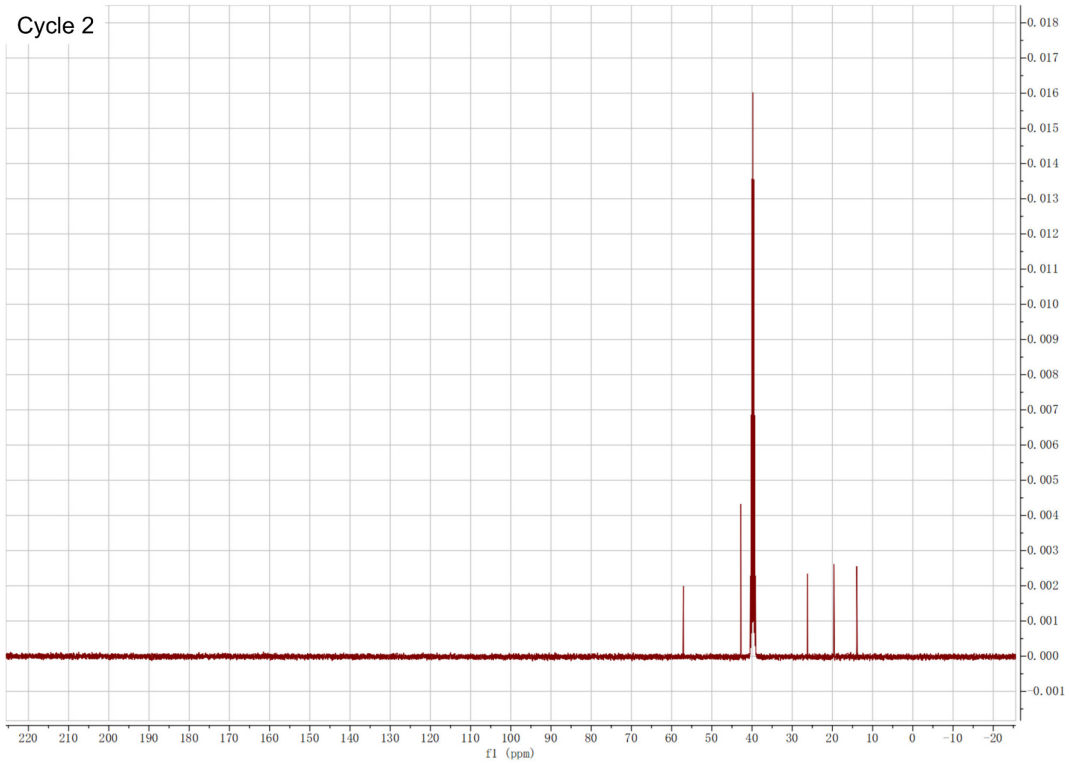


Figure S18. ^{13}C NMR of [DMBA][HSO_4] recovered after cycle 2.

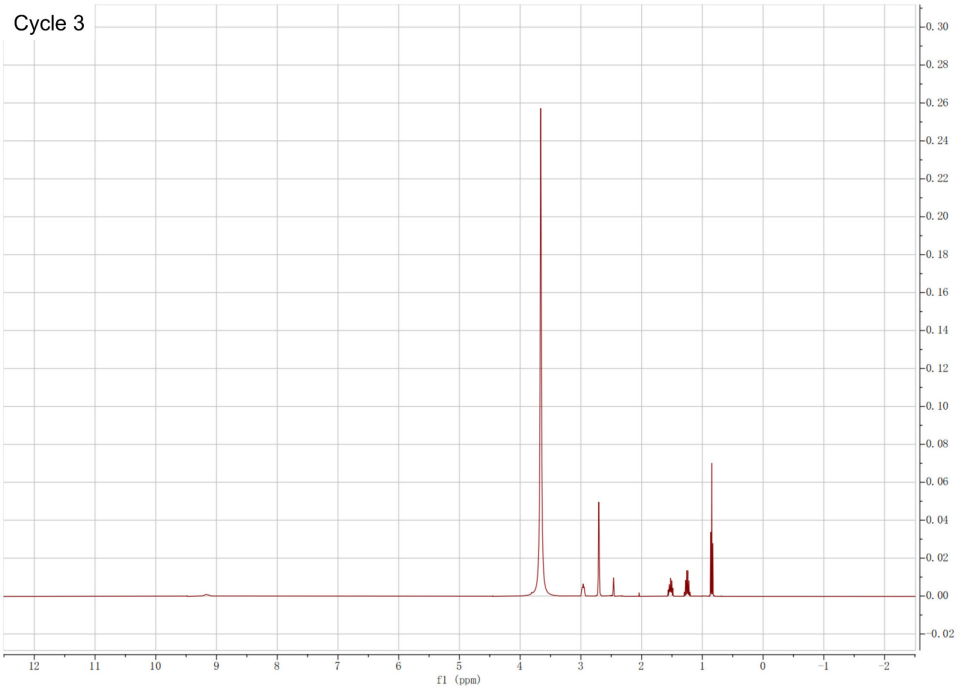


Figure S19. ^{1}H NMR of [DMBA][HSO_4] recovered after cycle 3.

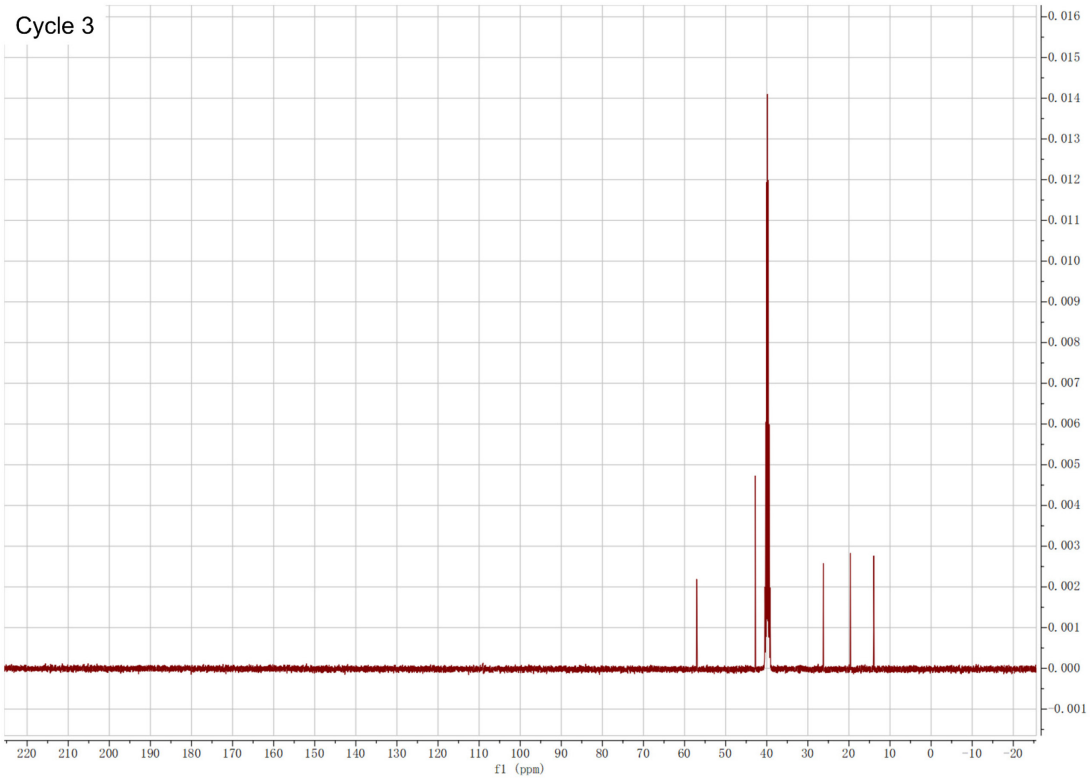


Figure S20. ^{13}C NMR of [DMBA][HSO_4] recovered after cycle 3.

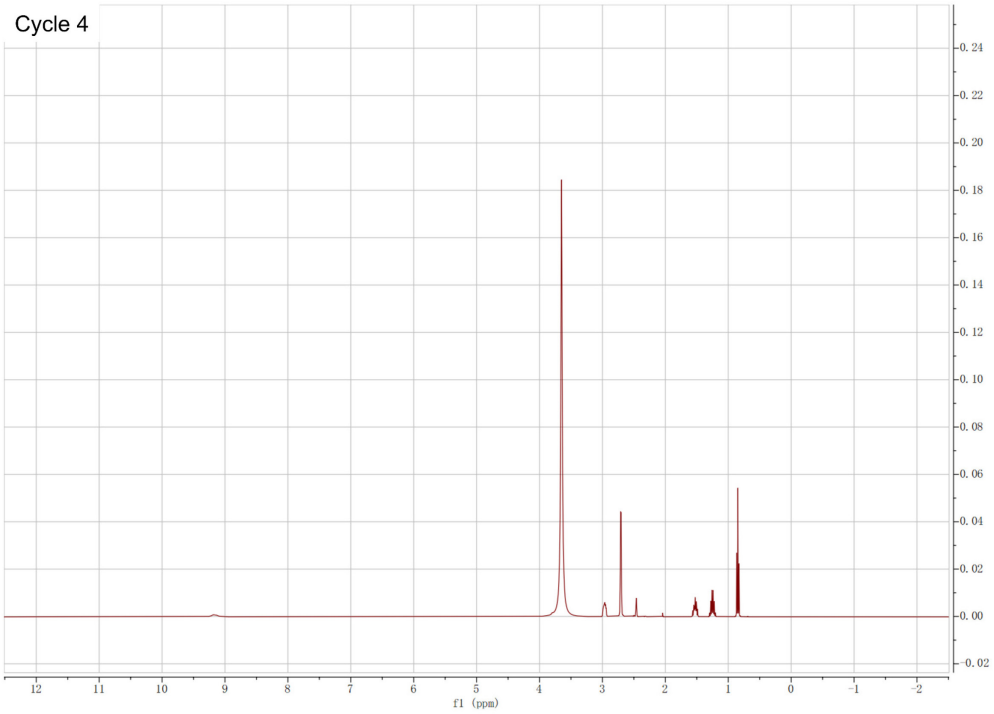


Figure S21. ^{1}H NMR of [DMBA][HSO_4] recovered after cycle 4.

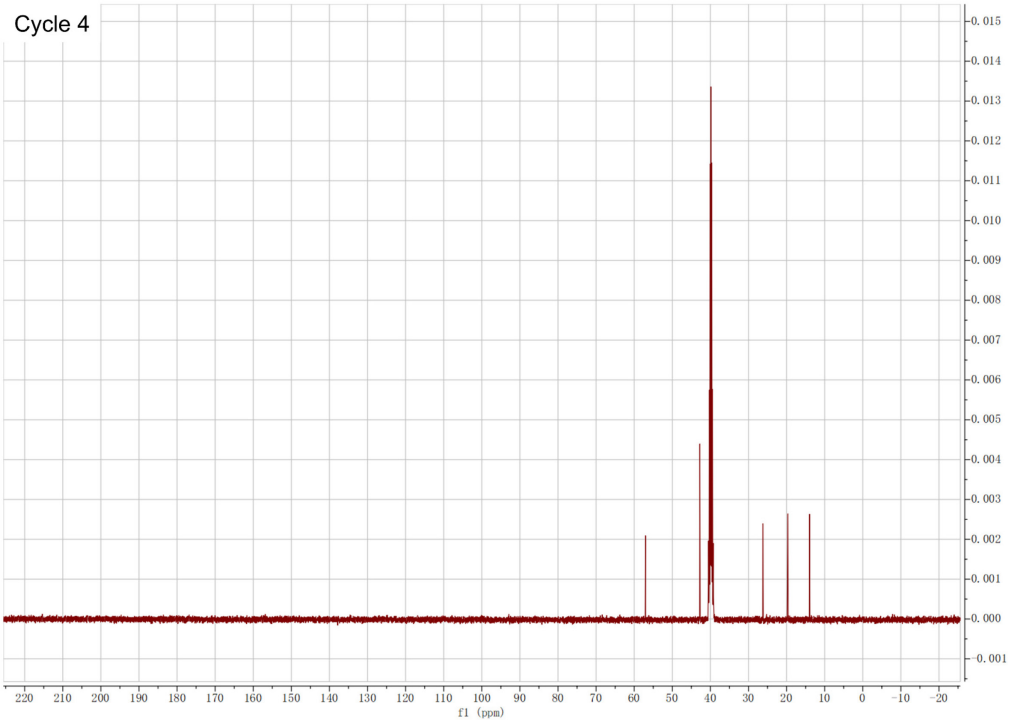


Figure S22. ^{13}C NMR of [DMBA][HSO_4] recovered after cycle 4.

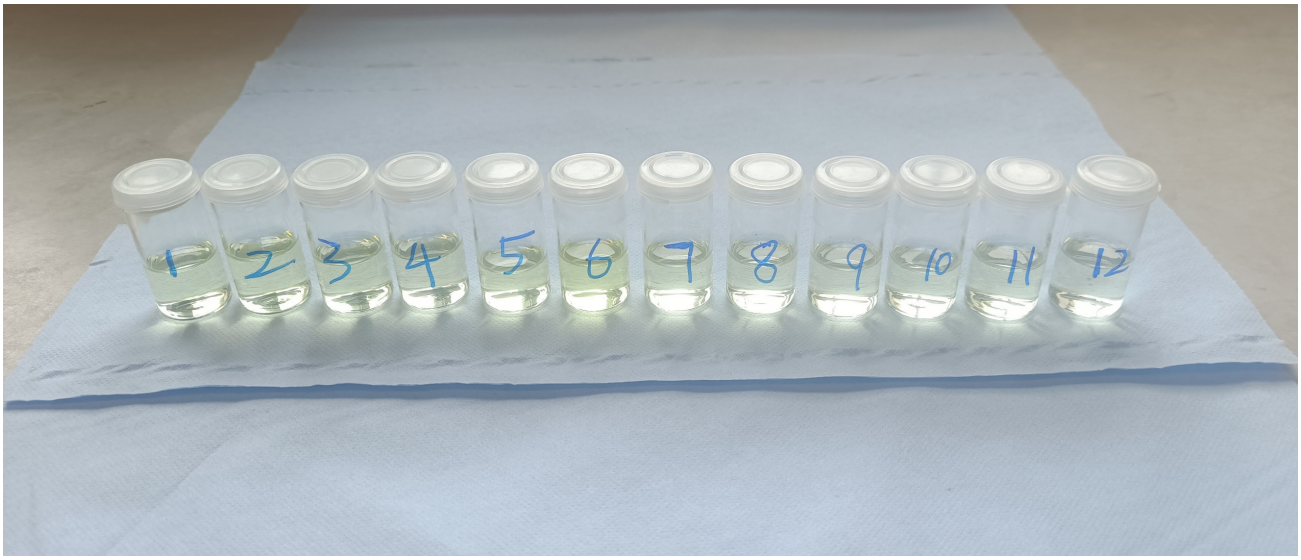


Figure S23. Furfural solutions collected at 10-min intervals from the semi-continuous furfural production system.

Table S2. List of the different utility prices employed for the economic estimation.

Utility	Price
Steam	0.1167 ($ kg^{-1})
Cooling water	0.0557 ($ m^{-3})
Electricity	0.3000 ($ kWh^{-1})

Table S3. List of parameters employed for the total capital cost estimation.

Parameter	Value
Direct field cost (DF)	Total installed costs calculated with Aspen
Direct field labor cost (DFLC)	0.25 × DF
Indirect field cost (IFC)	1.15 × DFLC
Total field cost (TFC)	DF + DFLC + IFC
Home office cost (HOC)	0.3 × DF
Other project cost (OPC)	0.03 × DF + 0.15 × (TFC + HOC)
Total project cost (TPC)	TFC + HOC + OPC

Table S4. List of parameters employed for the fixed cost estimation.

Parameter	Value
Maintenance (M)	0.1 × TFC
Laboratory	0.2 × LC [a]
Supervision	0.2 × (LC + M)
Plant overhead	0.5 × (LC + M)
Depreciation	0.1 × TFC
Insurance	0.01 × TFC
Local taxes	0.02 × TFC
Royalties	0.01 × TFC

[a] Labor cost (LC) was estimated based on 30 operators with an annual salary of $50,000 per operator.

Chapter 5:

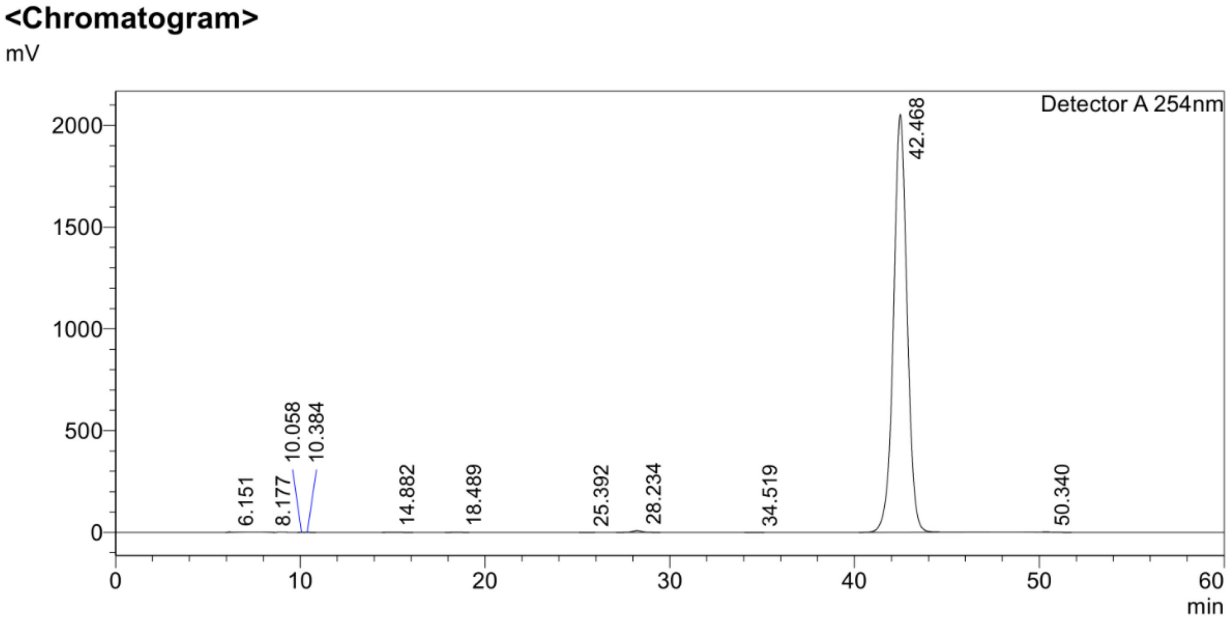


Figure S24. HPLC chromatogram (UV, λ = 254 nm) showing the furfural peak at *t* = 42.47 min. (Column: Aminex HPX-87H, 60 °C; mobile phase: 0.005 M H_2SO_4, 0.6 mL min^{-1} flow rate.)

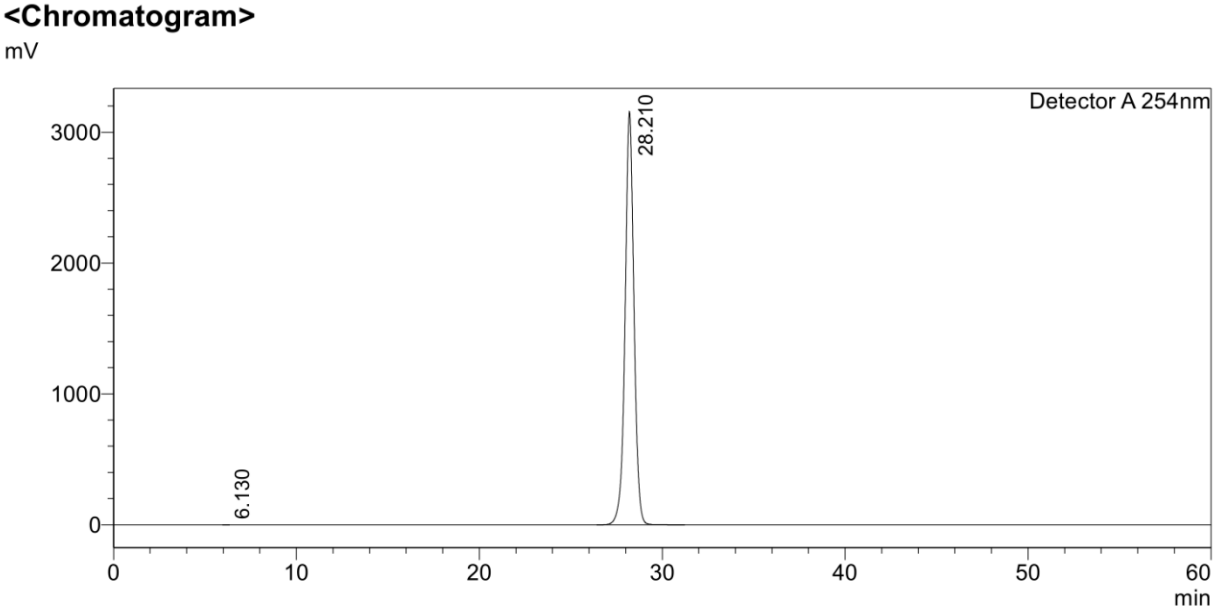


Figure S25. HPLC chromatogram (UV, λ = 254 nm) showing the furoic acid peak at *t* = 28.21 min. (Column: Aminex HPX-87H, 60 °C; mobile phase: 0.005 M H_2SO_4, 0.6 mL min^{-1} flow rate.)

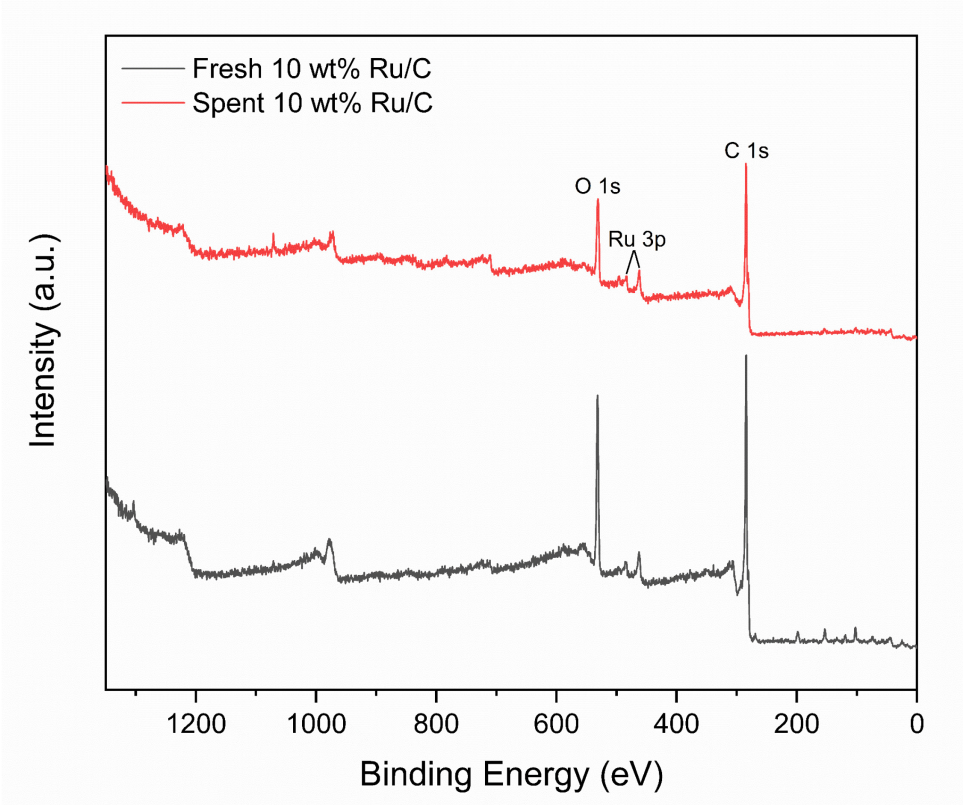


Figure S26. Full-range (survey) XPS spectra of fresh and spent 10 wt% Ru/C catalysts.

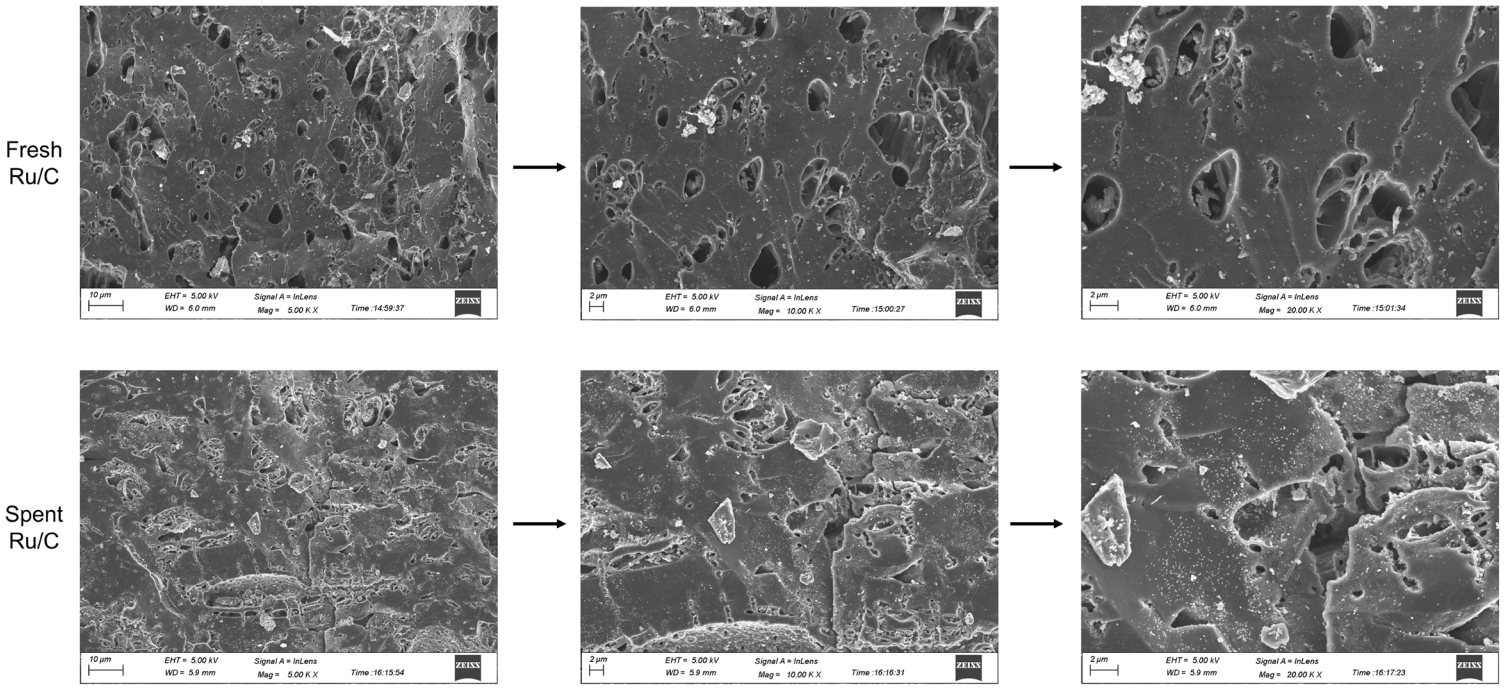


Figure S27. SEM micrographs of fresh and spent 10 wt% Ru/C at 5,000× to 20,000× magnification.

Permissions for the Reproduction of Copyright Materials:

Table S5. Summary of the copyright permissions.

Caption	Source of work	Copyright information	Permission request date
Figure 2.2	Greer AJ, Jacquemin J, Hardacre C. Industrial applications of ionic liquids. Molecules. 2020;25(21):5207. https://doi.org/10.3390/molecules25215207	Open Assess, Published by MDPI, Creative Commons Attribution (CC BY) 4.0 License	No additional permission is required
Figure 2.3	Baaqel H, Díaz I, Tulus V, Chachuat B, Guillén-Gosálbez G, Hallett JP. Role of life-cycle externalities in the valuation of protic ionic liquids–a case study in biomass pretreatment solvents. Green Chemistry. 2020;22(10):3132-40. https://doi.org/10.1039/D0GC00058B	Open Assess, Published by Royal Society of Chemistry, CC BY 3.0 Unported License	No additional permission is required
Figure 2.4	Dezashibi AH, Hallett JP, Fennell PS. Design and operation of a cost-effective reactor for large protic ionic liquid synthesis. Chemical Engineering and Processing-Process Intensification 2025;213:110312. https://doi.org/10.1016/j.cep.2025.110312	Open Assess, Published by Elsevier B.V, CC BY 4.0 License	No additional permission is required
Figure 2.6	Brethauer S, Shahab RL, Studer MH. Impacts of biofilms on the conversion of	Open Assess, Published by	No additional permission

	cellulose. Applied Microbiology and Biotechnology. 2020;104(12):5201-12. https://doi.org/10.1007/s00253-020-10595-y	Springer Nature, CC BY 4.0 License	is required
Figure 2.6	Rozmysłowicz B, Yeap JH, Elkhaiary AMI, Talebi Amiri M, Shahab RL, Questell-Santiago YM, et al. Catalytic valorization of the acetate fraction of biomass to aromatics and its integration into the carboxylate platform. Green Chemistry. 2019;21(10):2801-9. https://doi.org/10.1039/C9GC00513G	Copyright © 2019 The Royal Society of Chemistry	No additional permission is required for thesis
Figure 2.8	Lavoine N, Desloges I, Dufresne A, Bras J. Microfibrillated cellulose–Its barrier properties and applications in cellulosic materials: A review. Carbohydrate Polymers. 2012;90(2):735-64. https://doi.org/10.1016/j.carbpol.2012.05.026	Copyright © 2012 Elsevier Ltd. All rights reserved	22/09/2025
Figure 2.9	Ma C, Cai B, Zhang L, Feng J, Pan H. Acid-catalyzed conversion of cellulose into levulinic acid with biphasic solvent system. Frontiers in Plant Science. 2021;12:630807. https://doi.org/10.3389/fpls.2021.630807	Open Assess, Published by Frontiers, CC BY 4.0 License	No additional permission is required
Figure 2.10	Brandt-Talbot A, Gschwend FJV, Fennell PS, Lammens TM, Tan B, Weale J, et al. An economically viable ionic liquid for the fractionation of lignocellulosic biomass. Green Chemistry. 2017;19(13):3078-102. https://doi.org/10.1039/C7GC00705A	Open Assess, Published by Royal Society of Chemistry, CC BY 3.0 Unported License	No additional permission is required
Figure 2.11	Flores EM, Cravotto G, Bizzi CA, Santos D, Iop GD. Ultrasound-assisted biomass valorization to industrial interesting products: state-of-the-art, perspectives and challenges. Ultrasonics Sonochemistry. 2021;72:105455. https://doi.org/10.1016/j.ultsonch.2020.105455	Open Assess, Published by Elsevier B.V, CC BY-NonCommerial-NoDerivatives (NC-ND) 4.0 License	No additional permission is required
Figure 2.12	Enslow KR, Bell AT. The kinetics of Brønsted acid-catalyzed hydrolysis of hemicellulose dissolved in 1-ethyl-3-methylimidazolium chloride. RSC Advances. 2012;2(26):10028-36. https://doi.org/10.1039/C2RA21650G	Copyright © 2012 The Royal Society of Chemistry	No additional permission is required for thesis
Figure 2.13	Alonso DM, Wettstein SG, Mellmer MA, Gurbuz EI, Dumesic JA. Integrated conversion of hemicellulose and cellulose from lignocellulosic biomass. Energy & Environmental Science. 2013;6(1):76-80. https://doi.org/10.1039/C2EE23617F	Copyright © 2013 Royal Society of Chemistry	No additional permission is required for thesis
Figure 2.14	Xu S, Pan D, Wu Y, Song X, Gao L, Li W, et al. Efficient production of furfural from xylose and wheat straw by bifunctional chromium phosphate catalyst in	Copyright © 2018 Elsevier B.V. All rights reserved.	22/09/2025

	biphasic systems. Fuel Processing Technology. 2018;175:90-6. https://doi.org/10.1016/j.fuproc.2018.04.005		
Figure 2.15	Choudhary V, Sandler SI, Vlachos DG. Conversion of xylose to furfural using Lewis and Brønsted acid catalysts in aqueous media. ACS Catalysis. 2012;2(9):2022-8. https://doi.org/10.1021/cs300265d	Copyright © 2012, American Chemical Society	30/03/2026
Figure 2.15	Ye L, Han Y, Wang X, Lu X, Qi X, Yu H. Recent progress in furfural production from hemicellulose and its derivatives: Conversion mechanism, catalytic system, solvent selection. Molecular Catalysis. 2021;515:111899. https://doi.org/10.1016/j.mcat.2021.111899	Copyright © 2021 Elsevier B.V. All rights reserved.	30/03/2026
Figure 2.15	Wang Y, Li M, Wang Z, Liu S, O'Young L. Furfural production: A review on reaction mechanism and conventional production process. Industrial Crops and Products. 2025;230:121103. https://doi.org/10.1016/j.indcrop.2025.121103	Open Assess, Published by Elsevier B.V, CC BY-NC 4.0 License	No additional permission is required
Figure 2.16	Zhang Y, Cui H, Xia H. Recent Advances in the Synthesis of 2-Furoic Acid and 2, 5-Furandicarboxylic Acid from Furfural. ChemSusChem. 2025;18(3):e202401390. https://doi.org/10.1002/cssc.202401390	Copyright © 2024 Wiley-VCH GmbH	22/09/2025
Figure 2.17	Al Ghatta A, Aravenas RC, Wu Y, Perry JM, Lemus J, Hallett JP. New biobased sulfonated anionic surfactants based on the esterification of furoic acid and fatty alcohols: A green solution for the replacement of oil derivative surfactants with superior proprieties. ACS Sustainable Chemistry & Engineering. 2022;10(27):8846-55. https://doi.org/10.1021/acssuschemeng.2c01766	Open Assess, Published by American Chemical Society, CC BY 4.0 License	No additional permission is required
Figure 2.19	Yu X, Jin T, Wang H, Zhang G, Jia W, Peng L, et al. Heterogeneously-catalyzed aerobic oxidation of furfural to furancarboxylic acid with CuO-Promoted MnO2. Green Energy & Environment. 2023;8(6):1683-92. https://doi.org/10.1016/j.gee.2022.03.016	Open Assess, Published by Elsevier B.V, CC BY-NC-ND 4.0 License	No additional permission is required

References

1. Ang T-Z, Salem M, Kamarol M, Das HS, Nazari MA, Prabaharan N. A comprehensive study of renewable energy sources: Classifications, challenges and suggestions. Energy Strategy Reviews. 2022;43:100939.
2. Chen H, Wan K, Zheng F, Zhang Z, Zhang Y, Long D. Mechanism insight into photocatalytic conversion of lignin for valuable chemicals and fuels production: A state-of-the-art review. Renewable and Sustainable Energy Reviews. 2021;147:111217.
3. Sadekin S, Zaman S, Mahfuz M, Sarkar R. Nuclear power as foundation of a clean energy future: A review. Energy Procedia. 2019;160:513-8.
4. Gollakota ARK, Shu C-M. Chapter 4 - Comparisons between fossil fuels and bio-fuels. In: Shadangi KP, Sarangi PK, Mohanty K, Deniz I, Kiran Gollakota AR, editors. Bioenergy Engineering: Woodhead Publishing; 2023. p. 67-85.
5. Nagtode VS, Cardoza C, Yasin HKA, Mali SN, Tambe SM, Roy P, et al. Green surfactants (biosurfactants): a petroleum-free substitute for Sustainability— Comparison, applications, market, and future prospects. ACS Omega. 2023;8(13):11674-99.
6. Prasad W, Wani AD, Khamrui K, Hussain SA, Khetra Y. Green solvents, potential alternatives for petroleum based products in food processing industries. Cleaner Chemical Engineering. 2022;3:100052.
7. Stöcker M. Biofuels and biomass-to-liquid fuels in the biorefinery: catalytic conversion of lignocellulosic biomass using porous materials. Angewandte Chemie International Edition. 2008;47(48):9200-11.
8. Abbasi T, Abbasi SA. Biomass energy and the environmental impacts associated with its production and utilization. Renewable and Sustainable Energy Reviews. 2010;14(3):919-37.
9. Duku MH, Gu S, Hagan EB. A comprehensive review of biomass resources and biofuels potential in Ghana. Renewable and Sustainable Energy Reviews. 2011;15(1):404-15.
10. Ng DKS, Ng KS, Ng RTL. Integrated Biorefineries. In: Abraham MA, editor. Encyclopedia of Sustainable Technologies. Oxford: Elsevier; 2017. p. 299-314.
11. Brandt A, Gräsvik J, Hallett JP, Welton T. Deconstruction of lignocellulosic biomass with ionic liquids. Green Chemistry. 2013;15(3):550-83.
12. Louw J, Dogbe ES, Yang B, Görgens JF. Prioritisation of biomass-derived products for biorefineries based on economic feasibility: a review on the comparability of techno-economic assessment results. Renewable and Sustainable Energy Reviews. 2023;188:113840.
13. Hennecke AM, Faist M, Reinhardt J, Junquera V, Neeft J, Fehrenbach H. Biofuel greenhouse gas calculations under the European Renewable Energy Directive–A comparison of the BioGrace tool vs. the tool of the Roundtable on Sustainable Biofuels. Applied Energy. 2013;102:55-62.
14. Tan K, Lee K, Mohamed A, Bhatia S. Palm oil: Addressing issues and towards sustainable development. Renewable and Sustainable Energy Reviews. 2009;13(2):420-7.
15. Shahid MK, Batool A, Kashif A, Nawaz MH, Aslam M, Iqbal N, et al. Biofuels and biorefineries: Development, application and future perspectives emphasizing the environmental and economic aspects. Journal of Environmental Management. 2021;297:113268.
16. Chen M, Malaret F, Firth AEJ, Verdía P, Abouelela AR, Chen Y, et al. Design of a combined ionosolv-organosolv biomass fractionation process for biofuel production and high value-added

lignin valorisation. Green Chemistry. 2020;22(15):5161-78.
17. Giampietro M, Ulgiati S, Pimentel D. Feasibility of Large-Scale Biofuel Production: Does an enlargement of scale change the picture? BioScience. 1997;47(9):587-600.
18. Giampietro M, Ulgiati S. Integrated Assessment of Large-Scale Biofuel Production. Critical Reviews in Plant Sciences. 2005;24(5-6):365-84.
19. Brandt-Talbot A, Gschwend FJV, Fennell PS, Lammens TM, Tan B, Weale J, et al. An economically viable ionic liquid for the fractionation of lignocellulosic biomass. Green Chemistry. 2017;19(13):3078-102.
20. Shi J, Gladden JM, Sathitsuksanoh N, Kambam P, Sandoval L, Mitra D, et al. One-pot ionic liquid pretreatment and saccharification of switchgrass. Green Chemistry. 2013;15(9):2579-89.
21. Singhvi MS, Chaudhari S, Gokhale DV. Lignocellulose processing: a current challenge. RSC Advances. 2014;4(16):8271-7.
22. Espinoza-Acosta JL, Torres-Chávez PI, Carvajal-Millán E, Ramírez-Wong B, Bello-Pérez LA, Montaño-Leyva B. Ionic liquids and organic solvents for recovering lignin from lignocellulosic biomass. BioResources. 2014;9(2):3660-87.
23. Solomon BD. Biofuels and sustainability. Annals of the New York Academy of Sciences. 2010;1185(1):119-34.
24. Hennequin LM, Polizzi K, Fennell PS, Hallett JP. Rhododendron and Japanese Knotweed: invasive species as innovative crops for second generation biofuels for the ionoSolv process. RSC Advances. 2021;11(30):18395-403.
25. Liu C, Wang K, Zhao X, Chen Z, Yin X, Cai T, et al. Integrated lignocellulosic biorefinery for efficient production of furans and photothermal materials. Chemical Engineering Journal. 2023;453:139688.
26. Scapini T, Dos Santos MS, Bonatto C, Wancura JH, Mulinari J, Camargo AF, et al. Hydrothermal pretreatment of lignocellulosic biomass for hemicellulose recovery. Bioresource Technology. 2021;342:126033.
27. Zakzeski J, Bruijnincx PC, Jongerius AL, Weckhuysen BM. The catalytic valorization of lignin for the production of renewable chemicals. Chemical Reviews. 2010;110(6):3552-99.
28. Mosier N, Wyman C, Dale B, Elander R, Lee YY, Holtzapple M, et al. Features of promising technologies for pretreatment of lignocellulosic biomass. Bioresource Technology. 2005;96(6):673-86.
29. Lee H, Hamid SBA, Zain S. Conversion of lignocellulosic biomass to nanocellulose: structure and chemical process. The Scientific World Journal. 2014;2014(1):631013.
30. Mankar AR, Pandey A, Modak A, Pant K. Pretreatment of lignocellulosic biomass: A review on recent advances. Bioresource Technology. 2021;334:125235.
31. Jönsson LJ, Martín C. Pretreatment of lignocellulose: formation of inhibitory by-products and strategies for minimizing their effects. Bioresource Technology. 2016;199:103-12.
32. Sun S, Sun S, Cao X, Sun R. The role of pretreatment in improving the enzymatic hydrolysis of lignocellulosic materials. Bioresource Technology. 2016;199:49-58.
33. Brandt A, Hallett JP, Leak DJ, Murphy RJ, Welton T. The effect of the ionic liquid anion in the pretreatment of pine wood chips. Green Chemistry. 2010;12(4):672-9.
34. Tu W-C, Hallett JP. Recent advances in the pretreatment of lignocellulosic biomass. Current Opinion in Green and Sustainable Chemistry. 2019;20:11-7.
35. Kumar P, Barrett DM, Delwiche MJ, Stroeve P. Methods for pretreatment of lignocellulosic

biomass for efficient hydrolysis and biofuel production. Industrial & Engineering Chemistry Research. 2009;48(8):3713-29.
36. Gschwend FJ, Chambon CL, Biedka M, Brandt-Talbot A, Fennell PS, Hallett JP. Quantitative glucose release from softwood after pretreatment with low-cost ionic liquids. Green chemistry. 2019;21(3):692-703.
37. Gschwend FJV, Malaret F, Shinde S, Brandt-Talbot A, Hallett JP. Rapid pretreatment of Miscanthus using the low-cost ionic liquid triethylammonium hydrogen sulfate at elevated temperatures. Green Chemistry. 2018;20(15):3486-98.
38. Rafat AA, Verdía Barbará P, Ullah A, Kontturi E, Law RV, Hallett JP. Efficient extraction of carboxylated nanocellulose from ionoSolv pulps with alkaline H2O2 assisted oxidation. Cellulose. 2025;32(2):853-75.
39. Papajewski MP, Nisar S, Zhang C, Hallett JP, Albert J. Boosting furfural production by combining polyoxometalates and ionic liquids for effective fractionation of lignocellulosic biomass. RSC Advances. 2025;15(18):14259-63.
40. Yang SM, Shaffer MS, Brandt-Talbot A. High lignin content carbon fiber precursors wet-spun from low-cost ionic liquid water mixtures. ACS Sustainable Chemistry & Engineering. 2023;11(24):8800-11.
41. Boli E, Katsavrias T, Voutsas E. Viscosities of pure protic ionic liquids and their binary and ternary mixtures with water and ethanol. Fluid Phase Equilibria. 2020;520:112663.
42. Chambon CL, Verdía P, Fennell PS, Hallett JP. Process intensification of the ionoSolv pretreatment: effects of biomass loading, particle size and scale-up from 10 mL to 1 L. Scientific Reports. 2021;11(1):15383.
43. Gogate PR, Pandit AB. Application of cavitational reactors for cell disruption for recovery of intracellular enzymes. Journal of Chemical Technology & Biotechnology: International Research in Process, Environmental & Clean Technology. 2008;83(8):1083-93.
44. Suslick KS. The chemical effects of ultrasound. Scientific American. 1989;260(2):80-7.
45. Chisti Y, Moo-Young M. Disruption of microbial cells for intracellular products. Enzyme and Microbial Technology. 1986;8(4):194-204.
46. Flores EM, Cravotto G, Bizzi CA, Santos D, Iop GD. Ultrasound-assisted biomass valorization to industrial interesting products: state-of-the-art, perspectives and challenges. Ultrasonics Sonochemistry. 2021;72:105455.
47. Layman CN, Sou IM, Bartak R, Ray C, Allen JS. Characterization of acoustic streaming and heating using synchronized infrared thermography and particle image velocimetry. Ultrasonics Sonochemistry. 2011;18(5):1258-61.
48. Prempeh NYA, Nunekpeku X, Murugesan A, Li H. Ultrasound in the Food Industry: Mechanisms and Applications for Non-Invasive Texture and Quality Analysis. Foods. 2025;14(12):2057.
49. Artime IF, Al Ghatta A, Ouitrakoon P, Damilano G, Brandt-Talbot A, Hallett JP, et al. Surfactant-assisted ionic liquid fractionation of spruce produces a low molar weight and less condensed lignin. Industrial Crops and Products. 2025;235:121815.
50. Patel A, Shah AR. Integrated lignocellulosic biorefinery: Gateway for production of second generation ethanol and value added products. Journal of Bioresources and Bioproducts. 2021;6(2):108-28.
51. Cai CM, Zhang T, Kumar R, Wyman CE. Integrated furfural production as a renewable fuel

and chemical platform from lignocellulosic biomass. Journal of Chemical Technology & Biotechnology. 2014;89(1):2-10.
52. Dalvand K, Rubin J, Gunukula S, Clayton Wheeler M, Hunt G. Economics of biofuels: Market potential of furfural and its derivatives. Biomass and Bioenergy. 2018;115:56-63.
53. Al Ghatta A, Hallett JP. Bioderived furanic compounds as replacements for BTX in chemical intermediate applications. RSC Sustainability. 2023;1(4):698-745.
54. Lange J-P. Furfural manufacture and valorization–A selection of recent developments. Catalysis Today. 2024;435:114726.
55. Zhou Q, Ding A, Zhang L, Wang J, Gu J, Wu TY, et al. Furfural production from the lignocellulosic agro-forestry waste by solvolysis method–a technical review. Fuel Processing Technology. 2024;255:108063.
56. Zhou S, Zhang X, Zhan L, Song X, Li R, Wu Y. Future development for furfural production: Comparison of one-step and two-step strategies and life cycle assessment. Industrial Crops and Products. 2025;227:120807.
57. Yao B, Kang Q, Fu J, Liu Y, Ao W, Wang L, et al. Catalytic hydrolysis of corncob for production of furfural and cellulose-rich solids: Product characterization and analysis. Biomass and Bioenergy. 2023;168:106658.
58. Wang Q, Qi W, Wang W, Zhang Y, Leksawasdi N, Zhuang X, et al. Production of furfural with high yields from corncob under extremely low water/solid ratios. Renewable Energy. 2019;144:139-46.
59. Tian H, Quan Y, Yin Z, Yin C, Fu Y. Bioelectrochemical Purification of Biomass Polymer Derived Furfural Wastewater and Its Electric Energy Recovery. Polymers. 2023;15(16):3422.
60. Mariscal R, Maireles-Torres P, Ojeda M, Sádaba I, Granados ML. Furfural: a renewable and versatile platform molecule for the synthesis of chemicals and fuels. Energy & Environmental Science. 2016;9(4):1144-89.
61. Zeitsch KJ. The chemistry and technology of furfural and its many by-products: Elsevier; 2000.
62. Bao Y, Du Z, Liu X, Liu H, Tang J, Qin C, et al. Furfural production from lignocellulosic biomass: one-step and two-step strategies and techno-economic evaluation. Green Chemistry. 2024;26(11):6318-38.
63. Han X, Wang Y, Liu G, Wang M, Guo C, Shen J. A sustainable and low-cost route to 2, 5-furandicarboxylic acid by carboxylation of biomass-based furoic acid and CO2. Journal of CO2 Utilization. 2023;75:102572.
64. Rapado P, Faba L, Ordóñez S. Selective and stable production of furoic acid by furfural aerobic oxidation at controlled mild-pH conditions. Applied Catalysis A: General. 2024;670:119536.
65. Nocito F, Ditaranto N, Linsalata D, Naschetti M, Comparelli R, Aresta M, et al. Selective aerobic oxidation of furfural into furoic Acid over a highly recyclable MnO2@ CeO2 core–shell oxide: The role of the morphology of the catalyst. ACS Sustainable Chemistry & Engineering. 2022;10(26):8615-23.
66. Kim T, Bamford J, Gracida-Alvarez UR, Benavides PT. Life cycle greenhouse gas emissions and water and fossil-fuel consumptions for polyethylene furanoate and its coproducts from wheat straw. ACS Sustainable Chemistry & Engineering. 2022;10(8):2830-43.
67. Wu X, Guo H, Jia L, Xiao Y, Hou B, Gao Y, et al. Enhancement of Ru on furoic acid synthesis from furfural oxidation over Rux/δ-MnO2 catalysts. Molecular Catalysis. 2023;551:113604.

68. Al Ghatta A, Aravenas RC, Wu Y, Perry JM, Lemus J, Hallett JP. New biobased sulfonated anionic surfactants based on the esterification of furoic acid and fatty alcohols: A green solution for the replacement of oil derivative surfactants with superior proprieties. ACS Sustainable Chemistry & Engineering. 2022;10(27):8846-55.
69. Ferraz CP, Zieliński M, Pietrowski M, Heyte S, Dumeignil F, Rossi LM, et al. Influence of support basic sites in green oxidation of biobased substrates using Au-promoted catalysts. ACS Sustainable Chemistry & Engineering. 2018;6(12):16332-40.
70. Tian Q, Shi T, Sha Y. CuO and Ag2O/CuO catalyzed oxidation of aldehydes to the corresponding carboxylic acids by molecular oxygen. Molecules. 2008;13(4):948-57.
71. Sadier A, Paul S, Wojcieszak R. Selective Oxidation of Furfural at Room Temperature on a TiO2-Supported Ag Catalyst. Catalysts. 2022;12(8):805.
72. Papanikolaou G, Lanzafame P, Perathoner S, Centi G, Cozza D, Giorgianni G, et al. High performance of Au/ZTC based catalysts for the selective oxidation of bio-derivative furfural to 2-furoic acid. Catalysis Communications. 2021;149:106234.
73. Zhao W, Song S, Ding M, Luo W, Li L, Li X. Bypassing In Situ CO Poisoning in Furfural Conversion: Electron-Deficient Pd Single-Atom Alloys Enable One-Step Selective Synthesis of Tetrahydrofuran. Angewandte Chemie. 2025;137(32):e202507984.
74. Al Ghatta A, Perry JM, Maeng H, Lemus J, Hallett JP. Sustainable and efficient production of furoic acid from furfural through amine assisted oxidation with hydrogen peroxide and its implementation for the synthesis of alkyl furoate. RSC Sustainability. 2023;1(2):303-9.
75. Wasserscheid P, Welton T. Ionic Liquids in Synthesis: Wiley Online Library; 2008.
76. Brandt A, Ray MJ, To TQ, Leak DJ, Murphy RJ, Welton T. Ionic liquid pretreatment of lignocellulosic biomass with ionic liquid–water mixtures. Green Chemistry. 2011;13(9):2489-99.
77. Lei Z, Chen B, Koo Y-M, MacFarlane DR. Introduction: Ionic Liquids. ACS Publications; 2017. p. 6633-5.
78. Hurley FH, Wier TP. Electrodeposition of metals from fused quaternary ammonium salts. Journal of The Electrochemical Society. 1951;98(5):203.
79. Greer AJ, Jacquemin J, Hardacre C. Industrial applications of ionic liquids. Molecules. 2020;25(21):5207.
80. Wilkes JS, Levisky JA, Wilson RA, Hussey CL. Dialkylimidazolium chloroaluminate melts: a new class of room-temperature ionic liquids for electrochemistry, spectroscopy and synthesis. Inorganic Chemistry. 1982;21(3):1263-4.
81. Wilkes JS, Zaworotko MJ. Air and water stable 1-ethyl-3-methylimidazolium based ionic liquids. Journal of the Chemical Society, Chemical Communications. 1992(13):965-7.
82. Welton T. Ionic liquids: a brief history. Biophysical Reviews. 2018;10(3):691-706.
83. Rogers RD, Seddon KR. Ionic liquids--solvents of the future? Science. 2003;302(5646):792-3.
84. Joseph T, Sahoo S, Halligudi S. Brönsted acidic ionic liquids: A green, efficient and reusable catalyst system and reaction medium for Fischer esterification. Journal of Molecular Catalysis A: Chemical. 2005;234(1-2):107-10.
85. Wilkes JS. Properties of ionic liquid solvents for catalysis. Journal of Molecular Catalysis A: Chemical. 2004;214(1):11-7.
86. Plechkova NV, Seddon KR. Applications of ionic liquids in the chemical industry. Chemical Society Reviews. 2008;37(1):123-50.

87. Armand M, Endres F, MacFarlane DR, Ohno H, Scrosati B. Ionic-liquid materials for the electrochemical challenges of the future. Nature Materials. 2009;8(8):621-9.
88. Hasib-ur-Rahman M, Siaj M, Larachi F. Ionic liquids for CO2 capture—Development and progress. Chemical Engineering and Processing: Process Intensification. 2010;49(4):313-22.
89. Bates ED, Mayton RD, Ntai I, Davis JH. CO2 capture by a task-specific ionic liquid. Journal of the American Chemical Society. 2002;124(6):926-7.
90. Yao JG, Tan S-y, Metcalfe PI, Fennell PS, Kelsall GH, Hallett JP. Demetallization of Sewage Sludge Using Low-Cost Ionic Liquids. Environmental Science & Technology. 2021;55(8):5291-300.
91. Gschwend FJ, Hennequin LM, Brandt-Talbot A, Bedoya-Lora F, Kelsall GH, Polizzi K, et al. Towards an environmentally and economically sustainable biorefinery: heavy metal contaminated waste wood as a low-cost feedstock in a low-cost ionic liquid process. Green Chemistry. 2020;22(15):5032-41.
92. Earle MJ, Esperança JM, Gilea MA, Canongia Lopes JN, Rebelo LP, Magee JW, et al. The distillation and volatility of ionic liquids. Nature. 2006;439(7078):831-4.
93. Cao Y, Mu T. Comprehensive investigation on the thermal stability of 66 ionic liquids by thermogravimetric analysis. Industrial & Engineering Chemistry Research. 2014;53(20):8651-64.
94. Welton T. Room-temperature ionic liquids. Solvents for synthesis and catalysis. Chemical Reviews. 1999;99(8):2071-84.
95. Zhang S, Sun N, He X, Lu X, Zhang X. Physical properties of ionic liquids: database and evaluation. Journal of Physical and Chemical Reference Data. 2006;35(4):1475-517.
96. Ab Rani MA, Brant A, Crowhurst L, Dolan A, Lui M, Hassan NH, et al. Understanding the polarity of ionic liquids. Physical Chemistry Chemical Physics. 2011;13(37):16831-40.
97. Crowhurst L, Mawdsley PR, Perez-Arlandis JM, Salter PA, Welton T. Solvent–solute interactions in ionic liquids. Physical Chemistry Chemical Physics. 2003;5(13):2790-4.
98. Kamlet MJ, Taft R. The solvatochromic comparison method. I. The. beta.-scale of solvent hydrogen-bond acceptor (HBA) basicities. Journal of the American Chemical Society. 1976;98(2):377-83.
99. Reichardt C. Polarity of ionic liquids determined empirically by means of solvatochromic pyridinium N-phenolate betaine dyes. Green Chemistry. 2005;7(5):339-51.
100. Kamlet MJ, Abboud JLM, Abraham MH, Taft R. Linear solvation energy relationships. 23. A comprehensive collection of the solvatochromic parameters,. pi.*,. alpha., and. beta., and some methods for simplifying the generalized solvatochromic equation. The Journal of Organic Chemistry. 1983;48(17):2877-87.
101. Hayyan M, Mjalli FS, Hashim MA, AlNashef IM, Mei TX. Investigating the electrochemical windows of ionic liquids. Journal of Industrial and Engineering Chemistry. 2013;19(1):106-12.
102. Anouti M, Caillon-Caravanier M, Le Floch C, Lemordant D. Alkylammonium-based protic ionic liquids part I: preparation and physicochemical characterization. The Journal of Physical Chemistry B. 2008;112(31):9406-11.
103. El Abedin SZ, Pölleth M, Meiss S, Janek J, Endres F. Ionic liquids as green electrolytes for the electrodeposition of nanomaterials. Green Chemistry. 2007;9(6):549-53.
104. Vaughan J, Tu J, Dreisinger D. Ionic liquid electrodeposition of reactive metals. Mineral Processing and Extractive Metallurgy. 2008;117(2):113-7.
105. Belieres J-P, Angell CA. Protic ionic liquids: preparation, characterization, and proton free energy level representation. The Journal of Physical Chemistry B. 2007;111(18):4926-37.

106. Comminges C, Barhdadi R, Laurent M, Troupel M. Determination of viscosity, ionic conductivity, and diffusion coefficients in some binary systems: ionic liquids+ molecular solvents. Journal of Chemical & Engineering Data. 2006;51(2):680-5.
107. Abouelela AR, Nakasu PY, Hallett JP. Influence of pretreatment severity factor and Hammett acidity on softwood fractionation by an acidic protic ionic liquid. ACS Sustainable Chemistry & Engineering. 2023;11(6):2404-15.
108. Thomazeau C, Olivier-Bourbigou H, Magna L, Luts S, Gilbert B. Determination of an Acidic Scale in Room Temperature Ionic Liquids. Journal of the American Chemical Society. 2003;125(18):5264-5.
109. Hammett LP, Deyrup AJ. A series of simple basic indicators. I. The acidity functions of mixtures of sulfuric and perchloric acids with water1. Journal of the American Chemical Society. 1932;54(7):2721-39.
110. Yoo B, Jing B, Jones SE, Lamberti GA, Zhu Y, Shah JK, et al. Molecular mechanisms of ionic liquid cytotoxicity probed by an integrated experimental and computational approach. Scientific Reports. 2016;6(1):19889.
111. Stasiewicz M, Mulkiewicz E, Tomczak-Wandzel R, Kumirska J, Siedlecka EM, Gołębiowski M, et al. Assessing toxicity and biodegradation of novel, environmentally benign ionic liquids (1-alkoxymethyl-3-hydroxypyridinium chloride, saccharinate and acesulfamates) on cellular and molecular level. Ecotoxicology and Environmental Safety. 2008;71(1):157-65.
112. Ventura SP, Marques CS, Rosatella AA, Afonso CA, Goncalves F, Coutinho JA. Toxicity assessment of various ionic liquid families towards Vibrio fischeri marine bacteria. Ecotoxicology and Environmental Safety. 2012;76:162-8.
113. Peric B, Sierra J, Martí E, Cruañas R, Garau MA, Arning J, et al. (Eco) toxicity and biodegradability of selected protic and aprotic ionic liquids. Journal of Hazardous Materials. 2013;261:99-105.
114. Egorova KS, Ananikov VP. Toxicity of ionic liquids: eco (cyto) activity as complicated, but unavoidable parameter for task-specific optimization. ChemSusChem. 2014;7(2):336-60.
115. Swatloski RP, Holbrey JD, Rogers RD. Ionic liquids are not always green: hydrolysis of 1-butyl-3-methylimidazolium hexafluorophosphate. Green Chemistry. 2003;5(4):361-3.
116. Hulsbosch J, De Vos DE, Binnemans K, Ameloot R. Biobased ionic liquids: solvents for a green processing industry? ACS Sustainable Chemistry & Engineering. 2016;4(6):2917-31.
117. Trivedi TJ, Rao KS, Singh T, Mandal SK, Sutradhar N, Panda AB, et al. Task-specific, biodegradable amino acid ionic liquid surfactants. ChemSusChem. 2011;4(5):604-8.
118. Stock F, Hoffmann J, Ranke J, Störmann R, Ondruschka B, Jastorff B. Effects of ionic liquids on the acetylcholinesterase–a structure–activity relationship consideration. Green Chemistry. 2004;6(6):286-90.
119. Samorì C, Malferrari D, Valbonesi P, Montecavalli A, Moretti F, Galletti P, et al. Introduction of oxygenated side chain into imidazolium ionic liquids: evaluation of the effects at different biological organization levels. Ecotoxicology and Environmental Safety. 2010;73(6):1456-64.
120. Morton MD, Hamer CK. Ionic liquids–The beginning of the end or the end of the beginning?–A look at the life of ionic liquids through patent claims. Separation and Purification Technology. 2018;196:3-9.
121. Holbrey J, Plechkova N, Seddon K. Recalling coil. Green Chemistry. 2006;8(5):411-4.
122. Phillips GW, Falling SN, Godleski SA, Monnier JR. Continuous process for the manufacture

of 2, 5-dihydrofurans from γ, δ-epoxybutenes. Google Patents; 1994.
123. García-Verdugo E, Altava B, Burguete MI, Lozano P, Luis SV. Ionic liquids and continuous flow processes: a good marriage to design sustainable processes. Green Chemistry. 2015;17(5):2693-713.
124. Seddon KR. A taste of the future. Nature Materials. 2003;2(6):363-5.
125. Freemantle M. BASF's smart ionic liquid. Chemical & Engineering News. 2003;81(13):9-.
126. Maase M, Massonne K, Halbritter K, Noe R, Bartsch M, Siegel W, et al. Method for the separation of acids from chemical reaction mixtures by means of ionic fluids. Google Patents; 2008.
127. Green solutions from green waste: Lixea Ltd; [updated 2026/02/21]. Available from: https://www.lixea.co/.
128. We give dyes and fibers a second chance: DyeRecycle Ltd; [updated 2026/02/21]. Available from: https://www.dyerecycle.com/.
129. Hallett JP. Green chemistry startups: some lessons learned. Green Chemistry. 2025;27(2):403-12.
130. Deetlefs M, Seddon KR. Assessing the greenness of some typical laboratory ionic liquid preparations. Green Chemistry. 2010;12(1):17-30.
131. Price listing for [Emim][OAc] and [Emim][OTf] (10 kg scale): Proionic GmbH; [updated 2026/02/21]. Available from: https://www.proionic.com/il-catalog/.
132. Greaves TL, Drummond CJ. Protic ionic liquids: evolving structure–property relationships and expanding applications. Chemical Reviews. 2015;115(20):11379-448.
133. Snook GA, Greaves TL, Best AS. A comparative study of the electrodeposition of polyaniline from a protic ionic liquid, an aprotic ionic liquid and neutral aqueous solution using anilinium nitrate. Journal of Materials Chemistry. 2011;21(21):7622-9.
134. George A, Brandt A, Tran K, Zahari SMNS, Klein-Marcuschamer D, Sun N, et al. Design of low-cost ionic liquids for lignocellulosic biomass pretreatment. Green Chemistry. 2015;17(3):1728-34.
135. Reis CLB, e Silva LMA, Rodrigues THS, Félix AKN, de Santiago-Aguiar RS, Canuto KM, et al. Pretreatment of cashew apple bagasse using protic ionic liquids: enhanced enzymatic hydrolysis. Bioresource Technology. 2017;224:694-701.
136. Achinivu EC, Howard RM, Li G, Gracz H, Henderson WA. Lignin extraction from biomass with protic ionic liquids. Green Chemistry. 2014;16(3):1114-9.
137. Verdía P, Brandt A, Hallett JP, Ray MJ, Welton T. Fractionation of lignocellulosic biomass with the ionic liquid 1-butylimidazolium hydrogen sulfate. Green Chemistry. 2014;16(3):1617-27.
138. Greaves TL, Drummond CJ. Protic ionic liquids: properties and applications. Chemical Reviews. 2008;108(1):206-37.
139. Yoshizawa M, Xu W, Angell CA. Ionic liquids by proton transfer: Vapor pressure, conductivity, and the relevance of Δp K a from aqueous solutions. Journal of the American Chemical Society. 2003;125(50):15411-9.
140. Stoimenovski J, Izgorodina EI, MacFarlane DR. Ionicity and proton transfer in protic ionic liquids. Physical Chemistry Chemical Physics. 2010;12(35):10341-7.
141. Zhao C, Burrell G, Torriero AA, Separovic F, Dunlop NF, MacFarlane DR, et al. Electrochemistry of room temperature protic ionic liquids. The Journal of Physical Chemistry B. 2008;112(23):6923-36.
142. MacFarlane DR, Seddon KR. Ionic liquids—progress on the fundamental issues. Australian

Journal of Chemistry. 2007;60(1):3-5.
143. Chiappe C, Mezzetta A, Pomelli CS, Iaquaniello G, Gentile A, Masciocchi B. Development of cost-effective biodiesel from microalgae using protic ionic liquids. Green Chemistry. 2016;18(18):4982-9.
144. Chen L, Sharifzadeh M, Mac Dowell N, Welton T, Shah N, Hallett JP. Inexpensive ionic liquids:[HSO 4]−-based solvent production at bulk scale. Green Chemistry. 2014;16(6):3098-106.
145. Baaqel H, Díaz I, Tulus V, Chachuat B, Guillén-Gosálbez G, Hallett JP. Role of life-cycle externalities in the valuation of protic ionic liquids–a case study in biomass pretreatment solvents. Green Chemistry. 2020;22(10):3132-40.
146. Dezashibi AH, Hallett JP, Fennell PS. Design and operation of a cost-effective reactor for large protic ionic liquid synthesis. Chemical Engineering and Processing-Process Intensification. 2025;213:110312.
147. Anvari S, Szlęk A, Arteconi A, Desideri U, Rosen MA. Comparative study of steam injection modes for a proposed biomass-driven cogeneration cycle: Performance improvement and CO2 emission reduction. Applied Energy. 2023;329:120255.
148. Naik SN, Goud VV, Rout PK, Dalai AK. Production of first and second generation biofuels: A comprehensive review. Renewable and Sustainable Energy Reviews. 2010;14(2):578-97.
149. Stark A. Ionic liquids in the biorefinery: a critical assessment of their potential. Energy & Environmental Science. 2011;4(1):19-32.
150. Creutzig F, Ravindranath NH, Berndes G, Bolwig S, Bright R, Cherubini F, et al. Bioenergy and climate change mitigation: an assessment. GCB Bioenergy. 2015;7(5):916-44.
151. Müller C, Scapini T, Rempel A, Abaide ER, Camargo AF, Nazari MT, et al. Challenges and opportunities for third-generation ethanol production: A critical review. Engineering Microbiology. 2023;3(1):100056.
152. Abouelela AR, Tan S-y, Kelsall GH, Hallett JP. Toward a circular economy: decontamination and valorization of postconsumer waste wood using the ionoSolv process. ACS Sustainable Chemistry & Engineering. 2020;8(38):14441-61.
153. Chambon CL, Mkhize TY, Reddy P, Brandt-Talbot A, Deenadayalu N, Fennell PS, et al. Pretreatment of South African sugarcane bagasse using a low-cost protic ionic liquid: a comparison of whole, depithed, fibrous and pith bagasse fractions. Biotechnology for Biofuels. 2018;11(1):247.
154. Songstad D, Lakshmanan P, Chen J, Gibbons W, Hughes S, Nelson R. Historical perspective of biofuels: learning from the past to rediscover the future. In Vitro Cellular & Developmental Biology-Plant. 2009;45(3):189-92.
155. Zabed H, Sahu J, Suely A, Boyce A, Faruq G. Bioethanol production from renewable sources: Current perspectives and technological progress. Renewable and Sustainable Energy Reviews. 2017;71:475-501.
156. Ubando AT, Ng EAS, Chen W-H, Culaba AB, Kwon EE. Life cycle assessment of microalgal biorefinery: A state-of-the-art review. Bioresource Technology. 2022;360:127615.
157. Choudhary P, Khade M, Savant S, Musale A, Chelliah MS, Dasgupta S. Empowering blue economy: From underrated ecosystem to sustainable industry. Journal of Environmental Management. 2021;291:112697.
158. Fernand F, Israel A, Skjermo J, Wichard T, Timmermans KR, Golberg A. Offshore macroalgae biomass for bioenergy production: Environmental aspects, technological

achievements and challenges. Renewable and Sustainable Energy Reviews. 2017;75:35-45.
159. Mata TM, Martins AA, Caetano NS. Microalgae for biodiesel production and other applications: a review. Renewable and Sustainable Energy Reviews. 2010;14(1):217-32.
160. Chowdhury H, Loganathan B. Third-generation biofuels from microalgae: a review. Current Opinion in Green and Sustainable Chemistry. 2019;20:39-44.
161. Chisti Y. Biodiesel from microalgae. Biotechnology Advances. 2007;25(3):294-306.
162. Wang B, Li Y, Wu N, Lan CQ. CO2 bio-mitigation using microalgae. Applied Microbiology and Biotechnology. 2008;79(5):707-18.
163. Li Y, Horsman M, Wang B, Wu N, Lan CQ. Effects of nitrogen sources on cell growth and lipid accumulation of green alga Neochloris oleoabundans. Applied Microbiology and Biotechnology. 2008;81(4):629-36.
164. Li Y, Horsman M, Wu N, Lan CQ, Dubois - Calero N. Biofuels from microalgae. Biotechnology Progress. 2008;24(4):815-20.
165. Dimopoulou M, Kolonas A, Stagos D, Gortzi O. A Review of the Sustainability, Chemical Composition, Bioactive Compounds, Antioxidant and Antidiabetic Activity, Neuroprotective Properties, and Health Benefits of Microalgae. Biomass. 2025;5(1):11.
166. Rosenberg JN, Oyler GA, Wilkinson L, Betenbaugh MJ. A green light for engineered algae: redirecting metabolism to fuel a biotechnology revolution. Current Opinion in Biotechnology. 2008;19(5):430-6.
167. Raja R, Hemaiswarya S, Kumar NA, Sridhar S, Rengasamy R. A perspective on the biotechnological potential of microalgae. Critical Reviews in Microbiology. 2008;34(2):77-88.
168. Silva TAL, Varão LHR, Pasquini D. Lignocellulosic Biomass. In: Thomas S, Hosur M, Pasquini D, Jose Chirayil C, editors. Handbook of Biomass. Singapore: Springer Nature Singapore; 2024. p. 105-42.
169. Brethauer S, Shahab RL, Studer MH. Impacts of biofilms on the conversion of cellulose. Applied Microbiology and Biotechnology. 2020;104(12):5201-12.
170. Chen H. 3 - Lignocellulose biorefinery feedstock engineering. In: Chen H, editor. Lignocellulose Biorefinery Engineering: Woodhead Publishing; 2015. p. 37-86.
171. Vuković JP, Ti š ma M. The role of NMR spectroscopy in lignocellulosic biomass characterisation: A mini review. Food Chemistry: Molecular Sciences. 2024;9:100219.
172. Zhang L, Pu Y, Cort JR, Ragauskas AJ, Yang B. Revealing the molecular structural transformation of hardwood and softwood in dilute acid flowthrough pretreatment. ACS Sustainable Chemistry & Engineering. 2016;4(12):6618-28.
173. Rozmysłowicz B, Yeap JH, Elkhaiary AMI, Talebi Amiri M, Shahab RL, Questell-Santiago YM, et al. Catalytic valorization of the acetate fraction of biomass to aromatics and its integration into the carboxylate platform. Green Chemistry. 2019;21(10):2801-9.
174. Xie H, Du H, Yang X, Si C. Recent strategies in preparation of cellulose nanocrystals and cellulose nanofibrils derived from raw cellulose materials. International Journal of Polymer Science. 2018;2018(1):7923068.
175. Farooq A, Patoary MK, Zhang M, Mussana H, Li M, Naeem MA, et al. Cellulose from sources to nanocellulose and an overview of synthesis and properties of nanocellulose/zinc oxide nanocomposite materials. International Journal of Biological Macromolecules. 2020;154:1050-73.
176. Shendurse A, Khedkar C. Glucose: properties and analysis. Encyclopedia of Food and Health. 2016;3:239-47.

177. Zhang Z, Ortiz O, Goyal R, Kohn J. Chapter 23 - Biodegradable Polymers. In: Lanza R, Langer R, Vacanti J, editors. Principles of Tissue Engineering (Fourth Edition). Boston: Academic Press; 2014. p. 441-73.
178. Timell T. Recent progress in the chemistry of wood hemicelluloses. Wood Science and Technology. 1967;1(1):45-70.
179. Marinho E. Cellulose: A comprehensive review of its properties and applications. Sustainable Chemistry for the Environment. 2025;11:100283.
180. Pettersen RC. The chemical composition of wood. The Chemistry of Solid Wood. 1984;207:57-126.
181. Shrotri A, Kobayashi H, Fukuoka A. Chapter Two - Catalytic Conversion of Structural Carbohydrates and Lignin to Chemicals. In: Song C, editor. Advances in Catalysis. 60: Academic Press; 2017. p. 59-123.
182. Lavoine N, Desloges I, Dufresne A, Bras J. Microfibrillated cellulose–Its barrier properties and applications in cellulosic materials: A review. Carbohydrate Polymers. 2012;90(2):735-64.
183. Etale A, Onyianta AJ, Turner SR, Eichhorn SJ. Cellulose: a review of water interactions, applications in composites, and water treatment. Chemical Reviews. 2023;123(5):2016-48.
184. Channab B-E, El Idrissi A, Essamlali Y, Zahouily M. Nanocellulose: Structure, modification, biodegradation and applications in agriculture as slow/controlled release fertilizer, superabsorbent, and crop protection: A review. Journal of Environmental Management. 2024;352:119928.
185. Jang JH, So BR, Yeo HJ, Kang HJ, Kim MJ, Lee JJ, et al. Preparation of cellulose microfibril (CMF) from Gelidium amansii and feasibility of CMF as a cosmetic ingredient. Carbohydrate Polymers. 2021;257:117569.
186. Jang S-K, Jeong H, Choi I-G. The effect of cellulose crystalline structure modification on glucose production from chemical-composition-controlled biomass. Sustainability. 2023;15(7):5869.
187. Ren Z, Guo R, Zhou X, Bi H, Jia X, Xu M, et al. Effect of amorphous cellulose on the deformation behavior of cellulose composites: molecular dynamics simulation. RSC Advances. 2021;11(33):19967-77.
188. Qian X, Ding S-Y, Nimlos MR, Johnson DK, Himmel ME. Atomic and electronic structures of molecular crystalline cellulose Iβ: a first-principles investigation. Macromolecules. 2005;38(25):10580-9.
189. Montes H, Mazeau K, Cavaillé J. Secondary mechanical relaxations in amorphous cellulose. Macromolecules. 1997;30(22):6977-84.
190. Nechyporchuk O, Belgacem MN, Bras J. Production of cellulose nanofibrils: A review of recent advances. Industrial Crops and Products. 2016;93:2-25.
191. Henriksson G, Germgård U, Lindström ME. A review on chemical mechanisms of kraft pulping. Nordic Pulp & Paper Research Journal. 2024;39(3):297-311.
192. Xu H, Che X, Ding Y, Kong Y, Li B, Tian W. Effect of crystallinity on pretreatment and enzymatic hydrolysis of lignocellulosic biomass based on multivariate analysis. Bioresource Technology. 2019;279:271-80.
193. Li X, Kim TH, Nghiem NP. Bioethanol production from corn stover using aqueous ammonia pretreatment and two-phase simultaneous saccharification and fermentation (TPSSF). Bioresource Technology. 2010;101(15):5910-6.
194. Eminov S, Brandt A, Wilton-Ely JD, Hallett JP. The highly selective and near-quantitative

conversion of glucose to 5-hydroxymethylfurfural using ionic liquids. PLOS ONE. 2016;11(10):e0163835.
195. Eminov S, Filippousi P, Brandt A, Wilton-Ely JD, Hallett JP. Direct catalytic conversion of cellulose to 5-hydroxymethylfurfural using ionic liquids. Inorganics. 2016;4(4):32.
196. Sajid M, Zhao X, Liu D. Production of 2, 5-furandicarboxylic acid (FDCA) from 5-hydroxymethylfurfural (HMF): recent progress focusing on the chemical-catalytic routes. Green Chemistry. 2018;20(24):5427-53.
197. Miah MR, Ding J, Zhao H, Wang H, Chu Q, Fang B, et al. Enhancing the mechanical and barrier properties of biobased polyester incorporated with carboxylated cellulose nanofibers. Materials Today Communications. 2024;38:108538.
198. Gupta P, Bhandari S. 6 - Chemical Depolymerization of PET Bottles via Ammonolysis and Aminolysis. In: Thomas S, Rane A, Kanny K, V.K A, Thomas MG, editors. Recycling of Polyethylene Terephthalate Bottles: William Andrew Publishing; 2019. p. 109-34.
199. Xie H, Wu L, Li B-G, Dubois P. Modification of poly (ethylene 2, 5-furandicarboxylate) with biobased 1, 5-pentanediol: significantly toughened copolyesters retaining high tensile strength and O2 barrier property. Biomacromolecules. 2018;20(1):353-64.
200. Sun L, Wang J, Mahmud S, Jiang Y, Zhu J, Liu X. New insight into the mechanism for the excellent gas properties of poly (ethylene 2, 5-furandicarboxylate)(PEF): Role of furan ring's polarity. European Polymer Journal. 2019;118:642-50.
201. Zhao Y, Li Y, Dai Y, Zhang Y, Jiang M, Zhou G. High toughness, UV & blue light shielding and antibacterial bio-based PEF/TiO2 nanowires composites for packaging application. Polymer Degradation and Stability. 2023;218:110562.
202. Girisuta B, Janssen L, Heeres H. Kinetic study on the acid-catalyzed hydrolysis of cellulose to levulinic acid. Industrial & Engineering Chemistry Research. 2007;46(6):1696-708.
203. van Putten RJ, Soetedjo JN, Pidko EA, van der Waal JC, Hensen EJ, de Jong E, et al. Dehydration of different ketoses and aldoses to 5 - hydroxymethylfurfural. ChemSusChem. 2013;6(9):1681-7.
204. Kang S, Fu J, Zhang G. From lignocellulosic biomass to levulinic acid: A review on acid-catalyzed hydrolysis. Renewable and Sustainable Energy Reviews. 2018;94:340-62.
205. Ma C, Cai B, Zhang L, Feng J, Pan H. Acid-catalyzed conversion of cellulose into levulinic acid with biphasic solvent system. Frontiers in Plant Science. 2021;12:630807.
206. Werpy T, Petersen G. Top value added chemicals from biomass: volume I--results of screening for potential candidates from sugars and synthesis gas. National Renewable Energy Lab., Golden, CO (US); 2004.
207. Qaseem MF, Shaheen H, Wu A-M. Cell wall hemicellulose for sustainable industrial utilization. Renewable and Sustainable Energy Reviews. 2021;144:110996.
208. Kaur R, Krishna BB, Kumar A, Bhaskar T. Biomass Pyrolysis. In: Abraham MA, editor. Encyclopedia of Sustainable Technologies (Second Edition). Oxford: Elsevier; 2024. p. 252-65.
209. Ghaffar SH, Fan M. Structural analysis for lignin characteristics in biomass straw. Biomass and Bioenergy. 2013;57:264-79.
210. Wen J-L, Sun S-L, Xue B-L, Sun R-C. Recent advances in characterization of lignin polymer by solution-state nuclear magnetic resonance (NMR) methodology. Materials. 2013;6(1):359-91.
211. Khemthong P, Yimsukanan C, Narkkun T, Srifa A, Witoon T, Pongchaiphol S, et al. Advances in catalytic production of value-added biochemicals and biofuels via furfural platform

derived lignocellulosic biomass. Biomass and Bioenergy. 2021;148:106033.
212. Kabbour M, Luque R. Chapter 10 - Furfural as a platform chemical: From production to applications. In: Saravanamurugan S, Pandey A, Li H, Riisager A, editors. Biomass, Biofuels, Biochemicals: Elsevier; 2020. p. 283-97.
213. Kim H, Lee S, Lee J, Won W. Simultaneous production of 1, 6-hexanediol, furfural, and high-purity lignin from white birch: Process integration and techno-economic evaluation. Bioresource Technology. 2021;331:125009.
214. Foston M, Ragauskas AJ. Biomass characterization: recent progress in understanding biomass recalcitrance. Industrial Biotechnology. 2012;8(4):191-208.
215. Davin LB, Lewis NG. Lignin primary structures and dirigent sites. Current Opinion in Biotechnology. 2005;16(4):407-15.
216. Xu C, Arancon RAD, Labidi J, Luque R. Lignin depolymerisation strategies: towards valuable chemicals and fuels. Chemical Society Reviews. 2014;43(22):7485-500.
217. Ragauskas AJ, Beckham GT, Biddy MJ, Chandra R, Chen F, Davis MF, et al. Lignin valorization: improving lignin processing in the biorefinery. Science. 2014;344(6185):1246843.
218. Mainka H, Täger O, Körner E, Hilfert L, Busse S, Edelmann FT, et al. Lignin–an alternative precursor for sustainable and cost-effective automotive carbon fiber. Journal of Materials Research and Technology. 2015;4(3):283-96.
219. Li M, Pu Y, Ragauskas AJ. Current understanding of the correlation of lignin structure with biomass recalcitrance. Frontiers in Chemistry. 2016;4:45.
220. McKendry P. Energy production from biomass (part 1): overview of biomass. Bioresource Technology. 2002;83(1):37-46.
221. Saini JK, Saini R, Tewari L. Lignocellulosic agriculture wastes as biomass feedstocks for second-generation bioethanol production: concepts and recent developments. 3 Biotech. 2015;5(4):337-53.
222. Kim H, Ralph J. Solution-state 2D NMR of ball-milled plant cell wall gels in DMSO-d6/pyridine-d5. Organic & Biomolecular Chemistry. 2010;8(3):576-91.
223. Sun R, Sun X, Wang S, Zhu W, Wang X. Ester and ether linkages between hydroxycinnamic acids and lignins from wheat, rice, rye, and barley straws, maize stems, and fast-growing poplar wood. Industrial Crops and Products. 2002;15(3):179-88.
224. Tarasov D, Leitch M, Fatehi P. Lignin–carbohydrate complexes: properties, applications, analyses, and methods of extraction: a review. Biotechnology for Biofuels. 2018;11(1):269.
225. Sathitsuksanoh N, Holtman KM, Yelle DJ, Morgan T, Stavila V, Pelton J, et al. Lignin fate and characterization during ionic liquid biomass pretreatment for renewable chemicals and fuels production. Green Chemistry. 2014;16(3):1236-47.
226. Adler E. Lignin chemistry—past, present and future. Wood Science and Technology. 1977;11(3):169-218.
227. Vanholme R, Demedts B, Morreel K, Ralph J, Boerjan W. Lignin biosynthesis and structure. Plant Physiology. 2010;153(3):895-905.
228. Alvira P, Tomas-Pejo E, Ballesteros M, Negro MJ. Pretreatment technologies for an efficient bioethanol production process based on enzymatic hydrolysis: a review. Bioresource Technology. 2010;101(13):4851-61.
229. Axelsson L, Franzén M, Ostwald M, Berndes G, Lakshmi G, Ravindranath N. Jatropha cultivation in southern India: assessing farmers' experiences. Biofuels, Bioproducts and Biorefining.

2012;6(3):246-56.
230. Mensah M, Tia R, Adei E, De Leeuw NH. A DFT mechanistic study on base-catalyzed cleavage of the β-O-4 ether linkage in lignin: implications for selective lignin depolymerization. Frontiers in Chemistry. 2022;10:793759.
231. Eudes A, George A, Mukerjee P, Kim JS, Pollet B, Benke PI, et al. Biosynthesis and incorporation of side-chain-truncated lignin monomers to reduce lignin polymerization and enhance saccharification. Plant Biotechnology Journal. 2012;10(5):609-20.
232. Weng J-K, Li X, Bonawitz ND, Chapple C. Emerging strategies of lignin engineering and degradation for cellulosic biofuel production. Current Opinion in Biotechnology. 2008;19(2):166-72.
233. Welker CM, Balasubramanian VK, Petti C, Rai KM, DeBolt S, Mendu V. Engineering plant biomass lignin content and composition for biofuels and bioproducts. Energies. 2015;8(8):7654-76.
234. Chen H, Liu J, Chang X, Chen D, Xue Y, Liu P, et al. A review on the pretreatment of lignocellulose for high-value chemicals. Fuel Processing Technology. 2017;160:196-206.
235. Zhang YP. Reviving the carbohydrate economy via multi-product lignocellulose biorefineries. Journal of Industrial Microbiology and Biotechnology. 2008;35(5):367-75.
236. Pandey MP, Kim CS. Lignin depolymerization and conversion: a review of thermochemical methods. Chemical Engineering & Technology. 2011;34(1):29-41.
237. Collard F-X, Blin J. A review on pyrolysis of biomass constituents: Mechanisms and composition of the products obtained from the conversion of cellulose, hemicelluloses and lignin. Renewable and Sustainable Energy Reviews. 2014;38:594-608.
238. Ben H, Mu W, Deng Y, Ragauskas AJ. Production of renewable gasoline from aqueous phase hydrogenation of lignin pyrolysis oil. Fuel. 2013;103:1148-53.
239. Olcese RN, Lardier G, Bettahar M, Ghanbaja J, Fontana S, Carré V, et al. Aromatic chemicals by iron-catalyzed hydrotreatment of lignin pyrolysis vapor. ChemSusChem. 2013;6(8):1490-9.
240. Alonso DM, Bond JQ, Dumesic JA. Catalytic conversion of biomass to biofuels. Green Chemistry. 2010;12(9):1493-513.
241. Wang H, Pu Y, Ragauskas A, Yang B. From lignin to valuable products–strategies, challenges, and prospects. Bioresource Technology. 2019;271:449-61.
242. Tachon N, Benjelloun-Mlayah B, Delmas M. Organosolv wheat straw lignin as a phenol substitute for green phenolic resins. BioResources. 2016;11(3):5797-815.
243. Kai D, Ren W, Tian L, Chee PL, Liu Y, Ramakrishna S, et al. Engineering poly (lactide)–lignin nanofibers with antioxidant activity for biomedical application. ACS Sustainable Chemistry & Engineering. 2016;4(10):5268-76.
244. Savy D, Cozzolino V. Novel fertilising products from lignin and its derivatives to enhance plant development and increase the sustainability of crop production. Journal of Cleaner Production. 2022;366:132832.
245. Xu F, Zhu T-T, Rao Q-Q, Shui S-W, Li W-W, He H-B, et al. Fabrication of mesoporous lignin-based biosorbent from rice straw and its application for heavy-metal-ion removal. Journal of Environmental Sciences. 2017;53:132-40.
246. Sadeghifar H, Venditti R, Jur J, Gorga RE, Pawlak JJ. Cellulose-lignin biodegradable and flexible UV protection film. ACS Sustainable Chemistry & Engineering. 2017;5(1):625-31.

247. Maurya DP, Singla A, Negi S. An overview of key pretreatment processes for biological conversion of lignocellulosic biomass to bioethanol. 3 Biotech. 2015;5(5):597-609.
248. Ragauskas AJ, Nagy M, Kim DH, Eckert CA, Hallett JP, Liotta CL. From wood to fuels: integrating biofuels and pulp production. Industrial Biotechnology. 2006;2(1):55-65.
249. Humbird D, Davis R, Tao L, Kinchin C, Hsu D, Aden A, et al. Process design and economics for biochemical conversion of lignocellulosic biomass to ethanol: dilute-acid pretreatment and enzymatic hydrolysis of corn stover. National Renewable Energy Lab.(NREL), Golden, CO (United States); 2011.
250. Cheng F, Brewer CE. Producing jet fuel from biomass lignin: Potential pathways to alkylbenzenes and cycloalkanes. Renewable and Sustainable Energy Reviews. 2017;72:673-722.
251. Bajpai P. Chapter 12 - Pulping Fundamentals. In: Bajpai P, editor. Biermann's Handbook of Pulp and Paper (Third Edition): Elsevier; 2018. p. 295-351.
252. Dang VQ, Nguyen KL. A systematic approach for determination of optimal conditions for Lo-Solids™ kraft pulping of Eucalyptus nitens. Chemical Engineering Journal. 2007;133(1-3):97-103.
253. Kumar A, Prerna, Bilal M, Singh AK, Ratna S, Talluri Rameshwari KR, et al. Chapter 14 - Enzyme cocktail: a greener approach for biobleaching in paper and pulp industry. In: Bhat R, Kumar A, Nguyen TA, Sharma S, editors. Nanotechnology in Paper and Wood Engineering: Elsevier; 2022. p. 303-28.
254. Moussavi A, Bonhivers J-C, Filho RM, Mariano AP, Stuart PR. 26 - Applications of Process Integration Methodologies in the pulp and paper industry. In: Klemeš JJ, editor. Handbook of Process Integration (PI) (Second Edition): Woodhead Publishing; 2023. p. 783-810.
255. Fort DA, Remsing RC, Swatloski RP, Moyna P, Moyna G, Rogers RD. Can ionic liquids dissolve wood? Processing and analysis of lignocellulosic materials with 1-n-butyl-3-methylimidazolium chloride. Green Chemistry. 2007;9(1):63-9.
256. Obydenkova SV, Kouris PD, Hensen EJ, Smeulders DM, van der Meer Y, Boot MD. Industrial lignin from 2G biorefineries–assessment of availability and pricing strategies. Bioresource Technology. 2019;291:121805.
257. Chandra R, Iqbal HM, Vishal G, Lee H-S, Nagra S. Algal biorefinery: a sustainable approach to valorize algal-based biomass towards multiple product recovery. Bioresource Technology. 2019;278:346-59.
258. Huntley SK, Ellis D, Gilbert M, Chapple C, Mansfield SD. Significant increases in pulping efficiency in C4H-F5H-transformed poplars: improved chemical savings and reduced environmental toxins. Journal of Agricultural and Food Chemistry. 2003;51(21):6178-83.
259. Jawjit W, Kroeze C, Soontaranun W, Hordijk L. Future trends in environmental impact of eucalyptus-based Kraft pulp industry in Thailand: a scenario analysis. Environmental Science & Policy. 2008;11(6):545-61.
260. Bozell JJ, Petersen GR. Technology development for the production of biobased products from biorefinery carbohydrates—the US Department of Energy's "Top 10" revisited. Green Chemistry. 2010;12(4):539-54.
261. Baral NR, Shah A. Comparative techno-economic analysis of steam explosion, dilute sulfuric acid, ammonia fiber explosion and biological pretreatments of corn stover. Bioresource Technology. 2017;232:331-43.
262. Zhang L, Loh K-C, Zhang J. Enhanced biogas production from anaerobic digestion of solid

organic wastes: current status and prospects. Bioresource Technology Reports. 2019;5:280-96.
263. Wu Y, Guo H, Rahman MS, Chen X, Zhang J, Liu Y, et al. Biological pretreatment of corn stover for enhancing enzymatic hydrolysis using Bacillus sp. P3. Bioresources and Bioprocessing. 2021;8(1):92.
264. Zhang K, Johnson L, Vara Prasad PV, Pei Z, Wang D. Big bluestem as a bioenergy crop: A review. Renewable and Sustainable Energy Reviews. 2015;52:740-56.
265. Sharma SG, Arora R. Chapter 3 - Pretreatment strategies for woody biomass. In: Kumar D, Kumar S, Rajendran K, Ray RC, editors. Sustainable Biorefining of Woody Biomass to Biofuels and Biochemicals: Woodhead Publishing; 2024. p. 65-79.
266. Rajendran K, Drielak E, Sudarshan Varma V, Muthusamy S, Kumar G. Updates on the pretreatment of lignocellulosic feedstocks for bioenergy production–a review. Biomass Conversion and Biorefinery. 2018;8:471-83.
267. Moodley P, Trois C. 2 - Lignocellulosic biorefineries: the path forward. In: Ray RC, editor. Sustainable Biofuels: Academic Press; 2021. p. 21-42.
268. Ramanathan A, Begum KMMS, Pereira AO, Cohen C. Chapter 3 - Biomass gasification integrated with Fischer–Tropsch reactor: techno-economic approach. In: Ramanathan A, Begum KMMS, Pereira AO, Cohen C, editors. A Thermo-Economic Approach to Energy From Waste: Elsevier; 2022. p. 73-106.
269. Sambusiti C, Licari A, Solhy A, Aboulkas A, Cacciaguerra T, Barakat A. One-pot dry chemo-mechanical deconstruction for bioethanol production from sugarcane bagasse. Bioresource Technology. 2015;181:200-6.
270. Silva GGD, Couturier M, Berrin J-G, Buléon A, Rouau X. Effects of grinding processes on enzymatic degradation of wheat straw. Bioresource Technology. 2012;103(1):192-200.
271. Mani S, Tabil LG, Sokhansanj S. Grinding performance and physical properties of wheat and barley straws, corn stover and switchgrass. Biomass and Bioenergy. 2004;27(4):339-52.
272. Ramírez Cabrera PA, Lozano Pérez AS, Guerrero Fajardo CA. Design of a Knife Mill with a Drying Adaptation for Lignocellulose Biomass Milling: Peapods and Coffee Cherry. Designs. 2025;9(3):57.
273. Schell DJ, Harwood C. Milling of lignocellulosic biomass: results of pilot-scale testing. Applied Biochemistry and Biotechnology. 1994;45(1):159-68.
274. Gu B-J, Wang J, Wolcott MP, Ganjyal GM. Increased sugar yield from pre-milled Douglas-fir forest residuals with lower energy consumption by using planetary ball milling. Bioresource Technology. 2018;251:93-8.
275. Zhao X, Zhang L, Liu D. Biomass recalcitrance. Part II: Fundamentals of different pre-treatments to increase the enzymatic digestibility of lignocellulose. Biofuels, Bioproducts and Biorefining. 2012;6(5):561-79.
276. Lozano Pérez AS, Lozada Castro JJ, Guerrero Fajardo CA. Application of microwave energy to biomass: a comprehensive review of microwave-assisted technologies, optimization parameters, and the strengths and weaknesses. Journal of Manufacturing and Materials Processing. 2024;8(3):121.
277. Guo X, Zhang T, Shu S, Zheng W, Gao M. Compositional and structural changes of corn cob pretreated by electron beam irradiation. ACS Sustainable Chemistry & Engineering. 2017;5(1):420-5.
278. Baruah J, Nath BK, Sharma R, Kumar S, Deka RC, Baruah DC, et al. Recent trends in the

pretreatment of lignocellulosic biomass for value-added products. Frontiers in Energy Research. 2018;6:141.
279. Sun Y, Cheng J. Hydrolysis of lignocellulosic materials for ethanol production: a review. Bioresource Technology. 2002;83(1):1-11.
280. Leonowicz A, Matuszewska A, Luterek J, Ziegenhagen D, Wojtaś-Wasilewska M, Cho N-S, et al. Biodegradation of lignin by white rot fungi. Fungal Genetics and Biology. 1999;27(2-3):175-85.
281. Zhang S, Dong Z, Shi J, Yang C, Fang Y, Chen G, et al. Enzymatic hydrolysis of corn stover lignin by laccase, lignin peroxidase, and manganese peroxidase. Bioresource Technology. 2022;361:127699.
282. Highley TL, Kirk TK, Ibach R. Effect of Brown-Rot Fungi on Cellulose. In: O'Rear CE, Llewellyn GC, editors. Biodeterioration Research 2: General Biodeterioration, Degradation, Mycotoxins, Biotoxins, and Wood Decay. Boston, MA: Springer US; 1989. p. 511-25.
283. Tuomela M, Hatakka A. 6.16 - Oxidative Fungal Enzymes for Bioremediation. In: Moo-Young M, editor. Comprehensive Biotechnology (Second Edition). Burlington: Academic Press; 2011. p. 183-96.
284. Goodell B, Winandy JE, Morrell JJ. Fungal degradation of wood: Emerging data, new insights and changing perceptions. Coatings. 2020;10(12):1210.
285. Chai Y, Bai M, Chen A, Peng L, Shao J, Luo S, et al. Valorization of waste biomass through fungal technology: Advances, challenges, and prospects. Industrial Crops and Products. 2022;188:115608.
286. Salvachúa D, Prieto A, López-Abelairas M, Lu-Chau T, Martínez ÁT, Martínez MJ. Fungal pretreatment: an alternative in second-generation ethanol from wheat straw. Bioresource Technology. 2011;102(16):7500-6.
287. Zhang W, Diao C, Wang L. Degradation of lignin in different lignocellulosic biomass by steam explosion combined with microbial consortium treatment. Biotechnology for Biofuels and Bioproducts. 2023;16(1):55.
288. Sai Bharadwaj AVSL, Dev S, Zhuang J, Wang Y, Yoo CG, Jeon B-H, et al. Review of chemical pretreatment of lignocellulosic biomass using low-liquid and low-chemical catalysts for effective bioconversion. Bioresource Technology. 2023;368:128339.
289. Amiri H, Karimi K. Pretreatment and hydrolysis of lignocellulosic wastes for butanol production: Challenges and perspectives. Bioresource Technology. 2018;270:702-21.
290. Niju S, Swathika M, Balajii M. Chapter 10 - Pretreatment of lignocellulosic sugarcane leaves and tops for bioethanol production. In: Yousuf A, Pirozzi D, Sannino F, editors. Lignocellulosic Biomass to Liquid Biofuels: Academic Press; 2020. p. 301-24.
291. Panigrahi S, Dubey BK. A critical review on operating parameters and strategies to improve the biogas yield from anaerobic digestion of organic fraction of municipal solid waste. Renewable Energy. 2019;143:779-97.
292. Mood SH, Golfeshan AH, Tabatabaei M, Jouzani GS, Najafi GH, Gholami M, et al. Lignocellulosic biomass to bioethanol, a comprehensive review with a focus on pretreatment. Renewable and Sustainable Energy Reviews. 2013;27:77-93.
293. Chen X, Shekiro J, Franden MA, Wang W, Zhang M, Kuhn E, et al. The impacts of deacetylation prior to dilute acid pretreatment on the bioethanol process. Biotechnology for Biofuels. 2012;5(1):8.

294. Kuglarz M, Alvarado-Morales M, Karakashev D, Angelidaki I. Integrated production of cellulosic bioethanol and succinic acid from industrial hemp in a biorefinery concept. Bioresource Technology. 2016;200:639-47.
295. Martins JR, Schmatz AA, Salazar-Bryan AM, Brienzo M. Effect of dilute acid pretreatment on the sugarcane leaf for fermentable sugars production. Sugar Tech. 2022;24(5):1540-50.
296. Kim M, Day DF. Composition of sugar cane, energy cane, and sweet sorghum suitable for ethanol production at Louisiana sugar mills. Journal of Industrial Microbiology and Biotechnology. 2011;38(7):803-7.
297. Kim JS, Lee YY, Kim TH. A review on alkaline pretreatment technology for bioconversion of lignocellulosic biomass. Bioresource Technology. 2016;199:42-8.
298. Qin L, Li W-C, Liu L, Zhu J-Q, Li X, Li B-Z, et al. Inhibition of lignin-derived phenolic compounds to cellulase. Biotechnology for Biofuels. 2016;9(1):70.
299. Jiju PS, Patel AK, Shruthy NS, Shalu S, Dong C-D, Singhania RR. Sustainability through lignin valorization: recent innovations and applications driving industrial transformation. Bioresources and Bioprocessing. 2025;12(1):88.
300. Kim TH. Pretreatment of lignocellulosic biomass. Bioprocessing Technologies in Biorefinery for Sustainable Production of Fuels, Chemicals, and Polymers. 2013:91-110.
301. Wang S, Li F, Zhang P, Jin S, Tao X, Tang X, et al. Ultrasound assisted alkaline pretreatment to enhance enzymatic saccharification of grass clipping. Energy Conversion and Management. 2017;149:409-15.
302. Haque MA, Barman DN, Kang TH, Kim MK, Kim J, Kim H, et al. Effect of dilute alkali on structural features and enzymatic hydrolysis of barley straw (Hordeum vulgare) at boiling temperature with low residence time. Journal of Microbiology and Biotechnology. 2012;22(12):1681-91.
303. Kim S, Holtzapple MT. Lime pretreatment and enzymatic hydrolysis of corn stover. Bioresource Technology. 2005;96(18):1994-2006.
304. Oladi S, Aita GM. Optimization of liquid ammonia pretreatment variables for maximum enzymatic hydrolysis yield of energy cane bagasse. Industrial Crops and Products. 2017;103:122-32.
305. Labbé N, Kline LM, Moens L, Kim K, Kim PC, Hayes DG. Activation of lignocellulosic biomass by ionic liquid for biorefinery fractionation. Bioresource Technology. 2012;104:701-7.
306. Li C, Sun L, Simmons BA, Singh S. Comparing the recalcitrance of eucalyptus, pine, and switchgrass using ionic liquid and dilute acid pretreatments. BioEnergy Research. 2013;6(1):14-23.
307. Clough MT, Geyer K, Hunt PA, Mertes J, Welton T. Thermal decomposition of carboxylate ionic liquids: trends and mechanisms. Physical Chemistry Chemical Physics. 2013;15(47):20480-95.
308. Doherty TV, Mora-Pale M, Foley SE, Linhardt RJ, Dordick JS. Ionic liquid solvent properties as predictors of lignocellulose pretreatment efficacy. Green Chemistry. 2010;12(11):1967-75.
309. Abouelela AR, Hallett JP. Hazardous Creosote Wood Valorization via Fractionation and Enzymatic Saccharification Coupled with Simultaneous Extraction of the Embedded Polycyclic Aromatic Hydrocarbons Using Protic Ionic Liquid Media. ACS Sustainable Chemistry & Engineering. 2021;9(2):704-16.
310. Rajendran K, Taherzadeh MJ. Pretreatment of lignocellulosic materials. Bioprocessing of Renewable Resources to Commodity Bioproducts. 2014:43-75.
311. Bandyopadhyay-Ghosh S, Ghosh SB, Sain M. 19 - The use of biobased nanofibres in

composites. In: Faruk O, Sain M, editors. Biofiber Reinforcements in Composite Materials: Woodhead Publishing; 2015. p. 571-647.
312. Singh J, Suhag M, Dhaka A. Augmented digestion of lignocellulose by steam explosion, acid and alkaline pretreatment methods: a review. Carbohydrate Polymers. 2015;117:624-31.
313. Li J, Henriksson G, Gellerstedt G. Lignin depolymerization/repolymerization and its critical role for delignification of aspen wood by steam explosion. Bioresource Technology. 2007;98(16):3061-8.
314. Vivekanand V, Olsen EF, Eijsink VG, Horn SJ. Effect of different steam explosion conditions on methane potential and enzymatic saccharification of birch. Bioresource Technology. 2013;127:343-9.
315. Negro M, Alvarez C, Ballesteros I, Romero I, Ballesteros M, Castro E, et al. Ethanol production from glucose and xylose obtained from steam exploded water-extracted olive tree pruning using phosphoric acid as catalyst. Bioresource Technology. 2014;153:101-7.
316. Neves P, Pitarelo A, Ramos L. Production of cellulosic ethanol from sugarcane bagasse by steam explosion: Effect of extractives content, acid catalysis and different fermentation technologies. Bioresource Technology. 2016;208:184-94.
317. Guerrero AB, Ballesteros I, Ballesteros M. Optimal conditions of acid-catalysed steam explosion pretreatment of banana lignocellulosic biomass for fermentable sugar production. Journal of Chemical Technology & Biotechnology. 2017;92(9):2351-9.
318. Wang Z, Wu G, Jönsson LJ. Effects of impregnation of softwood with sulfuric acid and sulfur dioxide on chemical and physical characteristics, enzymatic digestibility, and fermentability. Bioresource Technology. 2018;247:200-8.
319. Palmisano P. Lignin conversion into bio-based chemicals. 2013.
320. Obydenkova SV, Kouris PD, Hensen EJ, Heeres HJ, Boot MD. Environmental economics of lignin derived transport fuels. Bioresource Technology. 2017;243:589-99.
321. Barros S. Brazil biofuels annual. USDA Foreign Agricultural Service Gain Report (BR13005). 2013.
322. Holtzapple M, Humphrey A, Taylor J. Energy requirements for the size reduction of poplar and aspen wood. Biotechnology and Bioengineering. 1989;33(2):207-10.
323. Clark T, Mackie K. Steam explosion of the softwood Pinus radiata with sulphur dioxide addition. I. Process optimisation. Journal of Wood Chemistry and Technology. 1987;7(3):373-403.
324. Akhlisah Z, Yunus R, Abidin Z, Lim B, Kania D. Pretreatment methods for an effective conversion of oil palm biomass into sugars and high-value chemicals. Biomass and Bioenergy. 2021;144:105901.
325. Juneja A, Kumar D, Rajendran K, Mittal A. 4 - Pretreatment technologies for lignocellulosic biomass refineries. In: Moodley P, Ray RC, Gueguim Kana EB, editors. Advances in Lignocellulosic Biofuel Production Systems: Woodhead Publishing; 2023. p. 81-106.
326. Kumar R, Strezov V, Weldekidan H, He J, Singh S, Kan T, et al. Lignocellulose biomass pyrolysis for bio-oil production: A review of biomass pre-treatment methods for production of drop-in fuels. Renewable and Sustainable Energy Reviews. 2020;123:109763.
327. Lee JM, Jameel H, Venditti RA. A comparison of the autohydrolysis and ammonia fiber explosion (AFEX) pretreatments on the subsequent enzymatic hydrolysis of coastal Bermuda grass. Bioresource Technology. 2010;101(14):5449-58.
328. Li C, Cheng G, Balan V, Kent MS, Ong M, Chundawat SPS, et al. Influence of physico-

chemical changes on enzymatic digestibility of ionic liquid and AFEX pretreated corn stover. Bioresource Technology. 2011;102(13):6928-36.
329. Chundawat SP, Pal RK, Zhao C, Campbell T, Teymouri F, Videto J, et al. Ammonia fiber expansion (AFEX) pretreatment of lignocellulosic biomass. JoVE (Journal of Visualized Experiments). 2020(158):e57488.
330. Uppugundla N, da Costa Sousa L, Chundawat SP, Yu X, Simmons B, Singh S, et al. A comparative study of ethanol production using dilute acid, ionic liquid and AFEX™ pretreated corn stover. Biotechnology for Biofuels. 2014;7(1):72.
331. Anastas PT, Hammond DG. Chapter 4 - Case Studies—Green Chemistry in Practice. In: Anastas PT, Hammond DG, editors. Inherent Safety At Chemical Sites: Elsevier; 2016. p. 23-118.
332. Patist A, Bates D. Ultrasonic innovations in the food industry: From the laboratory to commercial production. Innovative Food Science & Emerging Technologies. 2008;9(2):147-54.
333. Rehman MSU, Kim I, Chisti Y, Han J-I. Use of ultrasound in the production of bioethanol from lignocellulosic biomass. Energy Education Science and Technology Part A: Energy Science and Research. 2013;30(2):1931-410.
334. Sarwono A, Man Z, Muhammad N, Khan AS, Hamzah WSW, Rahim AHA, et al. A new approach of probe sonication assisted ionic liquid conversion of glucose, cellulose and biomass into 5-hydroxymethylfurfural. Ultrasonics Sonochemistry. 2017;37:310-9.
335. Chisti Y. Sonobioreactors: using ultrasound for enhanced microbial productivity. TRENDS in Biotechnology. 2003;21(2):89-93.
336. Sulaiman AZ, Ajit A, Yunus RM, Chisti Y. Ultrasound-assisted fermentation enhances bioethanol productivity. Biochemical Engineering Journal. 2011;54(3):141-50.
337. Montalbo-Lomboy M, Johnson L, Khanal SK, van Leeuwen JH, Grewell D. Sonication of sugary-2 corn: a potential pretreatment to enhance sugar release. Bioresource Technology. 2010;101(1):351-8.
338. Suslick KS. Sonochemistry. Science. 1990;247(4949):1439-45.
339. Rahim AHA, Man Z, Sarwono A, Muhammad N, Khan AS, Hamzah WSW, et al. Probe sonication assisted ionic liquid treatment for rapid dissolution of lignocellulosic biomass. Cellulose. 2020;27(4):2135-48.
340. Sukor NF, Jusoh R, Kamarudin NS, Abdul Halim NA, Sulaiman AZ, Abdullah SB. Synergistic effect of probe sonication and ionic liquid for extraction of phenolic acids from oak galls. Ultrasonics Sonochemistry. 2020;62:104876.
341. SriBala G, Chennuru R, Mahapatra S, Vinu R. Effect of alkaline ultrasonic pretreatment on crystalline morphology and enzymatic hydrolysis of cellulose. Cellulose. 2016;23(3):1725-40.
342. Ninomiya K, Kamide K, Takahashi K, Shimizu N. Enhanced enzymatic saccharification of kenaf powder after ultrasonic pretreatment in ionic liquids at room temperature. Bioresource Technology. 2012;103(1):259-65.
343. Yang W, Aljapur VK, Krishnamurthy K, Feng H, Yang R, Rababah TM. Expedited extraction of xylan from lignocellulosic biomass by power ultrasound. International Journal of Agricultural and Biological Engineering. 2010;2(4):76-83.
344. Sun RC, Sun XF, Ma XH. Effect of ultrasound on the structural and physiochemical properties of organosolv soluble hemicelluloses from wheat straw. Ultrasonics Sonochemistry. 2002;9(2):95-101.
345. Sherif N, Gadalla M, Kamel D. Acid-hydrolysed furfural production from rice straw bio-

waste: Process synthesis, simulation, and optimisation. South African Journal of Chemical Engineering. 2021;38(1):34-40.
346. Upare PP, Clarence RE, Shin H, Park BG. An overview on production of lignocellulose-derived platform chemicals such as 5-Hydroxymethyl Furfural, Furfural, Protocatechuic Acid. Processes. 2023;11(10):2912.
347. Devappa RK, Rakshit SK, Dekker RF. Forest biorefinery: Potential of poplar phytochemicals as value-added co-products. Biotechnology Advances. 2015;33(6):681-716.
348. Santos Viana G, Estevam Lau Bomfim JÁ, Pereira da Silva G, Souza de Carvalho Filho JF, Sanae Tokumoto M, Cesário Rangel F, et al. Design of heterogeneous catalysts for the conversion of furfural to C5 derivatives: a brief review. Catalysis Research. 2022;2(3):1-25.
349. Enslow KR, Bell AT. The kinetics of Brønsted acid-catalyzed hydrolysis of hemicellulose dissolved in 1-ethyl-3-methylimidazolium chloride. RSC Advances. 2012;2(26):10028-36.
350. Kangle N, Gaikwad K, Angal S. Manufacture of Furfural from Sugarcane Bagasse. International Journal of Engineering Research and Applications. 2023;13:96-102.
351. Dashtban M, Gilbert A, Fatehi P. Production of furfural: overview and challenges. Journal of Science & Technology for Forest Products and Processes. 2012;2(4):44-53.
352. Cañada-Barcala As, Rodriguez-Llorente D, Lopez L, Navarro P, Hernandez E, Águeda Vl, et al. Sustainable production of furfural in biphasic reactors using terpenoids and hydrophobic eutectic solvents. ACS Sustainable Chemistry & Engineering. 2021;9(30):10266-75.
353. Zhang T, Li W, Xiao H, Jin Y, Wu S. Recent progress in direct production of furfural from lignocellulosic residues and hemicellulose. Bioresource Technology. 2022;354:127126.
354. Nabarlatz D, Farriol X, Montane D. Kinetic modeling of the autohydrolysis of lignocellulosic biomass for the production of hemicellulose-derived oligosaccharides. Industrial & Engineering Chemistry Research. 2004;43(15):4124-31.
355. Liu L, Chang H-m, Jameel H, Park S. Furfural production from biomass pretreatment hydrolysate using vapor-releasing reactor system. Bioresource Technology. 2018;252:165-71.
356. Li X, Liu Q, Luo C, Gu X, Lu L, Lu X. Kinetics of furfural production from corn cob in γ-valerolactone using dilute sulfuric acid as catalyst. ACS Sustainable Chemistry & Engineering. 2017;5(10):8587-93.
357. Alonso DM, Wettstein SG, Mellmer MA, Gurbuz EI, Dumesic JA. Integrated conversion of hemicellulose and cellulose from lignocellulosic biomass. Energy & Environmental Science. 2013;6(1):76-80.
358. Zhang L, Yu H, Wang P, Li Y. Production of furfural from xylose, xylan and corncob in gamma-valerolactone using FeCl3· 6H2O as catalyst. Bioresource Technology. 2014;151:355-60.
359. Sener C, Motagamwala AH, Alonso DM, Dumesic JA. Enhanced furfural yields from xylose dehydration in the γ - Valerolactone/water solvent system at elevated temperatures. ChemSusChem. 2018;11(14):2321-31.
360. Yang T, Li W, Su M, Liu Y, Liu M. Production of furfural from xylose catalyzed by a novel calcium gluconate derived carbon solid acid in 1, 4-dioxane. New Journal of Chemistry. 2020;44(19):7968-75.
361. Song W, Liu H, Zhang J, Sun Y, Peng L. Understanding Hβ zeolite in 1, 4-dioxane efficiently converts hemicellulose-related sugars to furfural. ACS Catalysis. 2022;12(20):12833-44.
362. Romo JE, Miller KC, Sundsted TL, Job AL, Hoo KA, Wettstein SG. The effect of solvent polarity on autocatalytic furfural production confirmed by multivariate statistical analysis.

ChemCatChem. 2019;11(19):4715-9.
363. Wang Y, Li M, Wang Z, Liu S, O'Young L. Furfural production: A review on reaction mechanism and conventional production process. Industrial Crops and Products. 2025;230:121103.
364. Lin Q, Zhan Q, Li R, Liao S, Ren J, Peng F, et al. Solvent effect on xylose-to-furfural reaction in biphasic systems: combined experiments with theoretical calculations. Green Chemistry. 2021;23(21):8510-8.
365. Pholjaroen B, Li N, Wang Z, Wang A, Zhang T. Dehydration of xylose to furfural over niobium phosphate catalyst in biphasic solvent system. Journal of Energy Chemistry. 2013;22(6):826-32.
366. Xu S, Pan D, Wu Y, Song X, Gao L, Li W, et al. Efficient production of furfural from xylose and wheat straw by bifunctional chromium phosphate catalyst in biphasic systems. Fuel Processing Technology. 2018;175:90-6.
367. Choudhary V, Sandler SI, Vlachos DG. Conversion of xylose to furfural using Lewis and Brønsted acid catalysts in aqueous media. ACS Catalysis. 2012;2(9):2022-8.
368. Ye L, Han Y, Wang X, Lu X, Qi X, Yu H. Recent progress in furfural production from hemicellulose and its derivatives: Conversion mechanism, catalytic system, solvent selection. Molecular Catalysis. 2021;515:111899.
369. Gupta NK, Fukuoka A, Nakajima K. Amorphous Nb2O5 as a selective and reusable catalyst for furfural production from xylose in biphasic water and toluene. ACS Catalysis. 2017;7(4):2430-6.
370. Lima S, Neves P, Antunes MM, Pillinger M, Ignatyev N, Valente AA. Conversion of mono/di/polysaccharides into furan compounds using 1-alkyl-3-methylimidazolium ionic liquids. Applied Catalysis A: General. 2009;363(1-2):93-9.
371. Peleteiro S, da Costa Lopes AM, Garrote G, Parajó JC, Bogel-Łukasik R. Simple and efficient furfural production from xylose in media containing 1-butyl-3-methylimidazolium hydrogen sulfate. Industrial & Engineering Chemistry Research. 2015;54(33):8368-73.
372. Peleteiro S, Santos V, Garrote G, Parajó JC. Furfural production from Eucalyptus wood using an acidic ionic liquid. Carbohydrate Polymers. 2016;146:20-5.
373. Xia Q, Peng H, Zhang Y, Fu G, Liu Y, Xiao Z, et al. Microwave-assisted furfural production from xylose and bamboo hemicellulose in a biphasic medium. Biomass Conversion and Biorefinery. 2023;13(9):7895-907.
374. Gomes GR, Scopel E, Breitkreitz MC, Rezende CA, Pastre JC. Valorization of sugarcane bagasse C5-fraction by furfural production mediated by renewable glycine-based ionic liquid. Industrial Crops and Products. 2023;191:115940.
375. Steinbach D, Kruse A, Sauer J. Pretreatment technologies of lignocellulosic biomass in water in view of furfural and 5-hydroxymethylfurfural production-a review. Biomass Conversion and Biorefinery. 2017;7(2):247-74.
376. Ibeh CC. 3 - Amino and Furan Resins. In: Goodman SH, editor. Handbook of Thermoset Plastics (Second Edition). Westwood, NJ: William Andrew Publishing; 1998. p. 72-96.
377. Hoang AT. 2-Methylfuran (MF) as a potential biofuel: A thorough review on the production pathway from biomass, combustion progress, and application in engines. Renewable and Sustainable Energy Reviews. 2021;148:111265.
378. Zhang Y, Cui H, Xia H. Recent Advances in the Synthesis of 2-Furoic Acid and 2, 5-Furandicarboxylic Acid from Furfural. ChemSusChem. 2025;18(3):e202401390.

379. Lokhande P, Dhepe PL. Selective and robust Ru catalyst for the aqueous phase aerobic oxidation of furfural to 2-furoic acid. ACS Applied Materials & Interfaces. 2023;15(40):47004-15.
380. Douthwaite M, Huang X, Iqbal S, Miedziak PJ, Brett GL, Kondrat SA, et al. The controlled catalytic oxidation of furfural to furoic acid using AuPd/Mg (OH) 2. Catalysis Science & Technology. 2017;7(22):5284-93.
381. Ferraz CP, Da Silva AGM, Rodrigues TS, Camargo PHC, Paul S, Wojcieszak R. Furfural oxidation on gold supported on MnO2: Influence of the support structure on the catalytic performances. Applied Sciences. 2018;8(8):1246.
382. Kar S, Zhou Q-Q, Ben-David Y, Milstein D. Catalytic furfural/5-hydroxymethyl furfural oxidation to furoic acid/furan-2, 5-dicarboxylic acid with H2 production using alkaline water as the formal oxidant. Journal of the American Chemical Society. 2022;144(3):1288-95.
383. Yu X, Jin T, Wang H, Zhang G, Jia W, Peng L, et al. Heterogeneously-catalyzed aerobic oxidation of furfural to furancarboxylic acid with CuO-Promoted MnO2. Green Energy & Environment. 2023;8(6):1683-92.
384. Oyegoke T, Dumeignil F, E.-Yakubu Jibril B, Michel C, Wojcieszak R. Exploring catalytic oxidation pathways of furfural and 5-hydroxymethyl furfural into carboxylic acids using Au, Pt, and Pd catalysts: a comprehensive review. Catalysis Science & Technology. 2024;14(23):6761-74.
385. Shang C, Liu Z-P. Origin and activity of gold nanoparticles as aerobic oxidation catalysts in aqueous solution. Journal of the American Chemical Society. 2011;133(25):9938-47.
386. Gu Q, Sautet P, Michel C. Unraveling the role of base and catalyst polarization in alcohol oxidation on Au and Pt in water. ACS Catalysis. 2018;8(12):11716-21.
387. Ren Z, Yang Y, Wang S, Li X, Feng H, Wang L, et al. Pt atomic clusters catalysts with local charge transfer towards selective oxidation of furfural. Applied Catalysis B: Environmental. 2021;295:120290.
388. Thuriot-Roukos J, Khadraoui R, Paul Sb, Wojcieszak R. Raman spectroscopy applied to monitor furfural liquid-phase oxidation catalyzed by supported gold nanoparticles. ACS Omega. 2020;5(24):14283-90.
389. Román AM, Agrawal N, Hasse JC, Janik MJ, Medlin JW, Holewinski A. Electro-oxidation of furfural on gold is limited by furoate self-assembly. Journal of Catalysis. 2020;391:327-35.
390. Mori R. Replacing all petroleum-based chemical products with natural biomass-based chemical products: a tutorial review. RSC Sustainability. 2023;1(2):179-212.
391. Mignogna D, Szabó M, Ceci P, Avino P. Biomass energy and biofuels: perspective, potentials, and challenges in the energy transition. Sustainability. 2024;16(16):7036.
392. Cherubini F, Bird ND, Cowie A, Jungmeier G, Schlamadinger B, Woess-Gallasch S. Energy- and greenhouse gas-based LCA of biofuel and bioenergy systems: Key issues, ranges and recommendations. Resources, Conservation and Recycling. 2009;53(8):434-47.
393. Hill J, Nelson E, Tilman D, Polasky S, Tiffany D. Environmental, economic, and energetic costs and benefits of biodiesel and ethanol biofuels. Proceedings of the National Academy of Sciences. 2006;103(30):11206-10.
394. Farrell AE, Plevin RJ, Turner BT, Jones AD, O'hare M, Kammen DM. Ethanol can contribute to energy and environmental goals. Science. 2006;311(5760):506-8.
395. Chang K-L, Han Y-J, Wang X-Q, Chen X-M, Leu S-Y, Liu J-y, et al. The effect of surfactant-assisted ultrasound-ionic liquid pretreatment on the structure and fermentable sugar production of a water hyacinth. Bioresource Technology. 2017;237:27-30.

396. Agbor VB, Cicek N, Sparling R, Berlin A, Levin DB. Biomass pretreatment: Fundamentals toward application. Biotechnology Advances. 2011;29(6):675-85.
397. Binod P, Sindhu R, Singhania RR, Vikram S, Devi L, Nagalakshmi S, et al. Bioethanol production from rice straw: An overview. Bioresource Technology. 2010;101(13):4767-74.
398. Ovejero-Pérez A, Nakasu PYS, Hopson C, Costa JM, Hallett JP. Challenges and opportunities on the utilisation of ionic liquid for biomass pretreatment and valorisation. npj Materials Sustainability. 2024;2(1):7.
399. Liu C-Z, Wang F, Stiles AR, Guo C. Ionic liquids for biofuel production: Opportunities and challenges. Applied Energy. 2012;92:406-14.
400. Kardos N, Luche J-L. Sonochemistry of carbohydrate compounds. Carbohydrate Research. 2001;332(2):115-31.
401. Moholkar VS, Choudhury HA, Singh S, Khanna S, Ranjan A, Chakma S, et al. Physical and Chemical Mechanisms of Ultrasound in Biofuel Synthesis. In: Fang Z, Smith JRL, Qi X, editors. Production of Biofuels and Chemicals with Ultrasound. Dordrecht: Springer Netherlands; 2015. p. 35-86.
402. Luo J, Fang Z, Smith Jr RL. Ultrasound-enhanced conversion of biomass to biofuels. Progress in Energy and Combustion Science. 2014;41:56-93.
403. Sluiter A, Hames B, Hyman D, Payne C, Ruiz R, Scarlata C, et al. Determination of total solids in biomass and total dissolved solids in liquid process samples: Laboratory Analytical Procedure (LAP). National Renewable Energy Laboratory. 2008:2-5.
404. Sluiter A, Ruiz R, Scarlata C, Sluiter J, Templeton D. Determination of extractives in biomass. Laboratory Analytical Procedure (LAP). 2005;1617(4):1-16.
405. Gschwend FJ, Brandt A, Chambon CL, Tu W-C, Weigand L, Hallett JP. Pretreatment of lignocellulosic biomass with low-cost ionic liquids. Journal of Visualized Experiments: JoVE. 2016(114):54246.
406. Sluiter A, Hames B, Ruiz R, Scarlata C, Sluiter J, Templeton D, et al. Determination of structural carbohydrates and lignin in biomass. Laboratory Analytical Procedure. 2008;1617(1):1-16.
407. Resch MG, Baker J, Decker S. Low Solids Enzymatic Saccharification of Lignocellulosic Biomass: National Renewable Energy Laboratory Golden, CO; 2015.
408. Feroz S, Muhammad N, Dias G, Alsaiari MA. Extraction of keratin from sheep wool fibres using aqueous ionic liquids assisted probe sonication technology. Journal of Molecular Liquids. 2022;350:118595.
409. Bundhoo ZM, Mohee R. Ultrasound-assisted biological conversion of biomass and waste materials to biofuels: A review. Ultrasonics Sonochemistry. 2018;40:298-313.
410. Xiang Q, Lee Y, Pettersson PO, Torget RW. Heterogeneous aspects of acid hydrolysis of α-cellulose. Applied Biochemistry and Biotechnology. 2003;107(1):505-14.
411. Xiang Q, Kim JS, Lee Y. A comprehensive kinetic model for dilute-acid hydrolysis of cellulose. Applied Biochemistry and Biotechnology. 2003;106(1):337-52.
412. Koivu KA, Sadeghifar H, Nousiainen PA, Argyropoulos DS, Sipilä J. Effect of fatty acid esterification on the thermal properties of softwood kraft lignin. ACS Sustainable Chemistry & Engineering. 2016;4(10):5238-47.
413. Erden G, Filibeli A. Ultrasonic pre-treatment of biological sludge: consequences for disintegration, anaerobic biodegradability, and filterability. Journal of Chemical Technology &

Biotechnology. 2010;85(1):145-50.
414. Korzen L, Pulidindi IN, Israel A, Abelson A, Gedanken A. Single step production of bioethanol from the seaweed Ulva rigida using sonication. RSC Advances. 2015;5(21):16223-9.
415. Khanpit VV, Tajane SP, Mandavgane SA. Technoeconomic and life cycle analysis of soluble dietary fiber concentrate production from waste orange peels. Waste Management. 2023;155:29-39.
416. Nakasu PY, Piccoli V, Ovejero-Perez A, Kumar P, Al Ghatta A, Melanie S, et al. Fractionation of Squid Pens with Ionic Liquids— An Upgraded β-Chitin and Shellfish Protein Production. ACS Sustainable Chemistry & Engineering. 2025;13(7):2649-60.
417. Huang T-Y, Masum FH, Jiang Y, Li S, Curran SJ, Biruduganti MS, et al. Techno-Economic Analysis and Life Cycle Assessment of Alternative Fuels for Locomotives in the US Freight Rail Sector. Environmental Science & Technology. 2025;59(30):15741-50.
418. Gilardi M, Bisotti F, Berglihn OT, Tschentscher R, Hansen LD, Horn SJ, et al. From laboratory scale to innovative spruce-based biorefinery. Note II: Preliminary techno-economic assessment. In: Manenti F, Reklaitis GV, editors. Computer Aided Chemical Engineering. 53: Elsevier; 2024. p. 2653-8.
419. Al Ghatta A, Wilton-Ely JD, Hallett JP. From sugars to FDCA: a techno-economic assessment using a design concept based on solvent selection and carbon dioxide emissions. Green Chemistry. 2021;23(4):1716-33.
420. Sinnott R, Towler G. Chemical Engineering Design: SI Edition: Butterworth-Heinemann; 2019.
421. Shibukawa VP, Ramos L, Cruz-Santos MM, Prado CA, Jofre FM, de Arruda GL, et al. Impact of product diversification on the economic sustainability of second-generation ethanol biorefineries: a critical review. Energies. 2023;16(17):6384.
422. Strassberger Z, Tanase S, Rothenberg G. The pros and cons of lignin valorisation in an integrated biorefinery. RSC Advances. 2014;4(48):25310-8.
423. Yuan TQ, Xu F, Sun RC. Role of lignin in a biorefinery: separation characterization and valorization. Journal of Chemical Technology & Biotechnology. 2013;88(3):346-52.
424. Kammoun M, Margellou A, Toteva VB, Aladjadjiyan A, Sousa AF, Luis SV, et al. The key role of pretreatment for the one-step and multi-step conversions of European lignocellulosic materials into furan compounds. RSC Advances. 2023;13(31):21395-420.
425. Delbecq F, Wang Y, Muralidhara A, El Ouardi K, Marlair G, Len C. Hydrolysis of hemicellulose and derivatives—A review of recent advances in the production of furfural. Frontiers in Chemistry. 2018;6:146.
426. Al Ghatta A, Nakasu P, Hallett J. Implementation of furan-based building blocks in commodity chemical production: an opinion on scientific progress and economic viability. Current Opinion in Green and Sustainable Chemistry. 2023;41:100792.
427. Zhang H, Jiang M, Wu Y, Li L, Wang Z, Wang R, et al. Development of completely furfural-based renewable polyesters with controllable properties. Green Chemistry. 2021;23(6):2437-48.
428. Dick GR, Frankhouser AD, Banerjee A, Kanan MW. A scalable carboxylation route to furan-2, 5-dicarboxylic acid. Green Chemistry. 2017;19(13):2966-72.
429. Eseyin AE, Steele PH. An overview of the applications of furfural and its derivatives. International Journal of Advanced Chemistry. 2015;3(2):42-7.
430. Lee CBTL, Wu TY. A review on solvent systems for furfural production from lignocellulosic

biomass. Renewable and Sustainable Energy Reviews. 2021;137:110172.
431. Contreras-Zarazúa G, Sánchez-Ramírez E, Vazquez-Castillo JA, Ponce-Ortega JM, Errico M, Kiss AA, et al. Inherently safer design and optimization of intensified separation processes for furfural production. Industrial & Engineering Chemistry Research. 2018;58(15):6105-20.
432. Win DT. Furfural-gold from garbage. AU Journal of Technology. 2005;8(4):185-90.
433. Contreras-Zarazúa G, Martin-Martin M, Sánchez-Ramirez E, Segovia-Hernández JG. Furfural production from agricultural residues using different intensified separation and pretreatment alternatives. Economic and environmental assessment. Chemical Engineering and Processing-Process Intensification. 2022;171:108569.
434. Wirtz RA, Dague RR. Anaerobic treatment of a furfural-production wastewater. Waste Management. 1993;13(4):309-15.
435. Wang Z, Liu Z, Noor RS, Cheng Q, Chu X, Qu B, et al. Furfural wastewater pretreatment of corn stalk for whole slurry anaerobic co-digestion to improve methane production. Science of the Total Environment. 2019;674:49-57.
436. Román-Leshkov Y, Dumesic JA. Solvent effects on fructose dehydration to 5-hydroxymethylfurfural in biphasic systems saturated with inorganic salts. Topics in Catalysis. 2009;52:297-303.
437. Liu P, Sun L, Jia X, Zhang C, Zhang W, Song Y, et al. Efficient one-pot conversion of furfural into 2-methyltetrahydrofuran using non-precious metal catalysts. Molecular Catalysis. 2020;490:110951.
438. Guo X, Guo F, Li Y, Zheng Z, Xing Z, Zhu Z, et al. Dehydration of D-xylose into furfural over bimetallic salts of heteropolyacid in DMSO/H2O mixture. Applied Catalysis A: General. 2018;558:18-25.
439. Mittal A, Black SK, Vinzant TB, O'Brien M, Tucker MP, Johnson DK. Production of furfural from process-relevant biomass-derived pentoses in a biphasic reaction system. ACS Sustainable Chemistry & Engineering. 2017;5(7):5694-701.
440. Weingarten R, Cho J, Conner Jr WC, Huber GW. Kinetics of furfural production by dehydration of xylose in a biphasic reactor with microwave heating. Green Chemistry. 2010;12(8):1423-9.
441. Peleteiro S, da Costa Lopes AM, Garrote G, Bogel-Łukasik R, Parajó JC. Manufacture of furfural in biphasic media made up of an ionic liquid and a co-solvent. Industrial Crops and Products. 2015;77:163-6.
442. Yang Y, Hu CW, Abu-Omar MM. Synthesis of furfural from xylose, xylan, and biomass using AlCl3· 6 H2O in biphasic media via xylose isomerization to xylulose. ChemSusChem. 2012;5(2):405-10.
443. Eminov S, Wilton-Ely JD, Hallett JP. Highly selective and near-quantitative conversion of fructose to 5-hydroxymethylfurfural using mildly acidic ionic liquids. ACS Sustainable Chemistry & Engineering. 2014;2(4):978-81.
444. Al Ghatta A, Zhou X, Casarano G, Wilton-Ely JD, Hallett JP. Characterization and valorization of humins produced by HMF degradation in ionic liquids: A valuable carbonaceous material for antimony removal. ACS Sustainable Chemistry & Engineering. 2021;9(5):2212-23.
445. Ghatta AA, Wilton-Ely JD, Hallett JP. Rapid, High-Yield Fructose Dehydration to 5-Hydroxymethylfurfural in Mixtures of Water and the Noncoordinating Ionic Liquid [bmim][OTf]. ChemSusChem. 2019;12(19):4452-60.

446. Zhang L, Yu H, Wang P. Solid acids as catalysts for the conversion of d-xylose, xylan and lignocellulosics into furfural in ionic liquid. Bioresource Technology. 2013;136:515-21.
447. Zhang L, Yu H, Wang P, Dong H, Peng X. Conversion of xylan, d-xylose and lignocellulosic biomass into furfural using AlCl3 as catalyst in ionic liquid. Bioresource Technology. 2013;130:110-6.
448. Xu G, Tu Z, Hu X, Li M, Zhang X, Wu Y. Protic Brønsted acidic ionic liquids with variable acidity for efficient conversion of xylose and hemicellulose to furfural. Fuel. 2023;339:127334.
449. Ghatta AA, Wilton-Ely JD, Hallett JP. Strategies for the Separation of the Furanic Compounds HMF, DFF, FFCA, and FDCA from Ionic Liquids. ACS Sustainable Chemistry & Engineering. 2019;7(19):16483-92.
450. Peleteiro S, Rivas S, Alonso JL, Santos V, Parajó JC. Furfural production using ionic liquids: A review. Bioresource Technology. 2016;202:181-91.
451. Ntimbani RN, Farzad S, Görgens JF. Furfural production from sugarcane bagasse along with co-production of ethanol from furfural residues. Biomass Conversion and Biorefinery. 2022;12(11):5257-67.
452. Mao L, Zhang L, Gao N, Li A. FeCl3 and acetic acid co-catalyzed hydrolysis of corncob for improving furfural production and lignin removal from residue. Bioresource Technology. 2012;123:324-31.
453. Channiwala S, Parikh P. A unified correlation for estimating HHV of solid, liquid and gaseous fuels. Fuel. 2002;81(8):1051-63.
454. Wang H, Zhang J, Wang G, Xu R, Zhang P, Liu S, et al. Characteristics and kinetic analysis of co-combustion of brown coal and anthracite. Journal of Thermal Analysis and Calorimetry. 2016;126(2):447-54.
455. Almhofer L, Bischof RH, Madera M, Paulik C. Kinetic and mechanistic aspects of furfural degradation in biorefineries. The Canadian Journal of Chemical Engineering. 2023;101(4):2033-49.
456. Firth AE, Nakasu PY, Hallett JP, Matthews RP. Exploiting cation structure and water content in modulating the acidity of ammonium hydrogen sulfate protic ionic liquids. The Journal of Physical Chemistry Letters. 2024;15(9):2311-8.
457. Abushammala H, Mao J. A review on the partial and complete dissolution and fractionation of wood and lignocelluloses using imidazolium ionic liquids. Polymers. 2020;12(1):195.
458. Cruz AG, Scullin C, Mu C, Cheng G, Stavila V, Varanasi P, et al. Impact of high biomass loading on ionic liquid pretreatment. Biotechnology for Biofuels. 2013;6(1):52.
459. Wu H, Mora-Pale M, Miao J, Doherty TV, Linhardt RJ, Dordick JS. Facile pretreatment of lignocellulosic biomass at high loadings in room temperature ionic liquids. Biotechnology and Bioengineering. 2011;108(12):2865-75.
460. Zhu J, Pan X. Woody biomass pretreatment for cellulosic ethanol production: technology and energy consumption evaluation. Bioresource Technology. 2010;101(13):4992-5002.
461. Baral NR, Shah A. Techno - economic analysis of cellulose dissolving ionic liquid pretreatment of lignocellulosic biomass for fermentable sugars production. Biofuels, Bioproducts and Biorefining. 2016;10(1):70-88.
462. Klein - Marcuschamer D, Simmons BA, Blanch HW. Techno - economic analysis of a lignocellulosic ethanol biorefinery with ionic liquid pre - treatment. Biofuels, Bioproducts and Biorefining. 2011;5(5):562-9.

463. Zhao Z, Wang B, Theng BK, Lee X, Zhang X, Chen M, et al. Removal performance, mechanisms, and influencing factors of biochar for air pollutants: a critical review. Biochar. 2022;4(1):30.
464. Dunnigan L, Morton BJ, Ashman PJ, Zhang X, Kwong CW. Emission characteristics of a pyrolysis-combustion system for the co-production of biochar and bioenergy from agricultural wastes. Waste Management. 2018;77:59-66.
465. Jia J, Wu Y, Zhao D, Li B, Wang D, Wang F, et al. Molecular structure characterization analysis and molecular model construction of anthracite. PLOS ONE. 2022;17(9):e0275108.
466. Chen X, Ma X, Peng X, Lin Y, Yao Z. Conversion of sweet potato waste to solid fuel via hydrothermal carbonization. Bioresource Technology. 2018;249:900-7.
467. Zheng C, Ma X, Yao Z, Chen X. The properties and combustion behaviors of hydrochars derived from co-hydrothermal carbonization of sewage sludge and food waste. Bioresource Technology. 2019;285:121347.
468. Rafiq MK, Bachmann RT, Rafiq MT, Shang Z, Joseph S, Long R. Influence of pyrolysis temperature on physico-chemical properties of corn stover (Zea mays L.) biochar and feasibility for carbon capture and energy balance. PLOS ONE. 2016;11(6):e0156894.
469. Enders A, Hanley K, Whitman T, Joseph S, Lehmann J. Characterization of biochars to evaluate recalcitrance and agronomic performance. Bioresource Technology. 2012;114:644-53.
470. Yao Z, Ma X. Hydrothermal carbonization of Chinese fan palm. Bioresource Technology. 2019;282:28-36.
471. Yao Z, Ma X, Lin Y. Effects of hydrothermal treatment temperature and residence time on characteristics and combustion behaviors of green waste. Applied Thermal Engineering. 2016;104:678-86.
472. Spokas KA. Review of the stability of biochar in soils: predictability of O: C molar ratios. Carbon Management. 2010;1(2):289-303.
473. Liu Z, Quek A, Kent Hoekman S, Balasubramanian R. Production of solid biochar fuel from waste biomass by hydrothermal carbonization. Fuel. 2013;103:943-9.
474. Zhang L, Wang Q, Wang B, Yang G, Lucia LA, Chen J. Hydrothermal Carbonization of Corncob Residues for Hydrochar Production. Energy & Fuels. 2015;29(2):872-6.
475. Reza MT, Lynam JG, Uddin MH, Coronella CJ. Hydrothermal carbonization: Fate of inorganics. Biomass and Bioenergy. 2013;49:86-94.
476. Permchart W, Kouprianov VI. Emission performance and combustion efficiency of a conical fluidized-bed combustor firing various biomass fuels. Bioresource Technology. 2004;92(1):83-91.
477. Polesca C, Al Ghatta A, Passos H, Coutinho JA, Hallett JP, Freire MG. Sustainable keratin recovery process using a bio-based ionic liquid aqueous solution and its techno-economic assessment. Green Chemistry. 2023;25(10):3995-4003.
478. Abouelela AR, Al Ghatta A, Verdía P, Shan Koo M, Lemus J, Hallett JP. Evaluating the role of water as a cosolvent and an antisolvent in [HSO4]-based protic ionic liquid pretreatment. ACS Sustainable Chemistry & Engineering. 2021;9(31):10524-36.
479. Mari Selvam S, Balasubramanian P, Chintala M, Gujjala LKS. Techno-economic analysis of microwave pyrolysis of sugarcane bagasse biochar production. Biomass Conversion and Biorefinery. 2025;15(9):14229-39.
480. Pal P, Kumar R, Ghosh AK. Analysis of process intensification and performance assessment

for fermentative continuous production of bioethanol in a multi-staged membrane-integrated bioreactor system. Energy Conversion and Management. 2018;171:371-83.
481. Gómez Millán G, Bangalore Ashok RP, Oinas P, Llorca J, Sixta H. Furfural production from xylose and birch hydrolysate liquor in a biphasic system and techno-economic analysis. Biomass Conversion and Biorefinery. 2021;11:2095-106.
482. Ahn B, Park C, Liu JJ, Ok YS, Won W. Maximizing the utilization of lignocellulosic biomass: Process development and analysis. Renewable Energy. 2023;215:119004.
483. Al Rawas HK, Ferraz CP, Thuriot-Roukos J, Heyte S, Paul S, Wojcieszak R. Influence of Pd and Pt promotion in gold based bimetallic catalysts on selectivity modulation in furfural base-free oxidation. Catalysts. 2021;11(10):1226.
484. Dunlop AP. Process for manufacturing furoic acid and furoic acid salts. Google Patents; 1946.
485. Sustainable, biobased surfactants for cleaning products and industrial applications: Bioataraxis Ltd; [updated 2026/02/21]. Available from: https://www.bioatx.com/.
486. Alonso-Fagúndez N, Ojeda M, Mariscal R, Fierro J, Granados ML. Gas phase oxidation of furfural to maleic anhydride on V2O5/γ-Al2O3 catalysts: reaction conditions to slow down the deactivation. Journal of Catalysis. 2017;348:265-75.
487. Alba-Rubio A, Fierro J, León-Reina L, Mariscal R, Dumesic J, Granados ML. Oxidation of furfural in aqueous H2O2 catalysed by titanium silicalite: Deactivation processes and role of extraframework Ti oxides. Applied Catalysis B: Environmental. 2017;202:269-80.
488. Hengne A, Biradar N, Rode C. Surface species of supported ruthenium catalysts in selective hydrogenation of levulinic esters for bio-refinery application. Catalysis Letters. 2012;142(6):779-87.
489. Morgan DJ. Resolving ruthenium: XPS studies of common ruthenium materials. Surface and Interface Analysis. 2015;47(11):1072-9.
490. Liu C, Li R, Fan Y, Li S, Feng X, Feng L, et al. Liquid-mediated Ostwald ripening of Ag-based clusters supported on oxides. Nano Research. 2024;17(6):4971-8.
491. Hansen TW, DeLaRiva AT, Challa SR, Datye AK. Sintering of catalytic nanoparticles: particle migration or Ostwald ripening? Accounts of Chemical Research. 2013;46(8):1720-30.
492. Aktı N, Yildiz S. Exploring ultrasound-induced free radical formation: A comparative study in water and sour cherry juice using glutathione and terephthalic acid indicators. Ultrasonics Sonochemistry. 2025;112:107193.
493. Duque A, Manzanares P, Ballesteros M. Extrusion as a pretreatment for lignocellulosic biomass: Fundamentals and applications. Renewable Energy. 2017;114:1427-41.
494. Kumar AK, Sharma S. Recent updates on different methods of pretreatment of lignocellulosic feedstocks: a review. Bioresources and Bioprocessing. 2017;4(1):7.
495. Jain S, Kumar S. Advances and challenges in pretreatment technologies for bioethanol production: A comprehensive review. Sustainable Chemistry for Climate Action. 2024;5:100053.
496. Heredia-Olea E, Pérez-Carrillo E, Montoya-Chiw M, Serna-Saldívar SO. Effects of extrusion pretreatment parameters on sweet sorghum bagasse enzymatic hydrolysis and its subsequent conversion into bioethanol. BioMed Research International. 2015;2015(1):325905.
497. Wahid R, Hjorth M, Kristensen S, Møller HB. Extrusion as pretreatment for boosting methane production: effect of screw configurations. Energy & Fuels. 2015;29(7):4030-7.
498. Lamsal B, Yoo J, Brijwani K, Alavi S. Extrusion as a thermo-mechanical pre-treatment for

lignocellulosic ethanol. Biomass and Bioenergy. 2010;34(12):1703-10.
499. Zhou Z, Ouyang D, Liu D, Zhao X. Oxidative pretreatment of lignocellulosic biomass for enzymatic hydrolysis: Progress and challenges. Bioresource Technology. 2023;367:128208.
500. Li M, Foster C, Kelkar S, Pu Y, Holmes D, Ragauskas A, et al. Structural characterization of alkaline hydrogen peroxide pretreated grasses exhibiting diverse lignin phenotypes. Biotechnology for Biofuels. 2012;5(1):38.
501. Li J, Zha Y-N, Wang H-M, Tian J-N, Hou Q-X. Advances in lignin chemistry during pulping and bleaching. Industrial Crops and Products. 2025;229:121004.
502. Ho MC, Ong VZ, Wu TY. Potential use of alkaline hydrogen peroxide in lignocellulosic biomass pretreatment and valorization–A review. Renewable and Sustainable Energy Reviews. 2019;112:75-86.
503. García-Cubero MT, González-Benito G, Indacoechea I, Coca M, Bolado S. Effect of ozonolysis pretreatment on enzymatic digestibility of wheat and rye straw. Bioresource Technology. 2009;100(4):1608-13.
504. Ummalyma SB, Herojit N, Sukumaran RK. Alkaline hydrogen peroxide pretreatment of bamboo residues and its influence on physiochemical properties and enzymatic digestibility for bioethanol production. Frontiers in Energy Research. 2024;12:1444813.
505. Ferrer A, Vega A, Rodríguez A, Ligero P, Jiménez L. Milox fractionation of empty fruit bunches from Elaeis guineensis. Bioresource Technology. 2011;102(20):9755-62.
506. Zhao X, Cheng K, Liu D. Organosolv pretreatment of lignocellulosic biomass for enzymatic hydrolysis. Applied Microbiology and Biotechnology. 2009;82(5):815-27.
507. Zhang Z, Harrison MD, Rackemann DW, Doherty WO, O'Hara IM. Organosolv pretreatment of plant biomass for enhanced enzymatic saccharification. Green Chemistry. 2016;18(2):360-81.
508. Rabelo SC, Nakasu PYS, Scopel E, Araújo MF, Cardoso LH, Da Costa AC. Organosolv pretreatment for biorefineries: Current status, perspectives, and challenges. Bioresource Technology. 2023;369:128331.
509. Madhu R, Periasamy AP, Schlee P, Hérou S, Titirici M-M. Lignin: A sustainable precursor for nanostructured carbon materials for supercapacitors. Carbon. 2023;207:172-97.
510. Sun S-L, Wen J-L, Ma M-G, Sun R-C, Jones GL. Structural features and antioxidant activities of degraded lignins from steam exploded bamboo stem. Industrial Crops and Products. 2014;56:128-36.
511. Chundawat SPS, Balan V, Sousa LDc, Dale BE. 2 - Thermochemical pretreatment of lignocellulosic biomass. In: Waldron K, editor. Bioalcohol Production: Woodhead Publishing; 2010. p. 24-72.
512. Borand MN, Karaosmanoğlu F. Effects of organosolv pretreatment conditions for lignocellulosic biomass in biorefinery applications: a review. Journal of Renewable and Sustainable Energy. 2018;10(3).
513. Park N, Kim H-Y, Koo B-W, Yeo H, Choi I-G. Organosolv pretreatment with various catalysts for enhancing enzymatic hydrolysis of pitch pine (Pinus rigida). Bioresource Technology. 2010;101(18):7046-53.
514. Huijgen WJ, Smit AT, Reith JH, Uil Hd. Catalytic organosolv fractionation of willow wood and wheat straw as pretreatment for enzymatic cellulose hydrolysis. Journal of Chemical Technology & Biotechnology. 2011;86(11):1428-38.

515. Luo H, Abu-Omar MM. Chemicals From Lignin. In: Abraham MA, editor. Encyclopedia of Sustainable Technologies. Oxford: Elsevier; 2017. p. 573-85.
516. Taherzadeh MJ, Karimi K. Pretreatment of lignocellulosic wastes to improve ethanol and biogas production: a review. International Journal of Molecular Sciences. 2008;9(9):1621-51.
517. Zheng Y, Lin H-M, Wen J, Cao N, Yu X, Tsao GT. Supercritical carbon dioxide explosion as a pretreatment for cellulose hydrolysis. Biotechnology Letters. 1995;17(8):845-50.
518. Capolupo L, Faraco V. Green methods of lignocellulose pretreatment for biorefinery development. Applied Microbiology and Biotechnology. 2016;100(22):9451-67.
519. Narayanaswamy N, Faik A, Goetz DJ, Gu T. Supercritical carbon dioxide pretreatment of corn stover and switchgrass for lignocellulosic ethanol production. Bioresource Technology. 2011;102(13):6995-7000.
520. Lv H, Yan L, Zhang M, Geng Z, Ren M, Sun Y. Influence of Supercritical CO2 Pretreatment of Corn Stover with Ethanol-Water as Co-Solvent on Lignin Degradation. Chemical Engineering & Technology. 2013;36(11):1899-906.
521. Zheng Y, Lin HM, Tsao GT. Pretreatment for cellulose hydrolysis by carbon dioxide explosion. Biotechnology Progress. 1998;14(6):890-6.
522. Arce C, Kratky L. Mechanical pretreatment of lignocellulosic biomass toward enzymatic/fermentative valorization. iScience. 2022;25(7):104610.
523. Chen X, He D, Hou T, Lu M, Mosier NS, Han L, et al. Structure–property–degradability relationships of varisized lignocellulosic biomass induced by ball milling on enzymatic hydrolysis and alcoholysis. Biotechnology for Biofuels and Bioproducts. 2022;15(1):36.
524. Konan D, Koffi E, Ndao A, Peterson EC, Rodrigue D, Adjallé K. An overview of extrusion as a pretreatment method of lignocellulosic biomass. Energies. 2022;15(9):3002.
525. Millati R, Syamsiah S, Niklasson C, Cahyanto MN, Ludquist K, Taherzadeh MJ. Biological pretreatment of lignocelluloses with white-rot fungi and its applications: a review. BioResources. 2011;6(4):5224-59.
526. Pu Y, Hu F, Huang F, Davison BH, Ragauskas AJ. Assessing the molecular structure basis for biomass recalcitrance during dilute acid and hydrothermal pretreatments. Biotechnology for Biofuels. 2013;6(1):15.
527. Hoang AT, Nguyen XP, Duong XQ, Ağbulut Ü, Len C, Nguyen PQP, et al. Steam explosion as sustainable biomass pretreatment technique for biofuel production: Characteristics and challenges. Bioresource Technology. 2023;385:129398.
528. Bertran-Llorens S, Perondi F, de Freitas ALS, Chen J, van Erven G, Deuss PJ. Supercritical CO2 as effective wheat straw pretreatment for subsequent mild fractionation strategies. Chemical Engineering Journal. 2024;497:154491.